Synthesis, Characterization and Computational Studies of Binary and Ternary Intermetallic Compounds in the Systems Alkaline Earth Metal / Transition Metal / Tetrel Element

Lisa Siggelkow

Dissertation

Technische Universität München

TECHNISCHE UNIVERSITÄT MÜNCHEN

Lehrstuhl für Anorganische Chemie mit Schwerpunkt Neue Materialien

Synthesis, Characterization and Computational Studies of Binary and Ternary Intermetallic Compounds in the Systems Alkaline Earth Metal / Transition Metal / Tetrel Element

Lisa Siggelkow

Vollständiger Abdruck der von der Fakultät für Chemie der Technischen Universität München zur Erlangung des akademischen Grades eines

Doktors der Naturwissenschaften

genehmigten Dissertation.

Vorsitzender:	Univ.-Prof. Dr. Tom Nilges
Prüfer der Dissertation:	1. Univ.-Prof. Dr. Thomas F. Fässler
	2. Univ.-Prof. Dr. Wolfgang Domcke

Die Dissertation wurde am 11.10.2011 bei der Technischen Universität München eingereicht und durch die Fakultät für Chemie am 24.11.2011 angenommen.

By measuring the electrical properties of these substances we must travel like Jules Verne changing from horse to boat, from land (Zintl phase) to sea (intermetallic phase) quite frequently, with exclusive regard of the properties of the surfaces (the surfaces of the properties). The diver, however, has another view of the sea, than the sailor, because he can see the rich structures below the water surface. (Though he does not feel a spring flood or a hurricane). His view is comparable to the search of the local chemical bonding in intermetallic phases.

Having this in mind, we might be brave and try to probe the validity of the Zintl-Klemm concept in selected intermetallic phases as well.

Reinhard Nesper, *Prog. Solid St. Chem.* **1990**, *20*, 1 – 45.

Acknowledgment

I would like to express my sincere gratitude

to **Prof. Dr. T. F. Fässler** for accepting me as a PhD student in his group, the fascinating topic, a high amount of scientific freedom and constructive discussions.
to **Dr. Viktor Hlukhyy** for introducing me to the richness of solid state chemistry and for his constant help with words and deeds especially concerning problems of synthesis and structural chemistry.
to **Saskia Stegmaier** for valuable discussions, a lot of very thorough corrections and last but not least for a great partnership in the laboratory.
to **Dr. Bernhard Wahl** for his help concerning crystallographic problems, for valuable discussions and advices in every respect.
to **Dr. Sandra Scharfe** for a cup of tea whenever necessary.
to **Dr. Bele Boeddinghaus** for the SQUID measurements and for constant encouragement.
to **Priv.-Doz. Dr. Florian Kraus** for introducing me to the distillation of alkaline earth metals and for advices concerning my experimental work.
to **Prof. Dr. T. Nilges** for discussions about phase transitions.
to **Dr. Wilhelm Klein** for advices concerning crystallographic problems.
to **Dr. Andreas Kaltzoglou** for the time in the 'Praktikum für Lebensmittelchemiker' and for his introduction to the DTA.
to **Markus Waibel** for setting up a useful and efficient IT infrastructure.
to **Andrea Hoffmann** for proofreading this manuscript and for SQUID measurements.
to **Iryna Kurylyshyn** for proofreading this manuscript and for measurements on the APEX II.
to my trainees **Vanessa Rodig** and **Fabian Krause**, as well as to my students **Yun Zhang**, **Daniel Bülichen**, **Tilly Fleckenstein** and **Marianne Köpf** for their experimental work.

to **Ingrid Werner** for the EDX measurements.
to **Manuela Donaubauer** for her assistance and quick help concerning organizational questions.

Further, I would like to thank the **Universität Bayern e.V.** for a PhD scholarship, and the **TU München** for subsequent funding through a HWP PhD scholarship.

Many others have contributed to this work, by discussions, help in the laboratory or just by creating a great and friendly atmosphere. Therefore, I would like to thank all co-workers during my time in Prof. Fässler's group: **Dr. Prashanth W. Menezes** (for proofreading this manuscript), **Dr. Annette Spiekermann, Dr. Sung-Jin Kim, Dr. Florian Kiefer, Dr. Mike Evans, Dr. Antti Karttunen, Volodymyr Baran, Christian Benda, Haiyan He, Sebastian Baer, Patrick Woidy, Michael Zeilinger, Carina Dressel, Alexander Henze, Laura Jantke, Herta Slavik, Lorenzo Toffoletti** and **Ursula Madan-Singh** as well as all members of **Prof. Niewa's** and **Prof. Nilges' group**.

Finally, I would like to thank **my family** and **my friends** for their constant support. My special thanks go to my husband **Matthias Medger** for eternal patience and encouragement and last but not least for his steady technical support concerning my questions about Linux.

Contents

Organisation of this work

This work is composed as a paper style thesis. The content is organized as follows:

- Chapter 1: Introduction to the topic of intermetallics and polar intermetallic compounds.
- Chapter 2: Details on the employed experimental and computational methods.
- Chapter 3: Summary of all results of this thesis.
- Chapter 4: Publications. These form the main body of this thesis. If already published, the corresponding bibliographic citation and, if necessary, an additional appendix is given. The manuscripts in preparation for submission are embedded and followed by the corresponding supporting information.
- Chapter 5: General appendix.

Abbreviations

1b	one-bonded
2b	two-bonded
2θ	diffraction angle
ADP	anisotropic displacement parameter
Ae	alkaline earth metal
AIM	atoms in molecules
APW	augmented plane-wave
ASA	atomic-sphere approximation
COHP	crystal orbital hamilton population
d	interatomic distance
DFT	density functional theory
DOS	density of states
DTA	differential thermal analysis
E	elements of groups 13-15
EDX	energy dispersive X-ray spectroscopy
E_F	fermi energy
ELF	electron localization function
F	structure factor
FP	full potential
GGA	generalized gradient approximation
GooF	goodness of fit
h, k, l	Miller indices
I	intensity
ICDD	International Center for Diffraction Data
ICOHP	integrated crystal orbital Hamilton population
IDOS	integrated density of states
IPDS	imaging plate diffraction system
IP-PSD	imaging plate position sensitive detector

L-PSD	linear position sensitive detector
LAPW	linearized augmented plane-wave
LDA	local density approximation
LMTO	linear muffin-tin orbital
lo	local orbitals
λ	wavelength
mBJ	modified Becke-Johnson potential
Occ.	occupancy
R	residual factor
Re	rare earth metal
SEM	scanning electron microscopy
SQUID	superconducting quantum interference device
T	transition metal
T_b	temperature of the boiling point
TB	tight-binding
T_m	temperature of the melting point
Tt	tetrel element
U	thermal displacement parameter(s)
VEC	valence electron concentration
Z	formula units per unit cell

Abstract

The present thesis aims to extend the knowledge about the polar intermetallic compounds of the systems *Ae*/*T*/*Tt* (*Ae*: Mg, Ca, Sr, Ba; *T*: Ni, Co; *Tt*: Si, Ge, Sn). In this context a series of binary and ternary phases was discovered. The synthesized compounds were analyzed by powder and single crystal X-ray diffraction analysis, Energy Dispersive X-ray spectroscopy (EDX), Differential Thermal Analysis (DTA) and magnetic measurements testing for superconducting behavior. Next to the structural characterization of the compounds, a main focus is placed on the electronic structures. DFT calculations were carried out using the programs TB-LMTO-ASA as well as WIEN2K in order to provide a basis for the discussion of the electronic structures. The chemical bonding situations were discussed based on the Density Of States (DOS) curves, bandstructures including fatbands, Crystal Orbital Hamilton Populations (COHP), topological analyses of the Electron Localization Function (ELF) and Bader's Atoms in Molecules (AIM).

The first part of this thesis deals with the three binary phases Sr_7Ge_6, Ba_7Ge_6 and Ba_3Sn_2. A main focus is put on the bonding situation: while Ba_3Sn_2 is a semiconductor and can be classified as a Zintl phase by applying the (8-*N*) rule, Sr_7Ge_6 and Ba_7Ge_6 are metallic conductors and do not follow the Zintl-Klemm concept. Hence, the possibility of the formation of a partial double bond is discussed.

The second part of this thesis deals with ternary polar intermetallic compounds of the systems *Ae*/Ni/Ge (*Ae*: Mg, Ca, Sr, Ba). The crystal and electronic structures of the polar intermetallic compounds $BaNi_2Ge$, $Ca_4Ni_4Ge_3$, $CaNi_5Ge_3$, $Ca_{15}Ni_{68}Ge_{37}$, $Ca_7Ni_{49}Ge_{22}$, $Ba_2Ni_5Ge_4$ and two Laves phases of the system Mg/Ni/Ge are reported in detail. Furthermore, the rich chemistry of the systems *Ae*/Ni/Ge (*Ae*: Ca, Sr, Ba) is reviewed, analyzing the structural relationships between the various compounds. Here a description of polar intermetallic compounds in analogy to the Zintl-Klemm concept is discussed.

The third part comprises the polar intermetallic compounds $CaCo_2Si_2$ and $BaCo_2Ge_2$. These crystallize in the $ThCr_2Si_2$ structure type, which came to the focus of attention when one of its representatives, $(Ba_{0.6}K_{0.4})Fe_2As_2$, was reported to show

superconductivity with the high transition temperature of 38 K, being the first member of a new “122” family of superconducting intermetallic iron-arsenides. For $CaCo_2Si_2$ and $BaCo_2Ge_2$ the bonding situation, is discussed with main focus on the tunable *Tt*-*Tt* distance.

In the fourth part of this thesis new compounds of the systems *Ae*/Ni/Sn (*Ae*: Mg, Ca) are presented. The dimorphic polar intermetallic phase Ca_2NiSn_2 is introduced. Two different pathways for the structural transition from *mC*-Ca_2NiSn_2, with a three-dimensional Ni-Sn network, to *oP*-Ca_2NiSn_2, with two-dimensional Ni-Sn layers, are suggested. While the crystal structures of the two modifications of Ca_2NiSn_2 are comparable to those observed for the germanides, those of the intermetallic compounds $Mg_{0.39(2)}NiSn_{1.61(2)}$ and $Mg_{2.61(2)}Ni_4Sn_{3.39(2)}$ exclude themselves from such a comparison. Due to mixed occupancies of Mg and Sn, these structures are rather described as a network of Mg and Sn with cavities in which the Ni atoms are situated. Thus, $Mg_{0.39(2)}NiSn_{2.61(2)}$ and $Mg_{2.61(2)}Ni_4Sn_{3.39(2)}$ belong to the classical intermetallic phases. For example, the structure of $Mg_{2.61(2)}Ni_4Sn_{3.39(2)}$ can be described as intermediate between that of a Heusler and a Half-Heusler type phase.

Zusammenfassung

Mit der vorliegenden Arbeit soll das Wissen auf dem Gebiet der polaren intermetallischen Verbindungen der Systeme *Ae*/*T*/*Tt* (*Ae*: Mg, Ca, Sr, Ba; *T*: Ni, Co, *Tt*: Si, Ge, Sn) erweitert werden. In diesem Zusammenhang wurde eine Reihe von neuen binären und ternären Phasen identifiziert. Die Strukturen der synthetisierten Verbindungen wurden mittels Röntgenbeugung am Pulver und am Einkristall aufgeklärt. Des Weiteren wurden die Verbindungen mittels energiedispersiver Röntgenspektroskopie (EDX), Differenz-Thermoanalyse (DTA) und magnetischen Messungen zu supraleitendem Verhalten analysiert. Neben der Strukturaufklärung und -beschreibung wurde die elektronische Struktur der Verbindungen näher betrachtet. DFT Rechnungen wurden mit den Programmen TB-LMTO-ASA und WIEN2K durchgeführt. Die elektronischen Strukturen wurden auf Grundlage der berechneten Zustandsdichten (DOS) und der Bandstrukturen einschließlich Fatbands diskutiert. Ein besonderer Schwerpunkt wurde auf die Analyse der chemischen Bindung gelegt, hierzu wurden die Crystal Orbital Hamilton Populationen (COHP), die topologische Analyse der Elektronendichte (ELF) und Baders Atoms in Molecules (AIM) diskutiert.

Im ersten Teil dieser Arbeit werden die drei binären Phasen Sr_7Ge_6, Ba_7Ge_6 und Ba_3Sn_2 beschrieben. Diskussionsschwerpunkt ist dabei die Analyse der Bindungssituation: Ba_3Sn_2 ist ein Halbleiter und kann nach der (8-*N*)-Regel als Zintl-Phase klassifiziert werden. Sr_7Ge_6 und Ba_7Ge_6 liegen dagegen als metallische Leiter vor und können nicht mit dem Zintl-Klemm-Konzept beschrieben werden. Die Möglichkeit einer partiellen Doppelbindung wird daher diskutiert.

Der zweite Teil beschreibt ternäre polare intermetallische Verbindungen der Systeme *Ae*/Ni/Ge (*Ae*: Mg, Ca, Sr, Ba). Die Kristallstrukturen und Bindungsverhältnisse der Verbindungen $BaNi_2Ge$, $Ca_4Ni_4Ge_3$, $CaNi_5Ge_3$, $Ca_{15}Ni_{68}Ge_{37}$, $Ca_7Ni_{49}Ge_{22}$, $Ba_2Ni_5Ge_4$ und der zwei Laves-Phasen des Systems Mg/Ni/Ge werden detailliert untersucht. Ein weiteres Kapitel fasst die vielfältige Chemie der Systeme *Ae*/Ni/Ge zusammen und analysiert die strukturellen Beziehungen zwischen den verschiedenen Verbindungen. Eine

Beschreibung der polaren intermetallischen Verbindungen in Analogie zum Zintl-Klemm-Konzept wird diskutiert.

Im dritten Teil werden die polaren intermetallischen Verbindungen $CaCo_2Si_2$ und $BaCo_2Ge_2$ diskutiert. Diese kristallisieren im $ThCr_2Si_2$ Strukturtyp, der in den Fokus der Aufmerksamkeit rückte, als für $(Ba_{0.6}K_{0.4})Fe_2As_2$ Supraleitung mit einer hohen Sprungtemperatur von 38 K beobachtet wurde. Diese Verbindung begründete eine neue "122"-Familie supraleitender intermetallischer Eisen-Arsenide. Bezüglich der Bindungssituation wird für $CaCo_2Si_2$ und $BaCo_2Ge_2$ die variable *Tt*-*Tt* Bindung diskutiert.

Im letzen Teil dieser Arbeit werden neue Verbindungen der Systeme *Ae*/Ni/Sn (*Ae*: Mg, Ca) beschrieben. Zunächst wird die dimorphe polare intermetallische Phase Ca_2NiSn_2 vorgestellt. Für den Phasenübergang von *mC*-Ca_2NiSn_2 zu *oP*-Ca_2NiSn_2 (Übergang von dreidimensionalen Ni-Sn-Netzwerken zu zweidimensionalen Ni-Sn-Schichten) werden zwei unterschiedliche Mechanismen vorgeschlagen. Während die Kristallstrukturen beider Modifikationen von Ca_2NiSn_2 mit denen der Germanide vergleichbar sind, entziehen sich die intermetallischen Verbindungen $Mg_{0.39(2)}NiSn_{1.61(2)}$ und $Mg_{2.61(2)}Ni_4Sn_{3.39(2)}$ einem solchen Vergleich. Da unter anderem Positionen mit Mg/Sn Mischbesetzungen vorliegen, werden diese Strukturen als Mg/Sn Netzwerke, in deren Hohlräumen sich die Ni-Atome befinden, beschrieben. Somit gehören $Mg_{0.39(2)}NiSn_{2.61(2)}$ und $Mg_{2.61(2)}Ni_4Sn_{3.39(2)}$ zu den klassischen intermetallischen Phasen. Beispielsweise kann $Mg_{2.61(2)}Ni_4Sn_{3.39(2)}$ als Zwischenstufe einer Heusler und einer Halb-Heusler Phase beschrieben werden.

1 Introduction

1.1 Motivation

Ever since the beginning of human civilization intermetallic phases in the form of alloys have been an important part of culture. Until today they are used in various fields of industry. Recalling some of the more prominent examples, these are steels, due to their mechanical strength, conductors such as copper for electric lines and ferromagnets for magnetic recording media. Even in modern techniques alloys are employed: thermoelectric materials are used for power generation from temperature gradients or in Peltier elements for cooling or heating by applying a current, and superconducting alloys of niobium and tin are used to generate magnetic fields used in magnetic resonance imaging [1].

In the field of fundamental research, the discovery of high temperature superconductivity in intermetallic compounds, such as $(Ba_{0.6}K_{0.4})Fe_2As_2$, particularly attracted interest in recent years [2].

A large fraction of elements of the periodic table are metals and thus a large variety of intermetallic phases is conceivable. Their various crystal structures mirror a great diversity. The fascinating “Endless wonders” of the “Exploratory Synthesis in the Solid State” were described by J.D. Corbett [3, 4]. A sound understanding of the forces, which lead for a certain combination of metals to a defined crystal structure, is an essential key point for the development of new applicable materials. However, such understanding is still very limited and the discovery of new crystal structures is often the result of an exploratory synthesis.

The composition and crystal structure of an intermetallic phase define its properties. However, many alloys, which are applied nowadays, consist of a variety of elements and are, in terms of their structure-property relationships, often poorly understood. For example, even though intermetallic compounds such as Nb_3Sn and NbTi are used as superconducting materials for the production of large magnetic fields, up to today it is not possible to predict superconducting behaviour on the basis of the crystal structure of a compound. Nevertheless, some structure-property relationships have been identified: in the

case of iron arsenide superconductors with the parent compounds LnFeAsO (Ln: lanthanide) and $BaFe_2As_2$, T_c seems to be maximized when the bond angle As-Fe-As within the $FeAs_4$ tetrahedra is close to the ideal tetrahedral angle of 109.5° [5]. Furthermore, A. Simon identified the simultaneous presence of localized and delocalized valence electrons as a characteristic feature of superconductors. Analysing the electronic structure of these compounds, the coexistence of flat and steep bands at E_F is therefore a "fingerprint" of these superconducting substances [6, 7]. Further characteristics such as a van Hove singularity [8] have been identified and confirmed for various examples, like carbides (CaC_2) and rare earth metal carbide halides ($Se_2C_2X_2$) [7], the stannides $SrSn_3$ [9] and $BaSn_3$ [10] as well as the high temperature superconductor MgB_2 [11].

Not only the prediction of crystal structures and the corresponding properties of intermetallic phases but also the description of intermetallic bonding is a challenging topic. Chemists possess a distinct knowledge of chemical bonding in molecules, in which generally the valence concept (8-*N* rule) applies and directive, localized bonds are dominant. Similarly, the ionic bond between bonding partners of highly different electronegativities is well understood. In contrast, a lot of unanswered question remain regarding the bonding situation in intermetallic compounds [12-14]. A basic introduction on the electronic structure of crystalline compounds, concerning "A Chemist's View of Bonding in Extended structures" has been given by R. Hoffmann [15, 16]. Various further reviews discuss intermetallic compounds and their bonding situation (see for example [17-19] and references herein).

1.2 Classes of Intermetallic and Polar Intermetallic Compounds

The terms "intermetallic compounds" or "intermetallic phases" are loosely defined and describe compounds containing two or more metals. The terms are also applied for compounds containing not only s- and d-elements but also early p-elements, such as the nonmetals Si and Ge as well as the semimetal Sn. An intermetallic phase has a regular crystal structure with a distinct composition varying over a certain homogeneity range. In contrast, the term "alloy" describes a less defined mixture of intermetallic compounds.

As pointed out above, structures of intermetallic compounds are difficult to predict from their composition (see e.g. [20]) and intermetallic bonding is least understood compared to covalent and ionic bonding.

However, useful concepts to classify intermetallic compounds have been developed over the years. G. J. Miller *et al*. grouped intermetallic compounds according to the apparent electronic interactions such as (1) d-d (two transition metals), (2) d-sp (transition metal and main group metal) and (3) sp-sp (two main group metals) [21].

Alternatively, intermetallic compounds can be grouped into commonly used classes, such as Heusler and Half-Heusler phases, Hume-Rothery phases, Laves phases and Zintl phases. The former are assigned to the classical intermetallic phases and therefore contain mainly intermetallic bonding. The arrangement of the atoms in these phases is often explained by geometrical factors (e.g. Goldschmidt rules, Laves phases) as well as by the valence electron configuration (e.g. Hume-Rothery phases). In contrast to the metallic bonding observed in these classes of compounds, Zintl phases are salt-like and contain a cationic and an anionic substructure. In general metallic, ionic and even covalent bonding is present. On a Van Arkel-Ketelaar triangle [22, 23] Zintl phases are situated between intermetallic phases and ionic phases. Between Zintl phases and intermetallic phases a further class is situated, which is denoted here as “polar intermetallic compounds”.

In the following the classes of intermetallic compounds, Zintl phases as well as polar intermetallic compounds will be briefly introduced.

1.2.1 Heusler and Half-Heusler Phases

Full-Heusler and Half-Heusler phases crystallize in the composition TT'_2E and $TT'E$ (mostly T,T': transition metal, E: main group element of the group 13-15), respectively. The crystal structure of the Full-Heusler phase TT'_2E can be described as a superlattice of the CsCl type. The position A of the CsCl structure type is occupied by T', the position B is alternately occupied by T and E. For the Half-Heusler phases half of the positions of T' are unoccupied.

Prominent examples are $MnCu_2Al$ [24] as well as MgAgAs [25]. Frequently, Heusler phases are observed to be ferromagnetic and thus they are interesting materials for numerous applications.

1.2.2 Hume-Rothery Phases

Hume-Rothery phases are intermetallic compounds whose crystal structures depend on the number of valence electrons of the involved metals. The so-called valence electron concentration (VEC) is equal to the sum of all valence electrons divided by the number of atoms. Hume-Rothery phases within a certain range of VEC crystallize in the same close packed structures (α-, β-, γ-, ε- and η-Phases) and most of them cover a certain homogeneity range. A well known example is the system Cu/Zn (brass). With varying content of Cu and Zn and thus with varying VEC each of the five named structure types is realized. For instance, the phase CuZn crystallizes with the structure type of the β-phase. Intermetallic phases having the same VEC, such as Cu_5Sn, Cu_3Al and AgZn, crystallize in the same structure type.

1.2.3 Laves Phases

Laves phases are intermetallic compounds with the composition AB_2, the A atoms (alkaline and alkaline earth metals, transition metals of group 4-6 and rare earth metals) being larger than the B atoms (transition metals of group 7-8 and noble metals). The most prominent structure types of the Laves phases are $MgCu_2$, $MgZn_2$ and $MgNi_2$. The corresponding *Strukturbericht* symbols are C15, C14 and C36, respectively. Within these crystal structures the transition metals (*T*) Cu, Zn and Ni form T_4 tetrahedra which are connected via faces and vertices. The Mg atoms are situated in the cavities of the resulting network. In the $MgCu_2$ and $MgZn_2$ structure type the Mg atoms as well as the centers of gravity of the T_4 tetrahedra are arranged as the C atoms in cubic and hexagonal diamond, respectively. The coordination polyhedra observed in the Laves phases are A-centered 16 atom Frank-Kasper polyhedra and B-centered 12 atom icosahedra.

The formation of Laves phases is often discussed in terms of geometrical factors: The ideal ratio of the atomic radii or r_A/r_B is 1.225. Consequently, the Laves phase KNa_2, whose ratio of the atomic radii is close to the ideal one, was predicted. Indeed, it was found experimentally later on [26]. However, Laves phases with atomic ratio r_A/r_B between 1.05 ($NbZn_2$ [27]) and 1.65 (KAu_2 [28]) are also known today.

Furthermore, electronic factors such as the valence electron concentration (VEC) are supposed to influence the formation of Laves phases. For example, Witte and Laves observed a correlation of homogeneity ranges of the hexagonal and cubic structure types of Mg-based systems (such as Mg/Cu/Al, Mg/Cu/Zn, Mg/Ag/Zn, Mg/Cu/Si, Mg/Co/Zn) and the VEC [29]. However, the boundary values observed for VEC are only valid for a particular ternary system.

Various reviews discuss the manifold criteria influencing the formation and the crystal structure of Laves phases (see [30-32] and references herein).

1.2.4 Zintl Phases

Classical Zintl Phases

In 1935 Eduard Zintl described the structure of NaTl, concluding that the Tl atoms form a diamond network as each Na atom donates its valence electrons to Tl [33]. Since then the classical Zintl-Klemm concept [34-36] was successful explaining the crystal structures of many binary solid-state compounds and numerous reviews summarizing the manifold variety of Zintl phases have been written (selected reviews [37-42]). The classical Zintl-Klemm concept has been developed for salt-like valence compounds consisting of main group elements. In short, it is assumed that a complete electron transfer from the electropositive metal (such as alkali metal, alkaline earth metal or rare earth metal atoms) to the more electronegative element takes place. The anions thus generated form covalently bonded homoatomic polyanions which can be explained by the (8-*N*) rule and adopt the structure of the corresponding element (pseudoatom concept). The resulting salt-like Zintl phases are valence compounds of closed shell cations and polyanions. Hence, they are diamagnetic and semiconducting.

In the binary systems *Ae*/Ge (*Ae*: Ca, Sr, Ba) the crystal structures of most known compounds can be understood according to the Zintl-Klemm concept. For example, in CaGe [43], SrGe [44] and BaGe [45-47] (CrB structure type [45, 48]) the Ge atoms are two-bonded in analogy to the elements of group 16. Small alterations are observed concerning the resulting structural motif, since the Ge atoms form planar zigzag chains in contrast to the helical chains which are formed in specific modifications of the group 16 elements.

However, the predictive power of the Zintl-Klemm concept is limited: While it is possible to forecast the average number of bonds per atom, the final structure of the compound cannot be foreseen theoretically. For example, the binary germanides $CaGe_2$ [49], $SrGe_2$ [50] and $BaGe_2$ [51, 52] can all be described according to the Zintl-Klemm concept. The Ge atoms are three bonded in analogy to the elements of the group 15. Nevertheless, the structures of the polyanionic networks vary significantly. In $CaGe_2$ [49] the Ge atoms form a network of puckered 6^3 layers as observed in grey arsenic. $SrGe_2$ and $BaGe_2$ [51, 52] contain Ge_4^{4-} tetrahedra which are reminiscent of white phosphorus. Additionally, high pressure modifications exist for all three compounds. In β-$CaGe_2$ (hp) solely the stacking of the puckered 6^3 layers is changed [49]. The high pressure modification of $SrGe_2$ [53] also contains puckered 6^3 layers. In contrary, the high pressure modification of $BaGe_2$ [54] crystallizes in the $ThSi_2$ structure type [55], in which each Ge is planar coordinated by three further Ge atoms.

This limitation of the Zintl-Klemm concept is due to an over-simplification: a complete charge transfer leading to a cationic and an anionic substructure is assumed. Neither the fact that the charge transfer is incomplete, nor the further interactions of the anions and cations are considered. Only recently, F. Wang and G.J Miller discussed the Zintl-Klemm concept on the basis of the competing metallic, ionic and covalent interactions within the alkali metal trielides LiAl, LiTl, NaTl and KTl [56]. In the course of their work, they identified various further influences on the formation of Zintl phases, such as relativistic effects, electronegativity differences and atomic size ratios between the constituent elements.

Further, Zintl phases are often composed of metals and semimetals which retain their metallic character, i.e. the resistivity of resulting Zintl phases is considerable low and their magnetic susceptibility is positive and Pauli-like. As an example, the most often cited Zintl phase NaTl exhibits metallic conductivity [57]. Similarly, the binary phases Ca_5Ge_3 and CaGe can be rationalized according to the Zintl-Klemm concept, but exhibit metallic conductivity [58, 59]. This leads to the term “metallic Zintl phase” [41], referring to compounds having a non-zero DOS at E_F. Most often a gap or a pseudo gap is present close to E_F. The influence of cations, the electronegativity difference and anionic interlayer interactions on the metallic character of a Zintl phase have been studied on the basis of bandstructures for Zintl phases containing polyanionic networks related to grey arsenic

[60]. However, the metallic conductivity does not influence the utility of Zintl-Klemm concept itself [37].

Non-classical Zintl Phases

Intermetallic compounds containing anionic deltahedral clusters may be described as Zintl phases by extending the Zintl concept by the Wade rules, which are known from the boranes. Thus multicenter bonding, resulting from electron deficiency, is taken into account. For example, the phase K_4Ge_9 [61] contains Ge_9^{4-} cluster, whose structure can be described as a capped squared antiprism with C_{4v} symmetry. According to the Wade rules $(4n+4)$ electrons are expected for a nido cluster, which corresponds for $n = 9$ to the number of electrons in Ge_9^{4-} (40 electrons).

A further extension of the Zintl concept for electron poor polyanionic networks is the assumption of the formation of double bonds. Various silicides and germanides containing incompletely filled π^* systems have been described. Examples are branched chains of Si and Ge observed in $Ba_2Mg_3Si_4$ [62], $BaLiGe_2$ and $SrLiGe_2$ [63], $LiCa_2Ge_3$ [64] as well as Eu_2LiSi_3, Eu_2LiGe_3 and $Eu_xSr_{2-x}LiGe_3$ [65]. Stannides containing aromatic and conjugated systems are for example the compounds $Li_{9-x}EuSn_{6+x}$, $Li_{9-x}CaSn_{6+x}$, $Li_5Ca_7Sn_{11}$, $Li_6Eu_5Sn_9$, $LiMgEu_2Sn_3$ and $LiMgSr_2Sn_3$ [66]. Further, the superconducting binary phases $BaSn_3$ and $SrSn_3$ can be described as borderline cases of Zintl phases $Ae^{2+}[Sn_3]^{2-}$. It has been shown by analysis of the molecular orbitals that the isolated $[Sn_3]^{2-}$ unit is isoelectronic to $C_3R_3^+$. Thus, a π system, which is filled with two electrons, is present next to the two-electron-two-centre bonds and the free electron pairs [9, 10]. This concept has been recently applied to the high pressure phase $BaGe_3$ [67].

Additionally, R. Hoffmann and G. A. Papoian suggested an extension of the Zintl-Klemm concept for polar intermetallic compounds containing electron-rich networks of heavy late main group elements [18]. The essential feature here is the presence of hypervalent bonding, which is used to explain nonclassical local coordination such as one-dimensional linear chains or two-dimensional square sheets.

1.2.5 Polar Intermetallic Compounds

The term “polar intermetallic compounds” describes those phases, in which a charge transfer between a positively charged substructure and a negatively charged

substructure takes place. Thus, the term “polar” results. However, considerable interactions between the electropositive metals and the polyanionic substructures are present and the phases exhibit metallic conductivity.

The ternary polar intermetallic compounds obtained for the system *A*/*T*/*E* (*A*: alkaline metal, alkaline earth metal or rare earth metal, *T*: transition metal, *E*: elements of group 13-15) are mostly described with networks of T_xE_y, which are separated by *A* atoms. Considering the electronegativity of the constituting elements, a positively charged *A* atom and negatively charged T_xE_y substructures (often referred to as polyanionic) can be anticipated. The resulting crystal structures are reminiscent of Zintl phases. However, their negatively charged substructures are electron deficient and they cannot be rationalized according to the Zintl-Klemm concept and its extensions described above. Thus, for the description of the bonding situation of these ternary polar intermetallics, new concepts are required.

The corresponding crystal structures are frequently discussed starting from binary Zintl phases of the systems *A*/*E,* to which small amounts of *T* are added. Using this approach some open-ended questions remain. For example, in order to apply the Zintl-Klemm concept to ternary polar intermetallic compounds a charge has to be assigned to the transition metal. This is not a straight forward task, as the Zintl-Klemm concept often leads to positively charged transition metals while computational studies indicate a negative charge (see for example [68]). Further points under discussion are the often neglected influence of the cations on the crystal structure and the failure of the concept to explain the manifold crystal structures of the ternary polar intermetallic phases which are transition metal rich.

1.3 Scope and Outline of this Work

Within the last decades, research on polar intermetallic compounds of the system *A*/*T*/*Tt* (*A*: alkaline metal, alkaline earth metal or rare earth metal, *T*: transition metal, *Tt*: tetrel element) mainly focused on systems containing rare earth metals (see for example [69]). For these compounds strong interactions between the rare earth metals and the polyanionic substructures T_xTt_y are present.

In contrast, the systems *Ae*/*T*/*Tt* (*Ae*: Mg, Ca, Sr, Ba; *T*: Ni, Co; *Tt*: Si, Ge, Sn) were rather neglected. Thus, until recently a manifold variety of binary compounds but only a small number of ternary compounds were known in these systems. Particularly, with regard to the large number of binary compounds in the systems *T*/*Tt* and *Ae*/*Tt*, a rich chemistry of ternary polar intermetallic compounds could be expected. This was indeed confirmed prior to this work [70-73].

The present thesis aims to extend the knowledge about the polar intermetallic compounds of the systems *Ae*/*T*/*Tt* (*Ae*: Mg, Ca, Sr, Ba; *T*: Ni, Co; *Tt*: Si, Ge, Sn). In this context a series of binary and ternary phases was discovered. The synthesized compounds were analyzed by powder and single crystal X-ray diffraction analysis, Energy Dispersive X-ray spectroscopy (EDX), Differential Thermal Analysis (DTA) and magnetic measurements testing for superconducting behavior. Next to the structural characterization of the compounds, a main focus is placed on the electronic structures, which are easier understandable for the systems *Ae*/*T*/*Tt* than for the compounds of the systems *Re*/*T*/*Tt (Re*: rare earth metal atom*)*. DFT calculations were carried out using the programs TB-LMTO-ASA as well as WIEN2K in order to provide a basis for the discussion of the electronic structures. The chemical bonding situations were discussed based on the Density Of States (DOS) curves, bandstructures including fatbands, Crystal Orbital Hamilton Populations (COHP), topological analysis of the Electron Localization Function (ELF) and Bader's Atoms in Molecules (AIM).

The first part of this thesis deals with three binary phases Sr_7Ge_6, Ba_7Ge_6 and Ba_3Sn_2 (chapter 4.2). Here, a main focus is put on the bonding situation: while Ba_3Sn_2 is a semiconductor and can be classified as a Zintl phase by applying the (8-*N*) rule, Sr_7Ge_6 and Ba_7Ge_6 are metallic conductors and do not follow the Zintl-Klemm concept. Hence, the possibility of the formation of a partial double bond is discussed.

The second part of this thesis deals with polar intermetallic compounds of the systems *Ae*/Ni/Ge (*Ae*: Mg, Ca, Sr, Ba) (chapter 4.3). The crystal structures and bonding situations of the polar intermetallic compounds $BaNi_2Ge$ and $Ca_4Ni_4Ge_3$ ([74], chapter 4.3.1), $CaNi_5Ge_3$, $Ca_{15}Ni_{68}Ge_{37}$ and $Ca_7Ni_{49}Ge_{22}$ ([75, 76], chapter 4.3.2), $Ba_2Ni_5Ge_4$ ([77, 78], chapter 4.3.3) as well as the Laves phases of the system Mg/Ni/Ge (chapter 4.3.4) are reported in detail. The rich chemistry of the systems *Ae*/Ni/Ge (*Ae*: Ca, Sr, Ba) is reviewed in chapter 4.3.5, analyzing the structural relationships between the

various compounds. Here a description of polar intermetallic compounds in analogy to the Zintl-Klemm concept is discussed.

The third part comprises the polar intermetallic compounds $CaCo_2Si_2$ and $BaCo_2Ge_2$ ([79], chapter 4.4). These crystallize in the $ThCr_2Si_2$ structure type, which came to the focus of attention when one of its representatives, $(Ba_{0.6}K_{0.4})Fe_2As_2$, was reported to show superconductivity with the high transition temperature of 38 K, being the first member of a new "122" family of superconducting iron-arsenides [2]. For $CaCo_2Si_2$ and $BaCo_2Ge_2$ the bonding situation, with main focus on the tunable *Tt*-*Tt* distance, is discussed.

The fourth part of this thesis presents new compounds of the systems *Ae*/Ni/Sn (*Ae*: Mg, Ca) (chapter 4.5). For the system Ca/Ni/Sn the dimorphic polar intermetallic phase Ca_2NiSn_2 is introduced ([80], chapter 4.5.1). Two different mechanisms for phase transition from *mC*-Ca_2NiSn_2, which contains a three-dimensional Ni-Sn network, to *oP*-Ca_2NiSn_2, which contains two-dimensional Ni-Sn layers, are suggested. While the crystal structures of the two modifications of Ca_2NiSn_2 are comparable to those observed for the germanides, those of the intermetallic compounds of $Mg_{0.39(2)}NiSn_{1.61(2)}$ and $Mg_{2.61(2)}Ni_4Sn_{3.39(2)}$ exclude themselves from such a comparison (chapter 4.5.2). Due to the mixing of Mg and Sn, these structures are rather described as a network of Mg and Sn in whose cavities the Ni atoms are situated. Thus, $Mg_{0.39(2)}NiSn_{2.61(2)}$ and $Mg_{2.61(2)}Ni_4Sn_{3.39(2)}$ belong to the classical intermetallic phases. For example, $Mg_{2.61(2)}Ni_4Sn_{3.39(2)}$ can be described as an intermediate of a Heusler and a Half-Heusler type phase.

The composition triangles of the systems *Ae*/*T*/*Tt* (*Ae*: Mg, Ca, Sr, Ba; *T*: Ni, Co; *Tt*: Si, Ge, Sn), in which new polar intermetallic compounds are presented in this work, are given in the Appendix. They include all hitherto known binary and ternary phases.

1.4 References

[1] J. H. Westbrook, R. L. Fleischer, *Intermetallic Compounds Volume 2 - Practice*, Wiley, **1995**.

[2] M. Rotter, M. Pangerl, M. Tegel, D. Johrendt, *Angew. Chem. Int. Ed.* **2008**, *47*, 7949.

[3] J. D. Corbett, *Inorg. Chem.* **2000**, *39*, 5178.

[4] J. D. Corbett, *Inorg. Chem.* **2010**, *49*, 13.

[5] C.-H. Lee, A. Iyo, H. Eisaki, H. Kito, M. T. Fernandez-Diaz, T. Ito, K. Kihou, H. Matsuhata, M. Braden, K. Yamada, *J. Phys. Soc. Jpn.* **2008**, *77*.

[6] H. Mattausch, A. Simon, C. Felser, R. Dronskowski, *Angew. Chem. Int. Ed. Engl.* **1996**, *35*, 1685.

[7] A. Simon, *Angew. Chem. Int. Ed. Engl.* **1997**, *36*, 1789.

[8] O. K. Andersen, O. Jepsen, A. I. Liechtenstein, I. I. Mazin, *Phys. Rev. B* **1994**, *49*, 4145.

[9] T. F. Fässler, S. Hoffmann, *Z. Anorg. Allg. Chem.* **2000**, *626*, 106.

[10] T. F. Fässler, C. Kronseder, *Angew. Chem. Int. Ed. Engl.* **1997**, *36*, 2683.

[11] A. Simon, *Solid State Sciences* **2005**, *7*, 1451.

[12] L. C. Allen, J. K. Burdett, *Angew. Chem. Int. Ed. Engl.* **1995**, *34*, 2003.

[13] W. P. Anderson, J. K. Burdett, P. T. Czech, *J. Am. Chem. Soc.* **1994**, *116*, 8808.

[14] J. C. Schön, *Angew. Chem. Int. Ed. Engl.* **1995**, *34*, 1081.

[15] R. Hoffmann, *Solids and Surfaces - A Chemist's View of Bonding in Extended Structures*, VCH Publishers, New York, **1988**.

[16] R. Hoffmann, *Angew. Chem. Int. Ed. Engl.* **1987**, *26*, 846.

[17] R. Nesper, *Angew. Chem.* **1991**, *103*, 805.

[18] G. A. Papoian, R. Hoffmann, *Angew. Chem. Int. Ed.* **2000**, *39*, 2408.

[19] G. A. Landrum, R. Dronskowski, *Angew. Chem. Int. Ed. Engl.* **2000**, *39*, 1560.

[20] G. J. Miller, *Eur. J. Inorg. Chem.* **1998**, 523.

[21] O. Gourdon, D. Gout, G. J. Miller, in *Encyclopedia of Condensed Matter Physics*, **2005**.

[22] J. A. A. Ketelaar, *Chem. constitution: an introduction to the theory of the chemical bond, 2nd edn*, Elsevier, Amsterdam, **1958**.

[23] A. E. van Arkel, *Molecules and crystals in inorganic chemistry*, Interscience, New York, **1956**.

[24] O. Heusler, *Annalen Der Physik* **1934**, *19*, 155.

[25] H. N. Nowotny, W. Sibert, *Z. Metallk.* **1941**, *33*, 391.

[26] F. Laves, H. J. Wallbaum, *Z. Anorg. Allg. Chem.* **1942**, *250*, 110.

[27] C. L. Vold, *Acta Crystallogr.* **1961**, *14*, 1289.

[28] K. J. Range, F. Rau, U. Klement, *Acta Crystallogr., Sect. C: Cryst. Struct. Commun.* **1988**, *44*, 1485.

[29] F. Laves, H. Witte, *Metall-Wirtschaft, -Wissenschaft und -Technik* **1936**, *15*, 840.

[30] F. Stein, A. Palm, G. Sauthoff, *Intermetallics* **2005**, *13*, 1056.

[31] F. Stein, M. Palm, G. Sauthoff, *Intermetallics* **2004**, *12*, 713.

[32] D. Grüner, TU Dresden **2007**.

[33] E. Zintl, G. Woltersdorf, *Z. Elektrochem.* **1935**, *41*, 876.

[34] E. Zintl, *Angew. Chem.* **1939**, *52*, 1.

[35] W. Klemm, *Proc. Chem. Soc., London* **1958**, 329.

[36] W. Klemm, E. Busmann, *Z. Anorg. Allg. Chem.* **1963**, *319*, 297.

[37] S. M. Kauzlarich, *Chemistry, Structure, and Bonding of Zintl Phases and Ions*, VCH Publishers, Inc. , New York, **1996**.

[38] H. Schäfer, B. Eisenman, W. Müller, *Angew. Chem. Int. Ed. Engl.* **1973**, *12*, 694.

[39] J. D. Corbett, *Angew. Chem. Int. Ed.* **2000**, *39*, 670.

[40] S. Scharfe, F. Kraus, S. Stegmaier, A. Schier, T. F. Fässler, *Angew. Chem. Int. Ed.* **2011**, *50*, 3630.

[41] R. Nesper, *Prog. Solid State Chem.* **1990**, *20*, 1.

[42] *Zintl Phases: Principles and Recent Developements, 139*, Springer-Verlag, Editor T.F. Fässler **2011**.

[43] P. Eckerlin, H. J. Meyer, E. Wolfel, *Z. Anorg. Allg. Chem.* **1955**, *281*, 322.

[44] A. Betz, H. Schäfer, A. Weiss, *Z. Naturforsch., B: J. Chem. Sci.* **1967**, *B 22*, 103.

[45] W. Rieger, E. Parthe, *Acta Crystallogr.* **1967**, *22*, 919.

[46] F. Merlo, M. L. Fornasini, *J. Less Common Met.* **1967**, *13*, 603.

[47] V. V. Burnasheva, E. I. Gladyshevskii, *Inorg. Mater.* **1966**, *2*, 804.

[48] A. J. Frueh, *Acta Crystallogr.* **1951**, *4*, 66.

[49] P. H. Tobash, S. Bobev, *J. Solid State Chem.* **2007**, *180*, 1575.

[50] E. I. Gladyshevskii, P. I. Krypyakevych, *J. Struct. Chem.* **1965**, *6*, 148.

[51] J. T. Vaughey, G. J. Miller, S. Gravelle, E. A. Leon-Escamilla, J. D. Corbett, *J. Solid State Chem.* **1997**, *133*, 501.

[52] A. Betz, H. Schäfer, A. Weiss, R. Wulf, *Z. Naturforsch., B: J. Chem. Sci.* **1968**, *B 23*, 878.

[53] J. Evers, G. Oehlinger, A. Weiss, *Z. Naturforsch., B: J. Chem. Sci.* **1979**, *34*, 524.

[54] J. Evers, G. Oehlinger, A. Weiss, *Z. Naturforsch., B: J. Chem. Sci.* **1977**, *32*, 1352.

[55] G. Brauer, A. Mitius, *Z. Anorg. Allg. Chem.* **1942**, *249*, 325.

[56] F. Wang, G. J. Miller, *Inorg. Chem.* **2011**, *50*, 7625.

[57] G. Grube, A. Schmidt, *Zeitschrift für Elektrochemie und Angewandte Physikalische Chemie* **1936**, *42*, 201.

[58] A. V. Mudring, J. D. Corbett, *J. Am. Chem. Soc.* **2004**, *126*, 5277.

[59] J. Evers, A. Weiss, *Solid State Commun.* **1975**, *17*, 41.

[60] P. Alemany, M. Llunell, E. Canadell, *J. Comput. Chem.* **2008**, *29*, 2144.

[61] S. Ponou, T. F. Fässler, *Z. Anorg. Allg. Chem.* **2007**, *633*, 393.

[62] S. Wengert, R. Nesper, *Z. Anorg. Allg. Chem.* **1998**, *624*, 1801.

[63] D. G. Park, Y. Dong, F. J. DiSalvo, *J. Alloys Compd.* **2009**, *470*, 90.

[64] W. Müller, H. Schäfer, A. Weiss, *Z. Naturforsch., B: J. Chem. Sci.* **1971**, *B 26*, 5.

[65] Q. X. Xie, R. Nesper, *Z. Anorg. Allg. Chem.* **2006**, *632*, 1743.

[66] I. Todorov, S. C. Sevov, *Inorg. Chem.* **2005**, *44*, 5361.

[67] H. Fukuoka, Y. Tomomitsu, K. Inumaru, *Inorg. Chem.* **2011**, *50*, 6372.

[68] B. Sieve, X. Chen, J. Cowen, P. Larson, S. D. Mahanti, M. G. Kanatzidis, *Chemistry of Materials* **1999**, *11*, 2451.

[69] P. S. Salamakha, *Handbook on the Physics and Chemistry of Rare Earths* **1999**, *27*, 225.

[70] V. Hlukhyy, S. Eck, T. F. Fässler, *Inorg. Chem.* **2006**, *45*, 7408.

[71] V. Hlukhyy, T. F. Fässler, *Z. Anorg. Allg. Chem.* **2008**, *634*, 2316.

[72] V. Hlukhyy, F. Raif, P. Claus, T. F. Fässler, *Chem.-Eur. J.* **2008**, *14*, 3737.

[73] V. Hlukhyy, A. Senyshyn, D. Trots, T. F. Fässler, *HASYLAB Ann. Rep.* **2007**, *1*, 1021.

[74] L. Siggelkow, V. Hlukhyy, T. F. Fässler, *Z. Anorg. Allg. Chem.* **2010**, *636*, 1870.

[75] L. Siggelkow, V. Hlukhyy, B. Wahl, T. F. Fässler, *Eur. J. Inorg. Chem.* **2011**, 4012.

[76] L. Siggelkow, V. Hlukhyy, B. Wahl, T. F. Fässler, *Z. Anorg. Allg. Chem.* **2010**, *636*, 2077.

[77] L. Siggelkow, V. Hlukhyy, T. F. Fässler, *Z. Anorg. Allg. Chem.* **2011**, *637*, 2000.

[78] L. Siggelkow, V. Hlukhyy, T. F. Fässler, *Z. Anorg. Allg. Chem.* **2008**, *634*, 2090.

[79] L. Siggelkow, V. Hlukhyy, T. F. Fässler, *Z. Anorg. Allg. Chem.* **2010**, *636*, 378.

[80] L. Siggelkow, V. Hlukhyy, T. F. Fässler, *Eur. J. Inorg. Chem.* **2012**, 987.

2 Experimental Section

In the following the general experimental and analytical methods used in this work are described. The details concerning the synthesis and analysis of the individual compounds are presented in the respective chapters.

2.1 Synthesis

2.1.1 Elements Used for Synthesis

Starting materials for all syntheses are given in Table 2.1. The alkaline earth metals Ca, Sr and Ba are distilled before use. Ni, Co, Si, Ge and Sn are used as received.

Table 2.1 Starting chemicals, their purity, source and shape.

Element	Purity (%)	Manufacturer	Shape
Mg	99.5	ChemPur	pieces
Ca	99.5	Alfa Aesar	pieces
Sr	98	ChemPur	pieces
Ba	99.3	ChemPur	ingot
Ni	99.98	Alfa Aesar	wire
Ni	99.9	Acros Organics	powder
Co	99.9	Alfa Aesar	ingot
Si	99.9999	Alfa Aesar	pieces
Ge	99.999	ChemPur	pieces
Sn	99.999	ChemPur	granules

2.1.2 Distillation of the Alkaline Earth Metals

A distillation apparatus is set up in order to obtain pure alkaline earth metals Ca, Sr and Ba. The crucial parts of the distillation equipment are made of steel, since the alkaline

earth metals react with glass as well as quartz glass already at low temperatures and since they additionally have high melting and boiling points (T_m(Ca) = 839 °C, T_m(Sr) = 768 °C, T_m(Ba) = 710 °C, T_b(Ca) = 1482 °C, T_b(Sr) = 1380 °C, T_b(Ba) = 1380 °C [1]). The main parts of the distillation apparatus are a steel cylinder and a steel cooling finger, a condensation trap cooled with liquid nitrogen, a Penning vacuum gauge (Pfeiffer Vacuum, compact full range gauge) and a pumping station (Pfeiffer Vacuum, TMH 071 P). This pumping station consists of a membrane pump for the generation of a rough vacuum followed by a turbomolecular pump for the generation of a high vacuum (maximally 10^{-7} mbar possible). The apparatus is operated with argon with a purity of 99.998%. Traces of oxygen are removed from the inert gas stream using a BTS catalyst. Subsequently, the argon is dried using a molecular sieve (4 Å). The experimental set up is shown in Figure 2.1.

In a first step the steel cylinder containing an empty tantalum crucible is baked out. The steel cylinder is connected to the cooling finger using a flange with a copper joint. Further, it is connected via a high vacuum valve (VAT, Mini gate valve with toggle lever) to the condensation traps using flanges with rubber joints. The airtight equipment is then evacuated and refilled with argon several times until a dynamic high vacuum of at least 10^{-6} mbar is obtained. The resistance furnace is than heated to about 900 °C in order to remove last traces of oxygen and water from the walls of the steel cylinder. Further, the condensation traps are baked out using a Bunsen burner.

In a second step, the dried cylinder is refilled with argon and transferred into the glove box. Here, the tantalum crucible is filled with the alkaline earth metal to be distilled. The metal is covered with dried steel wool to prevent spilling of the liquid metal. Due to the tantalum crucible a reaction of the alkaline earth metal with the steel cylinder is avoided. Subsequently, the steel cylinder, which contains the tantalum crucible and the metal to be distilled, is reconnected to the distillation apparatus. A vacuum of 10^{-6} mbar is applied and the cooling traps are filled with liquid nitrogen before the temperature is raised to start the distillation. A first indication of the necessary temperatures and durations is found in [2]. With the used equipment the heating procedures given in Table 2.2 proved to be most effective. In a first step the apparatus is quickly heated to 500 °C and kept at that temperature to allow gases such as H_2 to evaporate.

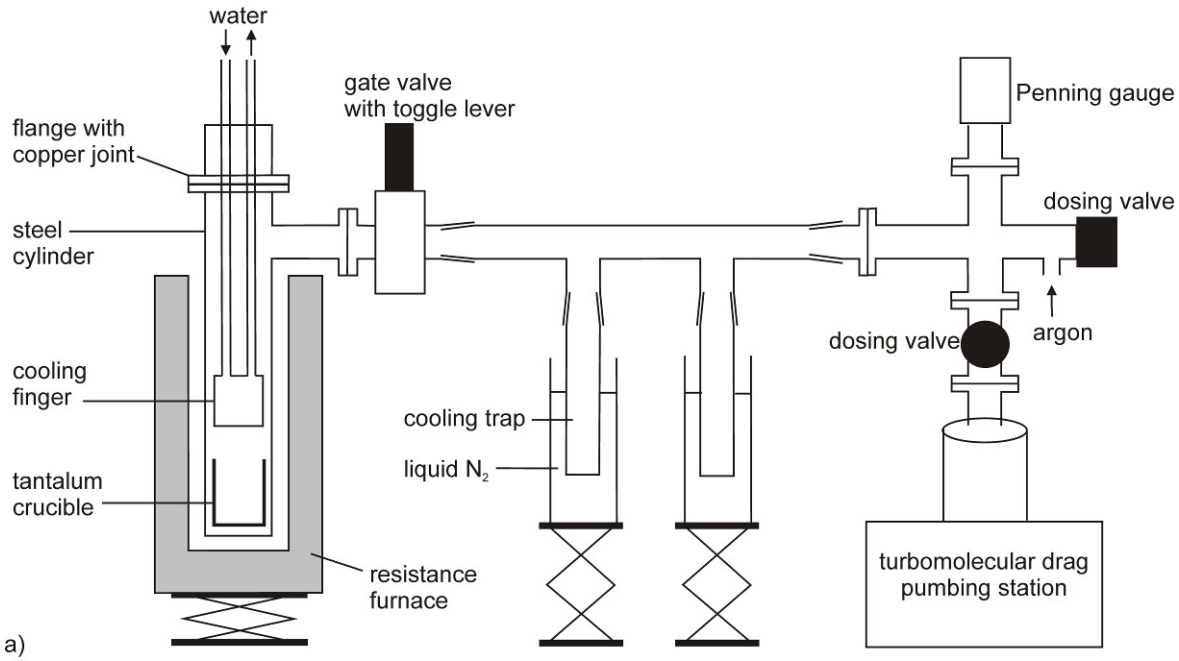

a)

b)

Figure 2.1 a) Schematic description of the distillation apparatus used for purification of Ca, Sr and Ba, b) photograph.

Table 2.2 Temperature programs used for the distillation of alkaline earth metals (Ca, Sr, Ba)

Calcium	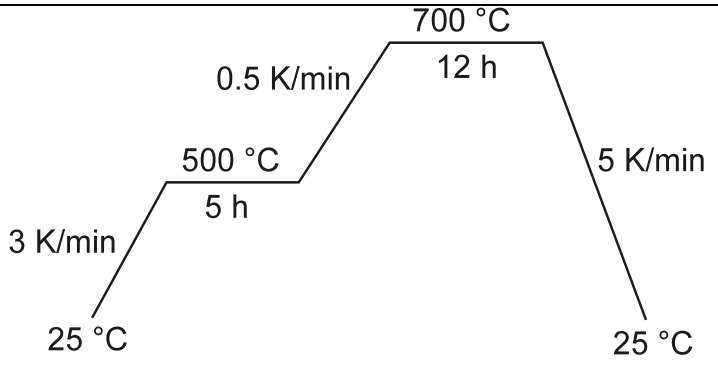
Strontium and Barium	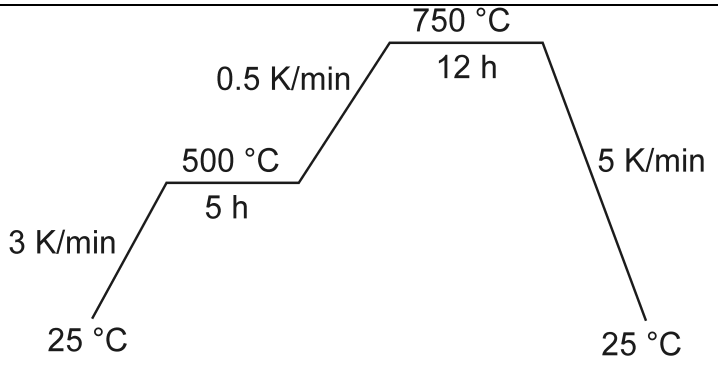

This process of evaporation can be nicely followed as the pressure rises significantly (up to 10^{-4} mbar) and declines again (10^{-6} mbar). After the initial pressure is reached again the respective distillation temperature is slowly approached.

After distillation the steel cylinder which is closed by the high vacuum gate valve is again transferred to the glove box. Beforehand, the water line needs to be dried thoroughly using acetone and compressed air. The valve closing the cylinder is opened in the glove box and the purified metal is separated from the cooling finger. The color of the obtained clean metals should be silvery-white. If the metals are of very high purities, they have a bright golden yellow color [1]. If the distillate is colored differently, it has to be thrown away, as most likely nitrates have been formed.

2.1.3 Synthesis

All manipulations are performed in an argon filled glove box (MBraun, MB 20 G, H_2O and O_2 levels < 0.1 ppm). Several methods such as arc melting as well as temperature treatments in induction and resistance furnaces are used for the syntheses.

Figure 2.2 Mini Arc Melting System, MAM-1, Johanna Otto GmbH, placed in an argon filled glove box.

Arc Melting

For the polar intermetallic phases of the system *Ae*/*T*/*Tt* (*Ae*: Ca, Sr, Ba; *T*: Ni, Co; *Tt*: Si, Ge, Sn) the synthesis is mostly performed by arc melting (Mini Arc Melting System, MAM-1, Johanna Otto GmbH). The used arc melting system has a water cooled sample holder made of copper and a slewable cathode made of tungsten. The whole system is installed inside the argon filled glove box. Therefore, inert reaction conditions are guaranteed (Figure 2.2).

Generally in a first step *T* and *Tt* are arc melted, allowing the transition metal (T_m(Ni) = 1453 °C, T_m(Co) = 1495 °C) and the tetrel element (T_m(Si) = 1410 °C, T_m(Ge) = 937 °C, T_m(Sn) = 232 °C) to react. The resulting reguli are arc melted and turned-over three times in order to ensure homogeneity. As evaporation of the elements is unlikely in this step, high temperatures (i.e. currents) can be chosen. In order to prevent a significant evaporation of the alkaline earth metal during arc melting, a lower temperature is applied in the second step when adding the *Ae* metals (T_m(Ca) = 839 °C,

T_m(Sr) = 769 °C, T_m(Ba) = 725 °C). Even using a lower current and thus a lower temperature, the arc melting has to be carried out carefully in order to choose a time span that allows to melt the metals, but that prevents significant evaporation. Similar to the first step, the resulting reguli are arc melted and turned-over three times in order to ensure homogeneity.

Preparation of the Ampoules

In order to expose the samples to a heat treatment either using an induction or a resistance furnace, the samples have to be enclosed in air tight ampoules.

Due to their chemical resistivity, high melting points and reluctance to undergo reactions with the relevant elements used in this work, welded niobium and tantalum ampoules are used as reaction containers. Figure 2.3 gives a photograph of these Ta/Nb ampoules. They are produced in the laboratory using Ta/Nb tubes which are cut in pieces of about 3 cm lengths (external diameter 10 mm, wall width 0.5 mm). The corresponding lids are stamped out of a Ta/Nb metal sheet (0.5 mm width). The Ta/Nb tubes are sealed at one end with a lid by arc welding (W electrode, Mini Arc Melting System, MAM-1, Johanna Otto GmbH, placed in the glove box) under reduced argon pressure.

Subsequently, all parts are washed successively in concentrated HNO_3, deionized water and acetone for about 15 minutes using an ultrasonic bath. Finally, the ampoules and the top lids are dried in an oven at 120°C over night.

Using a resistance furnace for further heat treatment, the Ta/Nb ampoules themselves have to be protected from oxidation. Thus, they are enclosed in quartz tubes. For this either small quartz tubes (external diameter 18 mm, wall width 1.5 mm), which are closed by welding using a H_2/O_2 burner, or larger Schlenk tubes of quartz (about 800 mm length, diameter 35 mm, wall width 2 mm), which are closed by a ground cap, are used.

Prior to closing the quartz tubes these are connected to a Schlenk line. The tubes are three times evacuated and refilled with argon. The ampoules are closed under vacuum ($\sim 10^{-3}$mbar).

Figure 2.3 Photograph of a closed (left) and an open (right) tantalum ampoule and the corresponding lid.

Figure 2.4 Photograph of a tantalum ampoule enclosed in a small quarz tube.

Induction Furnace

Arc melting procedures usually lead to samples of low crystallinity. In order to grow single crystals, the regulus obtained after arc melting is sealed in cylindrical tantalum or niobium ampoules as described above. The ampoules containing the sample are placed in a water-cooled sample chamber of an induction furnace (Hüttinger Elektronik, Freiburg, Typ TIG 2.5/300). The construction of this induction furnace is given in Figure 3.5. It is important, that the ampoules do not exceed the range of the water cooled copper coil, since they are heated solely in this area. Thus, if the upper part of the ampoule is not situated within the coil, the gaseous alkaline earth metals can migrate to the colder top lid and precipitate there.

The ampoules containing the samples are heated under flowing argon in the induction furnace. The temperature is measured using a pyrometer (SENSOR THERM GmbH, measurement range 900 °C – 2500 °C). This measurement is based on color changes of the sample. After the melting procedure the samples are cooled in about half an hour to a moderate temperature and finally cooled down to room temperature in about one minute by switching off the furnace.

Resistance Furnace

For the heat treatment of the intermetallic compounds synthesized by arc melting and for direct reaction of the elements two kinds of resistance furnaces are available.

Samples enclosed in large quartz Schlenk tubes are thermally treated in tubular ovens (Model LOBA, HTM REETZ GmbH, regulator of EUROTHERM Deutschland GmbH). A type S thermocouple is placed in the middle of the oven to monitor the actual temperature. Therefore, care has to be taken to place the sample close to this thermocouple. For safety reasons, the emerging parts of the Schlenk tubes are covered by a metal fencing to prevent flying parts from injuring the personnel in case of an explosion.

The thermal treatment of samples sealed in shorter quartz tubes is carried out using muffle furnaces (Nabertherm, Controller P330 / B180). The heating coils as well as the thermocouple are installed at the side panel of the muffle furnace. Therefore, the samples have to be placed close to the side walls.

a)

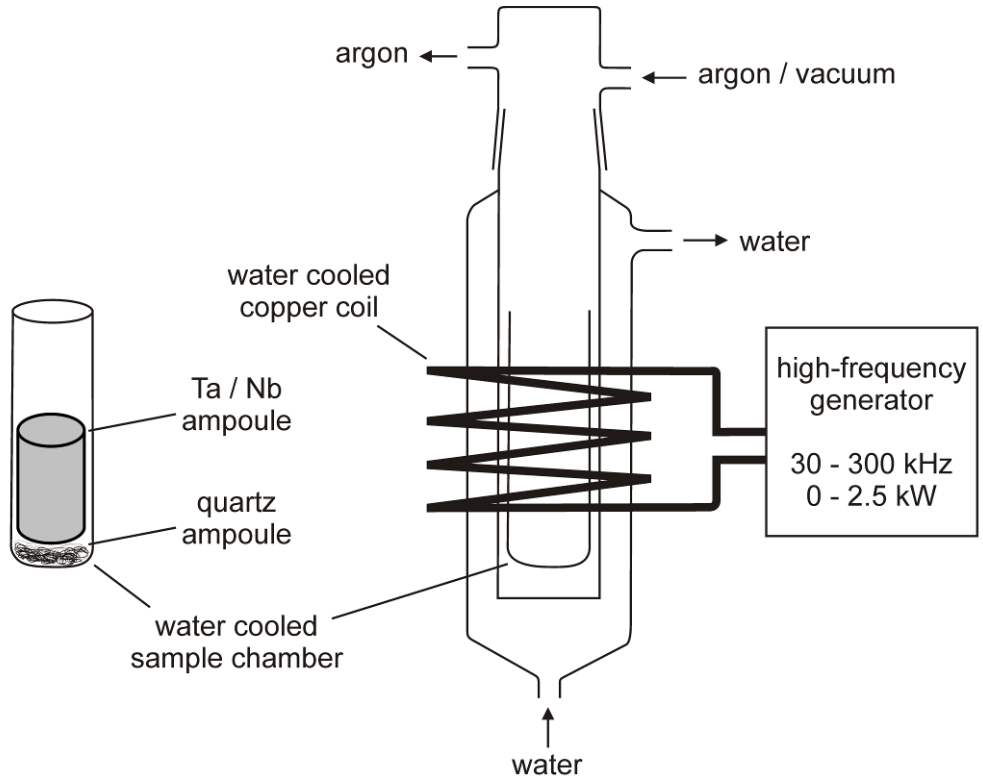

b)

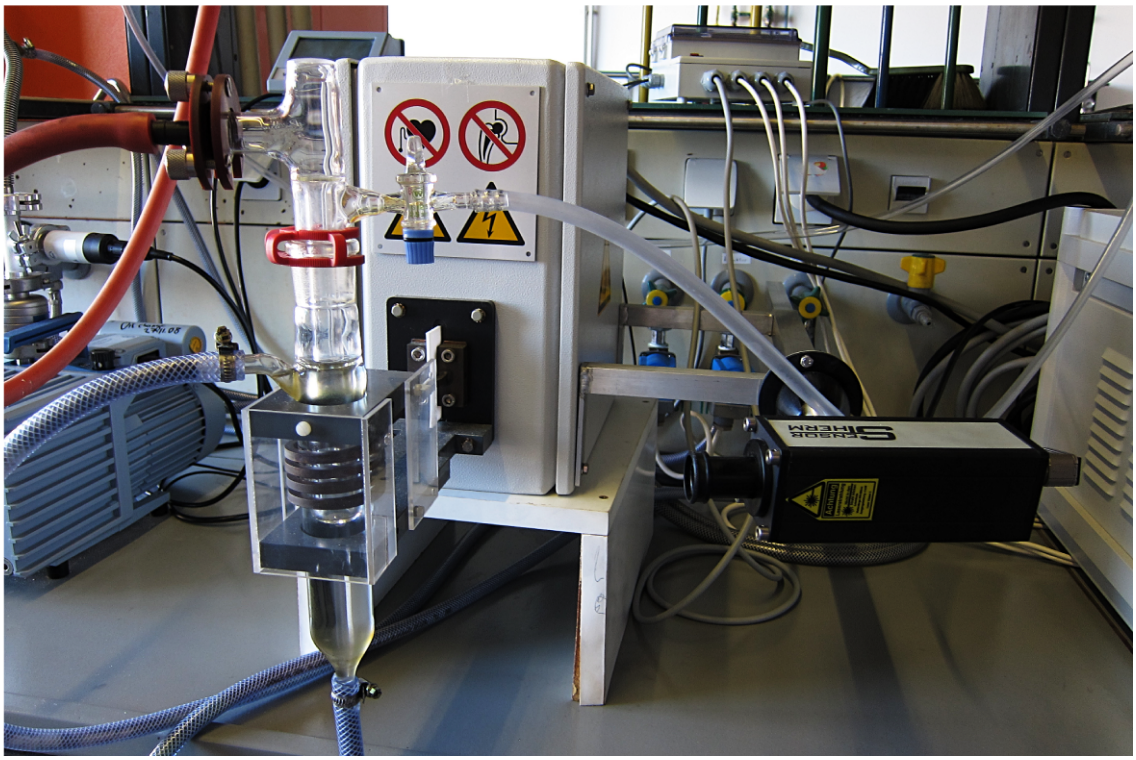

Figure 2.5 a) Schematic description and b) photograph of the induction furnace (Hüttinger Elektronik, Freiburg, Typ TIG 2.5/300).

2.2 X-ray Diffraction Studies and Structure Refinement

2.2.1 Powder X-ray Diffraction Analysis

The purity of the samples is checked by powder X-ray diffraction analysis using a STOE STADI P diffractometer (Fa. Stoe, Darmstadt) with Ge(111) monochromatized Cu-$K_{\alpha1}$ radiation (λ = 1.54056 Å). All measurements are carried out at room temperature. The samples are finely ground in an agate mortar to homogeneous powders. Depending on their air-stability, small amounts of powders are either fixed between two scotch tapes or filled into glass capillaries with internal diameters of 0.3 mm or 0.1 mm (Fa. Hilgenberg, diameter: wall width 0.01mm). The filled capillaries are then fused using a hot filament and sealed with melted wax under argon atmosphere. The measurements are carried out in transition geometry (sample between scotch tapes) or Debye Scherrer geometry (sample in capillary). For a first composition check a curved imaging plate detector is utilized. The time of measurement is about 15 minutes with an angular range of −10° to 130°. Data providing an adequate signal-to-background ratio as well as precise angular data are obtained using the linear position sensitive detector. A typical time of measurement is about 24 hours with an angular range of 2θ = 5° to 95°. The powder X-ray diffraction patterns are evaluated with the Stoe software package WinXPOW [3]. Phase analyses are performed using the imbedded PDF (powder diffraction files) databank of ICDD (international center for diffraction data) or data from the ICSD [4] and the Pearson's Crystal Data [5]. The lattice parameters of the synthesized intermetallic compounds are calculated from least-squares fits of measured and indexed reflections of the powder X-ray diffraction data using WinXPOW [3]. The measured powder X-ray diffraction patterns for all compounds introduced in this thesis are given either in the supporting information or the appendix of the respective publications.

2.2.2 Single Crystal X-ray Diffraction Analysis

Single crystals of air and moisture stable intermetallic compounds are fixed on the top of a glass fibre under a microscope using nail polish. Those of air and moisture sensitive intermetallic compounds are selected under a microscope in a glove box and fixed on the top of a glass fibre using grease. These glass fibres are then inserted into a glass capillary (Fa. Hilgenberg, diameter: 0.5 mm, wall width 0.01mm) which is fused using a hot filament. Whenever necessary, in order to guarantee dry conditions, the glass fibres as well as the glass capillaries are washed in hot aqua regia, rinsed in water and acetone and subsequently dried on a Schlenck line over argon before the preparation of the single crystals.

Single crystal X-ray diffraction intensity data are collected at room temperature using the following diffractometers with graphite monochromatized MoK_α (λ = 0.71073 Å) radiation: a) Oxford Diffraction Xcalibur3 equipped with a CCD detector and an open-flow N_2 blower (CryojetXL, Oxford Cryosystes) for the temperature range 90 – 300 K, b) STOE IPDS 2T with a rotating anode (Nonius, FR591), 2-circle goniometer, 180° ω range, unlimited ρ range, image plate detector system (IPDS) with active imaging plate diameter of 340 mm and $2\theta_{max}$ = 137° and c) APEX II also using a rotating anode (Nonius, FR591) and a CCD detector. Unit cell determination and data reduction are carried out with the corresponding software [6-8]. The raw data are corrected for background, polarization and Lorentz factor. Both empirical absorption correction [7] and numerical absorption correction [9, 10] are used for data correction. The crystal structures are determined using the program package SHELXTL [11]: the subroutine XPREP is used for space group determination, the structures are solved using direct methods (SHELXS-97) [12] and subsequently refined (full-matrix least-squares on F_o^2) with anisotropic atomic displacement parameters for all atoms (SHELXL-97) [13]. The coordinates of the atomic positions are chosen as suggested by the program STRUCTURE TIDY [14]. The graphical presentation of the various intermetallic compounds is realized with the program Diamond [15].

2.3 Scanning Electron Microscopy (SEM) and Energy Dispersive X-ray Spectroscopy (EDX)

The compositions of the crystals used for the single crystal structure determination are checked using a JEOL SEM 5900LV scanning electron microscope equipped with an Oxford Instruments INCA energy dispersive X-ray microanalysis system and a Si(Li) detector. An operating voltage of 20 kV is used. After single crystal X-ray diffraction analysis, the crystallites are fixed on a carbon pad on a cylindrical aluminum sample holder. A qualitative EDX analysis of well-shaped single crystals is performed in order to verify the absence of elements heavier than sodium. A semi-quantitative EDX (without usage of an internal standard) analysis is run to confirm the composition of the crystal.

2.4 Differential Thermal Analysis (DTA)

The thermal analyses are carried out in the temperature range 298 – 1373 K using custom-made niobium containers for the sample and as reference crucible (Netzsch DSC 404C). The niobium crucibles are loaded with 30 – 100 mg of powdered sample. Afterwards, they are closed mechanically by pressing the niobium in the upper part of the crucible using a pipe tong and subsequent welding. The DTA curves are recorded under continuous argon flow (50 mL min^{-1}) to prevent the corrosion of the crucibles at high temperatures. After the DTA experiments, the crucibles are opened in the glove box and the products are again analyzed by X-ray powder diffraction. The results of the thermo diagrams are evaluated with the software Proteus Analysis (Netzsch) [16].

2.5 Magnetic Measurements

The measurements concerning tests for superconductivity are performed on a MPMS XL 5 (Quantum Design) magnetometer with a temperature range of 1.7 – 400 K and magnetic fields up to 5 T. Approximately 30 mg of the samples are tightly sealed into a gelatin capsule and fixed in the center of a plastic straw. Prior to the measurement, the permanent field of the sample chamber is checked with a Hall probe and compensated with

a polarized field. Regarding superconductive transitions, the samples are cooled in the absence of a magnetic field and then heated in the presence of a field of 15 Oe from 1.8 K to 50 K.

2.6 Computational Methods

Within the density functional theory (DFT), the linear muffin-tin orbital (LMTO) method in the atomic sphere approximation (ASA) using the tight-binding (TB) program TB-LMTO-ASA [17] is used for most calculations of the electronic structures. The basis set used for the LMTO method is obtained by dividing up the unit cell into regions inside muffin-tin spheres and an interstitial region. In the ASA, the potential is spherically symmetric within the muffin-tin spheres and is negligible in the interstitial regions. For modelling the full potential the ASA radii of the spheres is changed, such that the total volume of the resulting spheres (Wiegner-Seitz spheres) is equal to the unit cell volume, i.e. space filling is obtained. The overlapping of the spheres should be no more than 16%. In the case of open structures, empty spheres (ES) are inserted to minimize the overlapping and to achieve space filling. The radii of the muffin-tin spheres and empty spheres are determined by means of a routine developed by Jepsen and Andersen [18]. The exchange-correlation term is calculated within the local density approximation (LDA) and is parameterized according to von Barth and Hedin [19]. The basis sets of short-ranged atom-centred TB-LMTOs are automatically generated and adjusted (used, downfolded using the Löwdin downfolding technique [20, 21] or deactivated).

Additionally, first-principle full-potential DFT calculations are performed with the program WIEN2K [22]. The basis set is obtained by a muffin tin construction of non-overlapping spheres, i.e. dividing the unit cell into non-overlapping atomic spheres and an interstitial region. For the spheres a linear combination of radial functions times spherical harmonics (atom like basis set) is used. The symmetry of the potential within the spheres is not subject to any restrictions (i.e. full-potential, FP). The basis set describing the interstitial region consists of a mixture of “linear augmented plane waves” (LAPW) as well as augmented plane waves to which local orbitals are added (APW+lo). For the exchange-correlation term different approximations can be chosen: Here, the Generalized Gradient Approximation (GGA) of Perdrew, Burke and Ernzerhof [23] as well as the

modified Becke-Johnson potential (mBJ) [24] are used. The further parameters for the calculations performed with WIEN2K are given in chapter 4.2.

All k-space integrations are performed by the tetrahedron method [25]. The analysis of the chemical bonding is based upon partial and total Density Of States (DOS) curves. Plots of bandstructures with fatbands are created for the band character analysis. In the fatband analysis the atomic orbital character is represented as a function of the band width.

As a quantitative measure of the bonding strength, the energy contributions of all electronic states for selected bonds are calculated by the Crystal Orbital Hamilton Populations (COHPs) [26]. From the analyses of the –iCOHP (integrated COHP) values, the contribution of the covalent part of a particular interaction to the total bonding energy of the crystal can be obtained.

For the graphical representations of the DOS curves, the bandstructure plots and the COHP curves the program Gnuplot [27] is used.

For an analysis of the chemical bonding the Electron Localization Function (ELF) [28-32], introduced by Becke and Edgecombe, is calculated. The ELF allows the topographical analysis of the electron density distribution and therefore is used to locate bonding and electron lone pairs. It can have values between 0 and 1. The ELF 2D slices through the crystal structures as well as isosurfaces displaying a certain ELF value are graphically represented using the program XCrySDen [33] and the program VESTA [34]. Further analyses of the electron densities are carried out using Bader's AIM (Atoms In Molecules) formalism and the corresponding analyses of the bond critical points [35].

2.7 References

[1] N. Wiberg, *Lehrburch der Anorganischen Chemie*, 102 ed., Walter de Gruyter, Berlin, New York, **2007**.

[2] G. Brauer, *Handbuch der präparativen anorganischen Chemie*, 3 ed., Ferdinand Enke Verlag Stuttgart, **1996**.

[3] STOE, WinXPOW Version 2.08, STOE & Cie GmbH, Darmstadt **2003**.

[4] FindIt, ICSD Database, Version 1.7.0 FIZ Karlsruhe, Germany, **2010**.

[5] P. Villars, K. Cenzual, Pearson's crystal Date: Crystal Structure Database for Inorganic Compounds (on CD-ROM) Version 1.0, Release 2007/8, ASM International, Materials Park, Ohio, USA,

[6] X-Area Stoe & Cie GmbH, **2008**.

[7] CrysAlis RED, *Scale3 / ABSPACK*, Version 1.171.33.34d, Oxford Diffraction Poland Sp. z o.o., **2009**.

[8] Bruker, APEX2, SAINT and SADABS, Bruker AXSinc., Madison, Wisconsin (USA), **2007**.

[9] X-RED32 - *Data Reduction Program*, Version 1.48, Stoe & Cie GmbH, Darmstadt (Germany), **2008**.

[10] X-SHAPE - *Crystal Optimization for Numerical Absorption Correction*, Version 2.11, STOE & Cie GmbH, Darmstadt (Germany), **2008**.

[11] G. M. Sheldrick, *Acta Crystallogr., Sect. A* **2008**, *64*, 112.

[12] G. M. Sheldrick, SHELXS-97 – *Program for the Determination of Crystal Structures*, University of Göttingen (Germany) **1997**.

[13] G. M. Sheldrick, SHELXL-97 – *Program for Crystal Structure Refinement*, University of Göttingen (Germany) **1997**.

[14] L. M. Gelato, E. Parthe, *J. Appl. Crystallogr.* **1987**, *20*, 139.

[15] K. Brandenburg, Diamond Version 3.2g, Crystal Impact GbR, Bonn, Germany, **2011**.

[16] NETZSCH-Gerätebau GmbH, Proteus - Thermal Analysis, Version 4.3.1, Selb (Germany), **2004**.

[17] M. v. Schilfgarde, T. A. Paxton, O. Jepsen, O. K. Andersen, G. Krier, The Stuttgart Tight-Binding LMTO-ASA program Version 4.7, Max-Planck-Institut für Festkörperforschung Stuttgart (Germany), **1998**

[18] O. Jepsen, O. K. Andersen, *Z. Phys. B* **1995**, *97*, 35.

[19] U. V. Barth, L. Hedin, *J. Phys. Chem. C* **1972**, *5*, 1629.

[20] O. K. Andersen, O. Jepsen, *Phys. Rev. Lett.* **1984**, *53*, 2571.

[21] O. K. Andersen, *Phys. Rev. B* **1975**, *12*, 3060.

[22] P. Blaha, K. Schwarz, G. K. H. Madsen, D. Kvasnicka, J. Luitz, WIEN2k_10.1 - An Augmented Plane Wave + Local Orbitals Program for Calculating Crystal Properties TU Wien, **2010**.

[23] J. P. Perdrew, S. Burke, M. Ernzerhof, *Phys. Rev. Lett.* **1996**, *77*, 3865.

[24] F. Tran, P. Blaha, *Phys. Rev. Lett.* **2009**, *102*, 226401.

[25] P. E. Blöchl, O. Jepsen, O. K. Andersen, *Phys. Rev. B* **1994**, *49*, 16223.

[26] R. Dronskowski, P. E. Blochl, *J. Phys. Chem.* **1993**, *97*, 8617.

[27] T. Williams, C. Kelley, gnuplot 4.4, **2011**.

[28] A. D. Becke, K. E. Edgecombe, *J. Chem. Phys.* **1990**, *92*, 5397.

[29] T. F. Fässler, *Chem. Soc. Rev.* **2003**, *32*, 80.

[30] T. F. Fässler, A. Savin, *Chemie in Unserer Zeit* **1997**, *31*, 110.

[31] A. Savin, R. Nesper, S. Wengert, T. F. Fassler, *Angew. Chem. Int. Ed. Engl.* **1997**, *36*, 1809.

[32] M. Kohout, F. R. Wagner, Y. Grin, *Theor. Chem. Acc.* **2002**, *108*, 150.

[33] A. Kokalj, *Comp. Mater. Sci.* **2003**, *28*, 155.

[34] K. Momma, F. Izumi, VESTA: a three-dimensional visualization system for electronic and structural analysis **2008**.

[35] R. F. W. Bader, *Atoms in Molecules - A Quantum Theory*, Oxford University Press, Oxford, **1990**.

3 Results and Discussion

3.1 Outline

In the course of this work, a series of new binary and ternary polar intermetallic compounds in the systems *Ae*/*T*/*Tt* (*Ae*: Mg, Ca, Sr, Ba; *T*: Co, Ni; *Tt*: Sr, Ge, Sn) was synthesized and characterized. Based on their compositions the compounds are grouped in four chapters:

- Binary intermetallic phases in the systems *Ae*/*Tt* (*Ae*: Sr, Ba; *Tt*: Ge, Sn)
- Polar intermetallic phases in the systems *Ae*/Ni/Ge (*Ae*: Mg, Ca, Sr, Ba)
- Polar intermetallic phases in the systems Ca/Co/Si and Ba/Co/Ge
- Polar intermetallic phases in the systems *Ae*/Ni/Sn (*Ae*: Mg, Ca)

In the following, the results concerning the crystal structures as well as the electronic structure of the synthesized polar intermetallic phases will be summarized; detailed descriptions are given in chapter 4.

3.2 Binary Intermetallic Phases in the Systems *Ae*/*Tt* (*Ae*: Sr, Ba; *Tt*: Ge, Sn)

3.2.1 Sr_7Ge_6, Ba_7Ge_6 and Ba_3Sn_2

See chapter 4.2.1: Sr_7Ge_6, Ba_7Ge_6 and Ba_3Sn_2 – Three New Binary Compounds Containing Dumbbells and Four-membered Chains of Tetrel Atoms with Considerable Ge-Ge π–Bonding Character

The Sr germanide Sr_7Ge_6 and the Ba germanide Ba_7Ge_6 were prepared by arc melting and subsequent annealing in welded tantalum ampoules in an induction and a resistance furnace, respectively. The Ba stannide Ba_3Sn_2 was prepared by direct reaction of the elements in welded tantalum ampoules using a resistance furnace. The compounds were investigated by powder and single crystal X-ray diffraction methods.

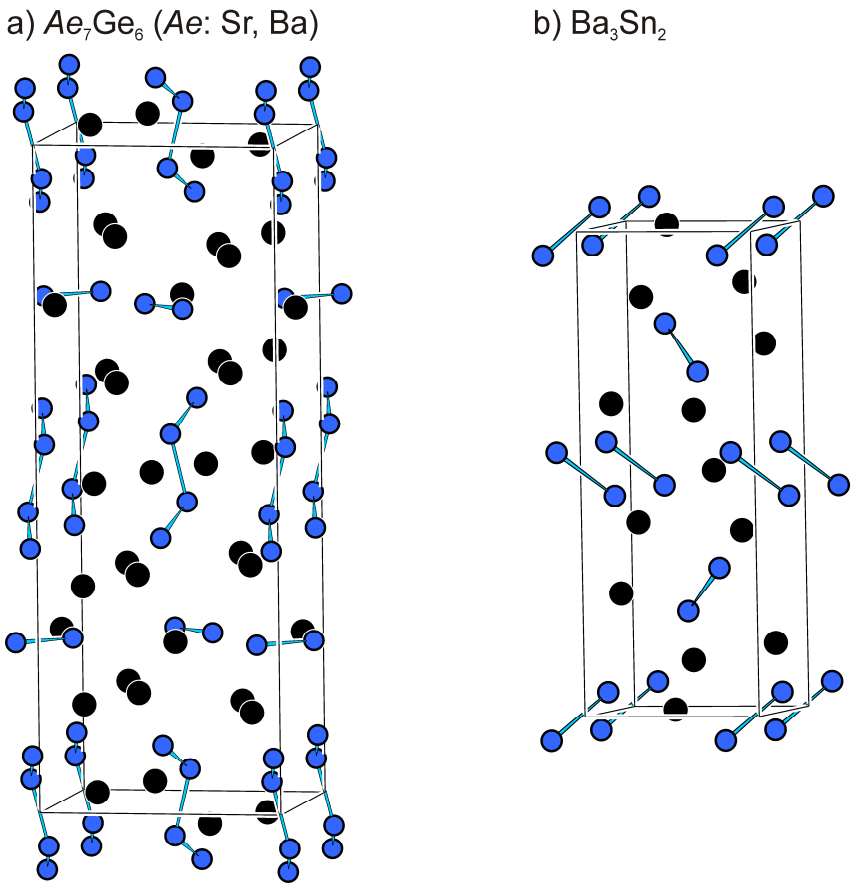

Figure 3.1 Crystal structures of a) Ae_7Ge_6 (*Ae*: Sr, Ba) and b) Ba_3Sn_2. The Sr and Ba atoms are drawn in black, the Ge and Sn atoms in blue.

Sr_7Ge_6 and Ba_7Ge_6 crystallize in the Ca_7Sn_6 structure type [1]. The main structure motifs in Sr_7Ge_6 and Ba_7Ge_6 are Ge_2 dumbbells and four-membered Ge_4 chains (see Figure 3.1). The planar Ge_4 chains adopt *trans* conformation.

According to the (8-*N*) rule and assuming singly bonded $(1b\text{-}Ge)^{3-}$ atoms (1b: one-bonded) and two-fold connected $(2b\text{-}Ge)^{2-}$ atoms (2b: two-bonded), electron precise $[Ge\text{-}Ge]^{6-}$ and $[Ge_4]^{10-}$ polyanions are expected. Since the seven alkaline earth metal atoms provide 14 electrons to the polyanionic structures of Sr_7Ge_6 and Ba_7Ge_6, these are two electrons short in order compensate the 16 negative charges according to the Zintl concept. However, the formation of a Ge=Ge double bond either in the Ge_2 dumbbells or Ge_4 four-membered chains would lead to an electronically balanced situation.

Ba_3Sn_2 crystallizes in an own structure type. It shows Sn_2 dumbbells as main structural motif and it can be rationalized according to the Zintl-Klemm concept as $(Ba^{2+})_3(1b\text{-}Sn^{3-})_2$.

DFT calculations using the program WIEN2K as well as the program TB-LMTO-ASA were carried out in order to provide a basis for the discussion of the chemical bonding situation. The calculated Density Of States (DOS) curves show metallic conductivity for electron deficient Ae_7Ge_6. This is in agreement with the Zintl-Klemm concept, as Ae_7Ge_6 violates the (8-*N*) rule. A band gap above E_F for Ba_7Ge_6 and a pseudo band gap above E_F for Sr_7Ge_6 and Ca_7Ge_6 indicate that doping with a trivalent rare earth metal might lead to electron precise Zintl phases, containing exclusively single bonds between the Ge atoms. A band gap of 0.73 eV was calculated for the semiconducting Ba_3Sn_2.

The topological analysis of the Electron Localization Function (ELF) for the three title compounds shows disynaptic valence basins for each short *Tt*-*Tt* contact. This is confirmed by a Bader analysis of the bond critical points.

The discussion of the possible Ge=Ge double bonding in Ae_7Ge_6 is carried out on the basis of the band structures including fatbands. Partial π bonding is observed for Ca_7Ge_6 within the Ge_4 four-membered chain, while for Ba_7Ge_6 partial π bonding is favoured in the Ge_2 dumbbells. Thus, two resonance structures including both structural motifs are suggested: $\{[Ge\text{-}Ge]^{6-}/[Ge{=}Ge{=}Ge{=}Ge]^{8-}\} \leftrightarrow \{[Ge{=}Ge]^{4-}/[Ge\text{-}Ge\text{-}Ge\text{-}Ge]^{10-}\}$

3.3 Polar Intermetallic Phases in the Systems *Ae*/Ni/Ge (*Ae*: Mg, Ca, Sr, Ba)

The main focus of this work is placed on the study of nickel germanides of alkaline earth metals.

The crystal structures and the electronic structures of the novel ternary polar intermetallic phases $BaNi_2Ge$ and $Ca_4Ni_4Ge_3$ ([2], chapter 4.3.1), $Ba_2Ni_5Ge_4$ ([3, 4], chapter 4.3.2) as well as $CaNi_5Ge_3$, $Ca_{15}Ni_{68}Ge_{37}$ and $Ca_7Ni_{48.9(4)}Ge_{22.1(4)}$ ([5], chapter 4.3.3) are presented in the following. While the nickel germanides of the alkaline earth metals Ca, Sr and Ba are structurally closely related, in the system Mg/Ni/Ge the Laves phases *cF*-$MgNi_{2-\delta}Ge_\delta$, Mg_2Ni_3Ge and *hP*-$MgNi_{2-x}Ge_x$ ($x = 0.70(6)$) are found (chapter 4.3.4). The hitherto known ternary polar intermetallic compounds in the systems *Ae*/Ni/Ge (*Ae*: Ca, Sr, Ba) are reviewed in chapter 4.3.5. Structural relationships between the various crystal structures are described. A topological construction principle of the crystal

structures of ternary polar intermetallic phases based on structural features of binary phases can be seen in analogy to the Zintl-Klemm concept.

3.3.1 $BaNi_2Ge$ and $Ca_4Ni_4Ge_3$

See chapter 4.3.1: $BaNi_2Ge$ and $Ca_4Ni_4Ge_3$ – Two Layered Structures with $^2_\infty[Ni_2Ge]$ and $^2_\infty[Ni_4Ge_3]$ Networks [2]

The polar intermetallic compounds $BaNi_2Ge$ and $Ca_4Ni_4Ge_3$ [2] were prepared by melting stoichiometric amounts of the elements in welded tantalum ampoules using an induction furnace. The crystal structures were investigated by both powder and single crystal X-ray diffraction methods. Both compounds crystallize in own structure types, showing related two-dimensional $^2_\infty[Ni_xGe_y]$ layers. These layers are shown in Figure 3.2a and Figure 3.2c.

The $^2_\infty[Ni_2Ge]$ layers in $BaNi_2Ge$ are based on corrugated 6^3 nets of Ni atoms. The resulting Ni hexagons are centered by Ge atoms and adopt a boat conformation. These layers are closely related with the $^2_\infty[Ni_2Ge]$ layers observed in $SrNi_2Ge$ [6], which also consist of Ni hexagons centered by Ge atoms. For $SrNi_2Ge$ the Ni hexagons show a chair conformation and thus a different puckering of the layers results (Figure 3.2b).

In chapter 4.3.5 $^1_\infty[Ni_2Ge_2]$ ribbons are introduced as a central structural motif for the ternary polar intermetallic compounds in the systems *Ae*/Ni/Ge (*Ae*: Ca, Sr, Ba). The $^2_\infty[Ni_2Ge]$ layers of $BaNi_2Ge$ and $SrNi_2Ge$ can be deduced from these ribbons by inserting a one-dimensional zigzag chain of Ni atoms as indicated in Figure 3.2a and Figure 3.2b.

Similarly, the $^2_\infty[Ni_4Ge_3]$ layers in $Ca_4Ni_4Ge_3$ can be deduced from these $^1_\infty[Ni_2Ge_2]$ ribbons by interconnecting such ribbons via Ni-Ge-Ni bridges (Figure 3.2c). The "bridging" Ge atom is two-fold coordinated and due to its outstanding position this bridge is a unique structure motif in the systems *Ae*/Ni/Ge. Further, the $^2_\infty[Ni_4Ge_3]$ layers of $Ca_4Ni_4Ge_3$ can described as a defect variant of the layers in $SrNi_2Ge$: removing two Ni atoms from the $^2_\infty[Ni_2Ge]$ (= $^2_\infty[Ni_6Ge_3]$) sheets leads to a deformed $^2_\infty[Ni_4Ge_3]$ layer.

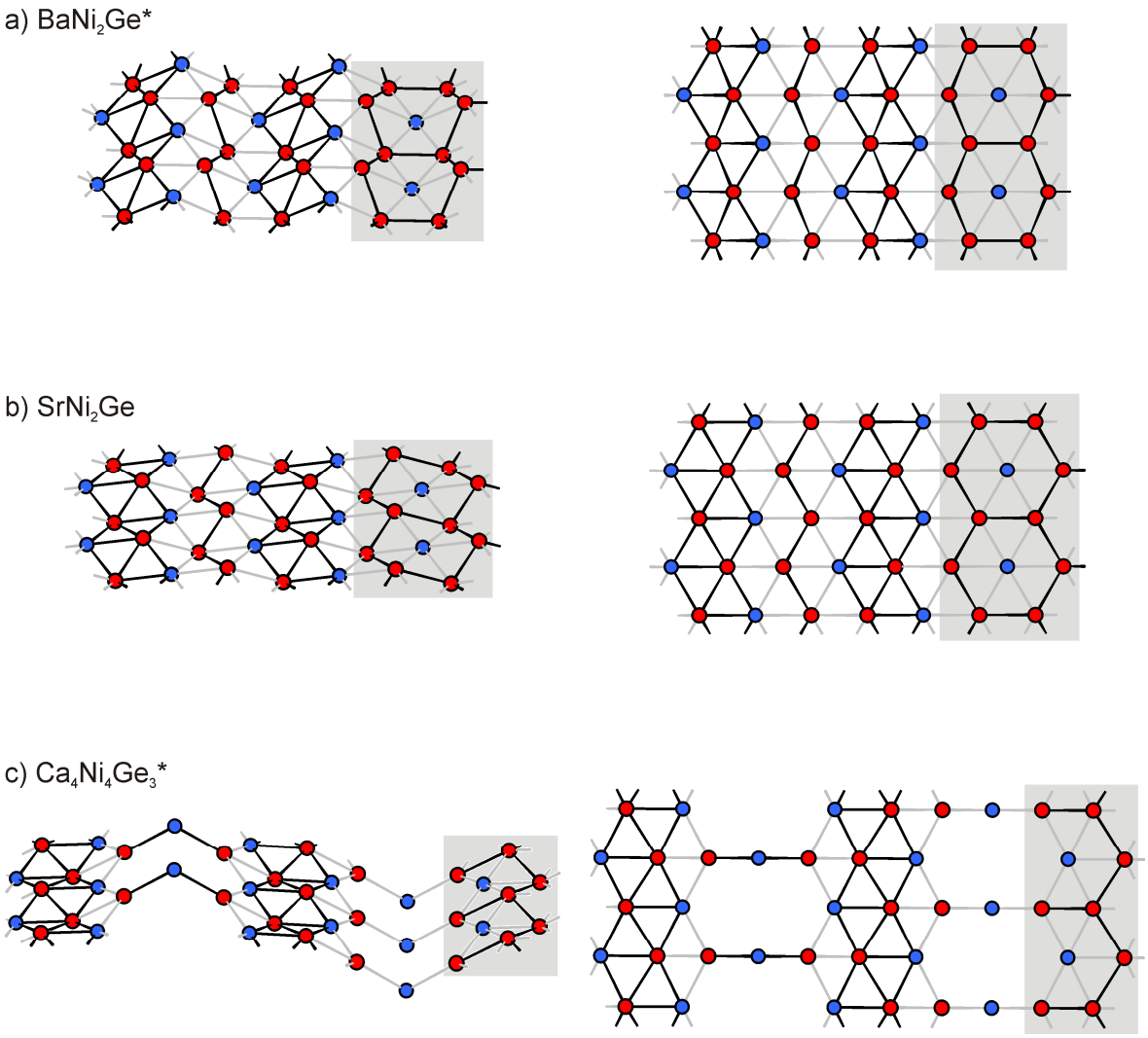

Figure 3.2 Ni-Ge layers in a) $BaNi_2Ge$, b) $SrNi_2Ge$ [6] and c) $Ca_4Ni_4Ge_3$. Compounds presented in this thesis are marked with *. Different structural motifs, such as the $^{1}_{\infty}[Ni_2Ge_2]$ ribbons, the zigzag chains of Ni atoms (a and b) and the Ni-Ge-Ni bridge (c) are emphasized using black bonds. The Ge-centered six-membered Ni_6 rings (a and b) as well as the defect variant of this motif (c) are highlighted with a grey background. Ni and Ge atoms are drawn in red and blue, respectively.

DFT calculations to $BaNi_2Ge$ and $Ca_4Ni_4Ge_3$ were carried out using the TB-LMTO-ASA program. The electronic structure and chemical bonding of the compounds is discussed on the basis of band structures including fatbands and a topological analysis of the ELF.

The band structure of $BaNi_2Ge$ reveals anisotropic metallic behaviour: Along lines that correspond to the direction perpendicular to the $^{2}_{\infty}[Ni_2Ge]$ layers a band gap at E_F and relatively flat bands are observed, while along the lines that correspond to the direction parallel to the layers the bands are significantly more dispersed.

For $Ca_4Ni_4Ge_3$ such anisotropy in the band structure is not observed and metallic behaviour is observed in all directions. The fatband analysis assigns the bands crossing E_F in the direction perpendicular to the layers to the (p) orbitals of the "bridging" Ge1 atom and thus to the significant puckering of the $^2_\infty[Ni_4Ge_3]$.

The topological analysis of the ELF reveals that electrons are mainly localized in lone pairs at the Ge atoms. The different shapes of the corresponding valence basins associated to the Ge atoms relate to their coordination within the $^2_\infty[Ni_xGe_y]$ layers.

3.3.2 $Ba_2Ni_5Ge_4$

See chapter 4.3.2: Synthesis, Structure and Chemical Bonding of $Ba_2Ni_5Ge_4$ – An Intermetallic Compound with a New Two-dimensional $^2_\infty[Ni_5Ge_4]$ Structural Motif [3]

The intermetallic compound $Ba_2Ni_5Ge_4$ [3] was prepared by arc melting stoichiometric mixtures of the elements and subsequent annealing in welded tantalum ampoules using a resistance furnace. The compound crystallizes in a new structure type and contains two-dimensional $^2_\infty[Ni_5Ge_4]$ slabs that are separated by Ba atoms. The slabs are shown in Figure 3.3b. They consist of a new combination of two structure motifs that are also present in other known intermetallic compounds in the system *Ae*/Ni/Ge (*Ae*: Ca, Sr, Ba). In detail, these are distorted $^1_\infty[Ni_2Ge_2]$ ribbons, which also occur in the low-temperature modification of $BaNi_2Ge_2$ [7], and distorted hexagonal prisms of the composition $Ni@Ni_6Ge_6$, that are present in the $SrNi_3Ge_2$ structure type [6].

In chapter 4.3.5 the crystal structure of $Ba_2Ni_5Ge_4$ is explained on the basis of the $^1_\infty[Ni_2Ge_2]$ ribbons as indicated in Figure 3.3. In Figure 3.3a two parallel ribbons are connected via Ni-Ge bonds. Hence, a *transoid* arrangement of the two ribbons results. The PbO-type layers observed in LT-$BaNi_2Ge_2$ are obtained by similar connection of the $^1_\infty[Ni_2Ge_2]$ ribbons. In Figure 3.3c two parallel ribbons are connected via Ni-Ge bonds in a way that leads to hexagonal prisms. In between the ribbons additional Ni atoms are situated and thus Ni-centered $Ni@Ni_6Ge_6$ hexagonal prisms result.

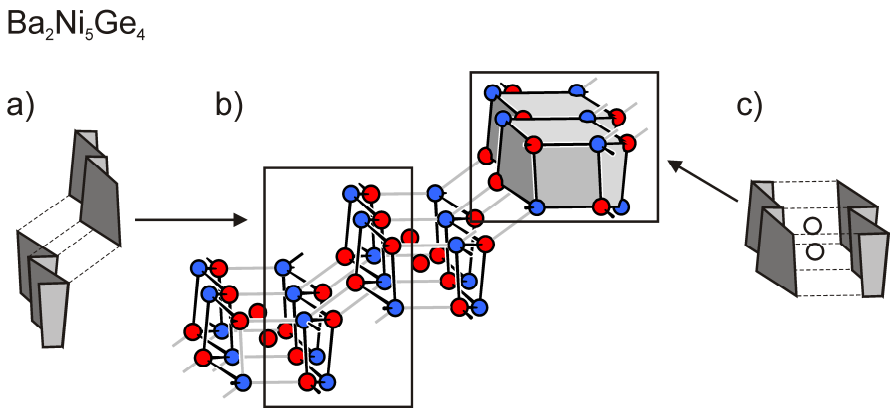

Figure 3.3 b) $^{2}_{\infty}[Ni_5Ge_4]$ layer of $Ba_2Ni_5Ge_4$, a) and c): schematic depictions of the structural motifs deduced from the basic module of the $^{1}_{\infty}[Ni_2Ge_2]$ ribbons. Ni and Ge atoms are drawn in red and blue, respectively.

DFT calculations for $Ba_2Ni_5Ge_4$ were carried out using the TB-LMTO-ASA program. The total DOS curve reveals metallic properties. A more detailed analysis of the band structure shows anisotropic characteristics with steep band along the lines that correspond to the directions parallel to the layers and flat bands along the lines that correspond to the direction perpendicular to the layers. This anisotropy is a trivial consequence from the two-dimensional Ni-Ge layers separated by Ba atoms in $Ba_2Ni_5Ge_4$. However, the flat bands along the lines that correspond to the directions perpendicular to the layers are close to E_F. This band characteristic was associated with a “fingerprint” for superconductivity [8-10]. Nevertheless, for $Ba_2Ni_5Ge_4$ no superconducting behavior was observed down to 1.8 K.

3.3.3 $CaNi_5Ge_3$, $Ca_{15}Ni_{68}Ge_{37}$ and $Ca_7Ni_{49}Ge_{22}$

See chapter 4.3.3: Complex Intermetallic Compounds: $CaNi_5Ge_3$, $Ca_{15}Ni_{68}Ge_{37}$ and $Ca_7Ni_{49}Ge_{22}$ – Three Multifaceted Ni-Ge Framework Structures Combining the Structural Motifs of Ni_3Ge and $CaNi_2Ge_2$ [5]

The polar intermetallic compounds $CaNi_5Ge_3$, $Ca_{15}Ni_{68}Ge_{37}$ and $Ca_7Ni_{48.9(4)}Ge_{22.1(4)}$ were prepared by arc melting of the elements and subsequent annealing in welded tantalum ampoules using an induction furnace. The compounds were investigated by powder and single crystal X-ray diffraction methods. All three compounds crystallize in own structure types. Their crystal structures (Figure 3.4) consist of complex three-dimensional networks of Ni and Ge atoms with two common motifs, namely different sections of the Ni_3Ge [11] structure as well as Ca-centered hexagonal prisms similar to those observed in $CaNi_2Ge_2$ [12].

The varying size and arrangement of the slabs of the Ni_3Ge structure lead to the different crystal structures of $CaNi_5Ge_3$, $Ca_{15}Ni_{68}Ge_{37}$ and $Ca_7Ni_{48.9(4)}Ge_{22.1(4)}$. Even though all three compounds show a three-dimensional network of Ni and Ge, regarding the cutouts of the Ni_3Ge structure a correlation between the Ca content and the dimensionality of the Ni-Ge substructures is noted: Within the series of the three compounds $Ca_7Ni_{48.9(4)}Ge_{22.1(4)}$, $CaNi_5Ge_3$ and $Ca_{15}Ni_{68}Ge_{37}$, the increasing Ca content leads different degrees of interconnection between the Ni_3Ge cutouts [5]. Neglecting the Ni and Ge atoms which are not part of these Ni_3Ge cutouts, the Ni-Ge substructures can be considered as three-, two- and one-dimensional structures, respectively. This is comparable to the series of Zintl phases $CaGe_2$, CaGe and Ca_2Ge, in which Ca scissors the Ge diamond structure under formation of two-, one- and “zero”-dimensional Ge substructures.

The coordination polyhedra of Ca are condensed rods of hexagonal prisms of Ni and Ge atoms, similar to those observed in $CaNi_2Ge_2$. In $CaNi_5Ge_3$ the primitive stacking of the layers of the Ni_3Ge structure and its neighbouring Ge atoms leads to homonuclear Ge-Ge bonds. In $Ca_7Ni_{48.9(4)}Ge_{22.1(4)}$ structural frustration leads to a mixed site occupancies of Ni and Ge in the isolated rods of face-sharing Ca-centered hexagonal prisms. In contrast, for the condensed rods of hexagonal prisms in $Ca_{15}Ni_{68}Ge_{37}$ and $Ca_7Ni_{48.9(4)}Ge_{22.1(4)}$ alternating Ni and Ge atoms are observed.

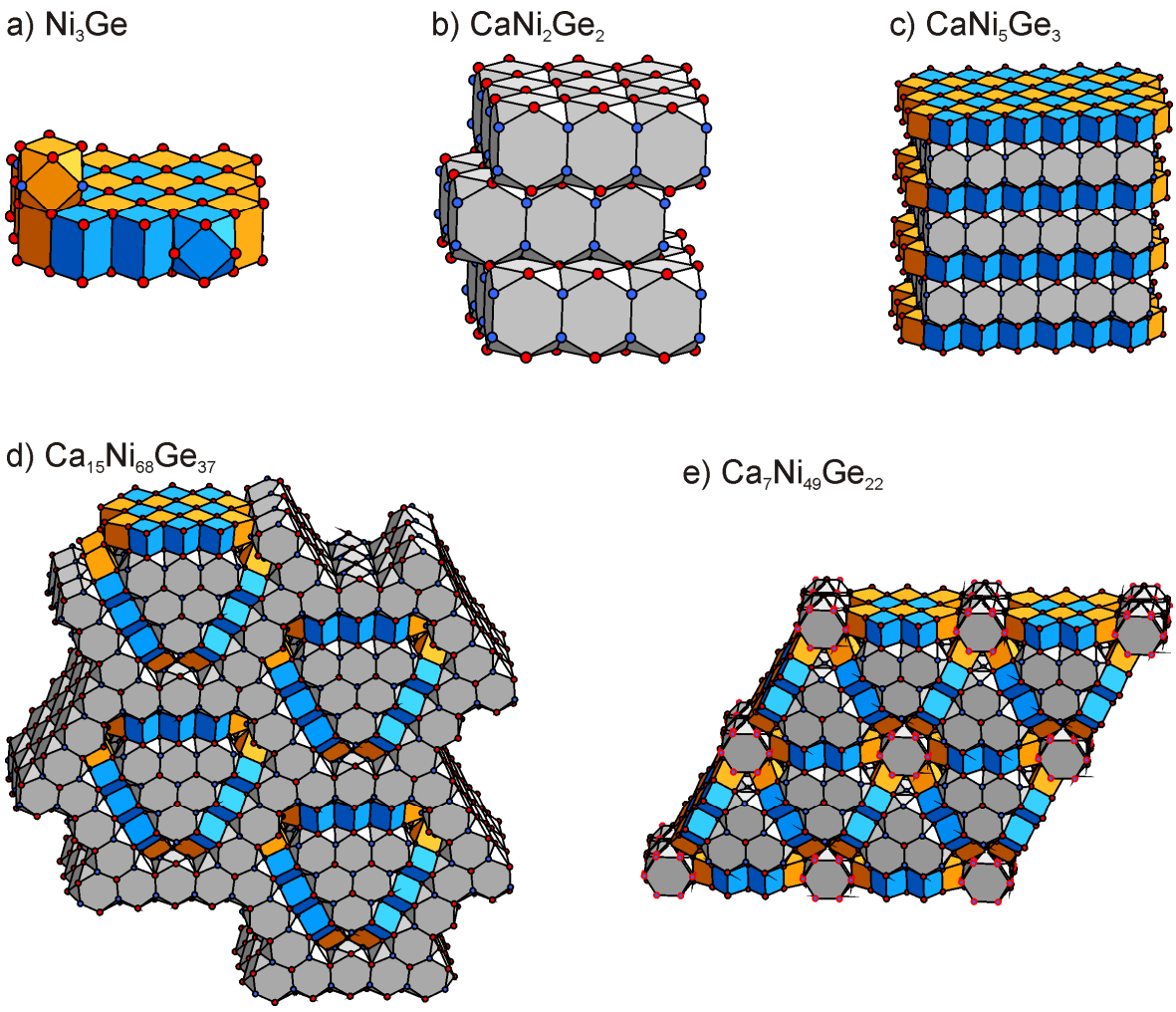

Figure 3.4 Crystal structures of a) Ni_3Ge, b) $CaNi_2Ge_2$, c) $CaNi_5Ge_3$, d) $Ca_{15}Ni_{68}Ge_{37}$ and e) $Ca_7Ni_{48.9(4)}Ge_{22.1(4)}$. Ge and Ni atoms are drawn as blue and red spheres, respectively. The Ge- and Ni-centered distorted cubes are drawn in blue and orange, respectively. The mixed occupied positions Ge/Ni in $Ca_7Ni_{48.9(4)}Ge_{22.1(4)}$ are shown as blue spheres with red borderlines.

Additionally to the structural elucidation, for $CaNi_5Ge_3$ the homonuclear Ge-Ge bonds in the Ca-centered polyhedra are discussed based on contour line diagrams of the ELF. A disynaptic valence basin confirms the covalent bonding between the Ge atoms.

3.3.4 Laves Phases in the System Mg/Ni/Ge

See chapter 4.3.4

The intermetallic phases in the system Mg/Ni/Ge differ from the compounds of the systems *Ae*/Ni/Ge (*Ae*: Ca, Sr, Ba). While the latter contain one-, two- or three-dimensional Ni-Ge substructures, only three-dimensional Ni-Ge structures are observed for the compounds $Mg_xNi_yGe_z$. However, the compound MgNiGe ([13], chapter 4.3.5) contains similar structural building units as the compounds *Ae*NiGe (*Ae*: Ca, Sr, Ba). In contrast, the Laves phases of the system Mg/Ni/Ge show pronounced Ni/Ge mixing and different structural characteristics.

The two new Laves phases Mg_2Ni_3Ge (superstructure of C15) and *hP*-$MgNi_{2-x}Ge_x$ ($x = 0.70(6)$, superstructure of C14) were synthesized by direct reaction of the elements in alumina crucibles enclosed in niobium ampoules using an induction furnace. Their crystal structures are depicted in Figure 3.5. Further, the existence of the previously reported cubic Laves phase *cF*-$MgNi_{2-\delta}Ge_\delta$ (C15, [14]) was confirmed for small values of δ. The cell parameters and crystal structures were determined by single crystal X-ray diffraction.

The Laves phase *cF*-$MgNi_{2-\delta}Ge_\delta$ (C15, [14]) crystallizes in the $MgCu_2$ structure type, with a solid solution of Ni and Ge on the position of the Cu atoms.

Mg_2Ni_3Ge ($MgNi_{2-x}Ge_x$ with $x = 0.5$) crystallizes with space group $R\bar{3}m$ in the Y_2Rh_3Ge structure type [15], which is a superstructure of the cubic Laves phase $MgCu_2$. The Ni atoms (Wyckoff positions 9*e*) build up Kagomé nets (3.6.3.6.). ABC stacking of the Kagomé nets leads to the cubic Laves phase C15. The triangular faces of the Ni Kagomé nets are capped alternately below and above by Ge atoms (Wyckoff position 3*b*), which themselves form hexagonal 3^6 nets. The resulting three-dimensional Ni-Ge network consists of vertex-sharing Ni_3Ge tetrahedra. Two interatomic distances occur: Ni-Ni distances within the Kagomé nets (2.55 Å) are significantly longer than the Ni-Ge distances between the Ge atoms of the 3^6 and the Ni atoms of the Kagomé nets (2.44 Å). Thus, the resulting Ni_3Ge tetrahedra are distorted.

The hexagonal Laves phase *hP*-$MgNi_{2-x}Ge_x$ ($x = 0.70(6)$) crystallizes in the space group $P6_3/mcm$ in a superstructure of the hexagonal Laves phase $MgZn_2$ (C14). No ordering comparable to Mg_2Ni_3Ge is observed.

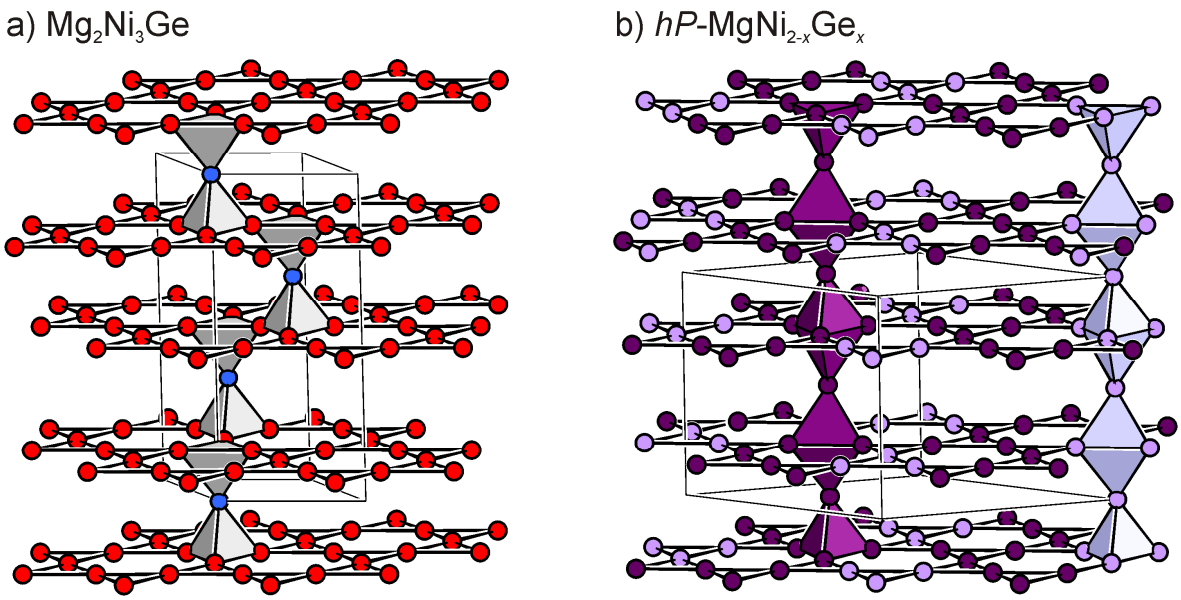

Figure 3.5 Ni-Ge networks of a) Mg_2Ni_3Ge and b) hP-$MgNi_{2-x}Ge_x$ (x = 0.70(6)). The Ni and Ge atoms are drawn in red and blue, respectively. The mixed occupied positions are shown in purple (Wyckoff position 12*j* and 4*d* in dark purple, Wyckoff positions 6*g* and 2*b* in light purple).

In contrast, mixed site occupancies of Ni and Ge occur in the Ni-Ge network, which contains Kagomé (3.6.3.6.) as well as hexagonal nets (3^6). A hexagonal stacking sequence AB of the Kagomé nets leads to the Laves phase C14. The Ni/Ge atoms of the hexagonal nets cap the trigonal faces of the Kagomé nets such that a three-dimensional network of vertex- and face-sharing tetrahedra of Ni/Ge results. In the cavities of this network the Mg atoms are situated. The structure refinement based on single crystal X-ray diffraction data leads to mixed occupied positions of Ni and Ge on the four Wyckoff positions 12*j*, 6*g*, 4*d* and 2*b*. Both positions of the Kagomé net (Ni1/Ge1 on 12*j* and Ni2/Ge2 on 6*g*) are occupied with 73(3)% Ni and thus are indistinguishable. In contrast, the positions of the hexagonal net (Ni3/Ge3 on 4*d* and Ni4/Ge4 on 2*b*) are occupied with 46(3)% and 34(5)% Ni, respectively.

In summary, starting with $MgNi_2$ and substituting Ni with Ge, thus raising the valence electron concentration (VEC), leads to the series of Laves phases C36 ($MgNi_2$ = $MgNi_{2-x}Ge_x$ with x = 0) → C15 (cF-$MgNi_{2-\delta}Ge_\delta$ with small values of δ) → superstructure of C15 (Mg_2Ni_3Ge = $MgNi_{2-x}Ge_x$ with x = 0.5) → superstructure of C14 (hP-$MgNi_{2-x}Ge_x$ = $MgNi_{2-x}Ge_x$ with x = 0.70(6)).

3.3.5 Nickel Germanides of Alkaline Earth Metals – Structural Peculiarities and Relationships

See chapter 4.3.5

In the course of this thesis as well as in further studies of the group of Prof. Fässler a manifold variety of new compounds in the systems *Ae*/Ni/Ge was discovered. A comprehensive overall description pointing out relationships between the various structures types was missing and is now given in chapter 4.3.5.

The discussion sheds light on numerous aspects concerning the crystal structures of the ternary polar intermetallic compounds. For example, the influence of an increasing *Ae* size on the dimensionality of the Ni-Ge polyanions is shown for the compounds of composition 1:1:1 and 1:2:2.

Further, $^{1}_{\infty}[Ni_2Ge_2]$ ribbons are shown to be a reoccurring structural motif. Most crystal structures can be described using these ribbons as a basic module. Exceptions are Ni rich compounds with a low *Ae* content in the systems *Ae*/Ni/Ge (*Ae*: Ca, Sr) and the clathrate $Ba_8Ni_{3.5}Ge_{42.1}$ [16, 17].

Additionally, the composition triangle containing all ternary polar intermetallic phases of the systems *Ae*/Ni/Ge provides a useful guideline to reveal structural relationships. Special attention is paid to the lines connecting the elements, i.e. the vertices of the triangle, with the (sometimes hypothetical) binary compounds of the simple compositions 2:1, 1:1 and 1:2. With the exception of the Ni rich compounds with low *Ae* content in the systems *Ae*/Ni/Ge (*Ae*: Ca, Sr) all known ternary compounds are situated on these lines. Comparing the crystal structures of these compounds, relationships are frequently visible along these lines. For example, the two-dimensional $^{2}_{\infty}[Ni_3Ge_2]$ layers of the polar intermetallic compound $Ca_2Ni_3Ge_2$ [18] are described as one-dimensional rods of vertex sharing $GeNi_4$ square pyramids which are further connected by Ge-centered Ni_6 hexagons. The $GeNi_4$ square pyramids are known from the PbO-type layers in CaNiGe [19] and the Ge-centered Ni_6 hexagons are condensed to $^{2}_{\infty}[Ni_2Ge]$ layers in $SrNi_2Ge$ [6]. The three compounds $Ca_2Ni_3Ge_2$, CaNiGe and $SrNi_2Ge$ are situated on the line connecting the element Ni with the binary phase *Ae*Ge, $Ca_2Ni_3Ge_2$ being positioned between CaNiGe and $SrNi_2Ge$.

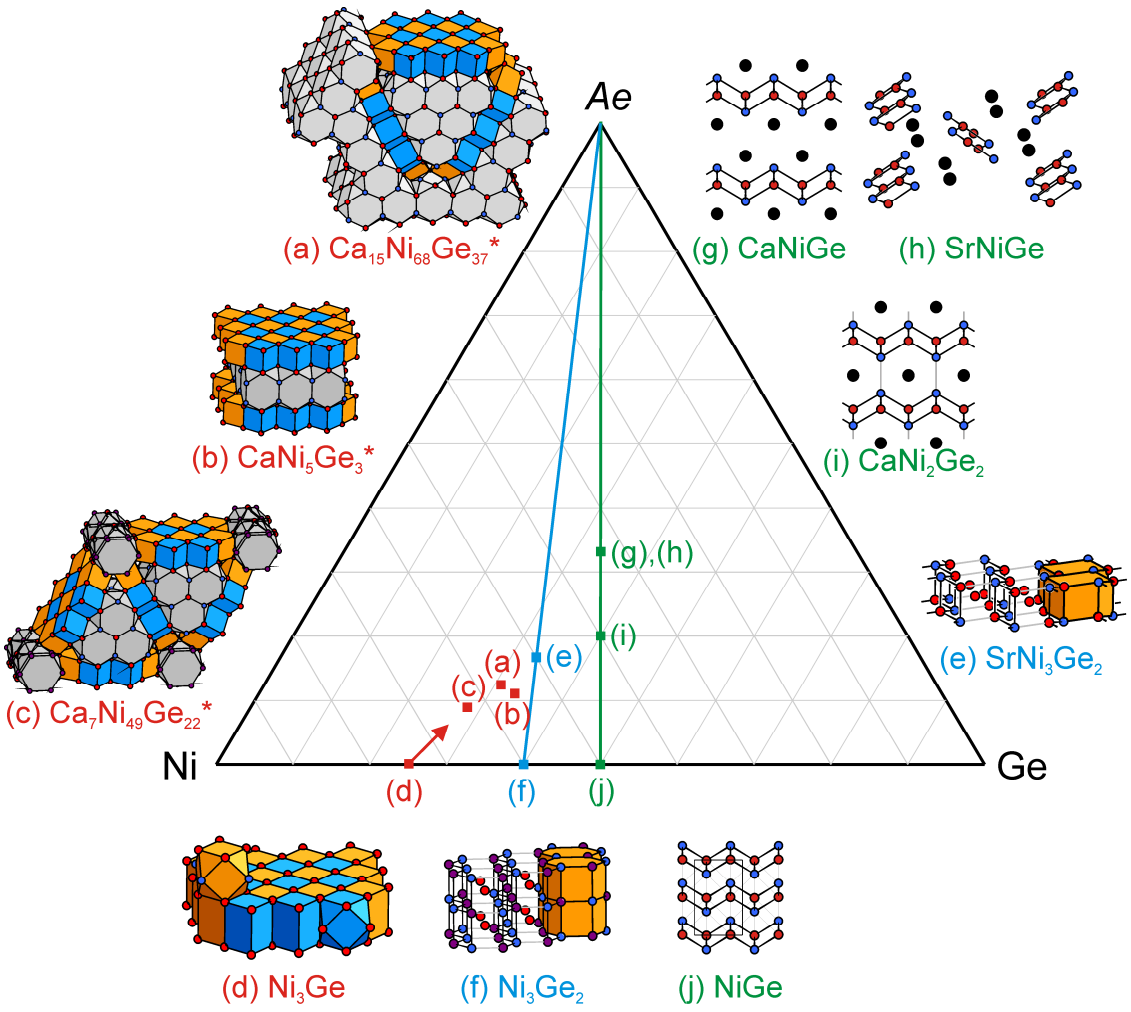

Figure 3.6 Composition triangle for the system *Ae*/Ni/Ge indicating structural relationships between selected binary and ternary compounds. Novel compounds investigated in this course of thesis are marked with *. Ni, Ge and Ni/Ge are drawn in red, blue and purple, respectively. Polyhedra centered by Ca, Ni and Ge are drawn in grey, orange and blue, respectively.

Not only the comparison of structural motifs observed in ternary intermetallic compounds proved beneficial for a better understanding of the crystal structures, but also the comparison with binary phases in the systems *Ae*/Ge, *Ae*/Ni and Ni/Ge is shown to be very useful. Structural motifs observed in ternary compounds with a composition at the extreme right (Ge rich) or left (Ni rich) of the composition triangle are often found in the binary compounds in the systems *Ae*/Ge and *Ae*/Ni, respectively. For example, the topology of the $^{2}_{\infty}[Ni_2Ge]$ network of $SrNi_2Ge$ [6] relates to that of the Ni network in Sr_2Ni_3 [20, 21].

The structural relationships between ternary polar intermetallic compounds and binary intermetallic phases in the system Ni/Ge are even more intriguing. Such relationships are depicted in Figure 3.6: Starting with NiGe [11] the addition of alkaline earth metal leads to *Ae*Ni_2Ge_2 [7, 12] and *Ae*NiGe [13, 19]. Similarly, the insertion of Sr in Ni_3Ge_2 [22] leads to $SrNi_3Ge_2$ [6]. To phrase it differently: the crystal structures of the ternary compounds *Ae*Ni_2Ge_2, *Ae*NiGe and $SrNi_3Ge_2$ contain three-, two- or one-dimensional networks that relate to the three-dimensional networks in the binary intermetallic compounds NiGe and Ni_3Ge_2, respectively. Ni rich compounds in the system Ca/Ni/Ge show Ni-Ge substructures formed of cutouts of the Ni_3Ge structure. Within the series of the three compounds $Ca_7Ni_{48.9(4)}Ge_{22.1(4)}$, $CaNi_5Ge_3$, and $Ca_{15}Ni_{68}Ge_{37}$, the increasing content of Ca leads to three-, two- and one-dimensional Ni-Ge substructures of the Ni_3Ge cutouts, respectively [5].

Based on these relationships, binary intermetallic compounds in the systems *T*/*Tt* suggest themselves as a reference point for the description of the crystal structures of ternary polar intermetallic compounds $Ae_xT_yTt_z$. The formal addition of *Ae* to a binary intermetallic phase T_xTt_y, leads to a ternary polar intermetallic compound. The electropositive element *Ae* transfers partially electrons to the more electronegative *T*-*Tt* network, which is thus reduced and adopts a structure reminiscent to those of binary intermetallic phases. This approach underlines that the understanding of binary intermetallic phases is a necessary basis for rationalization of the structures of *T*-*Tt* polyanions of ternary polar intermetallic compounds.

Furthermore, the usage of ternary composition triangle may even provide a concept to deduce “educated guesses” on the compositions and structure of new crystal structures.

3.4 Polar Intermetallic Phases in the Systems Ca/Co/Si and Ba/Co/Ge

3.4.1 $CaCo_2Si_2$ and $BaCo_2Ge_2$

See chapter 4.4.1: Synthesis, Structure and Chemical Bonding of $CaCo_2Si_2$ and $BaCo_2Ge_2$ − Two New Compounds with $ThCr_2Si_2$ Structure Type [23]

The intermetallic compounds $CaCo_2Si_2$ and $BaCo_2Ge_2$ are prepared by arc melting stoichiometric mixtures of the elements and subsequent annealing in welded tantalum ampoules using an induction furnace. The compounds were investigated by powder and single crystal X-ray diffraction methods.

Both title compounds crystallize in the $ThCr_2Si_2$ structure type (Figure 3.7). The Co-*Tt* networks consists of $[Co_2Tt_2]^{2-}$ (*Tt*: Si, Ge) PbO-type layers. The bigger Ae^{2+} (*Ae*: Ca, Ba) cations are situated between these layers. The layers may be described as being build up of $TtCo_4$ square pyramids. The Co atoms have a tetrahedral coordination environment with four nearest neighbours of *Tt*. The *Tt* atoms are situated on the top of the square pyramid with four nearest neighbours of Co. The two compounds demonstrate the tunable interlayer *Tt*-*Tt* distance between the tetrel elements in the $ThCr_2Si_2$ type structures ("122 compounds"). While for $CaCo_2Si_2$ a covalent Si-Si bond is present (d(Si-Si) = 2.58 Å), no Ge-Ge bond occurs for $BaCo_2Ge_2$ (d(Ge-Ge) = 3.55 Å).

The $CaCo_2Si_2$ and $BaCo_2Ge_2$ are isoelectronic to $BaFe_2As_2$ [24], the parent compound of new high temperature superconductors [25]. A structural parameter discussed in this context is the deformation of the *Tt*-Co-*Tt* bond angles as compared to the ideal tetrahedral angle. For superconducting iron arsenides the transition temperature T_c appears to be maximized if the As-Fe-As bond angle is close to the ideal tetrahedral angle of 109.5° [26]. However, for $CaCo_2Si_2$ and $BaCo_2Ge_2$ the *Tt*-Co-*Tt* bond angles deviate significantly from this value, with 117.4° and 120.4°, respectively.

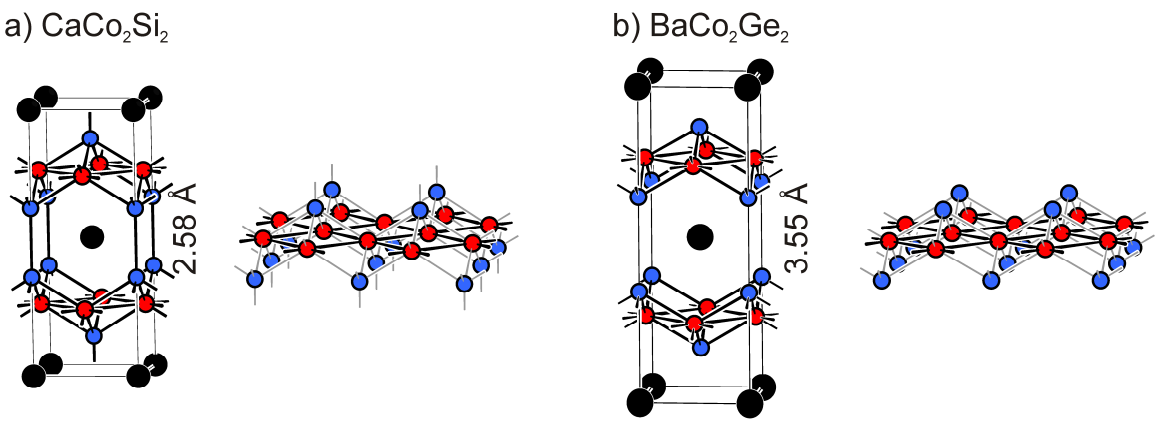

Figure 3.7 Crystal structures of a) $CaCo_2Si_2$ and b) $BaCo_2Ge_2$. Ca and Ba atoms are drawn in black, Co in red and Si and Ge in blue.

Computational studies concerning the electronic structures as well as the chemical bonding situation were carried out using the TB-LMTO-ASA program. The DOS curves reveal no band gap at the Fermi level, indicating metallic properties of the two compounds. A topological analysis of the ELF clearly shows covalent character of the Si-Si contact for $CaCo_2Si_2$ and the absence of Ge-Ge bonding interactions and lone pair formation in $BaCo_2Ge_2$.

3.5 Polar Intermetallic Phases in the Systems *Ae*/Ni/Sn (*Ae*: Mg, Ca)

3.5.1 Ca_2NiSn_2

See chapter 4.5.1: Ca_2NiSn_2 – A Polymorphic Intermetallic Phase. Atomic and Electronic Structure as well as a Topological Description of the Phase Transition by a Sigmatropic-Type Rearrangement of Ni and Sn Atoms [27]

Two modifications of the intermetallic compound Ca_2NiSn_2 [27] were prepared by arc melting stoichiometric amounts of the elements and subsequent annealing at various temperatures in welded tantalum ampoules using a resistance furnace. The crystal structures of the two modifications were investigated by X-ray diffraction both with powder and single crystal methods.

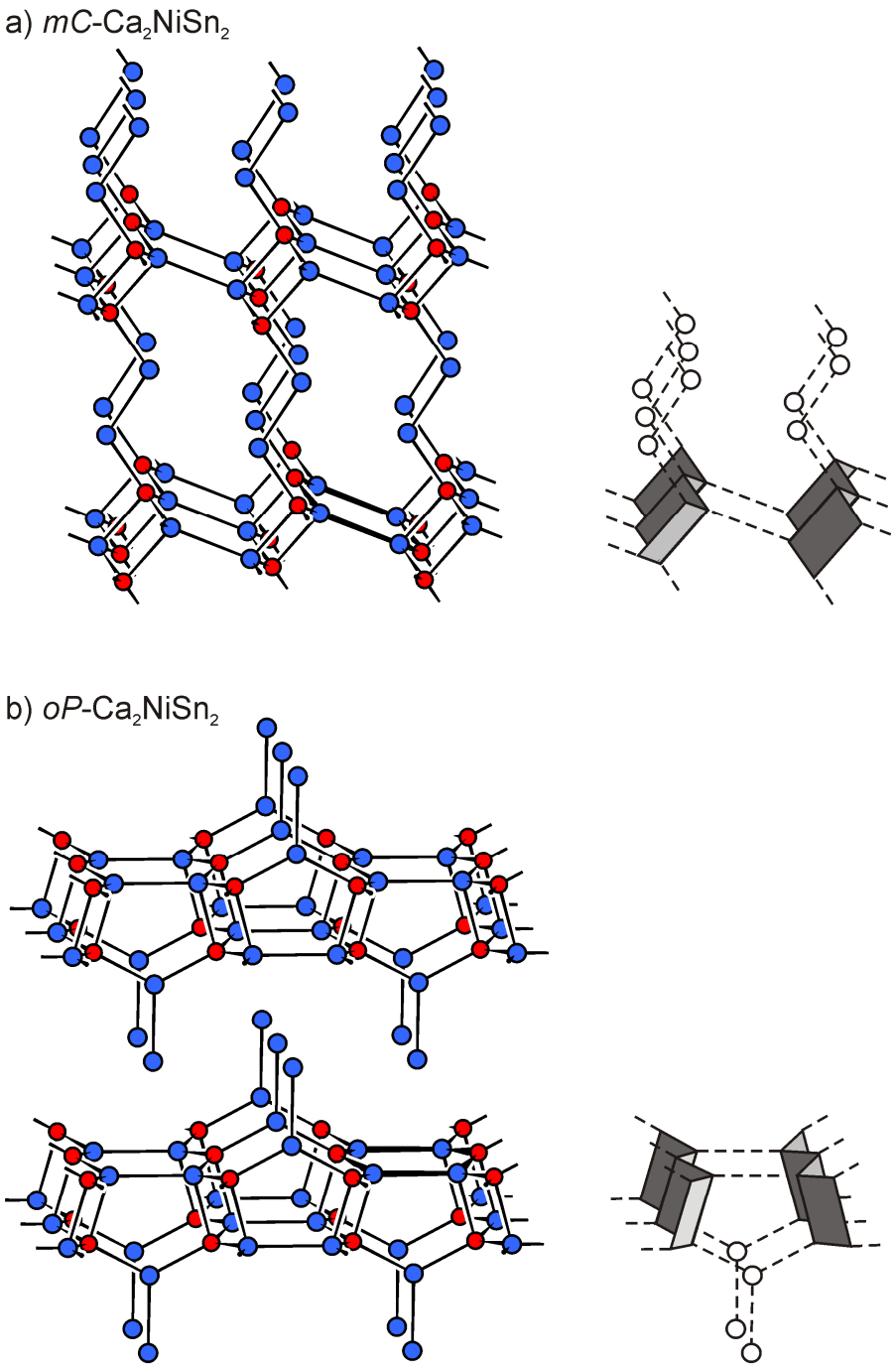

Figure 3.8 Left: Ni-Sn network of a) *mC*-Ca_2NiSn_2 and b) *oP*-Ca_2NiSn_2. Right: respective schematic descriptions of the networks. Ni and Sn atoms are drawn in red and blue, respectively.

The metastable monoclinic modification *mC*-Ca_2NiSn_2 is obtained by arc melting. The modification *mC*-Ca_2NiSn_2 was preserved when annealing the regulus obtained by arc melting at $T = 700$ °C to $T = 750$ °C. It crystallizes in the Zr_2CoSi_2-structure type [28]. The Ni-Sn substructure is a three-dimensional network built up of two-dimensional $^{2}_{\infty}[Ni_2Sn_2]$

layers which are interconnected via Sn_2 dumbbells. A schematic description of these layers is given in Figure 3.8. Parallel $^1_\infty[Ni_2Sn_2]$ ribbons, similar to the $^1_\infty[Ni_2Ge_2]$ ribbons observed in the systems *Ae*/Ni/Ge, are linked via Sn-Sn bonds. $^2_\infty[Ni_2Sn_2]$ layers with *transoid* arrangement of the ribbons result. The Ni atoms of these layers are further connected with the Sn_2 dumbbells. Thus, twelve-membered rings occur between the layers. The cavities of the resulting three-dimensional Ni-Sn network are filled with Ca atoms.

Using higher annealing temperatures ($T = 800$ °C to $T = 870$ °C) leads to the formation of the orthorhombic modification *oP*-Ca_2NiSn_2, which crystallizes in an own structure type with $^2_\infty[Ni_2Sn_4]$ layers. These layers are built up of $^1_\infty[Ni_2Sn_2]$ ribbons connected via Sn-Sn bonds. A *cisoid* arrangement of the ribbons results. Additionally, the Ni atoms of two such ribbons are connected via one side of a Sn_2 dumbbell. Five-membered Ni-Sn ring result. The layers are separated by Ca atoms.

For the crystal structures of the two modifications no group-subgroup relationship can be described. Consequently, the mechanism of the phase transition is most likely reconstructive. Nevertheless, two approaches for a topological description of the phase transition are given: The first describes the conversion between the structures by a simple shift of ribbons of atomic layers. The second approach involves a least motion process for the atom rearrangement, describing the topology of the phase transformation by an electrocyclic mechanism through Ni-Sn bond scission and formation in analogy to sigmatropic shift reactions known for organic molecules.

The chemical bonding of these compounds is discussed based on the results of DFT calculations using the TB-LMTO-ASA program. An analysis of the band structures and a topological analysis of the ELF reveals partial π bonding for the Sn_2 dumbbells in *mC*-Ca_2NiSn_2 and a short Sn-Sn contact in the Sn_2 dumbbells which is mainly dominated by (p) lone pairs in *oP*-Ca_2NiSn_2.

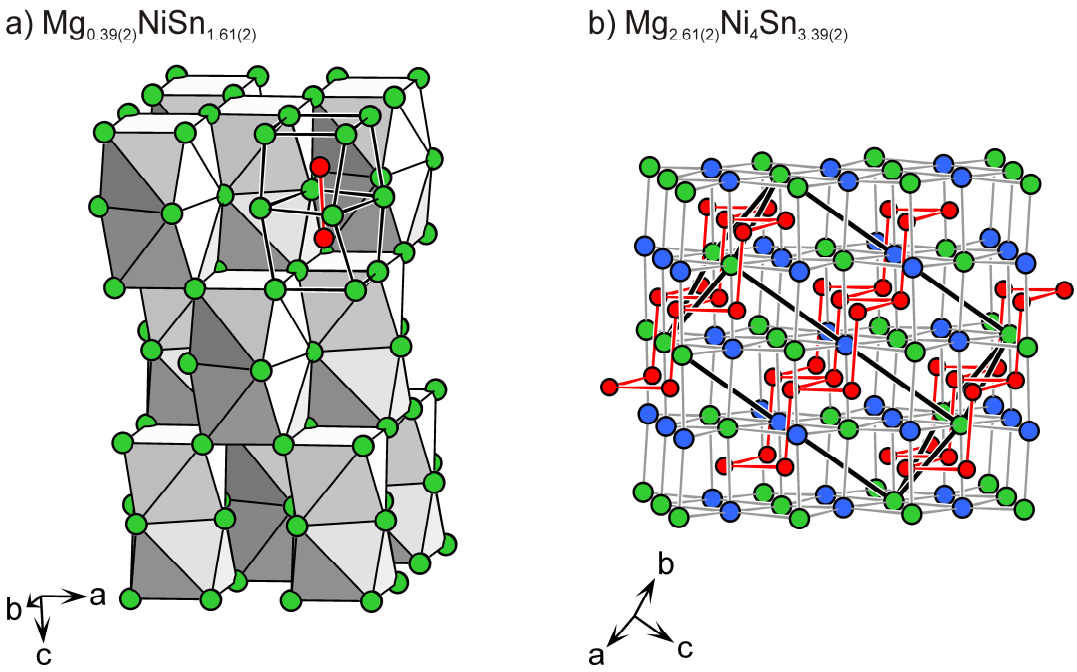

Figure 3.9 Crystal structures of a) $Mg_{0.39(2)}NiSn_{1.61(2)}$ and b) $Mg_{2.61(2)}Ni_4Sn_{3.39(2)}$. Mg/Sn mixed occupied positions are drawn as green spheres, Sn and Ni atoms as blue and red ones, respectively.

3.5.2 $Mg_{0.39(2)}NiSn_{1.61(2)}$ and $Mg_{2.61(2)}Ni_4Sn_{3.39(2)}$

See chapter 4.5.2: $Mg_{0.39(2)}NiSn_{1.61(2)}$ and $Mg_{2.61(2)}Ni_4Sn_{3.39(2)}$ – Two New Intermetallic Phases in the System Mg/Ni/Sn

Among the novel compounds presented in this work, the intermetallic phases in the system Mg/Ni/Sn take an exceptional position. While the compounds of the systems *Ae*/*T*/*Tt* (*Ae*: Ca, Sr, Ba; *T*: Co, Ni; *Tt*: Si, Ge, Sn) and even those of the system Mg/Ni/Ge contain one-, two- or three-dimensional *T*-*Tt* substructures which are reminiscent of the polyanions in Zintl phases, the intermetallic compounds in the system Mg/Ni/Sn exclude themselves from this description as Mg/Sn mixed occupied positions are formed.

Two novel intermetallic phases, $Mg_{0.39(2)}NiSn_{1.61(2)}$ and $Mg_{2.61(2)}Ni_4Sn_{3.39(2)}$, were synthesized by reaction of the elements in welded tantalum ampoules in a resistance furnace. The crystal structures were determined using single crystal X-ray diffraction data.

$Mg_{0.39(2)}NiSn_{1.61(2)}$ crystallizes in the α-$PdSn_2$ structure type [29], with Mg and Sn atoms mixing on the Sn positions of α-$PdSn_2$. The main building block of the crystal structure consists of two Ni-centred, face-linked square antiprisms. The resulting Ni-Ni

distance is 2.69 Å. The face-linked antiprisms are further connected via vertices to form a three-dimensional Mg/Sn-Mg/Sn network.

The coordination polyhedra of Ni observed for $Mg_{0.39(2)}NiSn_{1.61(2)}$ are compared to those of $Mg_{1.85(1)}NiSn_{0.15(1)}$, $Mg_{1.78(1)}NiSn_{0.22(1)}$ and $Mg_{1.60(1)}NiSn_{0.40(1)}$ [30]. All four intermetallic compounds can be described by the formula Mg_xNiSn_{2-x} with varying values of x. While the overall Mg/Sn : Ni ratio remains constant (2 : 1), the Mg : Sn ratio varies significantly. This is reflected by the different crystal structures. The coordination number of the Ni atoms in the Sn rich compound $Mg_{0.39(2)}NiSn_{1.61(2)}$ is 9 (8 Mg/Sn + 1 Ni) and two face-linked Ni-centred square antiprisms are found as a basic structure motif. In contrast, the coordination number of the Ni atoms in $Mg_{1.85(1)}NiSn_{0.15(1)}$, $Mg_{1.78(1)}NiSn_{0.22(1)}$ and $Mg_{1.60(1)}NiSn_{0.40(1)}$ is 10 (8 Mg/Sn + 2 Ni) and rods of face-linked Ni-centered antiprisms, which are further interlinked via their edges to a three-dimensional network, are found as structure motif.

In contrast to $Mg_{0.39(2)}NiSn_{1.61(2)}$ a partial ordering with positions occupied exclusively by Sn atoms and Mg/Sn mixed occupied positions is observed for $Mg_{2.61(2)}Ni_4Sn_{3.39(2)}$. The crystal structure of $Mg_{2.61(2)}Ni_4Sn_{3.39(2)}$ can be seen as an intermediate between a Heusler- and a half-Heusler-type structure. It crystallizes in an own structure type which can be described as a superstructure containing ordered vacancies of the Heusler-type phase $MgNi_2Sn$ [31]. The crystal structure of $Mg_{2.61(2)}Ni_4Sn_{3.39(2)}$ contains a distorted cubic network of Sn and Sn/Mg positions. 2/3 of the distorted cubic voids of this network are occupied by Ni. The coordination number of Ni is 10 (8 Mg/Sn + 2 Ni).

Only recently, the synthesis of a ternary intermetalloid cluster anion $[Ni_2Sn_7Bi_5]^{3-}$, analogue to that of the $Ni_2@(Mg/Sn)_{12}$ building block observed in $Mg_{0.39(2)}NiSn_{1.61(2)}$, was reported [32]. This reinforces the relationship between intermetalloid cluster anions obtained from solution based Zintl anion chemistry and intermetallic "solid state" compounds.

3.6 Conclusion

A rich chemistry of compounds in the systems *Ae*/*T*/*Tt* (*Ae*: Mg, Ca, Sr, Ba; *T*: Co, Ni; *Tt*: Si, Ge, Sn), reaching from intermetallic phases (e.g. $Mg_{0.39(2)}NiSn_{1.61(2)}$ and $Mg_{2.61(2)}Ni_4Sn_{3.39(2)}$) to polar intermetallic phases (e.g. nickel germanides of alkaline earth metal elements) to the Zintl phase Ba_3Sn_2, is presented within this thesis (see Figure 3.10).

No simple rule, such as the (8-*N*) rule for polyanions of Zintl phases, exists for the rationalization of the polar intermetallic phases. However, the importance of structural relationships between binary and ternary compounds of close-by composition is pointed out throughout this work. The usage of composition triangles is shown to be a useful tool to reveal such structural relationships.

Particular emphasis is put on structural relationships between ternary polar intermetallic compounds $Ae_xT_yTt_z$ and binary compounds of the systems *T*/*Tt*. The description of *T*-*Tt* substructures of ternary phases can be approached by formal addition of *Ae* to a binary intermetallic phase T_xTt_y. The *Ae* scissors the T_xTt_y structure under formation of three-, two- and one-dimensional *T*-*Tt* substructures.

Therefore, the results fo this work underline that for the understanding of ternary polar intermetallic phases the understanding of binary intermetallic phases is a necessary prerequisite. This applies in particular to the ternary polar intermetallic phases which are transition metal rich and have a low content of tetrel elements.

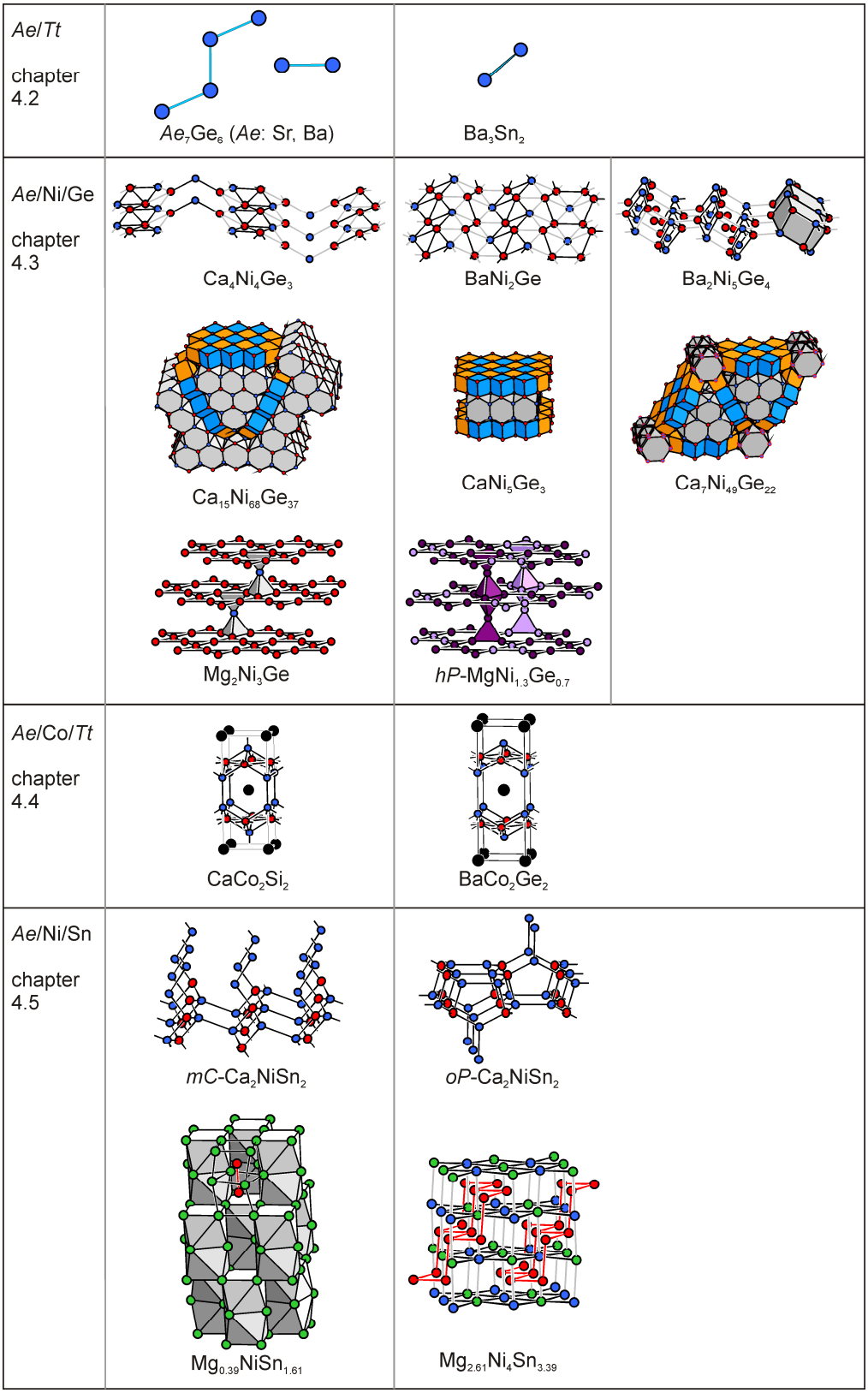

Figure 3.10 Overview of the intermetallic compounds presented in this thesis, showing characteristic structural motifs with emphasis on the *T*-*Tt* networks. Transition metals *T*, tetrel elements *Tt* and alkaline earth metals *Ae* are drawn in red, blue and black, respectively. Mixed occupied positions *Tt*/*T* and *Ae*/*Tt* are drawn in purple and green, respectively.

3.7 References

[1] A. Palenzona, P. Manfrinetti, M. L. Fornasini, *J. Alloys Compd.* **2000**, *312*, 165.

[2] L. Siggelkow, V. Hlukhyy, T. F. Fässler, *Z. Anorg. Allg. Chem.* **2010**, *636*, 1870.

[3] L. Siggelkow, V. Hlukhyy, T. F. Fässler, *Z. Anorg. Allg. Chem.* **2011**, *637*, 2000.

[4] L. Siggelkow, V. Hlukhyy, T. F. Fässler, *Z. Anorg. Allg. Chem.* **2008**, *634*, 2090.

[5] L. Siggelkow, V. Hlukhyy, B. Wahl, T. F. Fässler, *Eur. J. Inorg. Chem.* **2011**, 4012.

[6] V. Hlukhyy, T. F. Fässler, *Z. Anorg. Allg. Chem.* **2008**, *634*, 2316.

[7] V. Hlukhyy, A. Senyshyn, D. Trots, T. F. Fässler, *HASYLAB Ann. Rep.* **2007**, *1*, 1021.

[8] T. F. Fässler, C. Kronseder, *Angew. Chem. Int. Ed. Engl.* **1997**, *36*, 2683.

[9] H. Mattausch, A. Simon, C. Felser, R. Dronskowski, *Angew. Chem.* **1996**, *108*, 1805.

[10] H. Mattausch, A. Simon, C. Felser, R. Dronskowski, *Angew. Chem. Int. Ed. Engl.* **1996**, *35*, 1685.

[11] H. Pfisterer, K. Schubert, *Z. Metallk.* **1950**, *41*, 358.

[12] O. I. Bodak, E. I. Gladyshevskii, *Dopov. Akad. Nauk. Ukr. RSR* **1968**, *30*, 944.

[13] V. Hlukhyy, L. Siggelkow, T. F. Fässler, *in preparation* **2011**.

[14] M. Y. Teslyuk, V. Y. Markiv, *Sov. Phys. Crystallogr.* **1962**, *7*, 103.

[15] K. Cenzual, B. Chabot, E. Parthe, *J. Solid State Chem.* **1987**, *70*, 229.

[16] L. T. K. Nguyen, U. Aydemir, M. Baitinger, E. Bauer, H. Borrmann, U. Burkhardt, J. Custers, A. Haghighirad, R. Hofler, K. D. Luther, F. Ritter, W. Assmus, Y. Grin, S. Paschen, *Dalton Trans.* **2010**, *39*, 1071.

[17] L. T. K. Nguyen, U. Aydemir, M. Baitinger, J. Custers, A. Haghighirad, R. Hofler, K. D. Luther, F. Ritter, Y. Grin, W. Assmus, S. Paschen, *J. Electron. Mater.* **2010**, *39*, 1386.

[18] V. Hlukhyy, T. F. Fässler, *Z. Anorg. Allg. Chem.* **2010**, *636*, 100.

[19] V. Hlukhyy, N. Chumalo, V. Zaremba, T. F. Fässler, *Z. Anorg. Allg. Chem.* **2008**, *634*, 1249.

[20] P. Höhn, F. Nitsche, R. Kniep, *Z. Anorg. Allg. Chem.* **2008**, *634*, 2046.

[21] P. Höhn, S. Agrestini, A. Baranov, S. Hoffmann, M. Kohout, F. Nitsche, F. R. Wagner, R. Kniep, *Chem.-Eur. J.* **2011**, *17*, 3347.

[22] M. Ellner, T. Gödecke, K. Schubert, *J. Less-Common Met.* **1971**, *24*, 23.

[23] L. Siggelkow, V. Hlukhyy, T. F. Fässler, *Z. Anorg. Allg. Chem.* **2010**, *636*, 378.

[24] M. Pfisterer, G. Nagorsen, *Z. Naturforsch., B: J. Chem. Sci.* **1980**, *35*, 703.

[25] M. Rotter, M. Pangerl, M. Tegel, D. Johrendt, *Angew. Chem. Int. Ed.* **2008**, *47*, 7949.

[26] C.-H. Lee, A. Iyo, H. Eisaki, H. Kito, M. T. Fernandez-Diaz, T. Ito, K. Kihou, H. Matsuhata, M. Braden, K. Yamada, *J. Phys. Soc. Jpn.* **2008**, *77*.

[27] L. Siggelkow, V. Hlukhyy, T. F. Fässler, *Eur. J. Inorg. Chem.* **2012**, 987.

[28] J. P. Jarmoljuk, L. A. Lysenko, *Dopov. Akad. Nauk Ukr. RSR (Ser. A)* **1978**, 376.

[29] J. Nylen, G. F. J. Garcia, B. D. Mosel, R. Pottgen, U. Häussermann, *Solid State Sci.* **2004**, *6*, 147.

[30] V. Hlukhyy, U. C. Rodewald, R. Pottgen, *Z. Anorg. Allg. Chem.* **2005**, *631*, 2997.

[31] P. Rahlfs, *Metallwirtschaft, Metallwissenschaft, Metalltechnik* **1937**, *16*, 640.

[32] F. Lips, S. Dehnen, *Angew. Chem. Int. Ed.* **2011**, *50*, 955.

4 Publications

4.1 List of Publications

Binary Intermetallic Phases in the Systems *Ae*/*Tt* (*Ae*: Sr, Ba; *Tt*: Ge, Sn)

Sr_7Ge_6, Ba_7Ge_6 and Ba_3Sn_2 – Three New Binary Compounds Containing Dumbbells and Four-membered Chains of Tetrel Atoms with Considerable Ge-Ge π–Bonding Character

L. Siggelkow, V. Hlukhyy, T. F. Fässler, *to be submitted.*

Polar Intermetallic Phases in the Systems *Ae*/Ni/Ge (*Ae*: Mg, Ca, Sr, Ba)

$BaNi_2Ge$ and $Ca_4Ni_4Ge_3$ – Two Layered Structures with $^2_\infty[Ni_2Ge]$ and $^2_\infty[Ni_4Ge_3]$ Networks

L. Siggelkow, V. Hlukhyy, T. F. Fässler, *Z. Anorg. Allg. Chem.* **2010**, *636,* 1870–1879.

Synthesis, Structure and Chemical Bonding of $Ba_2Ni_5Ge_4$ – An Intermetallic Compound with a New Two-dimensional $^2_\infty[Ni_5Ge_4]$ Structural Motif

L. Siggelkow, V. Hlukhyy, T. F. Fässler, *Z. Anorg. Allg. Chem.* **2011**, *637*, 2000–2006.

Complex Intermetallic Compounds: $CaNi_5Ge_3$, $Ca_{15}Ni_{68}Ge_{37}$ and $Ca_7Ni_{49}Ge_{22}$ – Three Multifaceted Ni-Ge Framework Structures Combining the Structural Motifs of Ni_3Ge and $CaNi_2Ge_2$.

L. Siggelkow, V. Hlukhyy, B. Wahl, T. F. Fässler, *Eur. J. Inorg. Chem.* **2011**, 4012–4024.

Laves Phases in the System Mg/Ni/Ge

L. Siggelkow, T. F. Fässler, *in preparation.*

Nickel Germanides of Alkaline-Earth Metals – Structural Peculiarities and Relationships

L. Siggelkow, V. Hlukhyy, T. F. Fässler, *to be submitted.*

Polar Intermetallic Phases in the Systems Ca/Co/Si and Ba/Co/Ge

Synthesis, Structure and Chemical Bonding of $CaCo_2Si_2$ and $BaCo_2Ge_2$ – Two New Compounds with $ThCr_2Si_2$ Structure Type

L. Siggelkow, V. Hlukhyy, T. F. Fässler, *Z. Anorg. Allg. Chem.* **2010**, *636*, 378–384.

Polar Intermetallic Phases in the Systems *Ae*/Ni/Sn (*Ae* = Mg, Ca)

Ca_2NiSn_2 – a Polymorphic Intermetallic Phase: Atomic and Electronic Structure as well as a Topological Description of the Phase Transition by a Sigmatropic-Type Rearrangement of Ni and Sn Atoms

L. Siggelkow, V. Hlukhyy, T. F. Fässler, *Eur. J. Inorg. Chem.* **2012**,987–997.

$Mg_{0.39(2)}NiSn_{1.61(2)}$ and $Mg_{2.61(2)}Ni_4Sn_{3.39(2)}$ – Two New Intermetallic Phases in the System Mg/Ni/Sn

L. Siggelkow, T. F. Fässler, *in preparation.*

4.2 Binary Intermetallic Phases in the Systems *Ae*/*Tt* (*Ae*: Sr, Ba; *Tt*: Ge, Sn)

4.2.1 Sr_7Ge_6, Ba_7Ge_6 and Ba_3Sn_2 – Three New Binary Compounds Containing Dumbbells and Four-membered Chains of Tetrel Atoms with Considerable Ge-Ge π–Bonding Character

Sr_7Ge_6, Ba_7Ge_6 and Ba_3Sn_2 – Three New Binary Compounds Containing Dumbbells and Four-membered Chains of Tetrel Atoms with Considerable Ge-Ge π –Bonding Character

Lisa Siggelkow, Viktor Hlukhyy, Thomas F. Fässler

To be submitted

Abstract

The germanides Sr_7Ge_6 and Ba_7Ge_6 as well as the stannide Ba_3Sn_2 were prepared by arc melting and subsequent annealing in welded tantalum ampoules using induction as well as resistance furnaces. The compounds were investigated by powder and single crystal X-ray diffraction. Sr_7Ge_6 and Ba_7Ge_6 crystallize in the Ca_7Sn_6 structure type (space group *Pmna*, Z = 4: a = 7.777(2) Å, b = 23.595(4) Å, c = 8.563(2) Å, wR_2 = 0.081 (all data), 2175 independent reflections, 64 variable parameters for Sr_7Ge_6 and a = 8.0853(6) Å, b = 24.545(2) Å, c = 8.9782(8) Å, wR_2 = 0.085 (all data), 2307 independent reflections, 64 variable parameters for Ba_7Ge_6). Ba_3Sn_2 crystallizes in an own structure type with the space group $P4_32_12$, Z = 4, a = 6.6854(2) Å, c = 17.842(2) Å, wR_2 = 0.037 (all data), 1163 independent reflections, 25 variable parameters.

In Sr_7Ge_6 and Ba_7Ge_6 the Ge atoms are arranged as Ge_2 dumbbells and Ge_4 four-membered atom chains. Their crystal structures cannot be rationalized according to the (8-N) rule. In contrast, Ba_3Sn_2 presents Sn_2 dumbbells as a main structural motif and thereby can be described as an electron precise Zintl phase. The chemical bonding situation in these structures is discussed on the basis of partial and total Density Of States (DOS) curves, bandstructures including fatbands, topological analysis of the Electron Localization Function (ELF) as well as Bader analysis of the bond critical points using the programs TB-LMTO-ASA and WIEN2K. While Ba_3Sn_2 reveals semiconducting behaviour, all germanides Ae_7Ge_6 (Ae = Ca, Sr, and Ba) show metallic properties and a considerable π-bonding character between the Ge atoms of the four-membered chains and the

dumbbells. The π-bonding character of the germanides is best reflected by the resonance hybrid structures $\{[Ge–Ge]^{6-}/[Ge{=}Ge{=}Ge{=}Ge]^{8-}\} \leftrightarrow \{[Ge{=}Ge]^{4-}/[Ge–Ge–Ge–Ge]^{10-}\}$.

Keywords: Alkaline earth metal, Stannide, Germanide, Zintl phases, Intermetallic phase, Chemical bonding

Introduction

Binary compounds in the systems *Ae*/*Tt* (*Ae*: Ca, Sr, Ba; *Tt*: Ge, Sn) display a broad spectrum of structures – from polar intermetallic phases to "salt-like" Zintl phases [1, 2], whose structures can be rationalized according to the (8-*N*) rule. The interplay of localized and delocalized bonding governs the observed structures, leading to a variety of "zero"- to three-dimensional structural motifs of Ge and Sn atoms as well as to diverse electronic properties.

Starting from such binary compounds of the systems *Ae*/*Tt* we added transition metals (e.g. Ni and Co), in order to investigate the structural and electronic comportment of the resulting electron deficient polar intermetallic phases. In the course of these experiments we found two new binary intermetallic phases Ba_3Sn_2 and Ba_7Ge_6, both being at first synthesized in the presence of Ni and later on synthesized as a binary phase. Varying the alkaline earth metal led us to the new binary intermetallic phase Sr_7Ge_6.

The phase diagrams of the binary systems Sr/Ge and Ba/Ge were recently revised [3, 4]. In the system Sr/Ge the intermetallic compounds Sr_2Ge (anti-$PbCl_2$ structure type) [5], Sr_5Ge_3 (Cr_5B_3 structure type) [6], SrGe (CrB structure type) [7, 8], $SrGe_{1.85}$ (AlB_2 structure type) [4] and $SrGe_2$ ($BaSi_2$ structure type) [9] are described. Furthermore the phase $SrGe_{0.76}$ (SrSi structure type) was reported [10] but could not be confirmed by Pani *et al.* [4] and was corrected to $Sr_{10}[Al_4Ge_6]O$ by Röhr *et al.* [11]. The crystal structures of most compounds are in agreement with the Zintl-Klemm concept: In Sr_2Ge isolated Ge^{4-} atoms are observed, in Sr_5Ge_3 the Ge atoms form $[Ge\text{-}Ge]^{6-}$ dumbbells and non-bonded Ge^{4-} atoms, in SrGe the Ge atoms form zigzag chains, and in $SrGe_2$ tetrahedral Ge_4^{4-} anions are found. The Ge richest compound $SrGe_{5,56}$ [12] is a clathrate.

Similarly, in the system Ba/Ge most binary phases fulfill the (8-*N*) rule: in Ba_2Ge [13] (β-Co_2Si structure type) isolated Ge^{4-} atoms are observed, in Ba_5Ge_3 [14] (Ba_5Si_3 structure type) the Ge atoms are arranged as dumbbells as well as isolated atoms and in

BaGe [8, 15, 16] (CrB structure type) two-bonded Ge form zigzag chains. In *β*-Ba_3Ge_4 [17] (high temperature modification) isolated Ge_4^{6-} butterfly anions are present, in α-Ba_3Ge_4 [17] (low temperature modification) these Ge_4^{6-} butterfly anions are partly linked. In $BaGe_2$ ($BaSi_2$ structure type) [18-21] Ge_4^{4-} tetrahedral anions are found and in the high pressure modification of $BaGe_2$ ($ThCr_2$ structure type) three-bonded Ge atoms form a three-dimensional network. Only very recently the superconducting high pressure compound $BaGe_3$ [22], being isostructural to $BaSn_3$ [23, 24], was synthesized. The crystal structure of $BaSn_3$ has been interpreted as a borderline case between Zintl phases and intermetallic phases. It contains three-membered rings Sn_3^{2-} being isoelectronic to the aromatic ($C_3R_3^+$). The Ge-rich compounds Ba_6Ge_{25} [25-27], Ba_8Ge_{43} [28, 29], and $BaGe_5$ [30] are clathrates, among which $BaGe_5$ is a semiconducting Zintl phase.

In the phase diagram of the binary system Ba/Sn various compounds that present a broad spectrum of structural diversity were described. In analogy to the binary system Sr/Ge and Ba/Ge, the connectivity of the Sn polyanions leads to valence compounds: In Ba_2Sn [31] (β-Co_2Si structure type) non-bonded Sn^{4-} atoms are observed and in BaSn [15, 32] two-bonded Sn^{2-} atoms form chains. In Ba_3Sn_5 [33] square pyramidal Sn_5^{6-} were described as arachno clusters according to the Wade-Mingos electron counting rules. $BaSn_2$ [34] crystallizes in the $EuGe_2$ structure type in which the Sn atoms are arranged in analogy to the structure of grey arsenic, the layers being constructed from three-bonded Sn^- in accordance with the Zintl concept. $BaSn_3$ [23, 24] crystallizes in the $AuCu_3$ structure type, but as mentioned above a distortion of the Sn substructure accentuates Sn_3^{2-} rings with covalently bonded Sn atoms. $BaSn_3$ is a metal, due to the strong interactions between the π electron systems of the Sn_3^{2-} ring. $BaSn_5$ [35] crystallizes in a substitution variant of AlB_2. $BaSn_3$ and $BaSn_5$ as well as the Sr containing compounds $SrSn_3$ [36] and $SrSn_4$ [37] attracted attention due to their superconducting properties.

The title compounds Sr_7Ge_6 and Ba_7Ge_6 as well as the known phase Ca_7Ge_6 [38], crystallize in the Ca_7Sn_6 [39] structure type. The title phase Ba_3Sn_2 crystallizes in a new structure type. The synthesis, description and classification of the crystal structures in the context of the Zintl-Klemm concept as well as the description of the electronic structures of the title compounds will be presented in the following.

Experimental Section

Syntheses

Starting materials for the synthesis of the title phases Sr_7Ge_6, Ba_7Ge_6 and Ba_3Sn_2 were commercially available elements of high purity: ingots of strontium (ChemPur, 98%), barium (ChemPur, 99.5%), germanium pieces (ChemPur, 99.999%) and tin pieces (ChemPur, 99.999%). Strontium was redistilled before use. Barium, germanium and tin were used as received.

At first Ba_3Sn_2 and Ba_7Ge_6 were synthesized in the presence of nickel. Later on, the experiments described in the following lead to the binary phases. Sr_7Ge_6 was obtained varying the alkaline earth metal, starting with Ba_7Ge_6.

Sr_7Ge_6 and Ba_7Ge_6 could be obtained by arc melting of the elements on a water cooled copper hearth under argon atmosphere (Mini Arc Melting System, MAM-1, Johanna Otto GmbH). A ratio of 8 : 6 = *Ae* : Ge (overall mass of 0.7 g) was used in order to reduce the formation of the compounds SrGe and BaGe. The resulting samples were of low crystalline quality. In order to obtain a better crystallinity for Sr_7Ge_6 the reguli obtained from arc melting were sealed in tantalum ampoules under argon atmosphere (Mini Arc Melting System, MAM-1, Johanna Otto GmbH) and placed in a water-cooled sample chamber of an induction furnace (Hüttinger Elektronik, Freiburg, Typ TIG 2.5/300). The ampoules were first heated under a flow of argon to approximately T = 1080 °C and held at that temperature for 5 minutes. Consequently the samples were cooled within two hours to approximately T = 870 °C, and finally quenched by switching off the furnace. Small, irregularly shaped single crystals of the inductively melted sample of Sr_7Ge_6 were obtained by mechanical fragmentation. For Ba_7Ge_6 an analogue heat treatment in the induction furnace did not lead to crystals of acceptable quality. Thus, the crystal growth was performed by annealing the sample for a longer period of time: a tantalum tube containing a regulus of Ba_7Ge_6, which was produced by arc melting, was sealed in a quartz tube and heated in a resistance furnace to 950 °C for one day and then kept at 800 °C for a week (Nabertherm, Controller P330). Subsequently, the sample was quenched by throwing the quartz ampoule into water. Small single crystals were found

afterwards. The temperature programs for the crystal growth of Ba_7Ge_6 and Sr_7Ge_6 were chosen in accordance with the phase diagrams [3, 4], raising the temperature above the probable melting point, slow cooling and tempering at a temperature just below the melting point. Difficulties in the preparation due to the well crystallizing side compounds CaGe and Ca_5Ge_3 were already pointed out for isostructural Ca_7Ge_6 [38].

Ba_3Sn_2 could not be obtained by arc melting of the elements, but by reaction and subsequent annealing of the elements in a tantalum ampoule. Stoichiometric amounts (overall mass of 0.7 g) of the elements were sealed in a tantalum ampoule (argon atmosphere, Mini Arc Melting System, MAM-1, Johanna Otto GmbH) which was in turn sealed in a quartz ampoule and placed into a resistant furnace (Nabertherm P330). The furnace was heated up to 950 °C, held for two hours at this temperature and subsequently cooled to 700 °C. At this temperature the sample was tempered for two weeks. Finally the sample was quenched by throwing the quartz ampoule into water.

After cooling down to room temperature, all samples exhibited metallic lustre and could easily be separated from the tantalum crucible. All title phases are extremely air or moisture sensitive. Hence, every handling has to be carried out carefully in the argon filled glovebox.

Powder and Single Crystal X-ray Diffraction Studies and Structure Refinement

The purity of the samples was checked at room temperature using a STOE STADI P powder diffractometer with Ge monochromatized CuK_α radiation (λ = 1.54060 Å). The powder X-ray diffraction patterns showed that the samples of Sr_7Ge_6 and Ba_7Ge_6 contain Sr_5Ge_3 and BaGe as impurities, respectively. The sample of Ba_3Sn_2 contains as side products BaSn and Ba_2Sn. The lattice parameters of the title compounds Sr_7Ge_6 and Ba_7Ge_6 (see Table 1) were obtained from least-squares fits of the powder X-ray diffraction data using WinXPOW [40]. The powder X-ray diffraction patterns are given in the supporting information, Figure S1 to S3. All unit cell parameters as well as interatomic distances given in the article refer to the powder and single crystal X-ray diffraction data collected at room temperature for Sr_7Ge_6 and Ba_3Sn_2, respectively. The interatomic distances given for Ba_7Ge_6 refer to the single crystal X-ray diffraction data collected at 150 K.

The crystals of Sr_7Ge_6 and Ba_3Sn_2 were fixed in a glovebox on the top of glass fibres under the microscope using grease. These glass fibres were then inserted in glass capillaries which were fused on a hot filament. Due to the high air and moisture sensitivity of the samples, the glass fibres as well as the glass capillaries were washed in hot aqua regia, rinsed in water and acetone and subsequently dried on a Schlenck line over argon before the mounting of the single crystals. The air and moisture sensitive crystals of Ba_7Ge_6 were given into perfluoropolyalkylether directly after opening the tantalum ampoule. For data collection the crystals were fixed on a glass capillary and positioned in a 150 K cold N_2 stream using the crystal cap system.

Single crystal X-ray diffraction intensity data was collected using an IPDS 2T with graphite monochromatized MoK_α (λ = 0.71073 Å) radiation at room temperature for Sr_7Ge_6. An Oxford Diffraction Xcalibur3 diffractometer with graphite monochromatized MoK_α (λ = 0.71073 Å) radiation was used at T = 150 K for Ba_7Ge_6 and at room temperature for Ba_3Sn_2. The raw data were corrected for background, polarization and Lorentz factor. Further, the data set of Sr_7Ge_6 was corrected numerically for absorption [41, 42], while empirical absorption corrections were applied to the data of Ba_3Sn_2 and Ba_7Ge_6 [43].

The atomic position parameters were deduced for Sr_7Ge_6, Ba_7Ge_6 and Ba_3Sn_2 from an automatic interpretation of direct methods with SHELXS-97 [44]. The structures were refined using SHELXL-97 (full-matrix least-squares on F_o^2) [45] with anisotropic atomic displacement parameters for all atoms. To check for the correct composition, the occupancy parameters of both compounds were refined in a separate series of least-squares cycles. All sites were fully occupied. In the last cycles, the ideal occupancies were assumed again. No significant residual electron density was observed. For Ba_3Sn_2 crystals of both chiral space groups $P4_32_12$ and $P4_12_12$ were found. All relevant crystallographic data for the data collection and evaluation are listed in Table 1. The positional parameters and selected interatomic distances are listed in Tables 2 and 3. The anisotropic displacement parameters are given in the supporting information, Table S1 to S3.

Further details on the crystal structure investigations may be obtained from the Fachinformationszentrum Karlsruhe, 76344 Eggenstein-Leopoldshafen, Germany (fax: +49 7247 808 666; email: crysdata@fiz-karlsruhe.de), on quoting the depository number CSD-424097 (for Sr_7Ge_6), -424096 (for Ba_7Ge_6) and -424098 (for Ba_3Sn_2).

Table 1 Crystal data and structure refinement for Sr_7Ge_6, Ba_7Ge_6 and Ba_3Sn_2. All data given in this table as well as within the article refer to powder X-ray diffraction (XRD) data for Sr_7Ge_6, to single crystal XRD data at T = 150 K for Ba_7Ge_6 and to single crystal XRD data at T = 293 K for Ba_3Sn_2.

Empirical formula	**Sr_7Ge_6**	**Ba_7Ge_6**	**Ba_3Sn_2**
Formula weight	1048.88 g/mol	1396.92 g/mol	649.40 g/mol
Space group, Z	*Pnma* (62), 4	*Pnma* (62), 4	$P4_32_12$ (96), 4
Unit cell dimensions (powder XRD at 293 K)	a = 7.777(2) Å b = 23.595(4) Å c = 8.563(2) Å V = 1571.2(4) Å^3	a = 8.124(2) Å b = 24.627(5) Å c = 9.010(2) Å V = 1802.6(6) Å^3	-
Unit cell dimensions (single crystal XRD)	a = 7.790(2) Å b = 23.580(4) Å c = 8.590(2) Å V = 1577.9(4) Å^3	a = 8.0853(6) Å b = 24.545(2) Å c = 8.9782(8) Å V = 1781.8(2) Å^3	a = 6.6854(2) Å c = 17.842(2) Å V = 797.45(6) Å^3
Measurement temperature of the single crystal XRD	293 K	150 K	293 K
Calculated density	4.434 g/cm^3	5.21 g/cm^3	5.41 g/cm^3
Absorption coefficient	34.80 mm^{-1}	25.11 mm^{-1}	20.65 mm^{-1}
F(000)	1832	2336	1072
Crystal size	0.1 × 0.1 × 0.09 mm^3	0.09 × 0.04 × 0.01 mm^3	0.11 × 0.11 × 0.04 mm^3
θ range	3.5° to 29.3°	3.3 ° to 28.5°	3.3° to 30°
Range in hkl	±10, ±32, −10 < l < 11	±10, ±32, −12 < l < 9	±9, ±9, −24 < l < 25
Reflections collected	11306	14265	7720
Independent reflections	2175 (R_{int} = 0.057)	2307 (R_{int} = 0.117)	1163 (R_{int} = 0.055)
Reflections with $I \geq 2\sigma(I)$	1945 (R_{sigma} = 0.031)	1579 (R_{sigma} = 0.082)	1040 (R_{sigma} = 0.031)
Data/parameters	2175 / 64	2307 / 64	1163 / 25
GOF on F^2	1.225	0.918	1.034
Flack - parameter	-	-	−0.10 (4)
Final R indices with $I > 2\sigma(I)$	R_1 = 0.045 wR_2 = 0.078	R_1 = 0.043 wR_2 = 0.080	R_1 = 0.020 wR_2 = 0.036
R indices (all data)	R_1 = 0.054 wR_2 = 0.081	R_1 = 0.072 wR_2 = 0.085	R_1 = 0.026 wR_2 = 0.037
Extinction coefficient	-	-	0.0018(2)
Largest diff. peak and hole	1.53 / −1.52 e/Å^3	2.81 / –1.68 e/Å^3	0.94 / –0.62 e/Å^3

Table 2 Atomic coordinates and equivalent isotropic displacement parameters ($Å^2 \times 10^3$) for Ba_3Sn_2 (space group $P4_32_12$), Ba_7Ge_6 and Sr_7Ge_6 (space group *Pnma*).

Atom	Wyckoff position	*x*	*y*	*z*	U_{eq} ($Å^2$) $\times 10^3$
Sr_7Ge_6					
Sr1	8*d*	0.02881(9)	0.66236(3)	0.18027(8)	17(1)
Sr2	8*d*	0.13512(9)	0.13994(3)	0.31686(9)	20(1)
Sr3	8*d*	0.33814(8)	0.51827(3)	0.17850(8)	16(1)
Sr4	4*c*	0.3012(2)	¼	0.0285 (2)	22(1)
Ge1	8*d*	0.0046(1)	0.05218(3)	0.03745(9)	15(1)
Ge2	8*d*	0.1995(1)	0.59672(3)	0.47179(9)	16(1)
Ge3	4*c*	0.1761(2)	¼	0.5910(2)	24(1)
Ge4	4*c*	0.4067(2)	¼	0.3829(2)	19(1)
Ba_7Ge_6					
Ba1	8*d*	0.03641(8)	0.66166(2)	0.18234(7)	13(1)
Ba2	8*d*	0.12335(8)	0.13969(3)	0.31562(8)	15(1)
Ba3	8*d*	0.34451(8)	0.51910(2)	0.17649(7)	12(1)
Ba4	4*c*	0.2901(2)	¼	0.0315(2)	18(1)
Ge1	8*d*	0.0060(2)	0.05032(4)	0.0343(2)	11(1)
Ge2	8*d*	0.2113(2)	0.59522(4)	0.4747(2)	12(1)
Ge3	4*c*	0.1701(2)	¼	0.5842(2)	16(1)
Ge4	4*c*	0.3890(2)	¼	0.3873(2)	14(1)
Ba_3Sn_2					
Ba1	8*b*	0.84067(6)	0.58507(5)	0.11306(2)	24(1)
Ba2	4*a*	0.32832(5)	0.32832(5)	0	22(1)
Sn	8*b*	0.83096(7)	0.08756(5)	0.04712(2)	20(1)

After the X-ray diffraction measurements, the single crystals were analyzed with a JEOL SEM 5900LV scanning electron microscope equipped with an Oxford Instruments INCA energy dispersive X-ray microanalysis system. No impurity elements heavier than Na were observed. The semi-quantitative EDX analysis of well-shaped single crystals reveals the compositions given in molar ratio: Sr 8(1), Ge 5(1) for Sr_7Ge_6; Ba 7(1), Ge 6(2) for Ba_7Ge_6 and Ba 2.7(3), Sn 2.3(3) for Ba_3Sn_2, which within standard deviations corresponds to the ideal compositions of the title phases.

Table 3 Interatomic distances (Å) calculated with lattice parameters taken from powder X-ray diffraction (XRD) data for Sr_7Ge_6, from single crystal XRD data at T = 150 K for Ba_7Ge_6 and from single crystal XRD data at T = 293 K for Ba_3Sn_2.

		distance (Å)			distance (Å)
Sr_7Ge_6					
Ge1	Ge1	2.545(2) (1×)	Ge3	Ge4	2.528(2) (1×)
	Ge2	2.592(2) (1×)		Sr4	3.090(2) (1×)
	Sr1	3.210(1) (1×)		Sr1	3.182(2) (2×)
	Sr3	3.218(1) (1×)		Sr1	3.264(2) (2×)
	Sr3	3.309(2) (1×)		Sr2	3.515(2) (2×)
	Sr2	3.323(2) (1×)			
	Sr3	3.341(2) (1×)	Ge4	Sr4	3.144(2) (1×)
	Sr3	3.404(1) (1×)		Sr4	3.160(2) (1×)
	Sr2	3.755(1) (1×)		Sr1	3.318(2) (2×)
				Sr2	3.395(2) (2×)
Ge2	Sr1	3.224(1) (1×)		Sr2	3.581(2) (2×)
	Sr2	3.253(1) (1×)			
	Sr1	3.264(2) (1×)	Sr2	Sr4	3.809(2) (1×)
	Sr3	3.301(2) (1×)		Sr4	3.904(2) (1×)
	Sr2	3.330(2) (1×)		Sr2	4.0533(8) (2×)
	Sr2	3.380(2) (1×)			
	Sr3	3.603(2) (1×)	Sr3	Sr3	4.053(2) (1×)
	Sr4	3.649(1) (1×)		Sr3	4.0765(8) (2×)
Sr1	Sr4	3.749(2) (1×)			
	Sr4	3.862(2) (1×)			
	Sr3	3.901(1) (1×)			
	Sr1	4.0675(8) (2×)			
	Sr2	4.098(2) (1×)			
Ba_7Ge_6					
Ge1	Ge1	2.547(2) (1×)	Ge3	Ge4	2.502(3) (1×)
	Ge2	2.594(2) (1×)		Ba4	3.243(2) (1×)
	Ba3	3.369(2) (1×)		Ba1	3.333(2) (2×)
	Ba1	3.372(2) (1×)		Ba1	3.447(2) (2×)
	Ba3	3.468(2) (1×)		Ba2	3.645(2) (2×)
	Ba2	3.478(2) (1×)			
	Ba3	3.493(2) (1×)	Ge4	Ba4	3.293(2) (1×)
	Ba3	3.517(3) (1×)		Ba4	3.324(2) (1×)
				Ba1	3.476(2) (2×)
				Ba2	3.516(2) (2×)
Ge2	Ba3	3.371(2) (1×)		Ba2	3.774(2) (2×)
	Ba1	3.398(2) (1×)			
	Ba1	3.399(2) (1×)	Ba2	Ba4	3.957(1) (1×)
	Ba3	3.438(2) (1×)		Ba4	4.059(1) (1×)
	Ba2	3.473(2) (1×)		Ba2	4.211(1) (2×)
	Ba2	3.514(2) (1×)		Ba3	4.324(1) (1×)
	Ba3	3.759(2) (1×)			
	Ba4	3.833(2) (1×)			
Ba1	Ba4	3.919(1) (1×)	Ba3	Ba3	4.153(2) (1×)
	Ba3	4.032(1) (1×)		Ba3	4.253(1) (2×)

		distance (Å)			distance (Å)
	Ba4	4.061(2) (1×)			
	Ba1	4.221(1) (2×)			
	Ba2	4.296(1) (1×)			
Ba_3Sn_2					
Ba1	Sn	3.5286(5) (1×)	Ba1	Ba2	4.3299(6) (1×)
	Sn	3.5600(5) (1×)		Ba2	4.6214(5) (1×)
	Sn	3.6870(5) (1×)			
	Ba2	3.6898(5) (1×)	Ba2	Sn	3.6633(4) (2×)
	Sn	3.7368(5) (1×)		Sn	3.7886(6) (2×)
	Sn	3.8267(5) (1×)		Sn	3.8196(4) (2×)
	Sn	3.9386(6) (1×)			
	Ba1	4.0272(4) (2×)	Sn	Sn	2.9518(8) (1×)
	Ba2	4.2004(4) (1×)			

Table 4 Distances (Å) between Ge atoms and the corresponding integrated Crystal Orbital Hamilton Populations (−iCOHPs) values at E_F within Ca_7Ge_6 and Sr_7Ge_6 and Ba_7Ge_6. All −iCOHP values are in eV per bond.

			distance (Å)	−iCOHP (eV/bond)
Ca_7Ge_6				
Dumbbell	Ge3	-Ge4	2.529(3) Å	2.48
Four-membered chain	Ge1	-Ge1	2.526(2) Å	2.62
	Ge1	-Ge2	2.571(2) Å	2.42
		α (Ge2-Ge1-Ge1)	108.53(5)°	
Sr_7Ge_6				
Dumbbell	Ge3	-Ge4	2.528(2) Å	2.81
Four-membered chain	Ge1	-Ge1	2.545(2) Å	2.75
	Ge1	-Ge2	2.592(2) Å	2.49
		α (Ge2-Ge1-Ge1)	111.24(5)°	
Ba_7Ge_6				
Dumbbell	Ge3	Ge4	2.502(3) Å	2.92
Four-membered chain	Ge1	Ge1	2.547(2) Å	2.15
	Ge1	Ge2	2.594(2) Å	2.50
		α (Ge2-Ge1-Ge1)	113.29(7)°	

Electronic Structure Calculations

Computational studies concerning the electronic structures of the title compounds Ca_7Ge_6, Sr_7Ge_6, Ba_7Ge_6 and Ba_3Sn_2 were carried out using the program WIEN2K [46] as well as the program TB-LMTO-ASA [47]. This combination allows to obtain precisely calculated bandstructures with fatbands and total Density Of States (DOS) curves (using WIEN2K) as well as to carry out a topological analysis of the chemical bond using the Electron Localization Function (ELF) [48-50] (obtained from calculations with TB-LMTO-ASA). The latter is in turn supported by a Bader analysis of the bond critical points [51] (WIEN2K, Critic). Furthermore, from the analyses of the –iCOHP values (TB-LMTO-ASA) the contribution of the covalent part of a particular interaction to the total bonding energy is obtained.

First-principle full-potential DFT calculations were carried out using the program WIEN2K. For Ae_7Ge_6 (*Ae* = Ca, Sr, Ba) the exchange-correlation contribution was described by the Generalized Gradient Approximation (GGA) of Perdrew, Burke and Ernzerhof [52]. The modified Becke-Johnson (mBJ) functional [53] was used for Ba_3Sn_2, as it allows a more precise calculation of band gaps of semi conductors. Muffin-tin radii were chosen as 2.5 a.u. (≈ 1.32Å) for Ba and Sn in Ba_3Sn_2 and as 2.3 a.u. (≈ 1.22Å) for Ge and 2.45 a.u. (≈ 1.30Å) for the alkaline earth metal atoms in Ae_7Ge_6 (*Ae*: Ca, Sr, Ba). The plane-wave cutoff constant $R_{MT}K_{max}$ was set to 7.0 for all compounds. A cutoff energy of −7 Ry was used to separate the valence and core states. 1000 k points were used in the brillouin zone and convergence was reached below a residual changes of the charge density of 0.0001 $e^{-}\cdot cell^{-1}$ and below a variation of total energy of 0.00001 $Ry\cdot cell^{-1}$. The program package Critic [54] was used to calculate the ellipticity ε of a bond critical point.

Further calculations of the electronic structure employed the linear muffin-tin orbital (LMTO) method in the atomic sphere approximation (ASA) using the tight-binding (TB) program TB-LMTO-ASA [47]. The exchange-correlation term was calculated within the local density approximation (LDA) and was parameterized according to von Barth and Hedin [55]. The radii of the muffin-tin spheres and empty spheres were determined after Jepsen and Andersen [56]. The basis set of short-ranged [57] atom-centred TB-LMTOs contained s, d, f valence functions for Ba; s, d valence functions for Sr and Ca as well as s, p valence functions for Ge and Sn. Ba 6p, Sr 5p and 4f, Ca 4p, Ge 3d as well as Sn 5d and

4f orbitals were included using a downfolding technique. The graphical representations of the ELF were realised using the program VESTA [58].

Results and Discussion

The crystal structures of the title compounds Sr_7Ge_6, Ba_7Ge_6 and Ba_3Sn_2 are based on polyanionic units of tetrel elements that are separated by alkaline earth metal atoms. A common feature of the three title compounds are the Tt_2 dumbbells (*Tt*: tetrel). While in Ba_3Sn_2 exclusively Sn_2 dumbbells are present, in Ae_7Ge_6 (*Ae*: alkaline earth metal) Ge_4 four-membered atom chains occur beside the Ge_2 dumbbells.

Crystal Structure of Sr_7Ge_6 and Ba_7Ge_6

The title compounds Sr_7Ge_6 and Ba_7Ge_6 crystallize in the Ca_7Sn_6 structure type [39] (Sr_7Ge_6: *Pnma*, $Z = 4$, $a = 7.777(2)$ Å, $b = 23.595(4)$ Å, $c = 8.563(2)$ Å and Ba_7Ge_6: $a = 8.0853(6)$ Å, $b = 24.545(2)$ Å, $c = 8.9782(8)$ Å). The structure of the compounds was determined both from single crystal and powder X-ray diffraction data. Hitherto, only Ca_7Ge_6 is known to crystallize in this Ca_7Sn_6 structure type [38]. The crystal structure Ca_7Sn_6 was described with a focus on the Sn-centered trigonal prisms of Ca. The stacking of these trigonal prisms was compared to the one found in Sm_5Ge_4 [59]. No description considering the arrangement of the tetrel (*Tt*) atoms and *Tt*-*Tt* bonding was done.

The main structure motifs in Ae_7Ge_6 (*Ae* = Ca, Sr, Ba) are Ge_2 dumbbells as well as Ge_4 four-membered chains (Figure 1). The planar Ge_4 chain has a *trans* conformation. It compares well with the highly charged oligomeric or polymeric anions, which are observed in the ternary Zintl phases of the system *Ae*/Mg/*Tt* (*Ae*: Ca, Sr, Ba; *Tt*: Si, Ge) (see for example [60-62]) as well as *Ae*/Mg/Li/*Tt* (see for example [63-65]).

According to the (8-*N*) rule and assuming singly-bonded $(1b\text{-}Ge)^{3-}$ atoms (1b: one-bonded) and two-fold connected $(2b\text{-}Ge)^{2-}$ atoms (2b: two-bonded), electron precise $[Ge\text{-}Ge]^{6-}$ and $[Ge_4]^{10-}$ polyanions are expected. Since the seven alkaline earth atoms provide 14 electrons, the polyanionic structure of Sr_7Ge_6 and Ba_7Ge_6 is two electrons short in order to compensate the 16 negative charges expected by applying the (8-*N*)-rule. However, the formation of a Ge=Ge double bond either in the Ge_4

four-membered chain or in the Ge_2 dumbbell, would lead to an electronically balanced situation.

In Table 4 the Ge-Ge distances in the dumbbell as well as within the four-membered chain are given. For all compounds Ae_7Ge_6 short Ge-Ge bonds are observed for the dumbbells (Ca_7Ge_6: 2.529(3) Å, Sr_7Ge_6: 2.528(2) Å, Ba_7Ge_6: 2.502(3) Å). The Ge-Ge bonds within the Ge_4 chain are longer. The inner Ge1-Ge1 bond is of intermediate length, with 2.526(2) Å, 2.545(2) Å and 2.547(2) Å for *Ae* = Ca, Sr, and Ba, respectively. The longest bond is observed from Ge1 to the terminal Ge2 atoms with a Ge1-Ge2 bond length of 2.571(2) Å, 2.592(2) Å and 2.594(2) Å for *Ae* = Ca, Sr, and Ba, respectively. All distances are slightly longer than the Ge-Ge distance in α-Ge (2.45 Å [66]). This is generally attributed to the enhanced electrostatic repulsion between the negatively charged Ge atoms within the polyanions. The difference of the distances within the Ge_4 chain can be attributed to the different charges of the Ge atoms: a charge of 3− is assigned to the terminal Ge2, a charge of 2− is assigned to the two-bonded Ge1. Thus, due to the higher repulsion, the Ge1-Ge2 bond is expected to be longer than the Ge1-Ge1 bond. However, the bond distance of the dumbbell Ge3-Ge4 with Ge^{3-} atoms does not follow this argument, the Ge-Ge distances being the shortest observed in the compounds Ae_7Ge_6.

Even though a strong increase of the unit cell volume by approx 35 % is observed for Ae_7Ge_6 going from Ca (1339.2(4) $Å^3$) to Sr (1571.2(5) $Å^3$) to Ba (1781.8(2) $Å^3$) (corresponding to the size of the *Ae* atoms), the Ge-Ge bond lengths of the Ge polyanionic subunit in Ae_7Ge_6 (*Ae*: Ca, Sr, Ba) remains nearly unaffected. The distances within the four-membered chain rise slightly from Ca_7Ge_6 to Ba_7Ge_6 (Table 3 and 4). In the dumbbell the Ge-Ge distances are the same for Ca_7Ge_6 and Sr_7Ge_6, for Ba_7Ge_6 even a slightly shorter distance is found (Table 3 and 4). Summarizing, the Ge-Ge bond length varies maximally ±1% when exchanging the alkaline earth metal. This strongly confirms the covalent interaction between the Ge atoms. Note further, that the longest as well as the shortest Ge-Ge bond is observed for Ba_7Ge_6, the differences diminish for Sr_7Ge_6 and Ca_7Ge_6. Furthermore the angle α of the Ge_4 four-membered chain (shown in Figure 2b) is rising when going from Ca to Sr to Ba.

From a geometrical point of view, the Ge_4 chains and the Ge_2 dumbbells are arranged in layers parallel to the *ac* plane: layer A consists of the Ge_4 chains, which are oriented perpendicular to the layer plane, and layer B consists of Ge_2 dumbbells, which are aligned parallel to the layer. These layers are arranged following the sequence ABA'B'. A'

(at $y = 0$) is generated from A (at $y = ½$) by the mirror parallel to the *ac* plane at $y = ¼$. The layer B' (at $y = ¾$) is generated from the layer B (at $y = ¼$) by the inversion center.

Parallel to the strong increase of the unit cell volume going from Ca to Ba the distances between the anionic structural motifs rise: for *Ae* = Ca, Sr and Ba the shortest distance between the Ge_2 dumbbells is *d*(Ge4-Ge4) = 4.220(3) Å, *d*(Ge4-Ge4) = 4.506(2) Å and *d*(Ge4-Ge4) = 4.735(3) Å; the shortest distance between the Ge_4 chains is *d*(Ge1-Ge2) = 4.300(2) Å, *d*(Ge1-Ge2) = 4.613(2) Å and *d*(Ge1-Ge2) = 4.872(2) Å; and the distances between the polyanions in the layers A and B is 3.408(1) Å, 3.617(1) Å and 3.799(1) Å, respectively.

The coordination polyhedra of the Ge1 to Ge4 atoms in Sr_7Ge_6 and Ba_7Ge_6 are shown in Figure 2. As it was already described for Ca_7Sn_6 and Ca_7Ge_6 [38, 39], all coordination polyhedra of Ge consist of distorted triply-capped trigonal prisms of *Ae* atoms. Already 30 years ago, Schnering *et al.* have shown that the trigonal prismatic cationic structures, as found in α-$ThSi_2$ and AlB_2, are compatible hosts for polymeric anionic substructures [67]. In the title compounds Sr_7Ge_6 and Ba_7Ge_6, the trigonal prisms are built up of *Ae* atoms. The trigonal prism around Ge1 (Figure 2a) is capped twice with Ge and once with *Ae*, while the trigonal prisms around Ge2, Ge3 and Ge4 (Figure 2b, c, d) are capped with two *Ae* atoms and one Ge atom.

In binary and ternary germanides a broad range of Ge-Ge distances is observed: in the monogermanides *Ae*Ge the Ge-Ge bond length in the infinite Ge zigzag chains indicate the presence of single bonds, with bond length of 2.59 Å, 2.62 Å and 2.63 Å for *Ae* = Ca, Sr and Ba, respectively. The Ge-Ge bonds in the title compounds are shorter than these distances. In contrast, a conjugated double bond with mixed oxidation state of $^1_\infty[Ge^{2-}Ge^{1-}]$ was described for the infinite Ge_∞ chains in $BaLiGe_2$ and $SrLiGe_2$ [68] (*d*(Ge-Ge) = 2.48 Å to 2.50 Å in $LiSrGe_2$ and *d*(Ge-Ge) = 2.47 Å to 2.53 Å in $LiBaGe_2$). Within these planar Ge_∞ chains bonds with *cis* and *trans* conformation alternate. Similarly, extended incompletely filled π* systems are observed for example in $LiCa_2Ge_3$ [69] ((Ge-Ge) = 2.46 Å to 2.61 Å) as well as Eu_2LiSi_3, Eu_2LiGe_3 and $Eu_xSr_{2-x}LiGe_3$ [70] (*d*(Ge-Ge) = 2.46 Å to 2.61 Å). The shortest distances observed in these mentioned examples are slightly shorter than the Ge3-Ge4 distances in the title compounds Ae_7Ge_6. Nevertheless, the examples indicate that the Ge3-Ge4 bonds within the Ge_2 dumbbells as well as the Ge1-Ge1 bonds within the Ge_4 four-membered chains of the title compounds Ae_7Ge_6 might have a double bond character and that the involved atoms are oxidized.

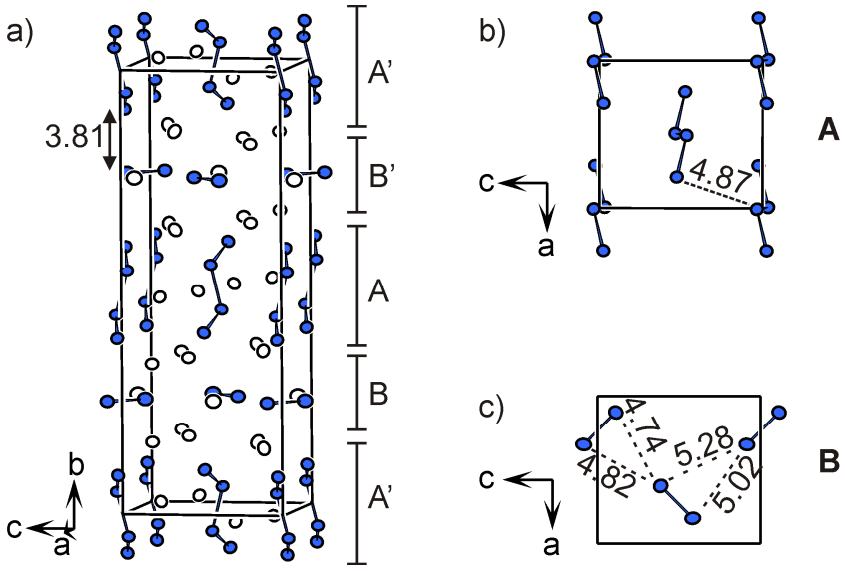

Figure 1 Crystal structure of Ae_7Ge_6, here shown for Ba_7Ge_6. a) unit cell of Ba_7Ge_6, the layers A / A' and B / B' are emphasized, b) layer A / A', c) layer B / B'. The Ba and Ge atoms are drawn in white and blue, respectively. The displacement ellipsoids are drawn with 95% probability level.

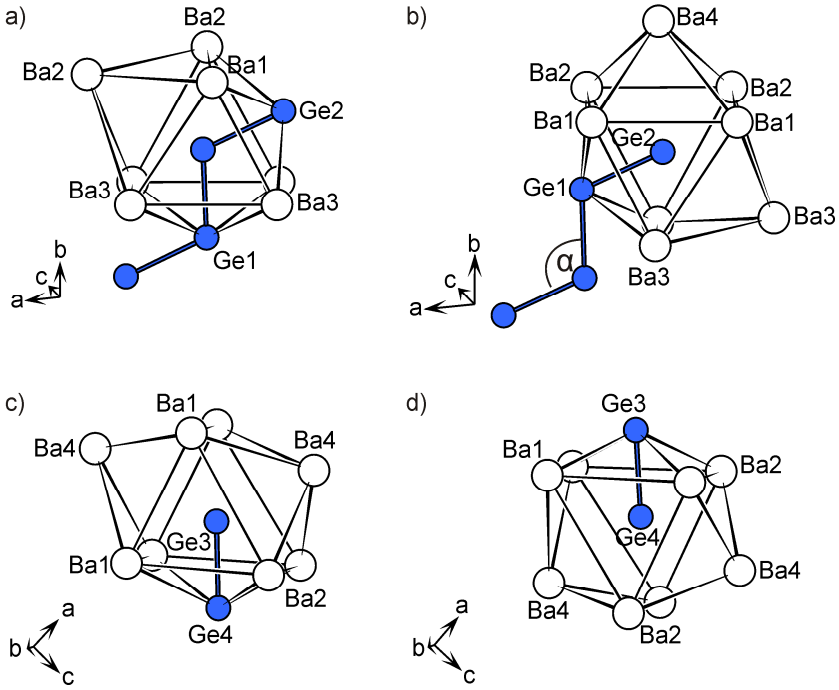

Figure 2 Coordination polyhedra of Ge1 to Ge4 in Ae_7Ge_6 here shown for Ba_7Ge_6. The Ba and Ge atoms are drawn in white and grey (printed version) / blue (electronic version), respectively.

For comparison, Ge=Ge double bonds in molecular compounds are considered. These are well known, for example in $[\{(dioxane)_{0.5}(Et_2O)LiGeC_6H_3\text{-}2,6\text{-}Mes_2\}_2]_\infty$ with a Ge=Ge distance of 2.33 Å [71]. Similar bond lengths are observed for Ge=Ge double bonds in neutral molecules such as $\{Ge(Me)C_6H_3\text{-}2,6\text{-}Trip_2\}_2$ (Trip = C_6H_3-2,4,6-i-Pr_3) with a Ge=Ge distance of 2.32 Å [72].

Crystal Structure of Ba_3Sn_2

The title compound Ba_3Sn_2 crystallizes in an own structure type, which was determined from single crystal X-ray diffraction data: $P4_32_12$ (96), $Z = 4$, $a = 6.6854(2)$ Å, $c = 17.842(2)$ Å. A crystal with the corresponding chiral space group $P4_12_12$ was also found. Ag_2HgO_2 crystallizes in the same space group with the same Wyckoff positions [73], presenting however a quite different atom arrangement.

The main structural motifs in Ba_3Sn_2 are Sn_2 dumbbells. Therefore, the compound can be described following the Zintl-Klemm concept as $(Ba^{2+})_3[(1b\text{-}Sn^{3-})_2]$ (1b: one-bonded) assuming a singly-bonded Sn_2 anionic unit. The unit cell of Ba_3Sn_2 is shown in Figure 3. The chiral space group $P4_32_12$ is reflected by the arrangement of the dumbbells in form of a double helix as shown in Figure 4. To illustrate the arrangement of the dumbbells, their centers are connected. The Sn-Sn distance within the dumbbells (2.9518(8) Å) of Ba_3Sn_2 lies between the distances in α-Sn (2.81 Å) and (metallic) β-Sn (3.02 Å and 3.18 Å [66]). The coordination polyhedron of one of the two equivalent Sn atoms in Ba_3Sn_2 is shown in Figure 5. It consists of nine Ba and one Sn atom and has 12 triangular and two quadrangular outer faces.

Hitherto, no compounds containing Sn_2 dumbbells were described in the system Ba/Sn (the compound Ba_5Sn_3, containing Sn_2^{6-} dumbbells and isolated Sn^{4-} atoms [74, 75], was described but was later identified as a hydride by Corbett *et al.* [76]). In the system Sr/Sn the compound Sr_5Sn_3 is observed [74, 77], containing Sn_2^{6-} dumbbells with Sn-Sn distance of 2.90 Å

In the system Ca/Sn [39] two intermetallic phases of close composition to the title compound Ba_3Sn_2 were described: $Ca_{31}Sn_{20}$ [78] contains Sn_2 dumbbells, Sn_5 five-membered chains and isolated Sn atoms, $Ca_{36}Sn_{23}$ [39] contains Sn_2 dumbbells, Sn_∞ infinite chains and isolated Sn atoms. The distances between the atoms of the Sn_2 dumbbells in $Ca_{31}Sn_{20}$ (3.05 Å and 3.15 Å) and in $Ca_{36}Sn_{23}$ (3.07 Å and 3.17Å) are

significantly longer than the corresponding Sn-Sn distance observed in Ba_3Sn_2. $Ca_{31}Sn_{20}$ and $Ca_{36}Sn_{23}$ possess rather complex structures and the application of the Zintl-Klemm concept is not straight forward, as the rather unusual linear coordination environment for two-bonded Sn atoms needs to be neglected. Until now no intermetallic phase of approximate composition 3 : 2 was observed in the system Sr/Sn. However, the existence of the plumbide $Sr_{31}Pb_{20}$ [79] was reported.

While dumbbells of tetrel elements occur frequently in more complex intermetallic compounds, structures that exclusively contain dumbbells Tt_2 are rare. Binary and pseudo binary examples are the silicides U_3Si_2 [80], Re_2Si_2Mg (*Re* = Y, La–Nd, Sm, Gd–Lu) [81] [82] and germanides Re_2Ge_2Mg (Re = La–Nd, Sm, Gd, Tb) [83, 84] containing Si_2 and Ge_2 dumbbells, respectively. The ternary compounds are ordered variants of the U_3Si_2 structure type. Even though the mentioned compounds have the same ratio (*Re*,Mg):*Tt* = 3:2 as found for Ba_3Sn_2, their crystal structures are different to that of the title compound. Furthermore, dumbbells of Ge and Sn are observed as exclusive structure motif in the structures of Li_9Ge_4 [85] and Na_9Sn_4 [86].

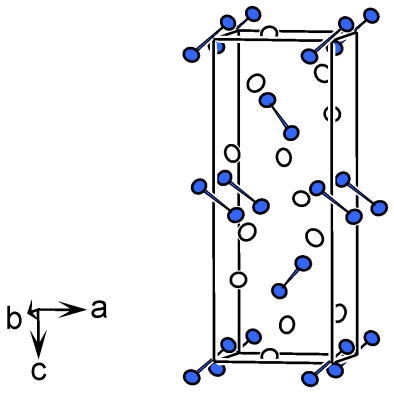

Figure 3 Crystal structure of Ba_3Sn_2; the Sn_2 dumbbells are emphasized. The Ba and Sn atoms are drawn in white and blue, respectively. The displacement ellipsoids are drawn at the 95% probability level.

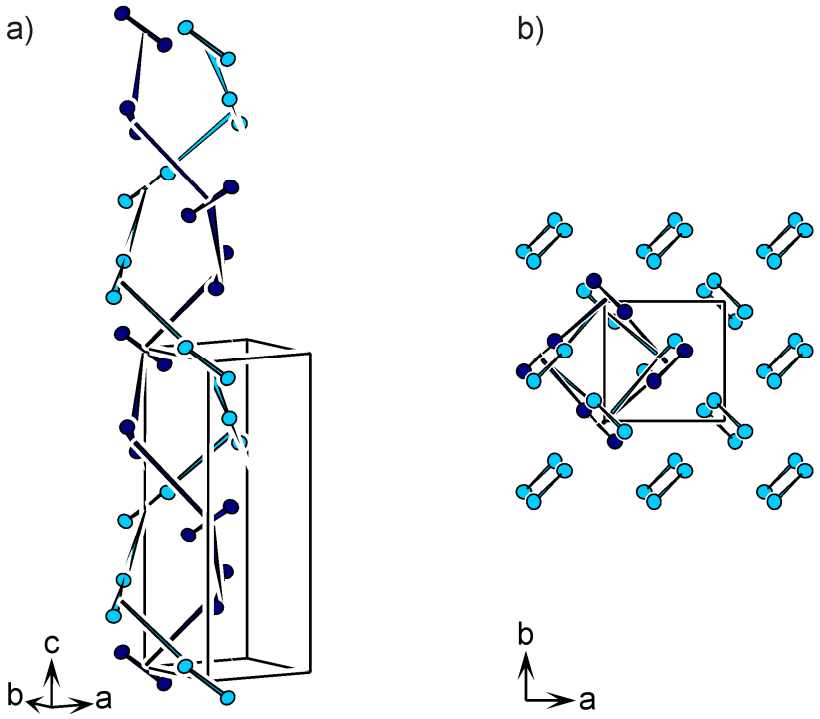

Figure 4 Arrangement of the Sn_2 dumbbells in Ba_3Sn_2 a) emphasizing the chiral axis b) along the *c*-axis. To illustrate the arrangement of the dumbbells, the centers of the neighbouring dumbbells are connected. The Sn atoms are drawn in light and dark blue. The displacement ellipsoids are drawn at the 95 % probability level.

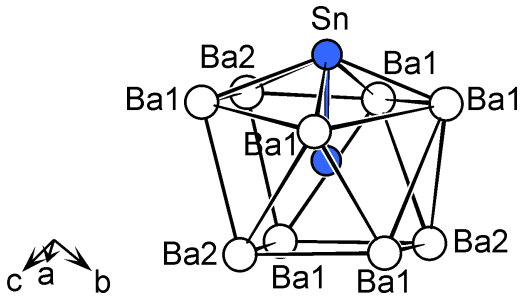

Figure 5 Coordination polyhedron of the Sn atoms in Ba_3Sn_2. The Ba and Sn atoms are drawn in white and grey (printed version) / blue (electronic version), respectively.

Chemical Bonding

Electronic Structure of Sr_7Ge_6 and Ba_7Ge_6

In order to analyze the electronic structure of the title phases, the total and partial DOS curves, the bandstructure including fatband representations (Figure 6, Figure 7) as well as the bond critical points (Table 5) were calculated for Ca_7Ge_6, Sr_7Ge_6 and Ba_7Ge_6 using the program WIEN2K. Further information about the bonding interaction between the Ge atoms is obtained by the Electron Localization Function (ELF, Figure 8 and Figure 9) and the integrated Crystal Overlap Hamiltonian Population (−iCOHP) (Table 4), which are calculated using the Stuttgart TB-LMTO-ASA program.

In Figure 6 total and partial DOS curves are shown in the range of −10 eV to 4 eV for Ba_7Ge_6, Sr_7Ge_6 and Ca_7Ge_6 including the orbital contributions of the Ge(s), Ge(p) and *Ae*(d) orbitals. E_F cuts a region of high Density Of States and therefore reveals clearly metallic properties of the phases Ae_7Ge_6. The DOS curve is divided in several sections: The narrow peaks between −10 eV and −5 eV are associated to the Ge(s) orbitals. Note that the partial DOS curves associated to the Ge1(s) and Ge2(s) orbitals (four-membered chain) are clearly separated from those associated to the Ge3(s) and Ge4(s) orbitals (dumbbell). Above −3 eV the DOS curve is dominated by the Ge(p) orbitals with some mixing of *Ae*(d) orbitals.

Above E_F for Ba_7Ge_6 a gap and for Sr_7Ge_6 and Ca_7Ge_6 a pseudo-gap with a rather low Density Of States is visible in the total DOS curves, which is also observable in the bandstructures (Figure 6). In the region from E_F to about 1 eV above E_F only few bands with high dispersion are observed along the lines which correspond to the directions parallel to the *ac* plane. In the case of Ba a small band gap of approximately 0.1 eV opens up at +0.5 eV above E_F. For Sr_7Ge_6 and Ca_7Ge_6 a pseudo-gap, which is broader (0.4 eV - 0.7 eV and 0.4 eV - 0.9 eV, respectively) is observed. For all three compounds an integrated DOS (iDOS) of 152 e^-/cell, corresponding to the valence electrons in Ae_7Ge_6, is found at E_F (iDOS taken from TB-LMTO-ASA). The integrated DOS at the gap / pseudo gap corresponds to an equivalent of 160 e^-/cell (at 0.5 eV for Ba_7Ge_6, at 0.7 eV for Sr_7Ge_6 and at 0.9 eV for Ca_7Ge_6). Thus, substitution of alkaline earth metal atoms with electron

richer elements such a trivalent rare earth metals corresponding to the addition of eight extra electrons per cell or two extra electrons per formula unit should lead to a semiconducting Zintl phase.

Further, for Ba_7Ge_6 (Figure 6a) one notices that along the lines corresponding to the direction of the *b* axis (Z → T, Y → Γ, X → S, R → U, highlighted in grey in Figure 6) the dispersion of the bands is relatively small and no band crosses E_F. At the point Γ one band streaks E_F. Significantly more dispersed bands that cross E_F are found along the lines that correspond to the directions perpendicular to the *b* axis and parallel to the *ac* plane (Γ → Z, T → Y, Γ → X, S → R). As described above, within the *ac* plane the layers of Ge_4 four-membered chains and Ge_2 dumbbells are located (layer A and layer B in Figure 1, respectively). As no band crosses E_F in the direction parallel to the *b* axis, the metallic property of Ba_7Ge_6 is anisotropic and occurs only parallel to the *ac* plane and thus parallel to the layers A and B. For Ca_7Ge_6 and Sr_7Ge_6 (Figure 6) the anisotropy concerning the dispersion of the bands is even more pronounced, flat bands are found in the sections parallel to the *b* axis and highly dispersed bands are found in the directions parallel to the *ac* plane. However, as the flat bands for Sr_7Ge_6 and Ca_7Ge_6 cross E_F, the anisotropic metallic conductivity, which is seen for Ba_7Ge_6, is broken; conduction is now possible along all directions.

In general, the bands of Ba_7Ge_6 are less dispersed than those of Sr_7Ge_6, and the highest dispersion is observed for Ca_7Ge_6. This trend correlates with an increasing charge transfer from *Ae* to Ge in the series Ba, Sr, and Ca which is underlined by the Bader charge distribution given in Table 5. This alteration of the dispersion and the corresponding influence on the band gap due to the substitution of elements of the same group is a well known phenomena for various semiconductors (e.g. for $BaSi_2$, $BaGe_2$ and $SrGe_2$ [87]).

In Figure 7 the partial DOS curves of the Ge(p) orbitals are given in the range of −3 eV to 2 eV for Ba_7Ge_6, Sr_7Ge_6 and Ca_7Ge_6. Additionally, the bandstructures including fatbands of the Ge1(p_z) and Ge2(p_z) orbitals (four-membered chain) as well as the Ge3(p_y) and Ge4(p_y) orbitals (dumbbell) are given. The shown fatbands ((p_z) of Ge1, Ge2 and (p_y) of Ge3, Ge4) correspond to the Ge(p) orbitals with the highest contribution at E_F. Further bandstructures including fatbands are given in the supporting information, Figure S4 to Figure S6.

Steep bands crossing E_F are observed in the directions Γ → Z and T → Y. These can be associated to the Ge1(p_z) and Ge2(p_z) orbitals. The Ge(p_z) orbitals are oriented

approximately perpendicular to the plane of the Ge_4 four-membered chains (layer A, parallel to the *ac* plane, Figure 1b). Thus, due to the depopulation of the π* states corresponding to the Ge(p_z) orbitals, π−bonding interaction of these Ge(p_z) orbitals is observed within the layer A containing the Ge_4 chains. Note that these bands associated to Ge1(p_z) and Ge2(p_z) are least dispersed for Ba_7Ge_6 and highest dispersed for Ca_7Ge_6, indicating least interaction of the Ge(p_z) orbitals within layer A for Ba_7Ge_6 and highest interaction of the Ge(p_z) orbitals within layer A for Ca_7Ge_6.

The steep bands crossing E_F in the direction S → R are associated to the Ge3(p_y) and Ge4(p_y) orbitals, which are oriented perpendicular to the layer B (parallel to the *ac* plane) containing the Ge_2 dumbbells (Figure 1c). Thus, interaction of (p) orbitals is also found for the Ge_2 dumbbell. Note that the bands associated to the Ge3(p_y) and Ge4(p_y) orbitals are least dispersed for Ca_7Ge_6 and highest dispersed for Ba_7Ge_6, indicating least interaction of the Ge(p_y) orbitals within the layer B for Ca_7Ge_6 and highest interaction of the Ge(p_y) orbitals within the layer B for Ba_7Ge_6. Additionally the band crossing E_F along the direction S → R is shifted around E_F to higher energy values going from Ca_7Ge_6 to Ba_7Ge_6. This indicates a more pronounced depopulation of the π* orbitals for Ba_7Ge_6 and therefore higher partial π−bonding within the Ge_2 dumbbells of Ba_7Ge_6.

Summarizing the analysis of the fatbands, interaction of the Ge(p) orbitals is observed in both layers A and B, which contain the Ge_4 four-membered chains as well as the Ge_2 dumbbells, respectively. However, for Ba_7Ge_6 the interaction of the Ge(p) orbitals is more pronounced within layer B containing the Ge_2 dumbbell, while for Ca_7Ge_6 the interaction of the Ge(p) orbitals is more pronounced within layer A containing the Ge_4 four-membered chain.

For a more quantitative analysis of the chemical bonding situation the Crystal Overlap Hamiltonian Population curves (supporting information, Figure S7 to Figure S9) as well as the integrated COHP (−iCOHP, Table 4) were calculated. Note that here the −iCOHP values do not relate to the corresponding bond length. However, for Sr_7Ge_6 and Ba_7Ge_6 the highest −iCOHP values are observed for the Ge3-Ge4 contact within the Ge_2 dumbbells (−iCOHP = 2.81 eV/bond for Sr_7Ge_6 and 2.92 eV/bond for Ba_7Ge_6), while for Ca_7Ge_6 the highest −iCOHP value is found for the Ge1-Ge1 contact within the Ge_4 four-membered chain (−iCOHP = 2.62 eV/bond). From a rather molecular point of view this enforces the assumption of partial π−bonding within the Ge_2 dumbbells as well as within the Ge_4 four-membered chain, the partial π−bonding being most pronounced within

the Ge_2 dumbbells for Ba_7Ge_6 and within the Ge_4 four-membered chain for Ca_7Ge_6. This is in good agreement with the analysis of the fatbands.

Furthermore, a topological analysis of the Electron Localization Function (ELF, Figure 8 and Figure 9) is shown. The following discussion of the ELF and the Bader analysis is restricted for Ba_7Ge_6, representatively for Ca_7Ge_6 and Sr_7Ge_6, as the general features are the same for all three compounds. The positions of the bond critical points (BCP) are given by the shortest distance of the BCP and the bond path (BP), which is connecting the atoms under consideration by a straight line. The exact values for Ca_7Ge_6 and Sr_7Ge_6 concerning the Bader analysis of the BCP are given in Table 5.

In Figure 8 the ELF in the vicinity of the Ge_2 dumbbell is presented. Figure 8a shows a two-dimensional contour line diagram of the ELF ranging from $\eta = 0.3$ to $\eta = 0.7$ parallel to the dumbbell. The cross section perpendicular to the dumbbell is given in Figure 8b. The isosurface of the ELF at $\eta = 0.59$ is given in Figure 8c. A different number of monosynaptic valence basins is associated to the Ge3 and Ge4 atoms due to the neighboring Ba atoms: two valence basins correspond to lone pairs of Ge4, while three valence basins display the lone pairs of Ge3. A disynaptic valence basin (①, Figure 8) indicating covalent bonding between Ge3-Ge4 is observed for all three compounds Ae_7Ge_6 in accordance with the high −iCOHP values (2.48 eV/bond, 2.81 eV/bond, 2.92 eV/bond for *Ae* = Ca, Sr, Ba, respectively). The disynaptic valence basin is observed below $\eta = 0.62$ slightly next to the bond. Similarly, the BCP obtained by Bader analysis is situated close to the bond path (d(BCP-BP) = 0.023 Å), with a charge of $\rho_{BCP} = 0.409\ e^{-}\cdot Å^{-3}$. The Laplacian $\nabla^2 \rho_{BCP} = -0.683\ e^{-}\cdot Å^{-5}$ confirms the covalent character of the bond.

In Figure 9 the ELF in the vicinity of the Ge_4 four-membered chain is presented. Figure a shows a contour line diagram of the ELF ranging from $\eta = 0.3$ to $\eta = 0.7$ parallel to the Ge_4 chain. Clearly two monosynaptic valence basins are observed for the Ge2 atoms, while only one monosynaptic valence basin is observed for each Ge1 atom. Disynaptic valence basins are seen for the Ge1-Ge2 ② as well as for the Ge1-Ge1 ③ contact. Figure 9b and Figure 9c show contour line diagrams perpendicular to the Ge2-Ge1 bond ② and the Ge1-Ge1 bond ③, respectively. Additionally, the isosurfaces of the ELF at $\eta = 0.63$ and $\eta = 0.6$ in the vicinity of the Ge_4 four-membered chain are shown in Figure 9d and Figure 9e, respectively.

The attractor at the Ge1-Ge2 bond ② appears below $\eta = 0.62$ and is situated slightly next to the bond path (BP). The bond critical point (BCP) obtained by the Bader analysis (Table 5) is likewise situated close to the bond path (BP) (d(BCP-BP) = 0.016 Å), the distance Ge2-BCP being shorter than the distance Ge1-BCP (d(Ge2-BCP) = 1.279(2) Å, d(Ge1-BCP) = 1.315(2) Å). The charge of $\rho_{BCP} = 0.367$ $e^{-}\cdot Å^{-3}$ and the negative value for $\nabla^2\rho_{BCP}$ (-0.377 $e^{-}\cdot Å^{-5}$) confirm the covalent character of the bond. The ellipticity $\varepsilon = 0.12$ indicates partial π−bonding, in agreement with the analysis of the fatbands and the COHP.

The attractor at the Ge1-Ge1 bond ③ appears below $\eta = 0.63$. As shown in Figure 9d three maxima are observed here, one being situated on the direct connection line between the Ge1 atoms, and two being situated above and below the plane of the Ge_4 unit. The resulting ellipsoid shape of the disynaptic valence basin is visible in Figure 9c. In analogy the Bader analysis reveals a bond critical point at the centre of the bond path (*xyz* = 0 0 0). The charge and the Laplacian of the BCP ($\rho_{BCP} = 0.394$ $e^{-}\cdot Å^{-3}$, $\nabla^2\rho_{BCP} = -0.571$ $e^{-}\cdot Å^{-5}$) confirm the covalent character of the bond. The high value found for the ellipticity ($\varepsilon = 0.24$) confirms the partial π−bonding.

Table 5 Results concerning the Bader analysis of Ba_3Sn_2, Ca_7Ge_6, Sr_7Ge_6 and Ba_7Ge_6 (BCP : bond critical point, *ε:* ellipticity)

	Ba_3Sn_2	Ca_7Ge_6	Sr_7Ge_6	Ba_7Ge_6
Charge distribution	Sn : −1.48	Ge1 : −1.05	Ge1 : −1.02	Ge1 : −0.90
		Ge2 : −1.51	Ge2 : −1.50	Ge2 : −1.28
		Ge3 : −1.43	Ge3 : −1.37	Ge3 : −1.14
		Ge4 : −1.82	Ge4 : −1.78	Ge4 : −1.55
BCP	Sn-Sn	Ge1-Ge1	Ge1-Ge1	Ge1-Ge1
x, y, z	0.9568, 0.9568, 0	0.5, 0, 0.5	0, 0, 0	0, 0, 0
ρ_{BCP} / ($e^- \cdot Å^{-3}$)	0.275	0.409	0.399	0.394
$\nabla^2 \rho_{BCP}$ / ($e^- \cdot Å^{-5}$)	0.165	−0.534	−0.483	−0.571
ε	0.00003	0.25	0.24	0.24
BCP	Ge1-Ge2	Ge1-Ge2	Ge1-Ge2	Ge1-Ge2
x, y, z	0.8384 , 0.5761, −0.0051	0.3451, 0.5744, 0.5034	0.1497, 0.0726, 0.0030	
ρ_{BCP} / ($e^- \cdot Å^{-3}$)	0.3790	0.3695	0.367	
$\nabla^2 \rho_{BCP}$ / ($e^- \cdot Å^{-5}$)	−0.307	−0.272	−0.377	
ε	0.15	0.13	0.12	
BCP	Ge3-Ge4	Ge3-Ge4	Ge3-Ge4	
x, y, z	0.8128, 0.25, 0.0091	0.2949, 0.25, 0.4881	0.2820, 0.25, 0.4871	
ρ_{BCP} / ($e^- \cdot Å^{-3}$)	0.396	0.398	0.409	
$\nabla^2 \rho_{BCP}$ / ($e^- \cdot Å^{-5}$)	−0.439	−0.489	−0.683	
ε	0.02	0.005	0.02	

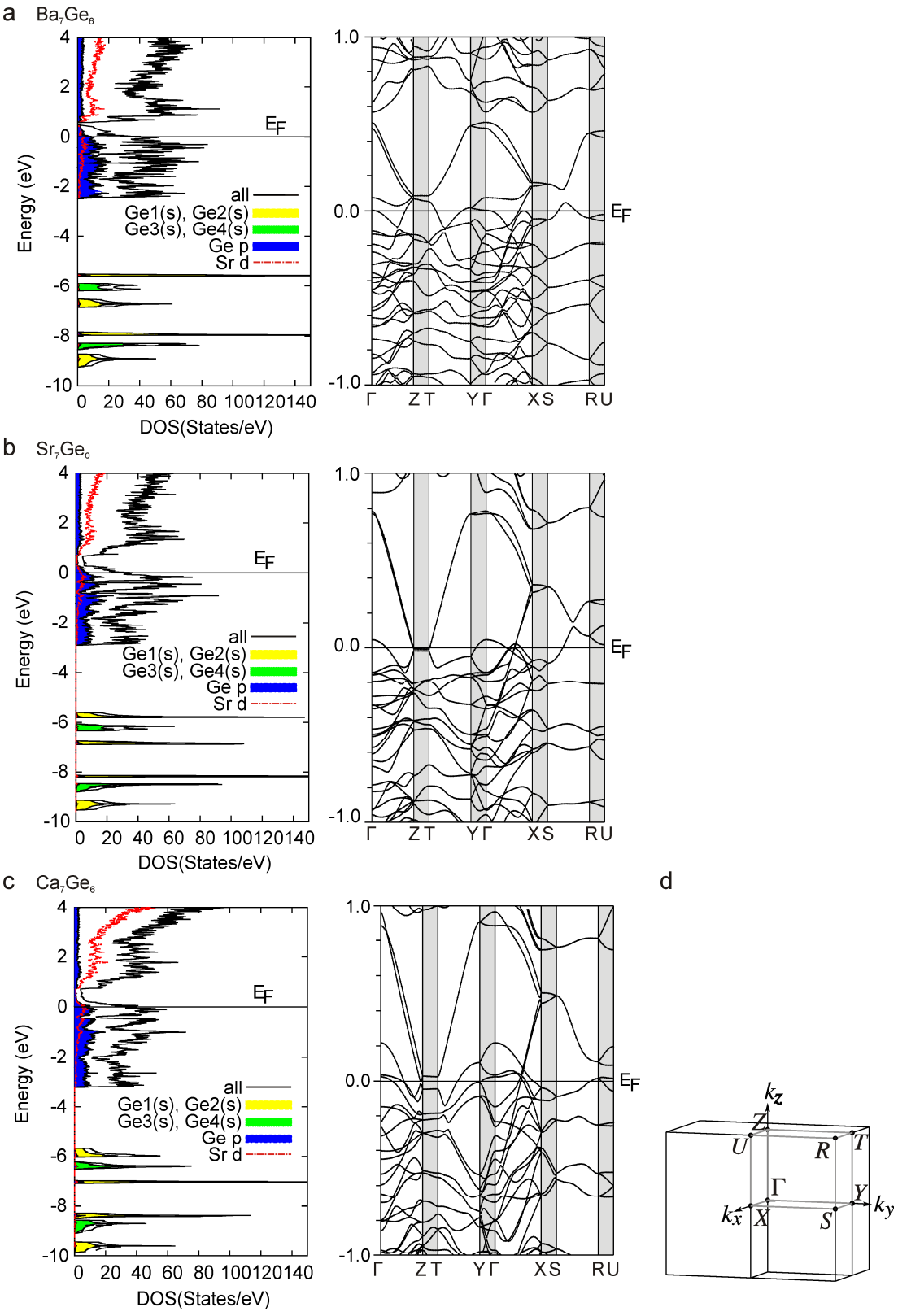

Figure 6 Total and partial DOS curves as well as bandstructures in the range of −1 eV to 1 eV for a) Ba_7Ge_6, b) Sr_7Ge_6, c) Ca_7Ge_6. The energy zero is taken at the Fermi level. The symmetry points in k space are given according to the Brillouin zone shown in (d) (with respect to the reciprocal conventional vectors).

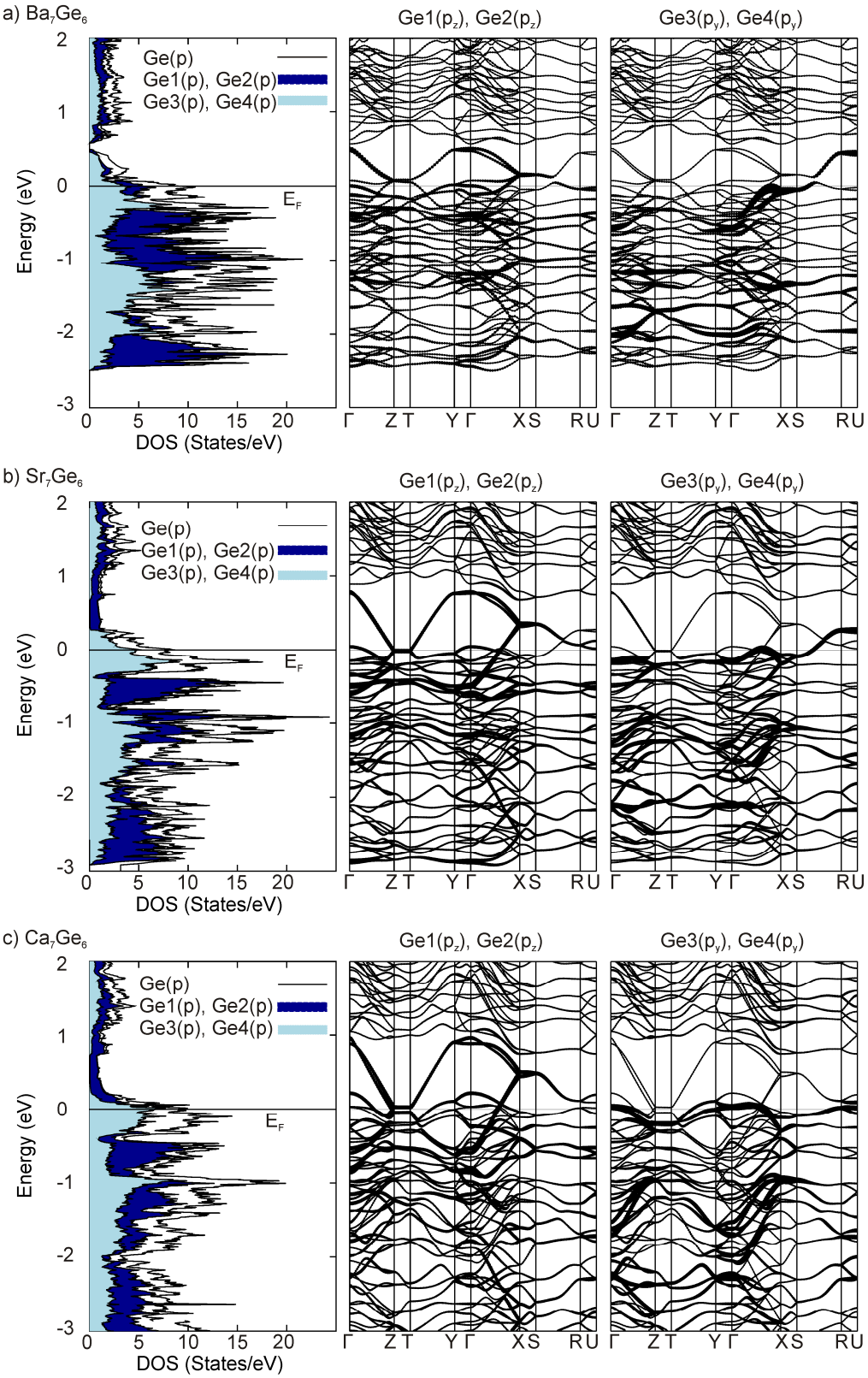

Figure 7 Partial DOS curves as well as bandstructures including fatbands in the range of −3 eV to 2 eV for a) Ba_7Ge_6, b) Sr_7Ge_6, c) Ca_7Ge_6. The energy zero is taken at the Fermi level. The symmetry points in k space are given according to the Brillouin zone shown in Figure 6d (with respect to the reciprocal conventional vectors).

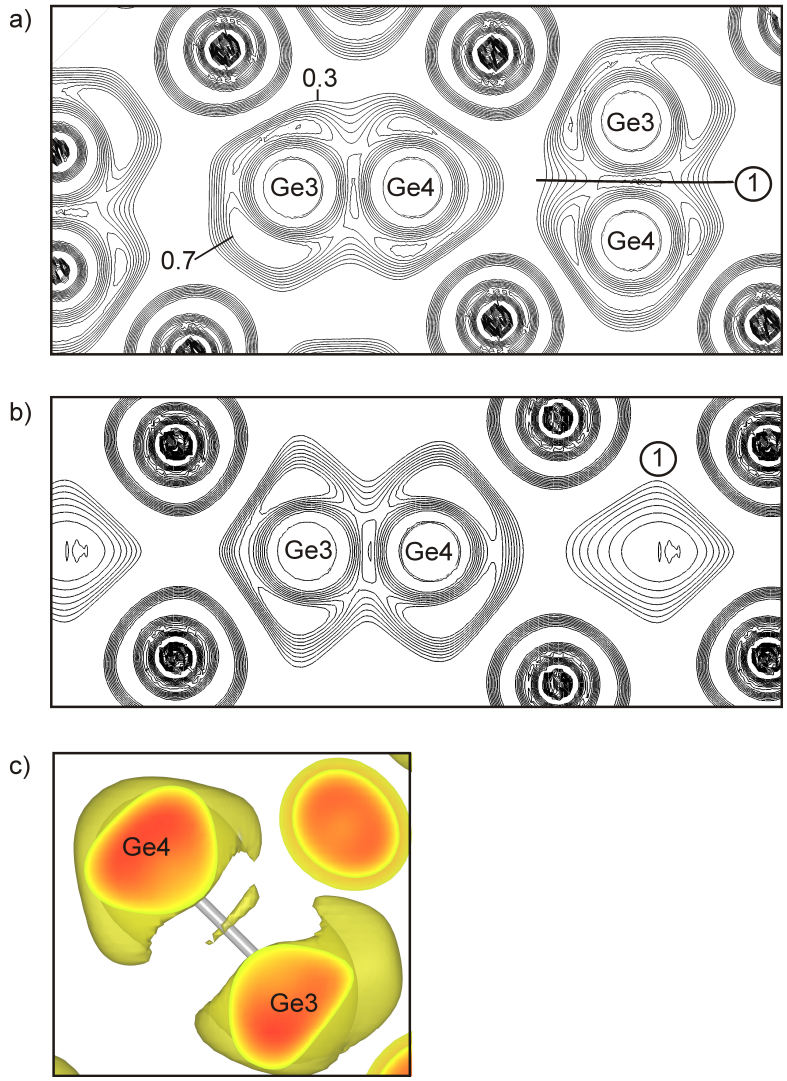

Figure 8 Topology of the ELF for the structural motif of the Ge-Ge dumbbell in Ba_7Ge_6, calculated from the all-electron density (TB-LMTO-ASA). Contour line diagrams of the ELF in steps of 0.05 ranging from η = 0.3 to η = 0.7 are given in (a) parallel to the Ge-Ge dumbbell and (b) perpendicular to the Ge3-Ge4 contact (*hkl* -101). A 3D ELF plot with isosurface at η = 0.59 presenting the bonding interactions is given in (c).

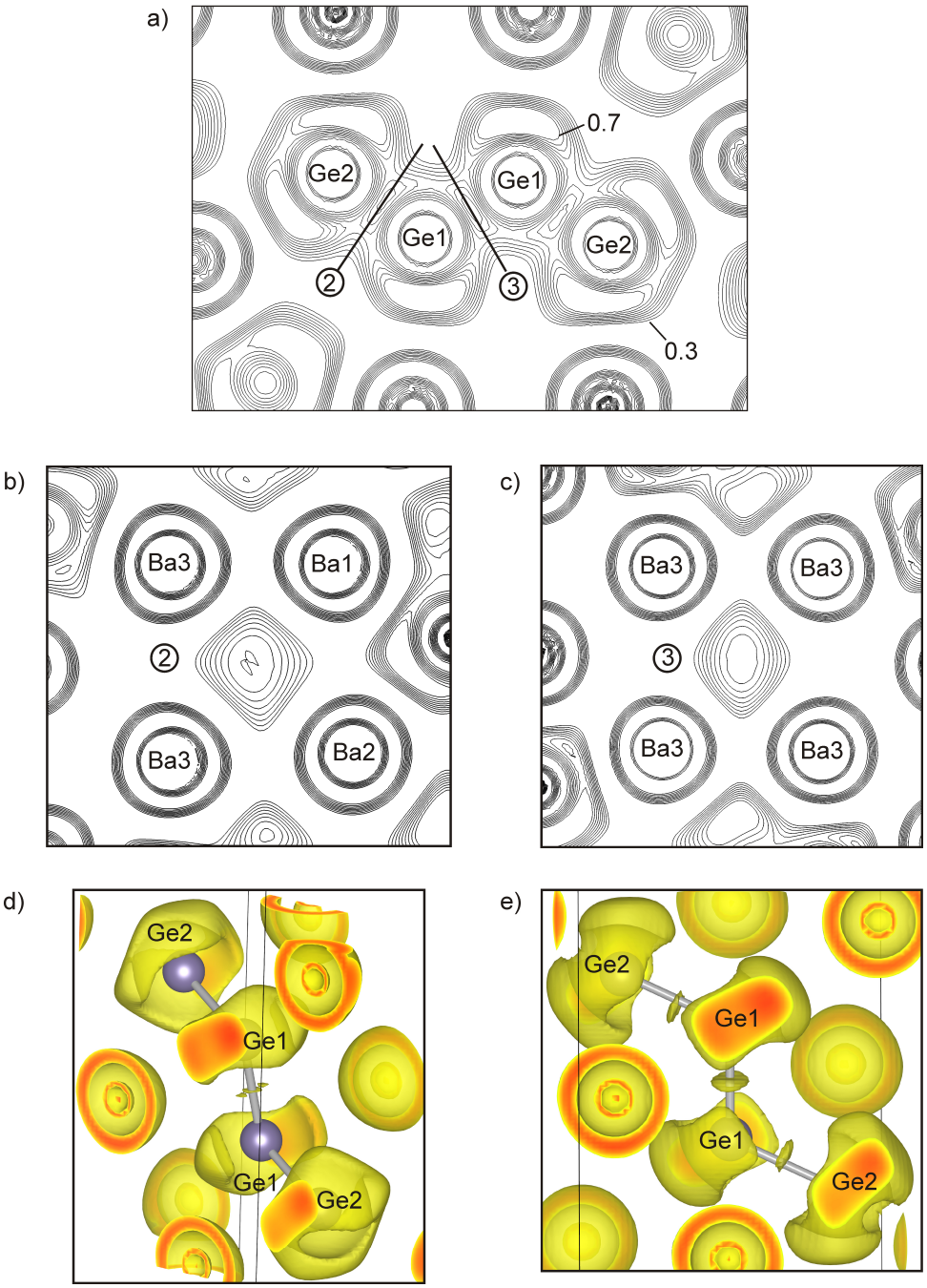

Figure 9 Topology of the ELF for the structural motif of the four-membered Ge_4 chain in Ba_7Ge_6, calculated from the all-electron density (TB-LMTO-ASA). Contour line diagrams of the ELF in steps of 0.05 ranging from $\eta = 0.3$ to $\eta = 0.7$ are given in (a) parallel to the Ge_4 chain, (b) perpendicular to the Ge1-Ge2 contact and (c) perpendicular to the Ge1-Ge1 contact. 3D ELF plots with isosurfaces at $\eta = 0.63$ and $\eta = 0.6$ presenting the bonding interactions are given in (d) and (e).

Electronic Structure of Ba_3Sn_2

The title phase Ba_3Sn_2 can be described as a Zintl phase and therefore is expected to be a semiconductor. This is confirmed by the calculation of the bandstructure and the Density Of States curves (WIEN2K). In order to optimize the calculated band gap the modified Becke-Johnson potential (mBJ) [53] was used to describe the exchange correlation potential. The results are shown in Figure 10. The DOS curve clearly shows a band gap which is 0.73eV wide. The bandstructure reveals the indirect character of this band gap. The states between −8eV and −5eV essentially originate from the Sn(s) orbitals, the states between −2.5eV and the Fermi level are dominated by the Sn(p) states. The integrated Crystal Overlap Hamiltonian Population (−iCOHP) indicates covalent bonding between Sn atoms (1.77eV/bond). The corresponding COHP curve is given in the supporting information, Figure S10.

In Figure 11 the Electron Localization Function (ELF) is presented. Figure 11a shows the section parallel to the Sn-Sn dumbbell. Figure 11b shows the contour lines of the plane perpendicular to the Sn-Sn bond. The isosurface in Figure 11c corresponds to the ELF value η = 0.5. Three attractors appear below η = 0.75 next to the Sn atoms and join at lower ELF values to a ring shaped monosynaptic valence basin. A disynaptic valence basin ④ is observed for values below $\eta = 0.52$. The first maximum is situated slightly next to the Sn-Sn bond path (BP). This is confirmed by the Bader analysis (Table 5): the bond critical point (BCP) obtained is situated slightly next to the Sn-Sn bond path (BP) (*xyz* = 0.9568 0.9568 0, *d*(BCP-BP) = 0.023 Å), with a charge of $\rho_{BCP} = 0.275\ e^{-}\cdot Å^{-3}$.

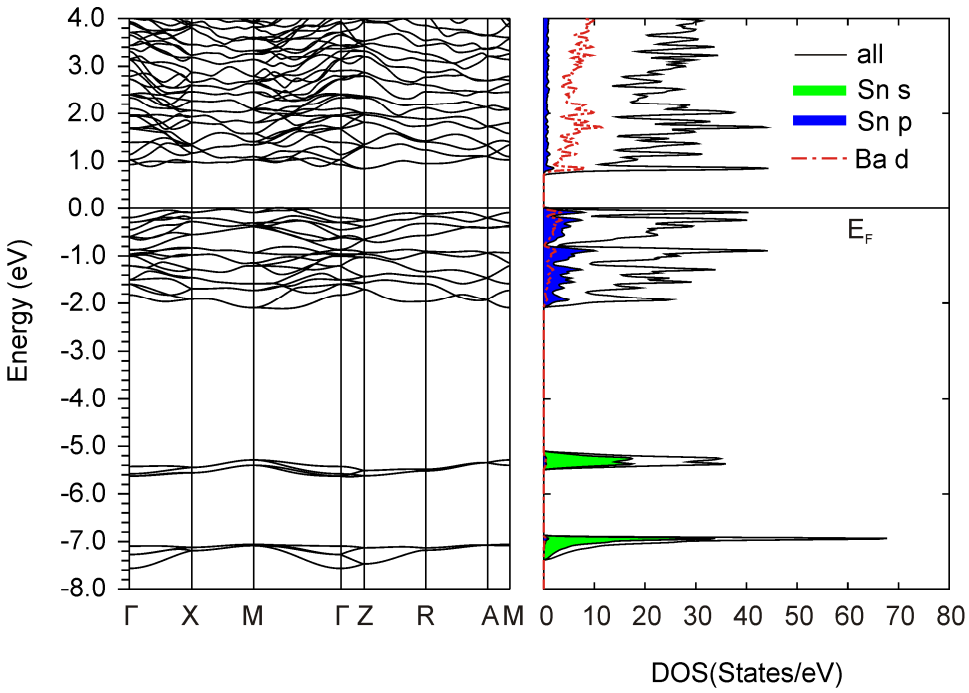

Figure 10 Ba_3Sn_2: a) Bandstructure with a band gap of 0.73 eV (WIEN2K), b) Total DOS curve and partial DOS curve, the energy zero is taken at the Fermi level (WIEN2K).

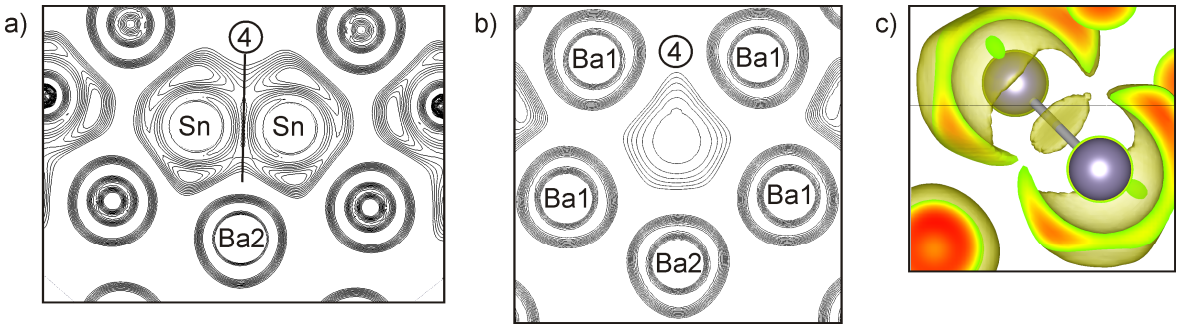

Figure 11 Topology of the ELF for the structural motif of the Sn-Sn dumbbell in Ba_3Sn_2, calculated from the all-electron density (TB-LMTO-ASA). Contour line diagrams of the ELF in steps of 0.05 ranging from η = 0.3 to η = 0.7 are given in (a) parallel to the Sn-Sn dumbbell and (b) perpendicular to the Sn-Sn contact. c) 3D ELF plots with isosurface at η = 0.5 presenting the bonding interactions.

Conclusion

Three new compounds Ba_3Sn_2, Ba_7Ge_6 and Sr_7Ge_6 were synthesized and structurally characterized. While Ba_3Sn_2 crystallizes in a new structure type, Ba_7Ge_6 and Sr_7Ge_6 crystallize in the Ca_7Sn_6 structure type. The crystal structures contain as main structural motifs Tt_2 dumbbells and, in case of *Tt* = Ge, Ge_4 four-membered chains. In spite of the simplicity of the crystal structures, the formation of such compounds as well as their crystal structures mostly still comes as a surprise. For example, the influence of the size of the alkaline earth metal atoms on the crystal structures cannot be predicted: while the crystal structures of the germanides with the composition *Ae* : Ge = 7 : 6 are not influenced by the size change of the alkaline earth metal atom, stannides and plumbides of the approximate composition *Ae* : *Tt* = 3 : 2 (*Ae*: Ca, Sr, Ba; *Tt*: Sn, Pb) display a variety of different crystal structures.

An analysis of the DOS curves and the bandstructures classifies Ba_3Sn_2 as a semiconductor, with a band gap of 0.73 eV, while the germanides Ae_7Ge_6 show metallic properties. This is in good agreement with the Zintl-Klemm concept assuming singly-bonded tetrel atoms only. The existence of a gap for Ba_7Ge_6 and a pseudo-gap for Sr_7Ge_6 and Ca_7Ge_6 just above E_F indicates that partial substitution of the alkaline earth metal atoms with electron richer elements such a trivalent rare earth metals should lead to semiconducting Zintl phases containing Ge atoms which are solely connected by covalent single bonds to other Ge atoms according to $[(1b\text{-}Ge)-(1b\text{-}Ge)]^{6-}$ and $[(1b\text{-}Ge)-(2b\text{-}Ge)-(2b\text{-}Ge)-(1b\text{-}Ge)]^{10-}$.

The topological analysis of the ELF, the −iCOHP values as well as a Bader analysis of the bond critical point show covalent bonding between the Sn atoms of the Sn_2 dumbbells in Ba_3Sn_2, as well as between the Ge atoms of the Ge_2 dumbbells and the Ge_4 four-membered chains in Ae_7Ge_6.

The analysis of the fatbands reveals that significant π−bonding interaction is present in Ae_7Ge_6. The analysis of the −iCOHP values indicates that for Ba_7Ge_6 the partial π−bonding is more pronounced within the Ge_2 dumbbell, while for Ca_7Ge_6 the partial π−bonding is more important within the Ge_4 four-membered chains. Thus, resonating hybrid structures including both structural motifs as given in equation (1) and (2) can be formulated:

$$\{[Ge = Ge - Ge - Ge]^{8-}\} \leftrightarrow \{[Ge - Ge = Ge - Ge]^{8-}\} \leftrightarrow [Ge \equiv Ge \equiv Ge \equiv Ge]^{8-}\} \quad (1)$$

$$\{[Ge - Ge]^{6-} / [Ge \equiv Ge \equiv Ge \equiv Ge]^{8-}\} \leftrightarrow \{[Ge = Ge]^{4-} / [Ge - Ge - Ge - Ge]^{10-}\} \quad (2)$$

For Ba_7Ge_6 the resonance hybrid at the right side of formula (2) is dominant, while for Ca_7Ge_6 it is shifted to the left side.

Acknowledgment. The authors like to thank M. Waibel for help concerning the preparation of single crystals of Ba_7Ge_6.

References

[1] E. Zintl, *Angew. Chem.* **1939**, *52*, 1.
[2] T. F. Fässler, S. Hoffmann, *Z. Kristallogr.* **1999**, *214*, 722.
[3] M. Pani, A. Palenzona, *J. Alloys Compd.* **2008**, *462*, L9.
[4] A. Palenzona, M. Pani, *J. Alloys Compd.* **2005**, *402*, 136.
[5] B. Eisenmann, H. Schäfer, K. Turban, *Z. Naturforsch., B: J. Chem. Sci.* **1975**, *30*, 677.
[6] R. Nesper, F. Zürcher, *Z. Kristallogr. - New Cryst. Struct.* **1999**, *214*, 21.
[7] A. Betz, H. Schäfer, A. Weiss, *Z. Naturforsch., B: J. Chem. Sci.* **1967**, *B 22*, 103.
[8] W. Rieger, E. Parthe, *Acta Crystallogr.* **1967**, *22*, 919.
[9] A. Betz, H. Schäfer, A. Weiss, R. Wulf, *Z. Naturforsch., B: J. Chem. Sci.* **1968**, *B 23*, 878.
[10] Eisenman.B, H. Schäfer, K. Turban, *Z. Naturforsch., B: J. Chem. Sci.* **1974**, *B 29*, 464.
[11] B. Eisenmann, M. Rhode, M. Wendorff, C. Röhr, *Z. Anorg. Allg. Chem.* **2008**, *634*, 153.
[12] H. Fukuoka, S. Yamanaka, E. Matsuoka, T. Takabatake, *Inorg. Chem.* **2005**, *44*, 1460.
[13] K. Turban, H. Schafer, *Z. Naturforsch., B: J. Chem. Sci.* **1973**, *B 28*, 220.
[14] R. Nesper, F. Zürcher, *Z. Kristallogr. - New Cryst. Struct.* **1999**, *214*, 22.
[15] F. Merlo, M. L. Fornasini, *J. Less Common Met.* **1967**, *13*, 603.
[16] V. V. Burnasheva, E. I. Gladyshevskii, *Inorg. Mater.* **1966**, *2*, 804.
[17] F. Zürcher, R. Nesper, *Angew. Chem. Int. Ed.* **1998**, *37*, 3314.
[18] V. G. Andrianov, K. A. Bol'shakov, E. B. Sokolov, A. V. Chirkin, A. V. Chirkin, P. I. Fedorov, *Inorg. Mater.* **1966**, *2*, 1784.
[19] A. Betz, H. Schäfer, A. Weiss, R. Wulf, *Z. Naturforsch., B: J. Chem. Sci.* **1968**, *B 23*, 878.

[20] R. Kröner, *Dissertation, Universität Stuttgart* **1989**.

[21] J. T. Vaughey, G. J. Miller, S. Gravelle, E. A. Leon-Escamilla, J. D. Corbett, *J. Solid State Chem.* **1997**, *133*, 501.

[22] H. Fukuoka, Y. Tomomitsu, K. Inumaru, *Inorg. Chem.* **2011**, *50*, 6372.

[23] T. F. Fässler, C. Kronseder, *Angew. Chem. Int. Ed. Engl.* **1997**, *36*, 2683.

[24] R. Kröner, K. Peters, H. G. von Schnering, *Z. Kristallogr. - New Cryst. Struct.* **1998**, *213*, 663.

[25] W. Carrillo-Cabrera, J. Curda, H. G. von Schnering, S. Paschen, Y. Grin, *Z. Kristallogr. - New Cryst. Struct.* **2000**, *215*, 207.

[26] H. Fukuoka, K. Iwai, S. Yamanaka, H. Abe, K. Yoza, L. Haming, *J. Solid State Chem.* **2000**, *151*, 117.

[27] S. J. Kim, S. Q. Hu, C. Uher, T. Hogan, B. Q. Huang, J. D. Corbett, M. G. Kanatzidis, *J. Solid State Chem.* **2000**, *153*, 321.

[28] W. Carrillo-Cabrera, S. Budnyk, Y. Prots, Y. Grin, *Z. Anorg. Allg. Chem.* **2004**, *630*, 2267.

[29] W. Carrillo-Cabrera, J. Curda, K. Peters, S. Paschen, M. Baenitz, Y. Grin, H. G. von Schnering, *Z. Kristallogr. - New Cryst. Struct.* **2000**, *215*, 321.

[30] U. Aydemir, L. Akselrud, W. Carrillo-Cabrera, C. Candolfi, N. Oeschler, M. Baitinger, F. Steglich, Y. Grin, *J. Am. Chem. Soc.* **2010**, *132*, 10984.

[31] G. Bruzzone, E. Franceschi, *J. Less Common Met.* **1978**, *57*, 201.

[32] W. Rieger, E. Parthe, *Acta Crystallographica* **1967**, *22*, 919.

[33] F. Zürcher, R. Nesper, S. Hoffmann, T. F. Fässler, *Z. Anorg. Allg. Chem.* **2001**, *627*, 2211.

[34] S. J. Kim, T. F. Fässler, *Z. Kristallogr. - New Cryst. Struct.* **2008**, *223*, 325.

[35] T. F. Fässler, S. Hoffmann, C. Kronseder, *Z. Anorg. Allg. Chem.* **2001**, *627*, 2486.

[36] T. F. Fässler, S. Hoffmann, *Z. Anorg. Allg. Chem.* **2000**, *626*, 106.

[37] S. Hoffmann, T. F. Fässler, *Inorg. Chem.* **2003**, *42*, 8748.

[38] A. Palenzona, P. Manfrinetti, M. L. Fornasini, *J. Alloys Compd.* **2002**, *345*, 144.

[39] A. Palenzona, P. Manfrinetti, M. L. Fornasini, *J. Alloys Compd.* **2000**, *312*, 165.

[40] STOE, WinXPOW Version 2.08, STOE & Cie GmbH, Darmstadt **2003**.

[41] X-RED32 - *Data Reduction Program*, Version 1.48, Stoe & Cie GmbH, Darmstadt (Germany), **2008**.

[42] X-SHAPE - *Crystal Optimization for Numerical Absorption Correction*, Version 2.11, STOE & Cie GmbH, Darmstadt (Germany), **2008**.

[43] CrysAlis RED, *Scale3 / ABSPACK*, Version 1.171.33.34d, Oxford Diffraction Poland Sp. z o.o., **2009**.

[44] G. M. Sheldrick, SHELXS-97 – *Program for the Determination of Crystal Structures*, University of Göttingen (Germany) **1997**.

[45] G. M. Sheldrick, SHELXL-97 – *Program for Crystal Structure Refinement*, University of Göttingen (Germany) **1997**.

[46] P. Blaha, K. Schwarz, G. K. H. Madsen, D. Kvasnicka, J. Luitz, WIEN2k_10.1 - An Augmented Plane Wave + Local Orbitals Program for Calculating Crystal Properties TU Wien, **2010**.

[47] M. v. Schilfgarde, T. A. Paxton, O. Jepsen, O. K. Andersen, G. Krier, The Stuttgart Tight-Binding LMTO-ASA program Version 4.7, Max-Planck-Institut für Festkörperforschung Stuttgart (Germany), **1998**

[48] A. D. Becke, K. E. Edgecombe, *J. Chem. Phys.* **1990**, *92*, 5397.

[49] T. F. Fässler, *Chem. Soc. Rev.* **2003**, *32*, 80.

[50] A. Savin, R. Nesper, S. Wengert, T. F. Fassler, *Angew. Chem. Int. Ed. Engl.* **1997**, *36*, 1809.

[51] R. F. W. Bader, *Atoms in Molecules - A Quantum Theory*, Oxford University Press, Oxford, **1990**.

[52] J. P. Perdrew, S. Burke, M. Ernzerhof, *Phys. Rev. Lett.* **1996**, *77*, 3865.

[53] F. Tran, P. Blaha, *Phys. Rev. Lett.* **2009**, *102*, 226401.

[54] A. Otero-de-la-Roza, M. A. Blanco, A. M. Pendas, V. Luana, *Comput. Phys. Commun.* **2009**, *180*, 157.

[55] U. V. Barth, L. Hedin, *J. Phys. Chem. C* **1972**, *5*, 1629.

[56] O. Jepsen, O. K. Andersen, *Z. Phys. B* **1995**, *97*, 35.

[57] O. K. Andersen, O. Jepsen, *Phys. Rev. Lett.* **1984**, *53*, 2571.

[58] K. Momma, F. Izumi, VESTA: a three-dimensional visualization system for electronic and structural analysis **2008**.

[59] G. S. Smith, Q. Johnson, A. G. Tharp, *Acta Crystallogr.* **1967**, *22*, 269.

[60] A. Currao, J. Curda, R. Nesper, *Z. Anorg. Allg. Chem.* **1996**, *622*, 85.

[61] F. Zürcher, S. Wengert, R. Nesper, *Inorg. Chem.* **1999**, *38*, 4567.

[62] S. Wengert, R. Nesper, *Z. Anorg. Allg. Chem.* **1998**, *624*, 1801.

[63] R. Nesper, S. Wengert, *Monatsh. Chem.* **1999**, *130*, 197.

[64] S. Wengert, R. Nesper, *Z. Anorg. Allg. Chem.* **2000**, *626*, 246.

[65] F. Zürcher, R. Nesper, *Z. Kristallogr. - New Cryst. Struct.* **2001**, *216*, 505.

[66] P. Villars, K. Cenzual*, Vol. Version 1.0*, ASM International @, Materials Park, Ohio, USA, **2007/8**.

[67] R. Nesper, H. G. von Schnering, *Mineralogy and Petrology* **1983**, *32*, 195.

[68] D. G. Park, Y. Dong, F. J. DiSalvo, *J. Alloys Compd.* **2009**, *470*, 90.

[69] W. Müller, H. Schäfer, A. Weiss, *Z. Naturforsch., B: J. Chem. Sci.* **1971**, *B 26*, 5.

[70] Q. X. Xie, R. Nesper, *Z. Anorg. Allg. Chem.* **2006**, *632*, 1743.

[71] A. F. Richards, M. Brynda, P. P. Power, *Chem. Commun.* **2004**, 1592.

[72] M. Stender, L. H. Pu, P. P. Power, *Organometallics* **2001**, *20*, 1820.

[73] S. Deibele, J. Curda, E. M. Peters, M. Jansen, *Chem. Commun.* **2000**, 679.

[74] W. Dörrscheidt, A. Widera, H. Schäfer, *Z. Naturforsch., B: J. Chem. Sci.* **1977**, *32*, 1097.

[75] G. Bruzzone, E. Franceschi, F. Merlo, *J. Less Common Met.* **1978**, *60*, 59.

[76] E. A. Leon-Escamilla, J. D. Corbett, *Inorg. Chem.* **2001**, *40*, 1226.

[77] E. A. Leon-Escamilla, J. D. Corbett, *J. Solid State Chem.* **2001**, *159*, 149.

[78] M. L. Fornasini, E. Franceschi, *Acta Crystallogr., Sect. B: Struct. Sci.* **1977**, *33*, 3476.

[79] A. K. Ganguli, A. M. Guloy, E. A. Leonescamilla, J. D. Corbett, *Inorg. Chem.* **1993**, *32*, 4349.

[80] W. H. Zachariasen, *Acta Crystallogr.* **1948**, *1*, 265.

[81] R. Kraft, R. Pöttgen, *Monatsh. Chem.* **2005**, *136*, 1707.

[82] Q. X. Xie, C. Kubata, M. Woerle, R. Nesper, *Z. Anorg. Allg. Chem.* **2008**, *634*, 2469.

[83] W. Choe, G. J. Miller, E. M. Levin, *J. Alloys Compd.* **2001**, *329*, 121.

[84] R. Kraft, R. Pöttgen, *Monatsh. Chem.* **2004**, *135*, 1327.

[85] V. Hopf, H. Schäfer, A. Weiss, *Z. Naturforsch., B: J. Chem. Sci.* **1970**, *B 25*, 653.

[86] W. Müller, K. Volk, *Z. Naturforsch., B: J. Chem. Sci.* **1978**, *33*, 275.

[87] D. B. Migas, V. L. Shaposhnikov, V. E. Borisenko, *Phys. Status Solidi B* **2007**, *244*, 2611.

Supporting Information

Table S1 Anisotropic displacement parameters (U_{ij} / Å^2) for Sr_7Ge_6

Atom	U_{11}	U_{22}	U_{33}	U_{12}	U_{13}	U_{23}
Sr1	0.0192(3)	0.0126(3)	0.0177(3)	-0.0004(2)	-0.0006(3)	-0.0002(2)
Sr2	0.0189(3)	0.0199(3)	0.0193(3)	-0.0033(2)	0.0019(3)	-0.0020(3)
Sr3	0.0166(3)	0.0151(3)	0.0169(3)	0.0010(2)	-0.0015(2)	-0.0020(2)
Sr4	0.0223(5)	0.0202(4)	0.0222(5)	0.00000	0.0006(4)	0.00000
Ge1	0.0165(3)	0.0124(3)	0.0167(3)	-0.0019(3)	-0.0002(3)	0.0009(3)
Ge2	0.0161(3)	0.0143(3)	0.0165(3)	0.0019(3)	0.0000(3)	0.0016(3)
Ge3	0.0181(5)	0.0191(5)	0.0359(7)	0.00000	0.0054(5)	0.00000
Ge4	0.0211(5)	0.0181(5)	0.0171(5)	0.00000	-0.0010(4)	0.00000

Table S2 Anisotropic displacement parameters (U_{ij} / Å^2) for Ba_7Ge_6

Atom	U_{11}	U_{22}	U_{33}	U_{12}	U_{13}	U_{23}
Ba1	0.0124(3)	0.0105(3)	0.0150(3)	-0.0008(2)	-0.0002(3)	0.0001(3)
Ba2	0.0140(3)	0.0161(3)	0.0142(4)	-0.0045(2)	0.0020(3)	-0.0022(3)
Ba3	0.0122(3)	0.0117(3)	0.0126(3)	0.0013(2)	-0.0009(3)	-0.0013(3)
Ba4	0.0164(5)	0.0161(5)	0.0212(5)	0.00000	0.0010(4)	0.00000
Ge1	0.0120(5)	0.0090(5)	0.0132(6)	-0.0015(4)	0.0006(5)	0.0005(4)
Ge2	0.0111(5)	0.0113(5)	0.0133(6)	0.0010(4)	0.0004(5)	0.0010(4)
Ge3	0.0117(8)	0.0147(8)	0.0206(10)	0.00000	0.0009(7)	0.00000
Ge4	0.0141(8)	0.0123(8)	0.0165(9)	0.00000	0.0012(7)	0.00000

Table S3 Anisotropic displacement parameters (Uij / Å^2) for Ba_3Sn_2

Atom	U_{11}	U_{22}	U_{33}	U_{12}	U_{13}	U_{23}
Ba1	0.0263 (2)	0.0185(2)	0.0271(2)	0.0010(2)	0.0045(2)	0.0025(2)
Ba2	0.0236(2)	0.0236(2)	0.0196(2)	-0.0017(2)	-0.0011 (2)	0.0011(2)
Sn	0.0226(2)	0.0189(2)	0.0179(2)	0.0004(2)	0.0018(2)	-0.0024(2)

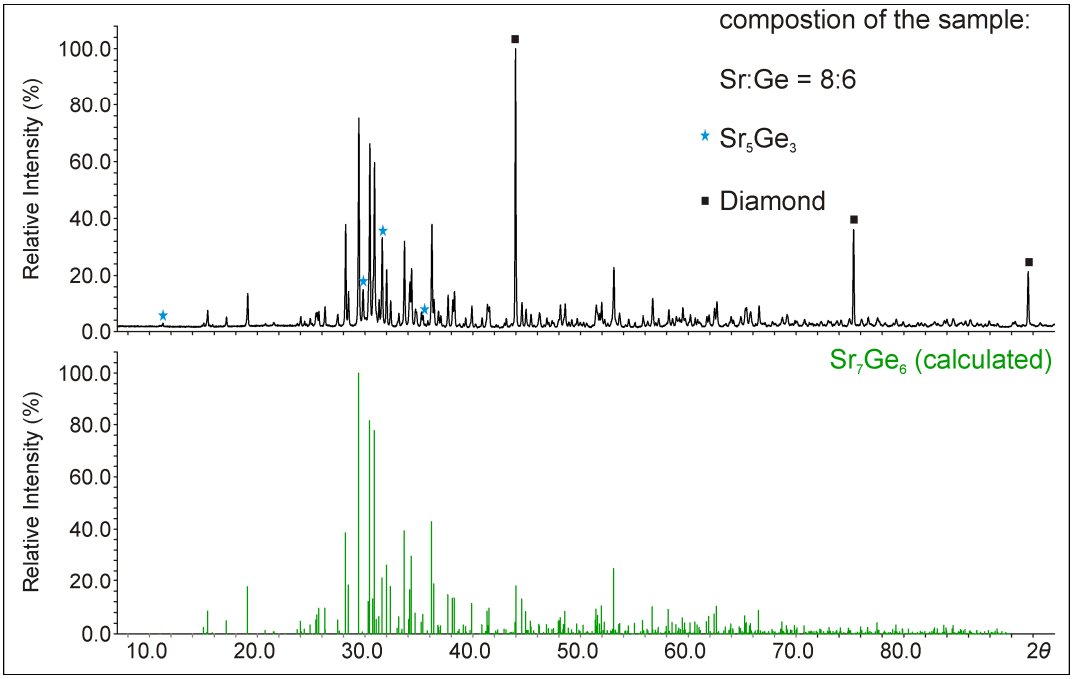

Figure S1 Experimental powder XRD pattern (top) from sample loading Sr : Ge = 8 : 6 and simulated powder XRD pattern (bottom) of Sr_7Ge_6. The experimental powder XRD pattern was recorded in Debye Scherrer geometry and its background has been subtracted. Reflections of Sr_5Ge_3 and diamond are labelled with a blue star and a black square, respectively.

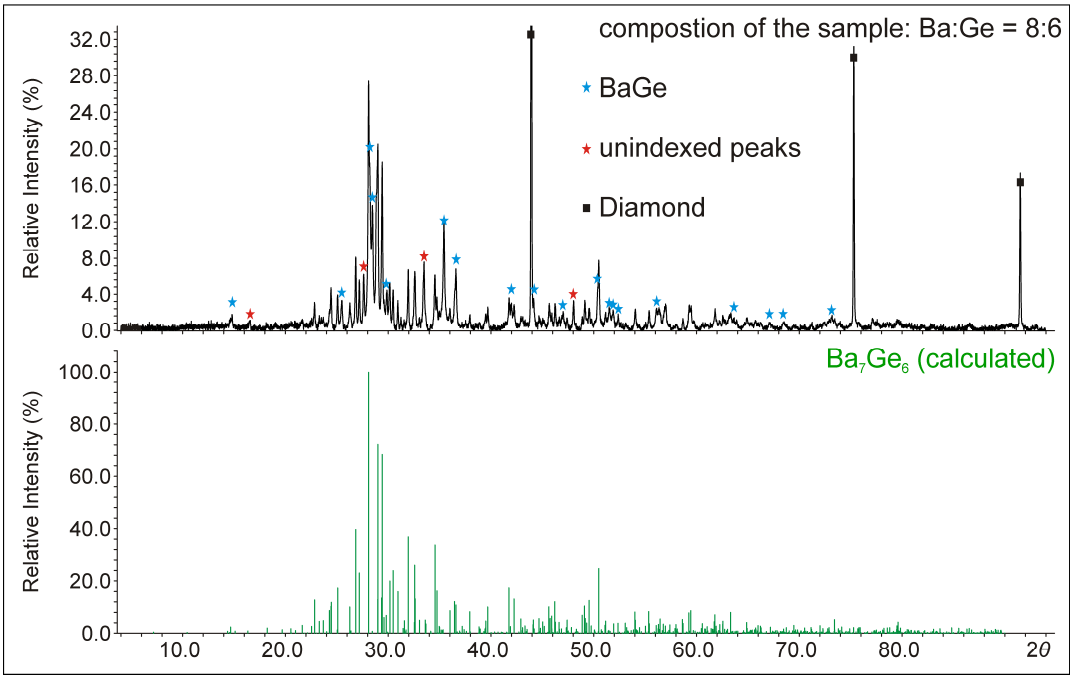

Figure S2 Experimental powder XRD pattern (top) from sample loading Ba : Ge = 8 : 6 and simulated powder XRD pattern (bottom) of Ba_7Ge_6. The experimental powder XRD pattern was recorded in Debye Scherrer geometry and its background has been subtracted. Reflections of BaGe, diamond as well as unindexed reflections are labelled with a blue star, a black square and a red star, respectively.

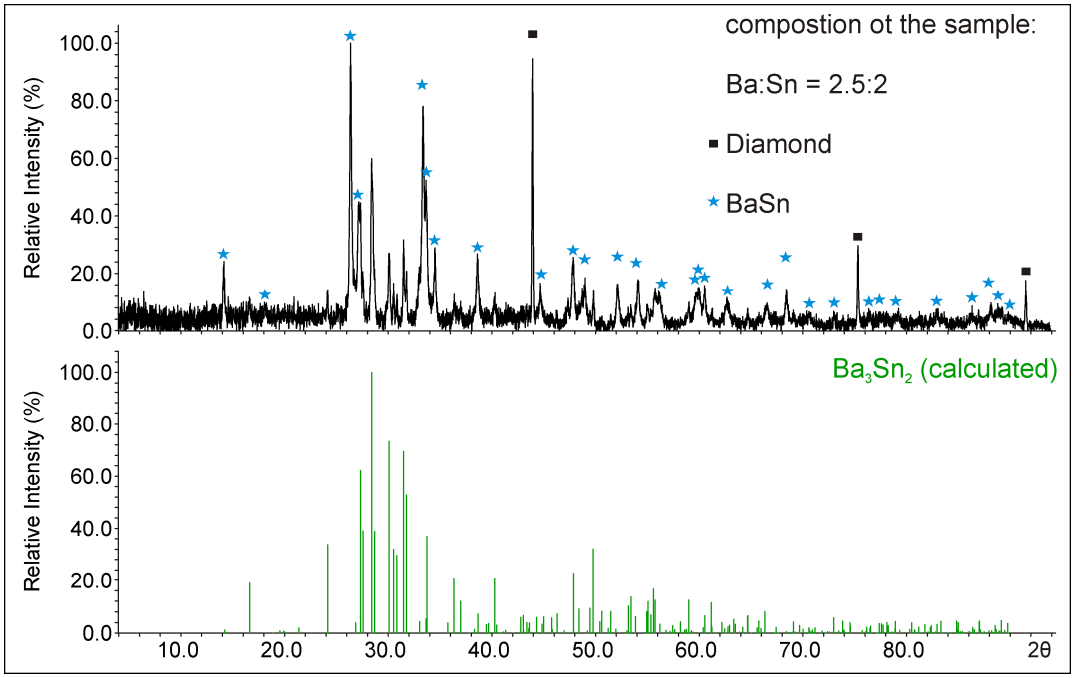

Figure S3 Experimental powder XRD pattern (top) from sample loading Ba : Sn = 2.5 : 2 and simulated powder XRD pattern (bottom) of Ba_3Sn_2. The experimental powder XRD pattern was recorded in Debye Scherrer geometry and its background has been subtracted. Reflections of BaSn and diamond are labelled with a blue star and a black square, respectively.

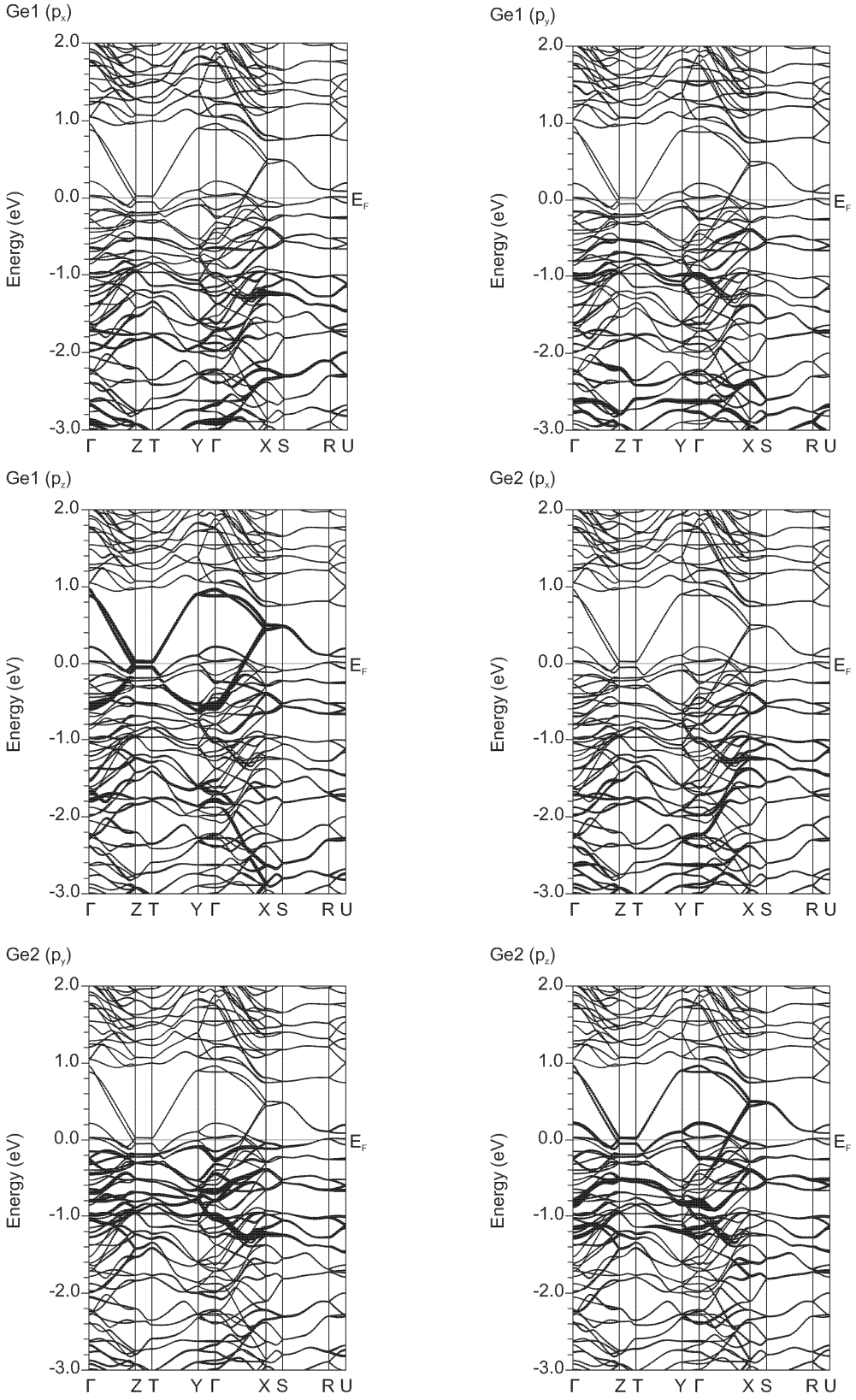

Figure S4 (I) Bandstructure including fatbands for Ca_7Ge_6 (WIEN2k)

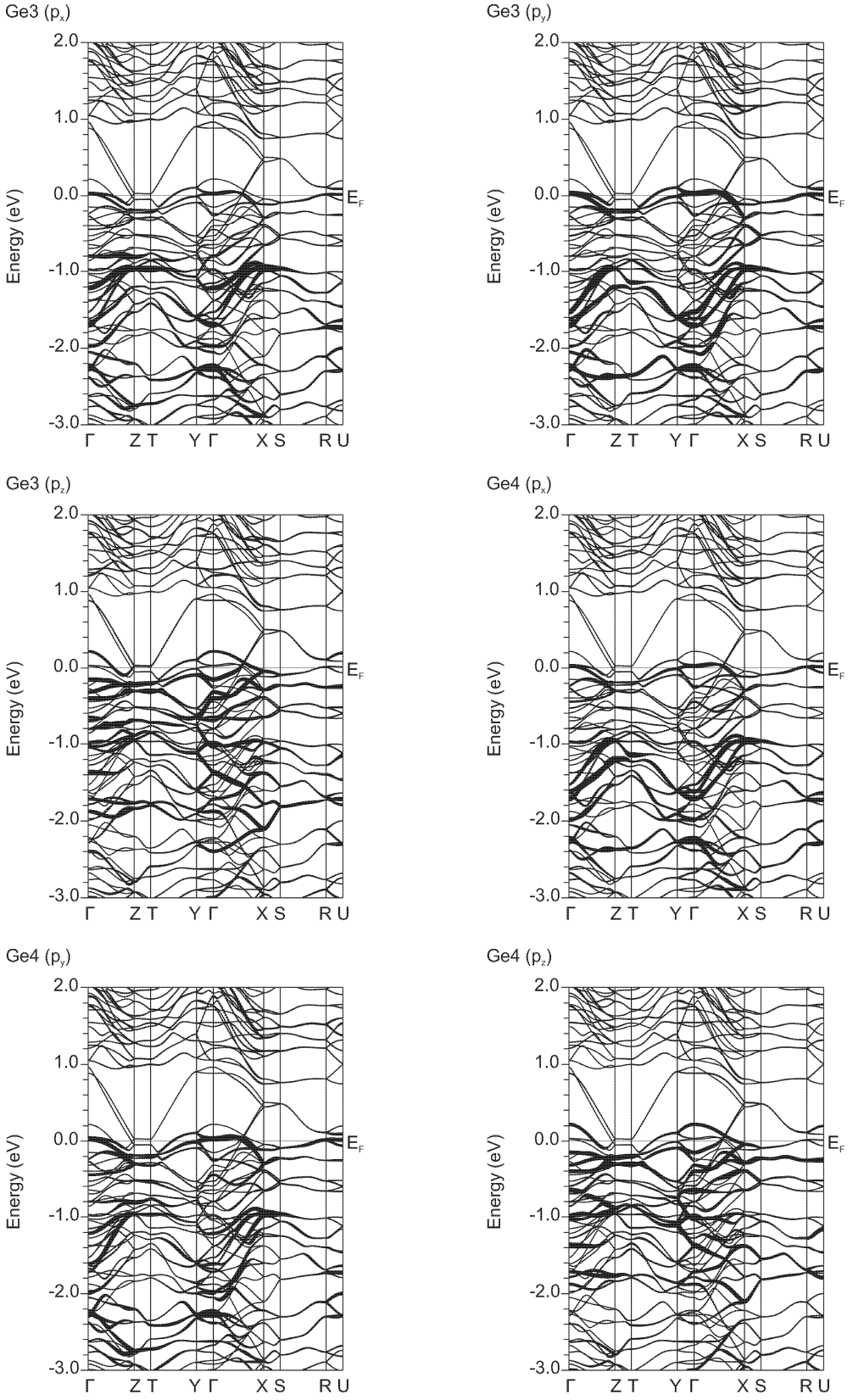

Figure S4 (II) Bandstructure including fatbands for Ca_7Ge_6 (WIEN2k)

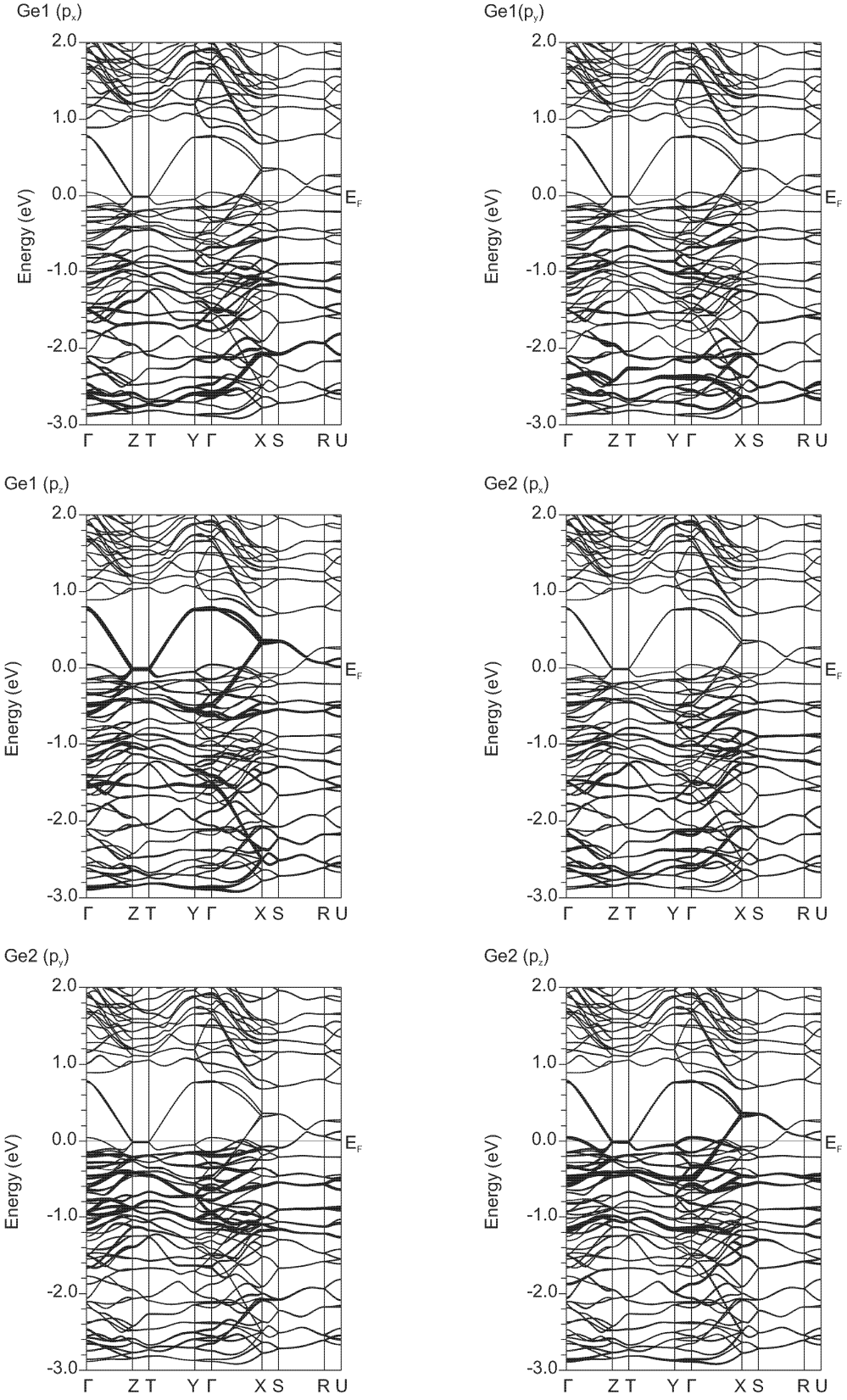

Figure S5 (I) Bandstructure including fatbands for Sr_7Ge_6 (Wien2k)

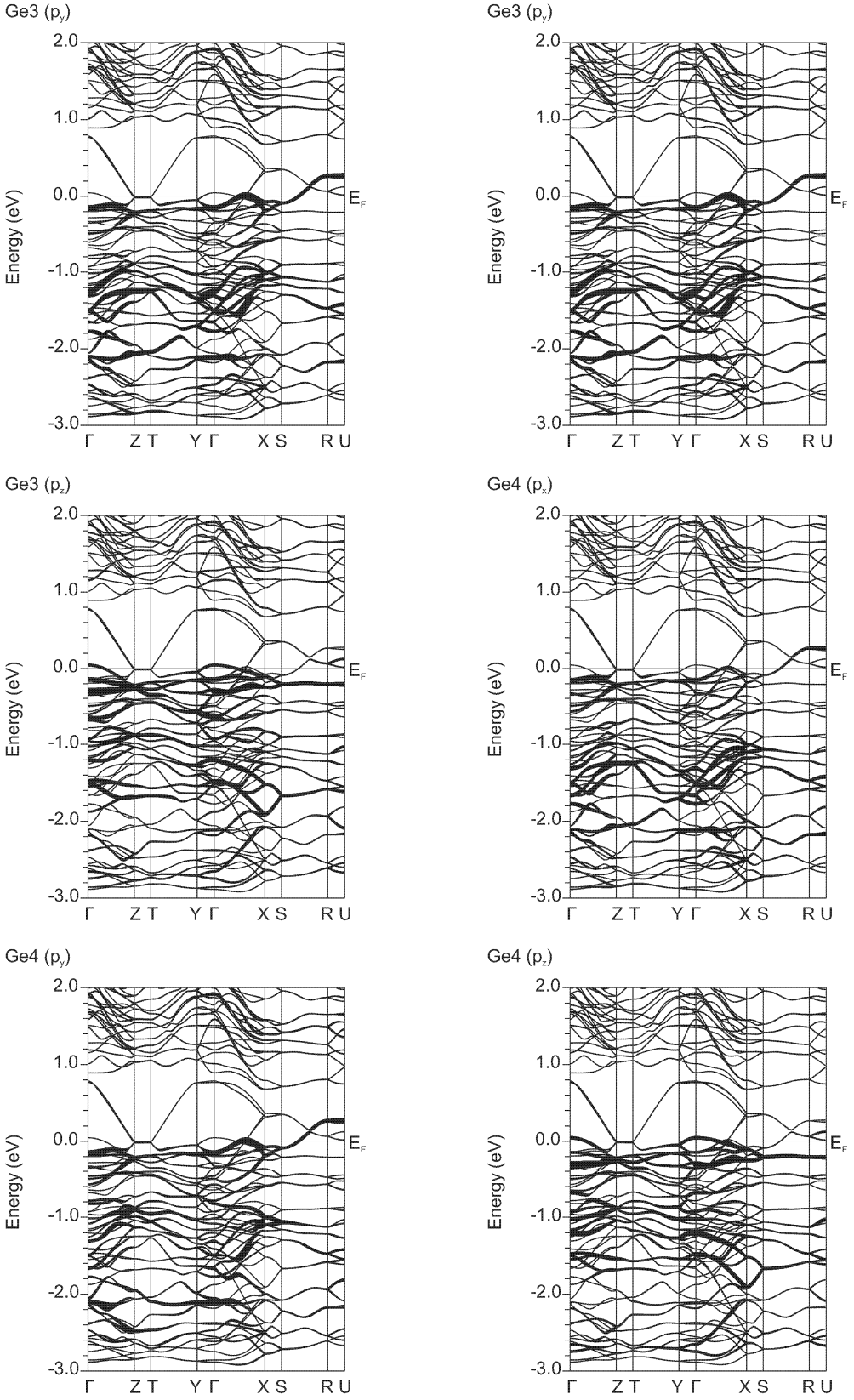

Figure S5 (II) Bandstructure including fatbands for Sr_7Ge_6 (WIEN2k)

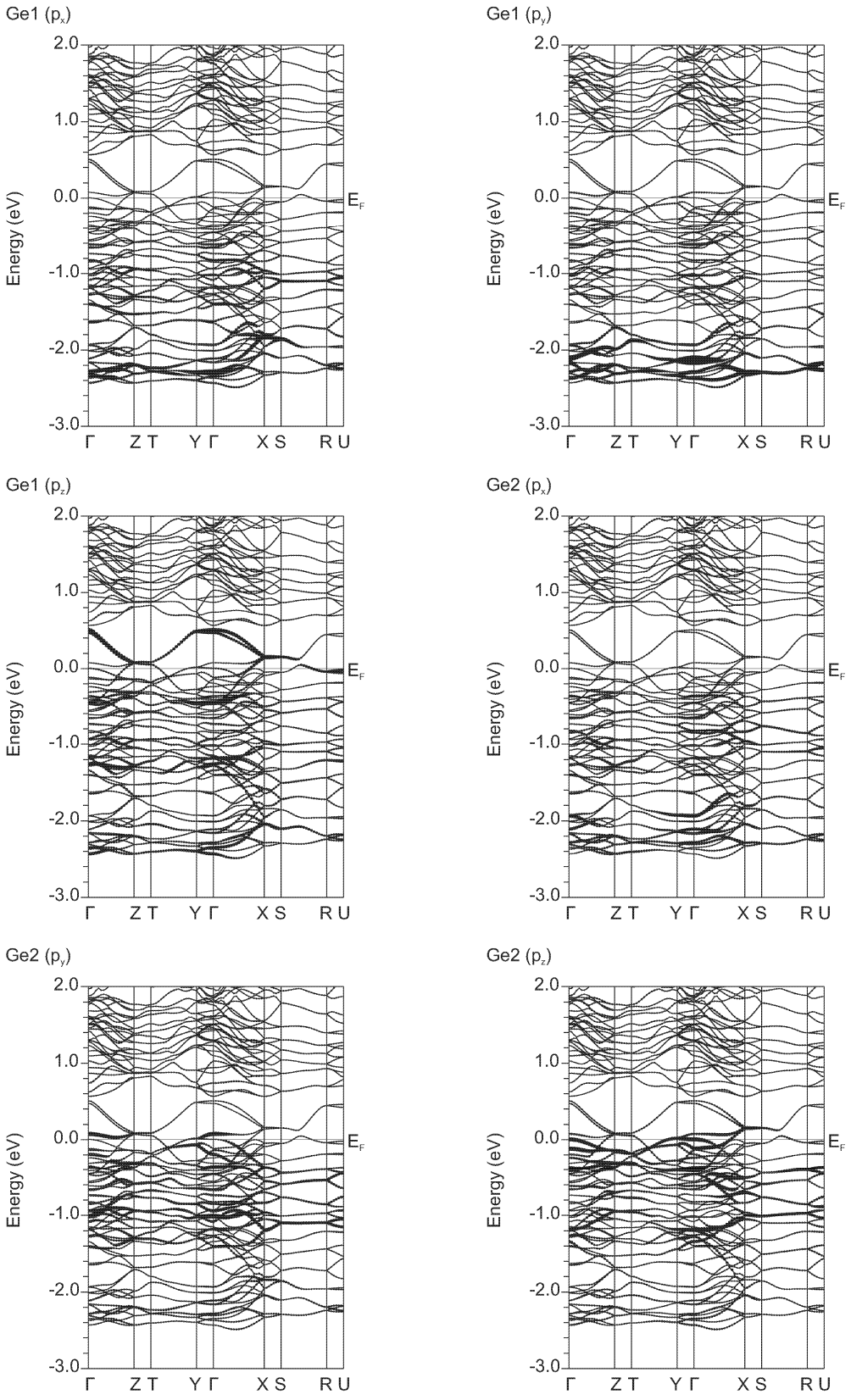

Figure S6 (I) Bandstructure including fatbands for Ba_7Ge_6 (WIEN2k)

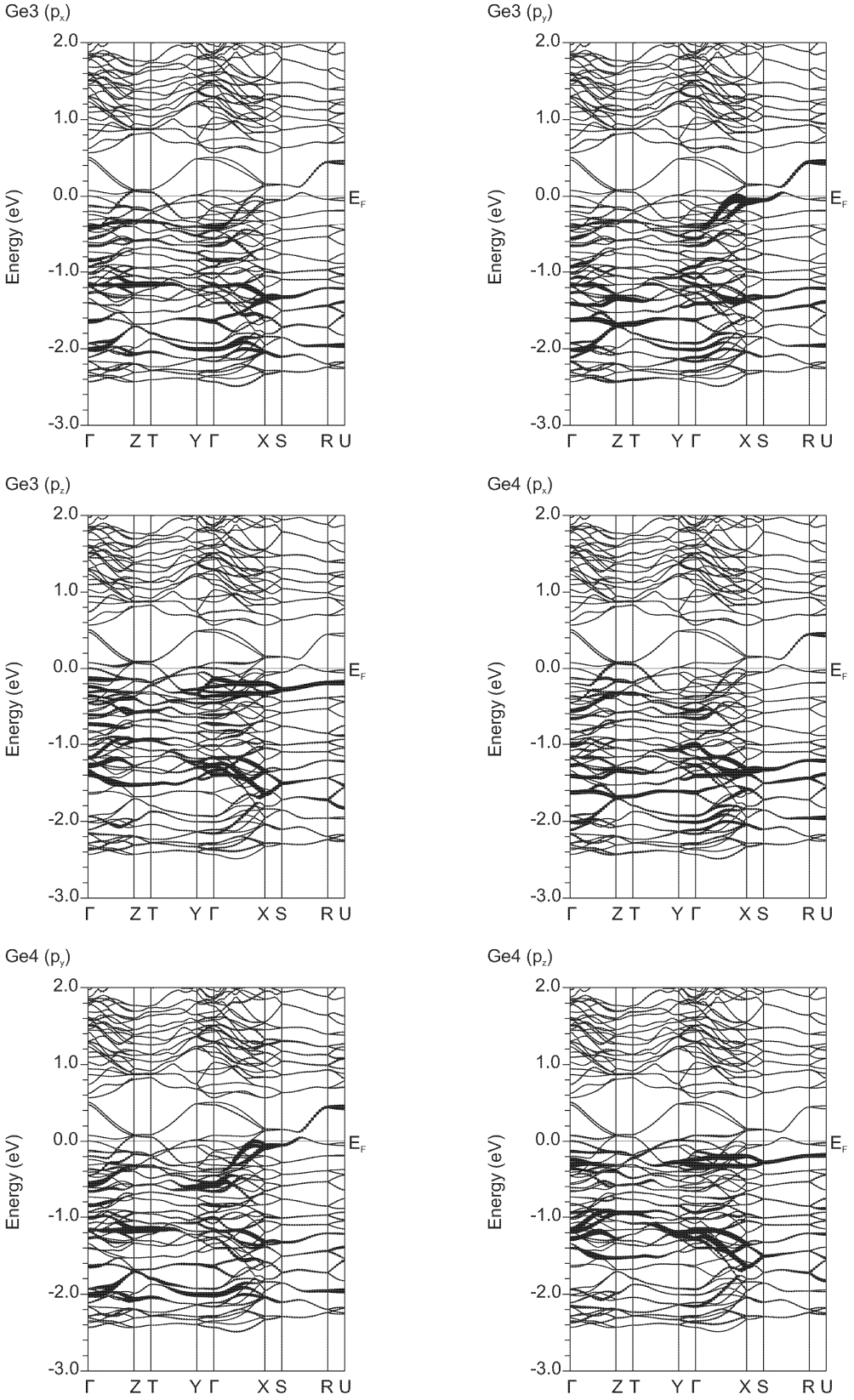

Figure S6 (II) Bandstructure including fatbands for Ba_7Ge_6 (WIEN2k)

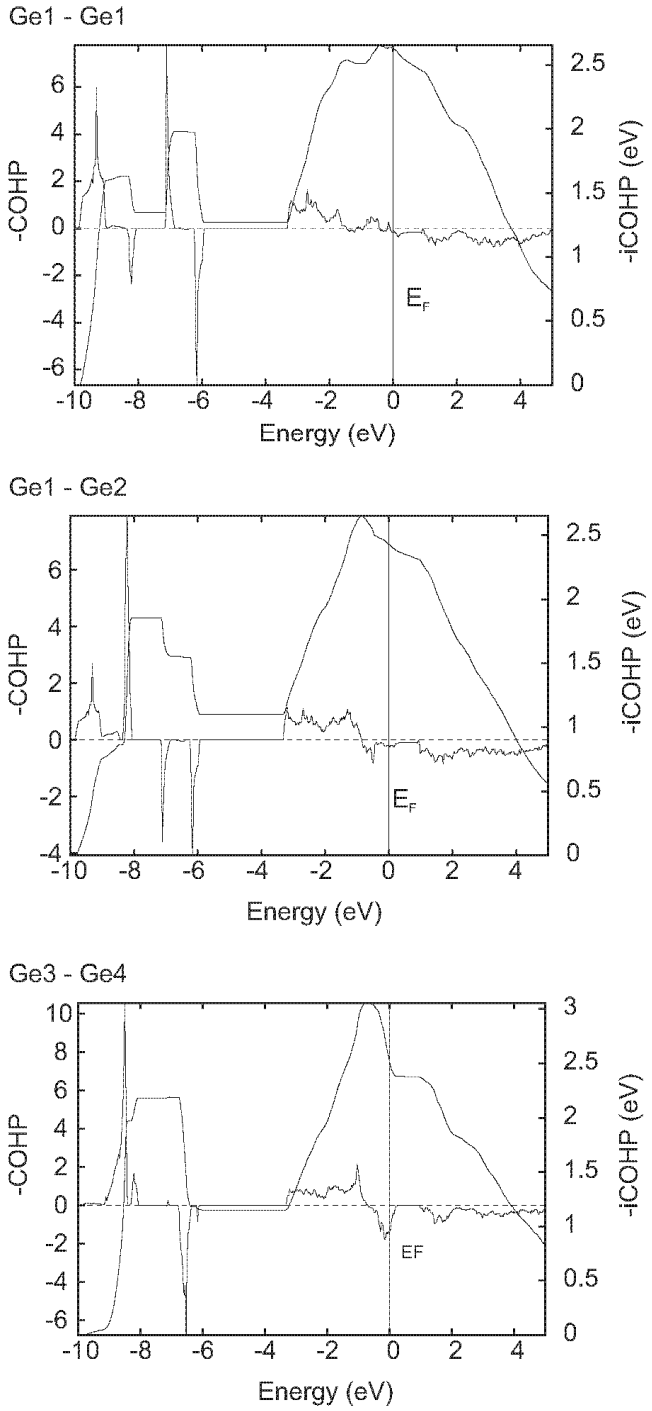

Figure S7 Crystal Orbital Hamilton Populations (COHP) and integrated Crystal Orbital Hamilton Populations (−iCOHP) curves for the Ge-Ge bonds in Ca_7Ge_6 (TB-LMTO-ASA).

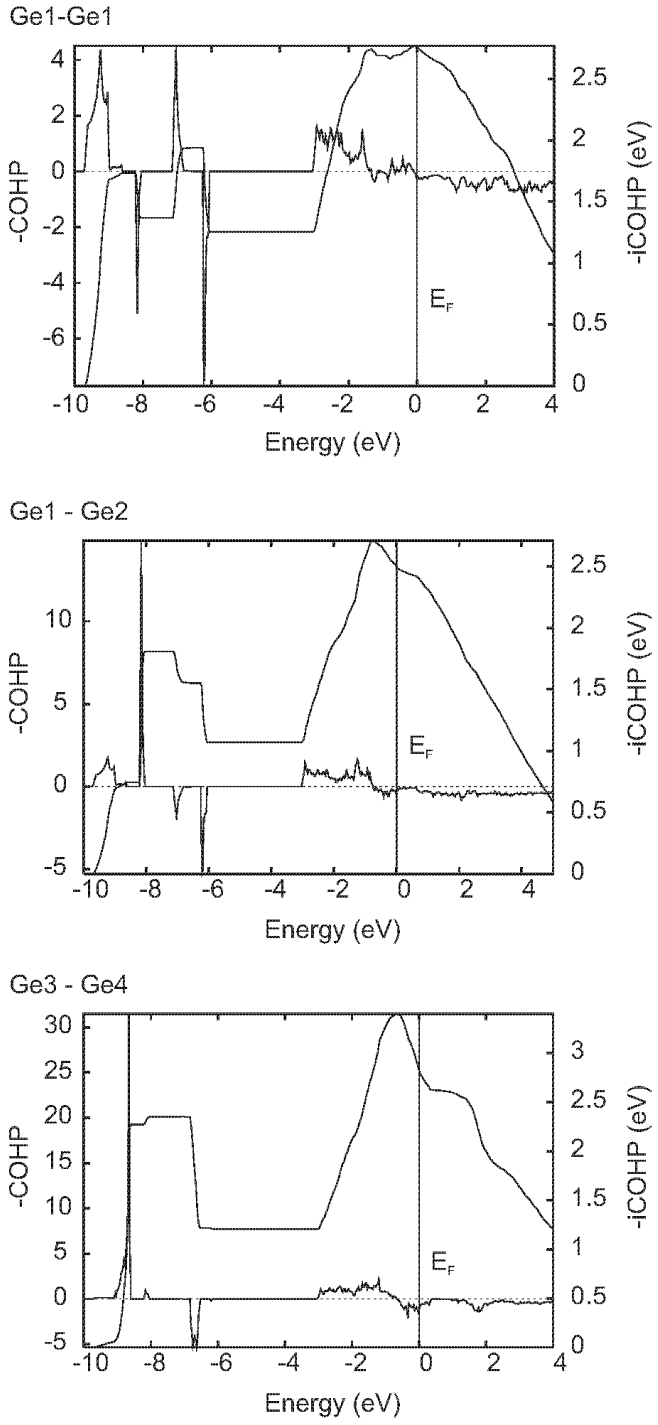

Figure S8 Crystal Orbital Hamilton Populations (COHP) and integrated Crystal Orbital Hamilton Populations (−iCOHP) curves for the Ge-Ge bonds in Sr_7Ge_6 (TB-LMTO-ASA).

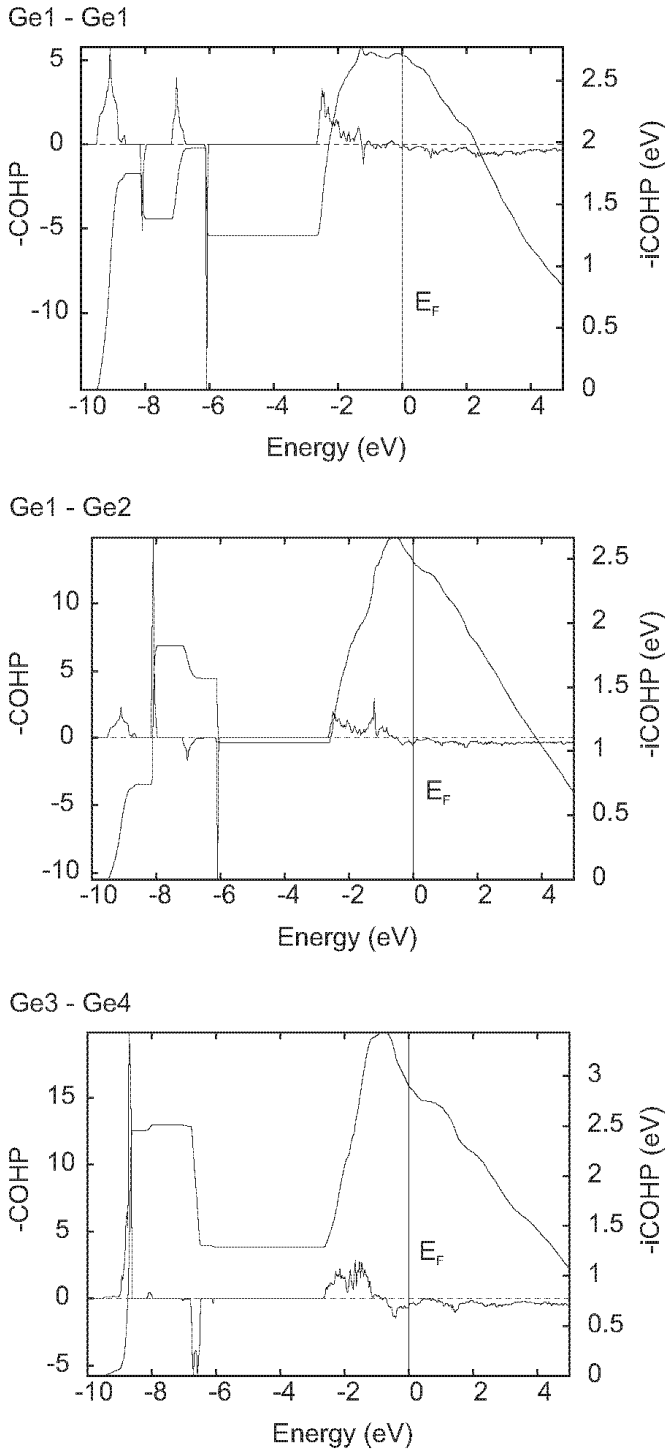

Figure S9 Crystal Orbital Hamilton Populations (COHP) and integrated Crystal Orbital Hamilton Populations (−iCOHP) curves for the Ge-Ge bonds in Ba_7Ge_6 (TB-LMTO-ASA).

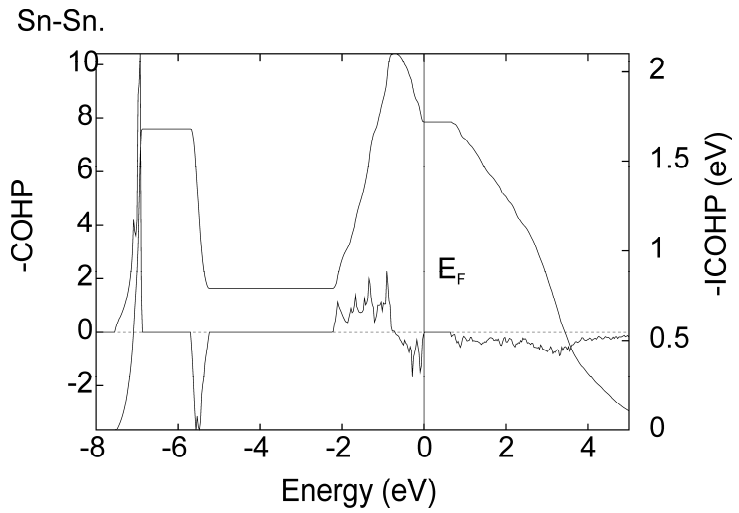

Figure S10 Crystal Orbital Hamilton Populations (COHP) and integrated Crystal Orbital Hamilton Populations (−iCOHP) curves for the Sn-Sn bond in Ba_3Sn_2 (TB-LMTO-ASA)

4.3 Polar Intermetallic Phases in the Systems *Ae*/Ni/Ge (*Ae*: Mg, Ca, Sr, Ba)

4.3.1 $BaNi_2Ge$ and $Ca_4Ni_4Ge_3$ – Two Layered Structures with $^2_\infty[Ni_2Ge]$ and $^2_\infty[Ni_4Ge_3]$ Networks

Published:

L. Siggelkow, V. Hlukhyy, T. F. Fässler, *Z. Anorg. Allg. Chem.* **2010**, *636*, 1870–1879.

Appendix

Table A1 Anisotropic displacement parameters (U_{ij} / Å^2) for $BaNi_2Ge$

Atom	U_{11}	U_{22}	U_{33}	U_{12}	U_{13}	U_{23}
Ba	0.0199(3)	0.0222(3)	0.0214(3)	0.00000	0.00000	0.00000
Ni	0.0118(4)	0.0141(4)	0.0236(4)	0.00000	0.0000(3)	0.00000
Ge	0.0116(4)	0.0132(4)	0.0245(5)	0.00000	0.00000	0.00000

Table A2 Anisotropic displacement parameters (U_{ij} / Å^2) for $Ca_4Ni_4Ge_3$

Atom	U_{11}	U_{22}	U_{33}	U_{12}	U_{13}	U_{23}
Ca1	0.0127(8)	0.0098(8)	0.0099(8)	0.00000	0.00000	0.00000
Ca2	0.0134(6)	0.0117(6)	0.0087(5)	0.00000	0.00000	-0.0006(4)
Ca3	0.0190(8)	0.0125(8)	0.0128(8)	0.00000	0.00000	0.0005(6)
Ni1	0.0090(4)	0.0128(4)	0.0068(4)	0.00000	0.00000	-0.0003(2)
Ni2	0.0100(4)	0.0115(4)	0.0087(4)	0.00000	0.00000	0.0016(3)
Ge1	0.0105(4)	0.0104(4)	0.0073(4)	0.00000	0.00000	0.00000
Ge2	0.0080(4)	0.0149(4)	0.0072(3)	0.00000	0.00000	0.0021(2)

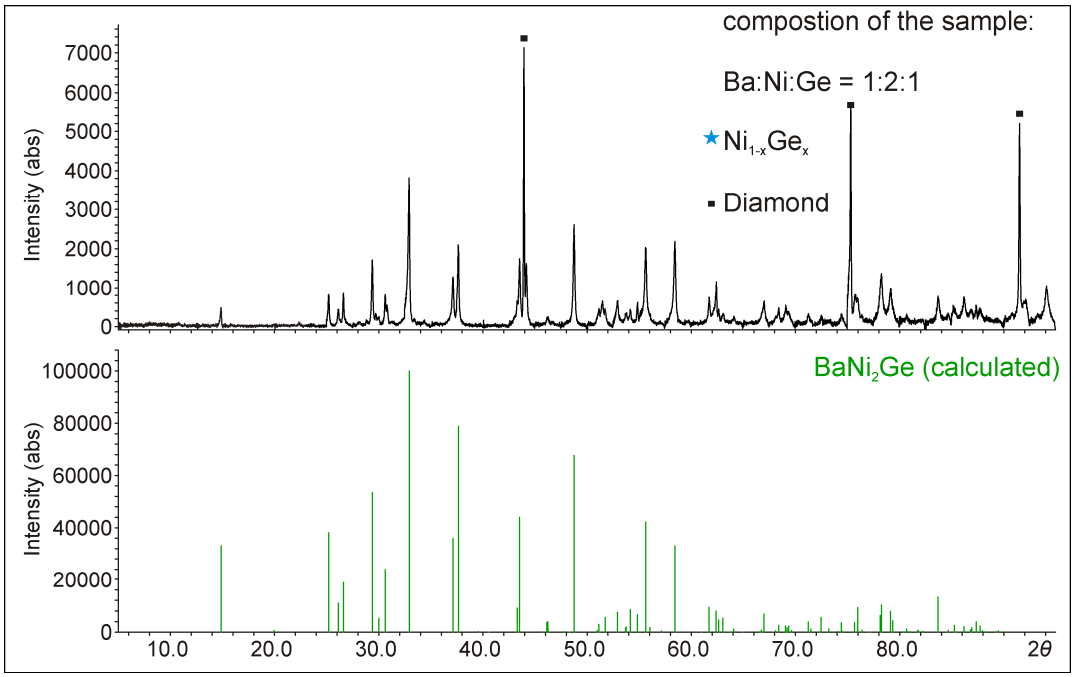

Figure A1 Experimental powder XRD pattern (top) from sample loading Ba : Ni : Ge = 1 : 2 : 1 and simulated powder XRD pattern (bottom) of $BaNi_2Ge$. The experimental powder XRD pattern was recorded in Debye Scherrer geometry and its background has been subtracted. Reflections of $Ni_{1-x}Ge_x$ and diamond are labelled with a blue star and a black square, respectively.

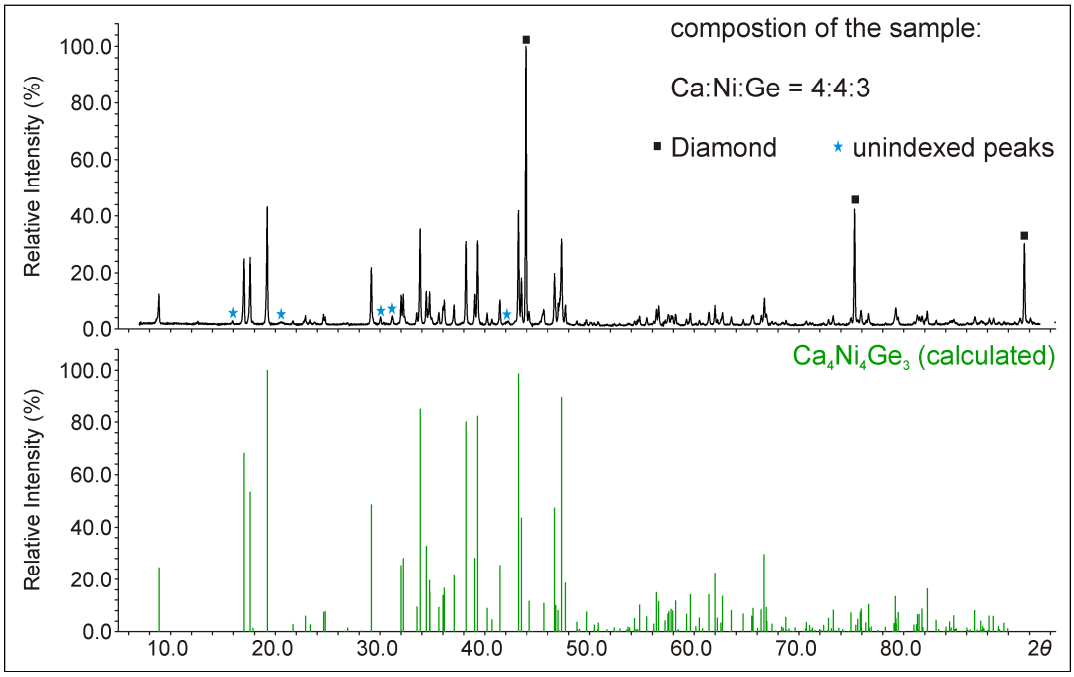

Figure A2 Experimental powder XRD pattern (top) from sample loading Ca : Ni : Ge = 4 : 4 : 3 and simulated powder XRD pattern (bottom) of $Ca_4Ni_4Ge_3$. The experimental powder XRD pattern was recorded in Debye Scherrer geometry and its background was subtracted. Reflections of diamond as well as unindexed reflections are labelled with a black squares and blue stars, respectively.

4.3.2 Synthesis, Structure and Chemical Bonding of $Ba_2Ni_5Ge_4$ – An Intermetallic Compound with a New Two-dimensional $^2_\infty[Ni_5Ge_4]$ Structural Motif

Published:

L. Siggelkow, V. Hlukhyy, T. F. Fässler, *Z. Anorg. Allg. Chem.* **2011**, *637*, 2000–2006.

4.3.3 Complex Intermetallic Compounds: $CaNi_5Ge_3$, $Ca_{15}Ni_{68}Ge_{37}$ and $Ca_7Ni_{49}Ge_{22}$ – Three Multifaceted Ni-Ge Framework Structures Combining the Structural Motifs of Ni_3Ge and $CaNi_2Ge_2$.

Published:

L. Siggelkow, V. Hlukhyy, B. Wahl, T. F. Fässler, *Eur. J. Inorg. Chem.* **2011**, 4012–4024.

Appendix

Table A1 Anisotropic displacement parameters (U_{ij} / Å^2) for $CaNi_5Ge_3$

Atom	U_{11}	U_{22}	U_{33}	U_{12}	U_{13}	U_{23}
Ge1	0.0139(2)	0.0139(2)	0.0128(4)	-0.0006(4)	0.00000	0.00000
Ge2	0.0085(4)	0.0085(4)	0.0131(8)	0.0003(2)	0.00000	0.00000
Ge3	0.0085(4)	0.0085(4)	0.0071(7)	0.00000	0.00000	0.00000
Ni1	0.0175(3)	0.0085(2)	0.0118(2)	-0.0010(2)	-0.0003(2)	0.0003(4)
Ni2	0.0092(6)	0.0092(6)	0.0115(14)	0.0000(5)	0.00000	0.00000
Ni3	0.0105(6)	0.0105(6)	0.008(2)	0.00000	0.00000	0.00000
Ca1	0.0091(3)	0.0091(3)	0.0133(6)	-0.001(1)	0.00000	0.00000

Table A2 Anisotropic displacement parameters (U_{ij} / Å^2) for $Ca_{15}Ni_{68}Ge_{37}$

Atom	U_{11}	U_{22}	U_{33}	U_{12}	U_{13}	U_{23}
Ca1	0.013(2)	0.014(2)	0.013(2)	0.006(2)	0.00000	0.00000
Ca2	0.015(2)	0.015(2)	0.013(2)	0.008(2)	0.00000	0.00000
Ca3	0.013(2)	0.009(2)	0.016(2)	0.0046(9)	0.00000	0.00000
Ca4	0.015(2)	0.015(2)	0.017(2)	0.007(1)	0.00000	0.00000
Ge1	0.0131(7)	0.0178(8)	0.0089(7)	0.0078(6)	0.00000	0.00000
Ge2	0.0168(8)	0.0142(7)	0.0137(7)	0.0082(7)	0.00000	0.00000
Ge3	0.0106(7)	0.0113(8)	0.0146(8)	0.0053(6)	0.00000	0.00000
Ge4	0.0133(8)	0.0104(7)	0.0090(7)	0.0068(6)	0.00000	0.00000
Ge5	0.0116(7)	0.0134(7)	0.0092(8)	0.0066(6)	0.00000	0.00000
Ge6	0.0095(7)	0.0107(9)	0.0112(9)	0.0054(5)	0.00000	0.00000
Ge7	0.0137(7)	0.0137(7)	0.012(2)	0.0061(9)	0.00000	0.00000
Ge8	0.013(2)	0.013(2)	0.021(2)	0.0063(6)	0.00000	0.00000
Ni1	0.016(1)	0.0153(9)	0.0096(9)	0.0072(8)	0.00000	0.00000
Ni2	0.018(1)	0.0160(9)	0.0105(9)	0.0090(8)	0.00000	0.00000
Ni3	0.019(1)	0.0163(9)	0.0114(9)	0.0112(7)	0.00000	0.00000
Ni4	0.018(1)	0.018(1)	0.0134(9)	0.0109(9)	0.00000	0.00000
Ni5	0.0127(9)	0.0145(9)	0.014(1)	0.0059(8)	0.00000	0.00000
Ni6	0.018(1)	0.0092(9)	0.017(2)	0.0071(8)	0.00000	0.00000
Ni7	0.0165(9)	0.0101(9)	0.0109(9)	0.0067(8)	0.00000	0.00000

Atom	U_{11}	U_{22}	U_{33}	U_{12}	U_{13}	U_{23}
Ni8	0.0159(9)	0.014(1)	0.015(1)	0.0092(7)	0.00000	0.00000
Ni9	0.0132(9)	0.0127(9)	0.016(2)	0.0068(7)	0.00000	0.00000
Ni10	0.014(1)	0.014(1)	0.015(2)	0.007(1)	0.00000	0.00000
Ni11	0.019(2)	0.019(2)	0.022(2)	0.015(2)	0.00000	0.00000
Ni12	0.016(2)	0.015(2)	0.018(2)	0.0077(7)	0.00000	0.00000
Ni13	0.015(1)	0.010(2)	0.019(2)	0.0047(6)	0.00000	0.00000
Ni14	0.0097(9)	0.0097(9)	0.024(2)	0.0049(5)	0.00000	0.00000

Table A3 Anisotropic displacement parameters (U_{ij} / Å^2) for $Ca_7Ni_{48.9(4)}Ge_{22.1(4)}$

Atom	U_{11}	U_{22}	U_{33}	U_{12}	U_{13}	U_{23}
Ge1	0.0267(9)	0.0267(9)	0.0163(9)	0.0103(8)	0.0040(5)	0.0040(5)
Ge2	0.0099(3)	0.0127(5)	0.0121(5)	0.0064(2)	0.00000	0.00000
Ge3	0.0100(3)	0.0093(4)	0.0106(4)	0.0046(2)	0.00000	0.00000
Ge4	0.0157(4)	0.0112(5)	0.0239(5)	0.0056(2)	0.00000	0.00000
Ni1	0.0267(9)	0.0267(9)	0.0163(9)	0.0103(8)	0.0040(5)	0.0040(5)
Ni2	0.0098(4)	0.0199(5)	0.0139(4)	0.0062(4)	0.00000	0.00000
Ni3	0.0094(4)	0.0109(4)	0.0250(5)	0.0054(4)	0.00000	0.00000
Ni4	0.0140(6)	0.0172(9)	0.030(1)	0.0086(4)	0.0001(4)	0.0002(7)
Ni5	0.0179(5)	0.0103(6)	0.0119(5)	0.0052(3)	0.00000	0.00000
Ni6	0.0111(4)	0.0082(5)	0.0130(5)	0.0041(3)	0.00000	0.00000
Ni7	0.0106(6)	0.0068(7)	0.0127(8)	0.0034(4)	0.00000	0.00000
Ni8	0.0095(6)	0.0095(6)	0.016(1)	0.0048(3)	0.00000	0.00000
Ca1	0.0098(6)	0.0130(8)	0.0122(8)	0.0065(4)	0.00000	0.00000
Ca2	0.010(2)	0.010(2)	0.022(4)	0.0052(8)	0.00000	0.00000

4.3.4 Laves Phases in the System Mg/Ni/Ge

Laves Phases in the System Mg/Ni/Ge

Lisa Siggelkow, Thomas F. Fässler

in preparation

Abstract

Two new Laves phases Mg_2Ni_3Ge and *hP*-$MgNi_{2-x}Ge_x$ (x = 0.70(6)) as well as the Laves phase *cF*-$MgNi_{2-\delta}Ge_\delta$, which was reported 50 years ago, were synthesized by direct reaction of the elements in alumina and tantalum crucibles using an induction furnace. The cell parameters and crystal structures were determined by single crystal X-ray diffraction.

cF-$MgNi_{2-\delta}Ge_\delta$ is observed for small values of δ. It crystallizes in the cubic $MgCu_2$ structure type with a solid solution of Ni and Ge. Mg_2Ni_3Ge crystallizes in the Y_2Rh_3Ge structure type, which is a superstructure of the cubic Laves phase $MgCu_2$. *hP*-$MgNi_{2-x}Ge_x$ (x = 0.70(6)) crystallizes as a superstructure of the hexagonal Laves phase $MgZn_2$, in which Ni/Ge mixed site occupancies occur.

Summarizing, starting with the binary Zintl phase $MgNi_2$ (C36) and gradually substituting Ni by Ge, thus rising the valence electron concentration (VEC), leads to the series of Laves phases C36 ($MgNi_2$ = $MgNi_{2-x}Ge_x$ with x = 0) → C15 (*cF*-$MgNi_{2-\delta}Ge_\delta$ with small values of δ) → superstructure of C15 (Mg_2Ni_3Ge = $MgNi_{2-x}Ge_x$ with x = 0.5) → superstructure of C14 (*hP*-$MgNi_{2-x}Ge_x$ = $MgNi_{2-x}Ge_x$ with x = 0.70(6)).

Keywords: Intermetallic compounds, Laves phases, Germanides

Introduction

Ever since their first description, Laves phases attracted the interest of the solid state community. They are the largest group of intermetallic compounds and their crystal structures appear at the first sight to be simple. Their composition is AB_2, A being the larger atom. The three primary Laves phase structure types are $MgCu_2$, $MgZn_2$ and $MgNi_2$, the corresponding *Strukturbericht* symbols are C15, C14 and C36. The three-dimensional networks of the atoms B are built up of vertex- and face-sharing tetrahedra. The centers of gravities of these B_4 tetrahedra as well as the Mg atoms themselves are arranged as the carbon atoms in cubic ($MgCu_2$) and hexagonal ($MgZn_2$) diamond. Further, the network of the B atoms can be described by stacking of atom layers, namely Kagomé nets (3.6.3.6.) and hexagonal nets (3^6). The B atoms of the 3^6 nets cap the triangular faces of the Kagomé nets such that the above mentioned B_4 tetrahedra result. Considering only the Kagomé nets, cubic stacking (ABC) leads to the crystal structure of $MgCu_2$, hexagonal stacking (AB) to the structure of $MgZn_2$ and a combination of these stacking sequences leads to the $MgNi_2$ structure type (ABAC). An extensive summary of these structure types and the various ways of description is given for example in [1, 2] and references therein.

Even though numerous factors controlling their phase stability – such as the ratio of atomic radii and the valence electron concentration of the involved elements – were discussed, the stability of the respective structures is not understood until today [3].

Contrasting this significant lack of understanding, a manifold variety of binary and ternary Laves phases has been described [4]. In addition to the intermetallic systems containing only one Laves phase polytype, a large number of binary and ternary intermetallic systems containing more than one Laves phase polytype is known.

For ternary Laves phases it is possible to differentiate between “true” ternary Laves phases, which are characterized by the fact that no corresponding binary Laves phase exists, and ternary Laves phases which result of the addition of a third element to a binary Laves phase. An example for a “true” ternary Laves phase is $Ta(Ni,Al)_2$ [5], i.e. $TaNi_2$ and $TaAl_2$ do not crystallize as a Laves phase. In contrast, mixing the two binary Laves phases $MgZn_2$ (C14) and $MgCo_2$ (C14) [6] leads for 20% to 60% Co on the position of the B atom to the C15 polytype [7]. Similarly, adding Al to $MgCu_2$ (C15) leads successively to the

C36 and the C14 polytypes [8]. Furthermore, long period stacking variations are reported in the system Mg/Cu/Al[9]. Intermetallic phases containing such long period stacking variations are called Komura phases [10]. Note that large homogeneity ranges, as observed in the examples given above, are typical for Laves phases.

Further, the above described ternary Laves phases exhibit mixed occupancies on the B position and no ordering takes place. Ordered ternary Laves phases, leading to superstructures of C15, C14 and C36, are rare but have been described. For example, Mg_2Cu_3Si crystallizes in the C14 polytype, the Cu atoms being situated on the Wyckoff position 6*h* (Kagomé net) and the Si atoms being situated on the Wyckoff position 2*a* (hexagonal 3^6 net) [11]. Mg_2Ni_3Si crystallizes in the Y_2Rh_3Ge structure type ([12], superstructure of C15), the Si atoms being situated on the Wyckoff position 3*b* (hexagonal 3^6 net) and the Ni atoms being situated on the Wyckoff position 9*e* (Kagomé net) [13].

In the system Mg/Ni/Ge various compounds were described: the Mg poor compound $MgNi_6Ge_6$ [14] crystallizes in the YCo_6Ge_6 structure type [14], which can be derived from the $CaCu_5$ structure type [15]. It contains Kagomé nets (3.6.3.6.) of Ni atoms which are stacked according to the primitive series AA. Ge atoms cap every triangle of the Ni atom layer. In the resulting hexagonal channel Mg and Ge atoms are positioned, each position being only half occupied. The phase $Mg_6Ni_{16}Ge_7$ [16] crystallizes in the $Mg_6Cu_{16}Si_7$ structure type [17, 18]. The Ni-Ge network is built up of Ni tetrahedra being capped by four further Ni atoms. The resulting Ni_8 polyhedra are capped by six Ge atoms which link these polyhedra to a three-dimensional network. The equiatomic polar intermetallic phase MgNiGe forms a three-dimensional network of four-fold connected Ni and Ge atoms [19]. The Mg rich compound Mg_3Ni_2Ge (Mn_3Ni_2Si structure type [20]) contains tetrahedra of Ni, each face being capped by a Ge atom. The fourfold capped tetrahedra are further connected via the Ge atoms to form a three-dimensional network [21]. For the three compounds $Mg_6Ni_{16}Ge_7$, MgNiGe and Mg_3Ni_2Ge the Mg atoms are situated in the cavities of the Ni-Ge networks. Summarizing, the polar intermetallic compounds described up to now in the system Mg/Ni/Ge consist of three-dimensional Ni-Ge networks. Such networks, in whose cavities the more electropositive alkaline earth metal are situated, are often discussed to be reminiscent of the polyanions observed in Zintl phases.

A binary Laves phase of the system Mg/Ni/Ge is $MgNi_2$, which crystallizes in its own structure type with the *Strukturbericht* symbol C36. Adding Ge to this binary phase leads to the ternary Laves phase $MgNi_{2-x}Ge_x$ (x = 0.4), which crystallizes in the $MgCu_2$

structure type (C15) and was reported almost 50 years ago [22]. This phase will be named *cF*-$MgNi_{2-\delta}Ge_{\delta}$ in the following. Our studies in the system Mg/Ni/Ge led to two further Laves phases, namely Mg_2Ni_3Ge ($MgNi_{2-x}Ge_x$ (x = 0.50), which crystallizes in the Y_2Rh_3Ge structure type, and *hP*-$MgNi_{2-x}Ge_x$ (x = 0.70(6)), which crystallizes in a superstructure of the $MgZn_2$ structure type (C14). The synthesis and crystal structures of these Laves phases will be described in the following.

Experimental Section

Syntheses

The starting materials for the synthesis of the Laves phases of the system Mg/Ni/Ge were commercially available elements of high purity: magnesium (ChemPur, 99.5%), nickel powder (Acros, 99.9%) and germanium pieces (ChemPur, 99.999%).

In a first attempt, the air stable compounds Mg_2Ni_3Ge and *hP*-$MgNi_{2-x}Ge_x$ were synthesized by reaction of the elements in welded tantalum ampoules, using overall amounts of 0.7 g of the elements. The tantalum ampoules were charged with the elements and welded shut with a tantalum lid (Mini Arc Melting System, MAM-1, Johanna Otto GmbH, placed in an argon filled glove box). These tantalum ampoules were then placed in a water-cooled sample chamber of an induction furnace (Hüttinger Elektronik, Freiburg, Typ TIG 2.5/300) and were heated under flowing argon up to approximately 950 °C for half an hour. After this melting procedure the samples were cooled within half an hour to approximately 800 °C and finally cooled down to room temperature in about one minute by switching off the furnace.

In detail, the reaction of the elements in the ratio Mg : Ni : Ge = 45 : 40 : 15 in a welded tantalum ampoule led to a mixture of Mg_2Ni_3Ge, Mg_3Ni_2Ge and Mg_2Ge [23]. The reaction of the elements in the ratio Mg : Ni : Ge = 2 : 2 : 1 led to a mixture of *hP*-$MgNi_{2-x}Ge_x$ (x = 0.70(6)), Mg_2Ni_3Ge, Mg_3Ni_2Ge and Mg_2Ge. The mixture of the elements in the ratio Mg : Ni : Ge = 6 : 11 : 1 led to a mixture of *cF*-$MgNi_{2-\delta}Ge_{\delta}$ as well as Mg_2Ni [24] and $MgNi_2$ [25].

After cooling these samples to room temperature the sample exhibited metallic lustre. Single crystals of Mg_2Ni_3Ge, *hP*-$MgNi_{2-x}Ge_x$ (x = 0.70(6)) and *cF*-$MgNi_{2-\delta}Ge_{\delta}$ were

isolated from the crushed samples. However, a semi-quantitative EDX analysis of the single crystals revealed the presence of about 3(1)% tantalum in the samples.

Therefore, the synthesis was repeated using alumina crucibles. In order to avoid the evaporation of magnesium, the alumina crucible containing the elements was enclosed into a welded niobium ampoule. These were placed in the water-cooled chamber of the induction furnace and the heat treatment was repeated as described above. Again, the samples exhibited metallic lustre and single crystals were successfully isolated.

In detail, the reaction of the elements in the ratio Mg : Ni : Ge = 2 : 1 : 1 lead to a mixture of the compounds *hP*-$MgNi_{2-x}Ge_x$ ($x = 0.70(6)$), Mg_2Ni_3Ge, Mg_3Ni_2Ge and Mg_2Ge.

Single Crystal X-ray Diffraction Studies and Structure Refinement

Air stable crystals of Mg_2Ni_3Ge, *hP*-$MgNi_{2-x}Ge_x$ as well as a *cF*-$MgNi_{2-\delta}Ge_\delta$ were fixed on the tip of a glass fiber with nail polish under normal atmosphere. Note that the crystal of *cF*-$MgNi_{2-\delta}Ge_\delta$ was obtained from a sample synthesized in a tantalum crucible. Single crystal X-ray diffraction intensity data were collected at room temperature using a Oxford Diffraction Xcalibur3 diffractometer with a Sapphire 3 CCD detector using graphite monochromatized MoK_α (λ = 0.71073 Å) radiation for Mg_2Ni_3Ge and *cF*-$MgNi_{2-\delta}Ge_\delta$. The data were processed using the Oxford CrysAlis RED software including an empirical absorption correction with ABSPACK [26]. For *hP*-$MgNi_{2-x}Ge_x$ a Bruker APEX-II with CCD detector with graphite monochromatized MoK_α ($\lambda = 0.71073$ Å) radiation was used and the data was processed using the Bruker software SAINT and SADABS including an empirical absorption correction [27]. All raw data were corrected for background, polarization and Lorentz factor.

The atomic position parameters were deduced from an automatic interpretation of direct methods with SHELXS-97 [28]. The structures were refined using SHELXL-97 (full-matrix least-squares on F_o^2) [29] with anisotropic atomic displacement parameters for all atoms. As a check for the correct composition, the occupancy parameters were refined in a separate series of least-squares cycles. All relevant crystallographic data for the data collection and evaluation are listed in Table 1. The positional parameters and selected interatomic distances are listed in Tables 2 and 3. The anisotropic displacement parameters are given in the supporting information (Table S1 to S3).

For Mg_2Ni_3Ge, which was synthesized in an alumina crucible, all sites were fully occupied. Free refinement of the occupancy factors for the different sites led to values of 1.00(2) for Mg, 1.01(1) for Ni and 0.99(1) for Ge.

For *cF*-$MgNi_{2-\delta}Ge_\delta$ as well as *hP*-$MgNi_{2-x}Ge_x$ mixed occupancies for all Ni and Ge are observed. For the refinement of the mixed occupancies, positions and atomic displacement parameters (ADPs) for Ni and Ge were set to be equal at the respective atom sites. Particular free variables with an overall occupancy of 1 were applied to determine the occupation ratio at these positions. For both compounds *cF*-$MgNi_{2-x}Ge_x$ as well as *hP*-$MgNi_{2-x}Ge_x$ a high correlation between the occupancy parameters, the overall scale factor and the atomic displacement parameters was observed. Therefore, the obtained values for δ and x have to be questioned carefully.

For *cF*-$MgNi_{2-\delta}Ge_\delta$ synthesized in a tantalum ampoule the variable δ was chosen in order to emphasize that the existence of Ge on the B positions cannot be shown crystallographically and is merely assumed due to the results of the semi-quantitative EDX analysis. Free refinement of δ for *cF*-$MgNi_{2-\delta}Ge_\delta$ led to $\delta = 0.02(17)$, which is even significantly smaller than the error margin. However, this indicates, that already small amounts of Ge added to $MgNi_2$ (C36) lead to *cF*-$MgNi_{2-\delta}Ge_\delta$, which crystallizes in the $MgCu_2$ structure type (C15), with a solid solution of Ni and Ge as described in [22].

For *hP*-$MgNi_{2-x}Ge_x$ ($x = 0.70(6)$) synthesized in an alumina crucible the indexing of the data led to the space group $P6_3/mcm$ parameters and the unit cell a = 8.6946(2) Å, c = 7.8127(3) Å). The refinement led to a superstructure of $MgZn_2$ with Ni/Ge mixed site occupancies on the Wyckoff positions 12*j* (73(2) % Ni), 6*g* (73(3) % Ni), 4*d* (46(3) % Ni) and 2*b* (34(5) % Ni) and Mg on the Wyckoff position 12*k*. Overall, the refinement led to $x = 0.70(6)$.

Powder X-ray Diffraction Studies

The purity of the sample was checked using a STOE STADI P powder diffractometer using Ge monochromatized CuK_α (λ = 1.54056 Å) radiation. Data were recorded at room temperature within the 2θ range of 5 - 95° from a sample prepared in a glass capillary (0.3 mm diameter). The analysis of the powder X-ray diffraction data was carried out using the program package WinXPOW [30]. The corresponding powder X-ray diffraction patterns are given in the supporting information (Figure S1 and Figure S2).

The powder X-ray diffraction data allows to differ between the cubic Laves phase *cF*-$MgNi_{2-\delta}Ge_{\delta}$ and the ordered superstructure Mg_2Ni_3Ge. However, due to the quality of the data no distinction between the hexagonal Laves phase *hP*-$MgNi_{2-x}Ge_x$ and a hypothetical solid solution of the $MgZn_2$ structure type, crystallizing in the hexagonal space group $P6_3/mmc$, is possible.

EDX Measurement

After X-ray diffraction measurements the single crystals were analyzed with a JEOL SEM 5900LV scanning electron microscope equipped with an Oxford Instruments INCA energy dispersive X-ray microanalysis system. A qualitative EDX analysis of well-shaped single crystals confirmed the presence of Mg, Ni and Ge. The semi-quantitative EDX analysis of all samples synthesised using tantalum ampoules revealed the presence of about 3(1) % Ta. A semi-quantitative EDX analysis concerning the Ni/Ge ratio confirmed the ratios observed by single crystal X-ray diffraction: For the cubic phase *cF*-$MgNi_{2-\delta}Ge_{\delta}$ a Ni/Ge ratio of 10(3) was obtained. For Mg_2Ni_3Ge a Ni/Ge ratio of 2.9(7) (calculated: 3) and for the Ge richtest phase *hP*-$MgNi_{2-x}Ge_x$ (x = 0.70(6)) a Ni/Ge ratio of 2.3(4) (calculated: 1.9) were obtained.

Table 1 Crystal data and structure refinement for *cF*-$MgNi_{2-\delta}Ge_{\delta}$, Mg_2Ni_3Ge and *hP*-$MgNi_{2-x}Ge_x$ ($x = 0.70(6)$).

Empirical formula	***cF*-$MgNi_{2-\delta}Ge_{\delta}$**	**Mg_2Ni_3Ge**	***hP*-$MgNi_{2-x}Ge_x$ ($x = 0.70(6)$)**
Formula weight	142.03 g/mol	297.34 g/mol	151.45 g/mol
Space group, Z	$Fd\bar{3}m$, $Z = 8$	$R\bar{3}m$, $Z = 3$	$P6_3/mcm$, $Z = 12$
Unit cell dimensions	$a = 6.8774(2)$ Å $V = 325.292(16)$ Å^3	$a = 5.107(4)$ Å $c = 11.45(2)$ Å $V = 258.6(4)$ Å^3	$a = 8.6946(2)$ Å $c = 7.8127(3)$ Å $V = 511.48(3)$ Å^3
Calculated density	5.800 g/cm^3	5.728 g/cm^3	5.900 g/cm^3
Absorption coefficient	23.031 mm^{-1}	24.851 mm^{-1}	26.445 mm^{-1}
$F(000)$	545	420	850
Crystal size	0.04 × 0.06 × 0.06 mm^3	0.02 × 0.04 × 0.04 mm^3	0.06 × 0.06 × 0.02 mm^3
θ range	5.1 ° to 32.5°	5° to 26°	2.7° to 48°
Range in *hkl*	±10, −10 < k < 8, ±10	−6 < h < 5, ±6, ±13	±18, ±18, −15 < l < 16
Reflections collected	1377	496	36783
Independent reflections	43 ($R_{int} = 0.075$)	79 ($R_{int} = 0.036$)	929 ($R_{int} = 0.032$)
Reflections with $I \geq 2\sigma(I)$	39 ($R_{sigma} = 0.020$)	76 ($R_{sigma} = 0.020$)	370 ($R_{sigma} = 0.008$)
Data/parameters	43 / 6	79 / 11	929 / 26
GOF on F^2	0.804	1.202	1.021
Final R indices [$I > 2\sigma(I)$]	$R_1 = 0.021$ $wR_2 = 0.056$	$R_1 = 0.015$ $wR_2 = 0.037$	$R_1 = 0.022$ $wR_2 = 0.039$
R indices (all data)	$R_1 = 0.034$ $wR_2 = 0.086$	$R_1 = 0.015$ $wR_2 = 0.037$	$R_1 = 0.043$ $wR_2 = 0.048$
Extinction coefficient	0.008(3)	0.047(3)	0.001(1)
Largest diff. peak and hole	1.10 / –1.23 e/Å^3	0.45 / –0.36 e/Å^3	0.94 / –1.13 e/Å^3

Table 2 Atomic coordinates and equivalent isotropic displacement parameters U_{eq} (Å^2 × 10^3) for *cF*-$MgNi_{2-\delta}Ge_{\delta}$ (space group $Fd\bar{3}m$), Mg_2Ni_3Ge (space group $R\bar{3}m$) and *hP*-$MgNi_{2-x}Ge_x$ (x = 0.70(6)) (space group $P6_3/mmc$)

Atom	Wyckoff position	Occupancy ≠ 1	*x*	*y*	*z*	U_{eq} (Å^2) × 10^3
***cF*-$MgNi_{2-\delta}Ge_{\delta}$**						
Mg	8*b*		3/8	3/8	3/8	17(2)
Ni	16*c*	0.98(17)	0	0	0	13(1)
Ge	16*c*	0.02(17)	0	0	0	13(1)
Mg_2Ni_3Ge						
Mg	6*c*		2/3	1/3	0.9581(2)	12(1)
Ni	9*d*		1/3	1/6	1/6	10(1)
Ge	3*a*		0	0	0	10(1)
***hP*-$MgNi_{2-x}Ge_x$ (x = 0.70(6))**						
Mg	12*k*		0	0.6665(3)	0.9359(2)	11(1)
Ni1	12*j*	0.73(2)	0.16106(8)	0.6667(2)	¼	10(1)
Ge1	12*j*	0.27(2)	0.16106(8)	0.6667(2)	¼	10(1)
Ni2	6*g*	0.73(3)	0	0.8275(2)	¼	10(1)
Ge2	6*g*	0.27(3)	0	0.8275(2)	¼	10(1)
Ni3	4*d*	0.46(3)	1/3	2/3	½	10(1)
Ge3	4*d*	0.54(3)	1/3	2/3	½	10(1)
Ni4	2*b*	0.34(5)	0	0	½	11(1)
Ge4	2*b*	0.66(5)	0	0	½	11(1)

Table 3 Interatomic distances (Å) calculated with the lattice parameters, taken from X-ray diffraction single crystal data.

		distance(Å)			distance(Å)
***cF*-$MgNi_{2-\delta}Ge_{\delta}$**					
Mg	Ni/Ge	2.8512(1) (12×)	Ni/Ge	Ni/Ge	2.4315(1) (6×)
	Mg	2.978(1) (4×)			
Mg_2Ni_3Ge					
Mg	Ni	2.806(4) (3×)	Ni	Ge	2.411(3) (2×)
	Mg	2.857(6) (1×)		Ni	2.553(2) (4×)
	Ni	2.926(3) (6×)			
	Ge	2.987(3) (3×)			
	Mg	2.987(3) (3×)			
***hP*-$MgNi_{2-x}Ge_x$ (x = 0.70(6))**					
Mg	Ni1/Ge1	2.825(2) (2×)	Ni1/Ge1	Ni2/Ge2	2.4238(7) (1×)
	Ni1/Ge1	2.826(2) (1×)		Ni1/Ge1	2.426(2) (1×)
	Ni1/Ge1	2.899(3) (4×)		Ni3/Ge3	2.4615(3) (2×)
	Ni2/Ge2	2.901(2) (2×)		Ni1/Ge1	2.5946(9) (2×)
	Mg	2.904(2) (1×)			
	Ni3/Ge3	2.941(2) (2×)	Ni2/Ge2	Ni4/Ge4	2.4624(6) (2×)
	Ni4/Ge4	2.943(3) (1×)		Ni2/Ge2	2.597(2) (2×)
	Mg	3.064(5) (3×)			

Results and Discussion

Crystal Structure of cF-$MgNi_{2-\delta}Ge_{\delta}$ (C15)

cF-$MgNi_{2-\delta}Ge_{\delta}$ crystallizes in the $MgCu_2$ structure type with the space group $Fd\bar{3}m$ and the unit cell parameter a = 6.8774(2) Å. The presence of Ge is not shown crystallographically. However, the presence of Ge is shown by EDX and thus a mixed occupancy of Ni and Ge is assumed on the Wyckoff position 16*c*. The presence of Ge indicates, that already the addition of small amounts of Ge to the Laves phas $MgNi_2$ (C36) leads to a cubic Laves phase C15 with Ni/Ge mixed site occupancy on the Wyckoff position 16*c*.

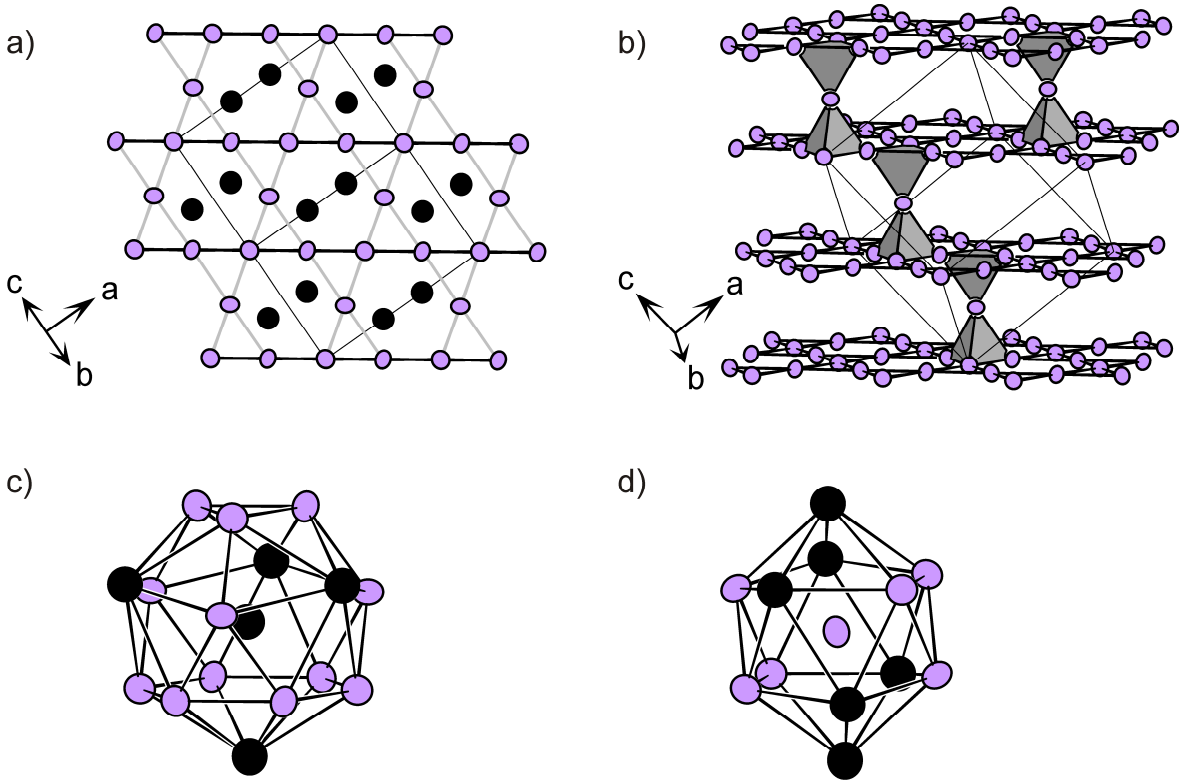

Figure 1 Crystal structure of *cF*-$MgNi_{2-x}Ge_x$ (x = 0.02(17)). (a) and (b) Ni/Ge network of vertex-sharing tetrahedra, emphasizing the bonds within the Kagomé nets (black) as well as the bonds towards the capping Ni/Ge atoms (grey). (c) coordination polyhedron of Mg. (d) coordination polyhedron of Ni/Ge. The Mg and Ni/Ge atoms are drawn in black and purple, respectively. The displacement ellipsoids are drawn with 95 % probability level.

The crystal structure of *cF*-$MgNi_{2-\delta}Ge_\delta$ is shown in Figure 1 and was described for $MgCu_2$ thoroughly elsewhere (e.g. [1] and references therein). It consists of a three-dimensional network of vertex-sharing tetrahedra of Ni/Ge atoms. In the cavities of this network the Mg atoms are situated. Both, the Mg atoms as well as the centers of gravity of the Ni/Ge tetrahedra are arranged as the C atoms in cubic diamond.

Further, the three-dimensional Ni/Ge network can be described as being built up of two atom layers: a Kagomé net (3.6.3.6.) and a hexagonal net (3^6). The block consisting of both layers is stacked according to a cubic stacking ABC. The Ni/Ge atoms of the hexagonal net cap the trigonal faces of the Kagomé net such that vertex sharing tetrahedra of Ni/Ge result. The edges of the tetrahedra are constant (d(Ni/Ge-Ni/Ge) = 2.4315(1) Å).

In Figure 1c and 1d the coordination polyhedra of Mg and Ni/Ge are given. For Mg a Frank-Kasper polyhedron with CN = 16 (4 Mg + 12 Ni/Ge) is found. The coordination polyhedron of Ni/Ge is a distorted icosahedron, i.e. CN = 12 (6 Mg + 6 Ni/Ge).

Crystal Structure of Mg_2Ni_3Ge

Mg_2Ni_3Ge crystallizes in the Y_2Rh_3Ge structure type [12], which is a superstructure of the cubic Laves phase $MgCu_2$ (C15). The space group is $R\bar{3}m$, with the unit cell parameters a = 5.107(4) Å and c = 11.45(2) Å. Its crystal structure is shown in Figure 2. The Ni atoms are situated on the Wyckoff positions 9*e* and build up the Kagomé nets (3.6.3.6.). The triangular faces of the Kagomé nets are capped alternately below and above by Ge atoms (Wyckoff position 3*b*), which themselves form hexagonal nets (3^6). Within the Kagomé net the Ni-Ni distances are constant (d(Ni-Ni) = 2.553(2) Å). The Ni-Ge distances between the Ge atoms of the 3^6 and the Kagomé nets are significantly shorter (d(Ni-Ge) = 2.441(3) Å). Therefore, the resulting Ni_3Ge tetrahedra are distorted. However, the arrangement of the tetrahedra remains unchanged in comparison to $MgCu_2$.

In Figure 2c – 2e the coordination polyhedra of Mg, Ni and Ge are given. The Frank-Kasper polyhedron obtained for Mg contains 4 × Mg, 9 × Ni and 3 × Ge (CN = 16). The distorted icosahedron obtained for Ni contains 6 × Mg, 4 × Ni and 2 × Ge (CN = 12) and the distorted icosahedron of Ge contains 6 × Mg and 6 × Ni (CN = 12).

In Figure 3 the group-subgroup relationship between $MgCu_2$ and Mg_2Ni_3Ge is shown, using a compact graphical representation as introduced by *Bärnighausen* [31, 32]. Starting from the $MgCu_2$ structure type a *translationengleiche* transition of index 4 (*t*4) leads to the structure of Mg_2Ni_3Ge with the space group $R\bar{3}m$. The Wyckoff position of the Mg atoms is changed from 8*b* to 6*c*. The site symmetry is reduced, but no splitting takes place. In contrast, the Wyckoff position 16*c* of the Cu atoms is split into two symmetry independent positions 9*e* (Ni) and 3*b* (Ge). Thus, an ordered superstructure of the cubic C15 Laves phase is formed here.

Furthermore, the title phase Mg_2Ni_3Ge can be described as an ordered variant of the rhombohedral Laves phase $TbFe_2$ [33]. The $TbFe_2$ structure type derives from $MgCu_2$ by slight distortion. The space group is $R\bar{3}m$, with the unit cell parameters a = 5.18 Å and c = 12.79 Å and the Wyckoff positions 6*c* (Tb), 9*e* (Fe1) and 3*b* (Fe2). Thus, replacing Tb by Mg, Fe1 by Ni and Fe2 by Ge leads to the crystal structure of Mg_2Ni_3Ge.

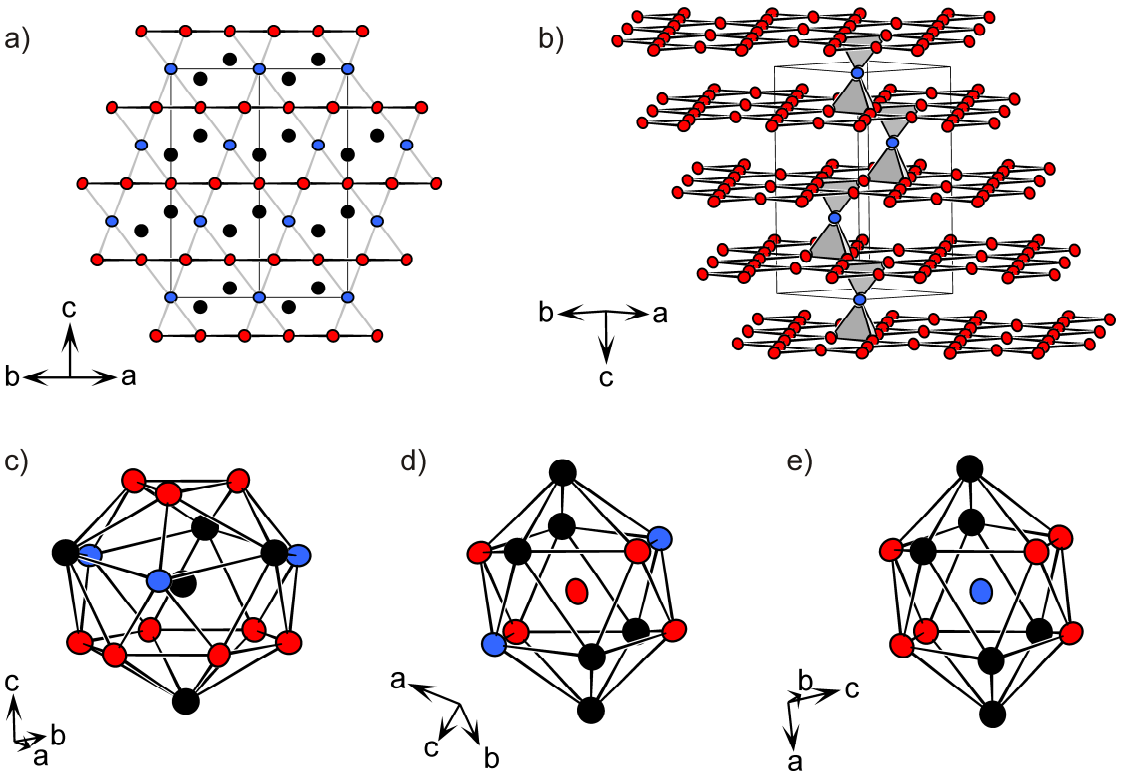

Figure 2 Crystal structure of Mg_2Ni_3Ge. (a) and (b) $^{3}_{\infty}[Ni_3Ge]$ network of vertex-sharing tetrahedra, emphasizing the bonds within Ni atoms of the Kagomé nets (black) as well as the bonds towards the capping Ge atoms (grey). (c) coordination polyhedron of Mg. (d) coordination polyhedron of Ni. (e) coordination polyhedron of Ge. The Mg, Ni and Ge atoms are drawn in black, red and blue, respectively. The displacement ellipsoids are drawn with 95 % probability level.

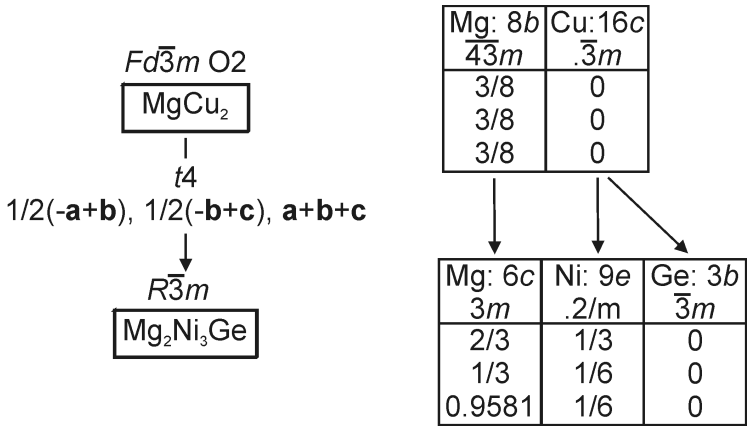

Figure 3 Group-subgroup relationship of $MgCu_2$ and Mg_2Ni_3Ge. The index for the *translationengleiche* (*t*) transition as well as the unit cell transformation is given.

Crystal Structure of hP-$MgNi_{2-x}Ge_x$ (x = 0.70(6))

The hexagonal Laves phase *hP*-$MgNi_{2-x}Ge_x$ (x = 0.70(6)) crystallizes in an own structure type with the space group $P6_3/mcm$ and the unit cell parameters a = 8.6946(2) Å and c = 7.8127(3) Å. The crystal structure is a superstructure of the hexagonal Laves phase $MgZn_2$ and is presented in Figure 4. The three-dimensional Ni-Ge network can be described as being built up of vertex- and face-sharing tetrahedra of Ni/Ge atoms. In the cavities of this network the Mg atoms are situated. Both, the Mg atoms as well as the centers of gravity of the Ni/Ge tetrahedra are arranged as the C atoms in hexagonal lonsdaleit, thus the arrangement of the Ni/Ge tetrahedra remains unchanged in comparison to the $MgZn_2$ structure type. Further, the network contains Kagomé (3.6.3.6.) as well as hexagonal nets (3^6). A hexagonal stacking sequence AB of the Kagomé nets leads to the hexagonal Laves phase C14. The Ni/Ge atoms of the hexagonal net cap the trigonal faces of the Kagomé net such that vertex- and face-sharing tetrahedra of Ni/Ge result.

The Kagomé as well as the hexagonal nets are shown in detail in Figure 4c and 4d. The structure solution of the single crystal intensity data from X-ray diffraction led to Ni/Ge mixed site occupancies on the four Wyckoff positions 12*j*, 6*g*, 4*d* and 2*b*. Both positions of the Kagomé net (Ni1/Ge1 on 12*j* and Ni2/Ge2 on 6*g*) are occupied with 73(3)% Ni and hence are indistinguishable. In contrast, the positions of the hexagonal net (Ni3/Ge3 on 4*d* and Ni4/Ge4 on 2*b*) are occupied with 46(3)% and 34(5)% Ni, respectively. A comparable preferential site occupation, in which the minority compound preferably occupies the positions of the 3^6 nets, is also observed for example in the case of $TiFe_{2-x}Al_x$ [34] and $NbCr_{2-x}Co_x$ [35]. Concerning the title compound *hP*-$MgNi_{2-x}Ge_x$ (x = 0.70(6)), the question needs to be raised, whether another strategy concerning the synthesis might lead to a more pronounced ordering on the different positions.

The Ni/Ge-Ni/Ge distances within the Kagomé net vary between 2.42 Å and 2.60 Å. The longer distances (d(Ni1/Ge1-Ni1/Ge1) = 2.595(1) Å and d(Ni2/Ge2-Ni2/Ge2) = 2.597(2) Å) correspond to the triangular faces of the Kagomé net which are capped by further Ni/Ge atoms of the 3^6 hexagonal net. The shorter distances (d(Ni1/Ge1-Ni2/Ge2) = 2.424(1) Å and d(Ni1/Ge1-Ni1/Ge1) = 2.426(2) Å) correspond to the Ni/Ge-Ni/Ge bonds between the capped triangular faces. The Ni/Ge-Ni/Ge distances between the Kagomé net and the capping atoms are slightly longer

(d(Ni1/Ge1-Ni3/Ge3) = 2.4615(3) Å and d(Ni2/Ge2-Ni4/Ge4) = 2.4624(6) Å) than the Ni/Ge-Ni/Ge bonds of the capped triangular faces within the Kagomé net.

In Figure 5 the coordination polyhedra of Mg and Ni/Ge are given. For Mg a Frank-Kasper polyhedron with CN = 16 (4 Mg + 12 Ni/Ge) is found. The coordination polyhedra of the Ni/Ge atoms are distorted icosahedra, i.e. CN = 12 (6 Mg + 6 Ni/Ge). The arrangement of the Ni/Ge and Mg atoms within the polyhedron is similar for Ni1/Ge1 and Ni2/Ge2 as well as for Ni3/Ge3 and Ni4/Ge4.

In Figure 6 the group-subgroup relationship between $MgZn_2$ and hP-$MgNi_{2-x}Ge_x$ (x = 0.70(6)) is discussed. Starting from the $MgZn_2$ structure type a *klassengleiche* transition of index 3 (k3) leads to the structure of hP-$MgNi_{2-x}Ge_x$ with the space group $P6_3/mcm$. The Wyckoff position of the Mg atoms is changed from 4f to 12k, a reduction of the site symmetry but no splitting takes place. In contrast, the Wyckoff position of the Zn1 atoms 6h is split into two positions of independent site symmetry 12j (Ni1/Ge1) and 6g (Ni2/Ge2). Similarly, the Wyckoff position of the Zn2 atoms (2a) is split to 4d (Ni3/Ge3) and 2b (Ni4/Ge4).

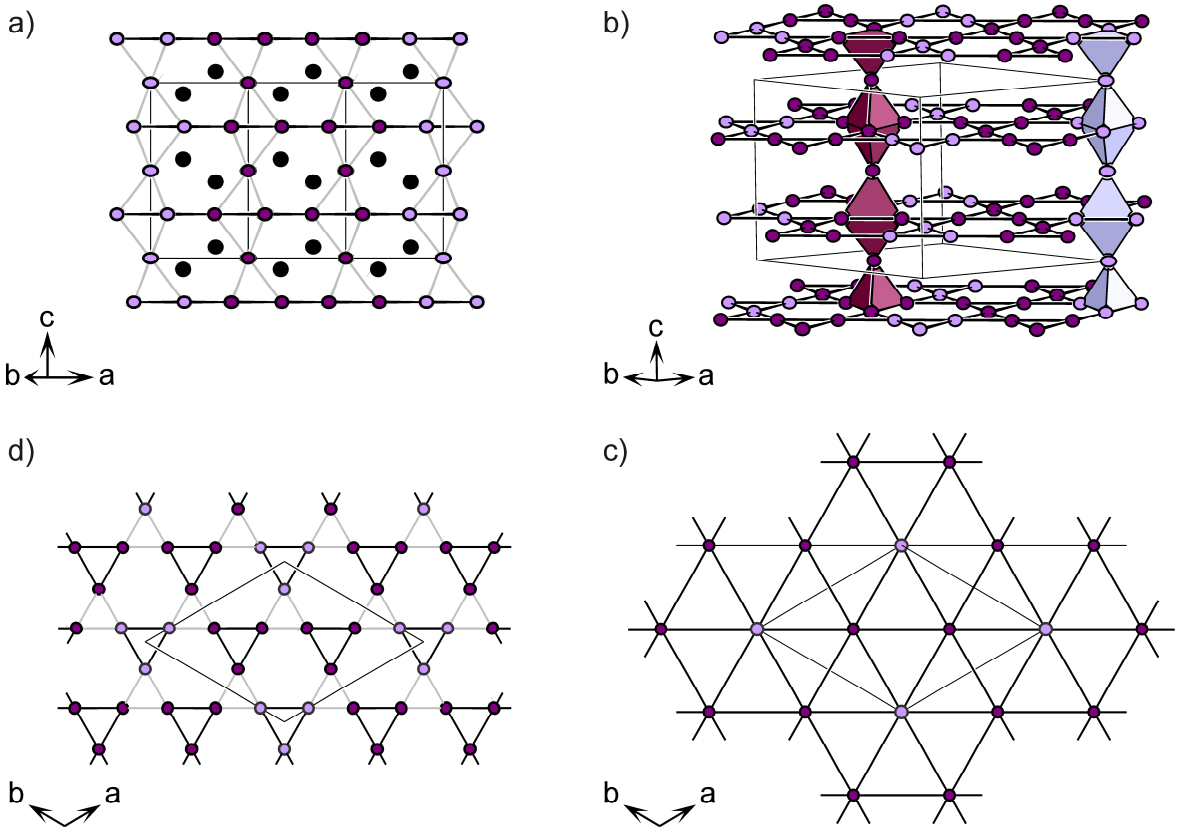

Figure 4 Crystal structure of *hP*-$MgNi_{2-x}Ge_x$ (x = 0.70(6)). (a) and (b) $^{3}_{\infty}[Ni_3Ge]$ network of vertex- and face-sharing tetrahedra, emphasizing the bonds within the Kagomé nets (black) as well as the bonds towards the capping Ni/Ge atoms (grey). (c) Kagomé net 3.6.3.6 emphasizing with black bonds the trigonal faces which are capped by Ni/Ge atoms of the hexagonal 3^6 layers shown in (d). The Mg atoms are drawn as black spheres. The Ni/Ge atoms on Wyckoff position 12*j* and 4*d* are drawn in dark-purple, those on Wyckoff position 6*g* and 2*a* are drawn in light-purple, respectively. The displacement ellipsoids are drawn with 95 % probability level.

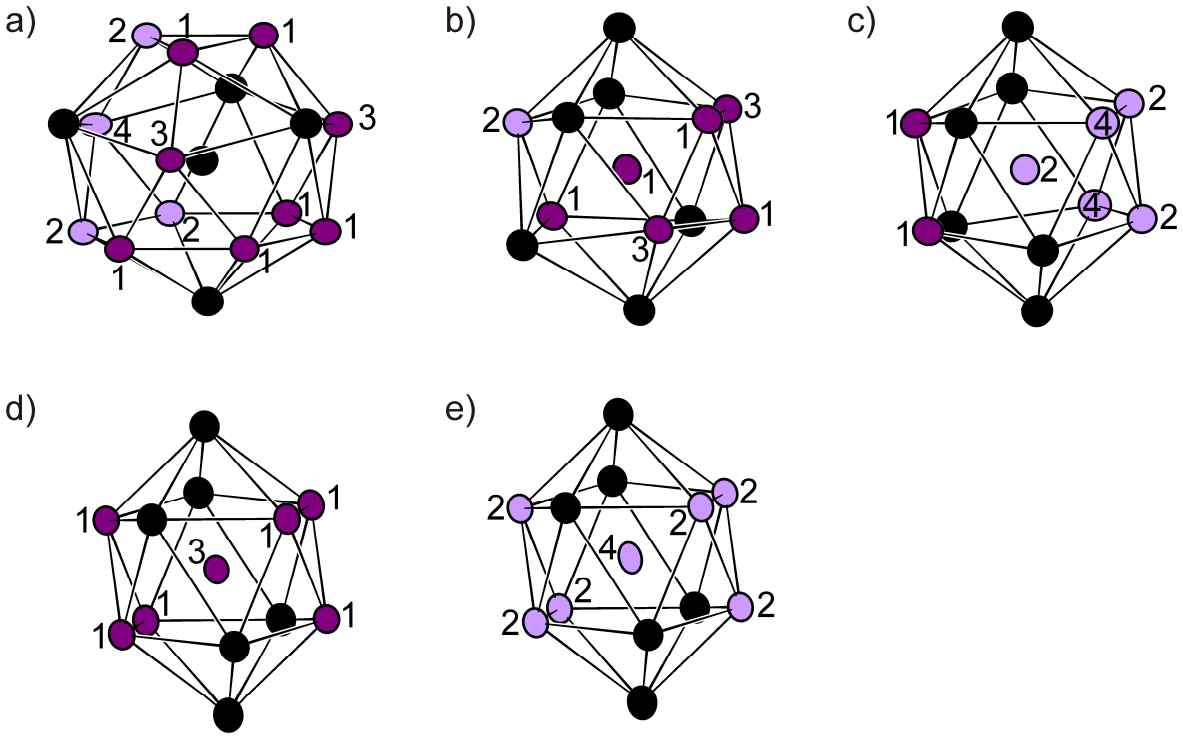

Figure 5 Crystal structure of *hP*-$MgNi_{2-x}Ge_x$ (x = 0.70(6)). Coordination polyhedra of (a) Mg, (b) Ni1/Ge1, (c) Ni2/Ge2, (d) Ni3Ge3 and (e) Ni4/Ge4. The Mg atoms are drawn as black spheres. The Ni/Ge atoms on Wyckoff position 12*j* and 4*d* are drawn in dark-purple, those on Wyckoff position 6*g* and 2*a* are drawn in light-purple, respectively. The displacement ellipsoids are drawn with 95 % probability level.

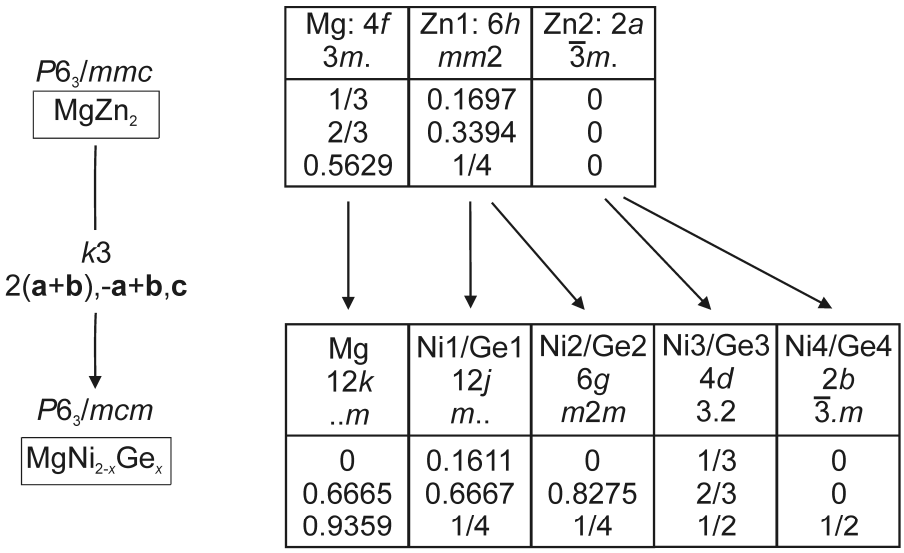

Figure 6 group-subgroup relationship of $MgZn_2$ and *hP*-$MgNi_{2-x}Ge_x$ (x = 0.70(6)). The index for the *klassengleiche* (*k*) transition as well as the unit cell transformation is given.

Summary and Conclusion

Two new Laves phases Mg_2Ni_3Ge and *hP*-$MgNi_{2-x}Ge_x$ (x = 0.70(6)) as well as the Laves phase *cF*-$MgNi_{2-\delta}Ge_\delta$, which was reported 50 years ago, were synthesized. The cell parameters and crystal structures were determined by single crystal X-ray diffraction.

cF-$MgNi_{2-\delta}Ge_\delta$ is only observed for small values of δ. It crystallizes in the cubic $MgCu_2$ structure type with a solid solution of Ni and Ge. Mg_2Ni_3Ge crystallizes in the Y_2Rh_3Ge structure type, which is a superstructure of the cubic Laves phase $MgCu_2$. *hP*-$MgNi_{2-x}Ge_x$ (x = 0.70(6)) crystallizes as a superstructure of the hexagonal Laves phase $MgZn_2$. Ni/Ge mixed site occupancies occur with a preferential site occupation of the Ge atoms on the Wyckoff positions 4*d* and 2*b*.

Starting with the binary Zintl phase $MgNi_2$ (C36) and gradually substituting Ni by Ge, thus rising the valence electron concentration (VEC), leads to the series of Laves phases C36 ($MgNi_2$ = $MgNi_{2-x}Ge_x$ with x = 0) → C15 (*cF*-$MgNi_{2-\delta}Ge_\delta$ with small values of δ) → superstructure of C15 (Mg_2Ni_3Ge = $MgNi_{2-x}Ge_x$ with x = 0.5) → superstructure of C14 (*hP*-$MgNi_{2-x}Ge_x$ = $MgNi_{2-x}Ge_x$ with x = 0.70(6)). Certainly experiments concerning the homogeneity ranges, a more pronounced ordering of *hP*-$MgNi_{2-x}Ge_x$ as well as a more precise determination of the values of δ and x for *cF*-$MgNi_{2-\delta}Ge_\delta$ and *hP*-$MgNi_{2-x}Ge_x$ are a worthwhile topic of further research. Due to the existence of MgNiGe [19] it is unlikely that values of $x > 1$ will be observed for the Laves phases $MgNi_{2-x}Ge_x$.

Intermetallic compounds of the system *Ae*/Ni/Ge (*Ae*: Mg, Ca, Sr, Ba) often contain two- or three-dimensional Ni-Ge networks which are reminiscent of the polyanions observed in Zintl phases. Due to the high content of Ni and due to the mixed occupancies of Ni and Ge such a comparison is not possible for the Laves phases discussed here. However, Laves phases, for example $KBi_{2-x}Pb_x$ [36], were discussed previously in the context of the Zintl-Klemm concept.

References

[1] D. Grüner, TU Dresden **2007**.

[2] R. L. Johnston, R. Hoffmann, *Z. Anorg. Allg. Chem.* **1992**, *616*, 105.

[3] F. Stein, M. Palm, G. Sauthoff, *Intermetallics* **2004**, *12*, 713.

[4] F. Stein, A. Palm, G. Sauthoff, *Intermetallics* **2005**, *13*, 1056.

[5] Y. Mishima, S. Ochiai, T. Suzuki, *Acta Metallurgica* **1985**, *33*, 1161.

[6] K. H. J. Buschow, *Solid State Commun.* **1975**, *17*, 891.

[7] K. H. J. Buschow, H. Kropp, E. Dormann, *J. Magn. Magn. Mater.* **1981**, *23*, 257.

[8] E. V. Melnik, V. V. Kinzhibalo, *Russian Metallurgy* **1981**, 154.

[9] Y. Komura, Y. Kitano, *Acta Crystallogr., Sect. B: Struct. Sci.* **1977**, *33*, 2496.

[10] Y. Komura, *Acta Crystallogr.* **1962**, *15*, 770.

[11] H. Witte, *Metallwirtschaft, Metallwissenschaft, Metalltechnik* **1939**, *18*, 459.

[12] K. Cenzual, B. Chabot, E. Parthe, *J. Solid State Chem.* **1987**, *70*, 229.

[13] D. Noreus, L. Eriksson, L. Gothe, P. E. Werner, *J. Less Common Met.* **1985**, *107*, 345.

[14] W. Buchholz, H. U. Schuster, *Z. Anorg. Allg. Chem.* **1981**, *482*, 40.

[15] W. Haucke, *Z. Anorg. Allg. Chem.* **1940**, *244*, 17.

[16] V. Y. Markiv, M. Y. Teslyuk, E. I. Gladyhevskii, *Dopov. Akad. Nauk Ukr. RSR* **1964**, *7*, 914.

[17] K. L. Holman, E. Morosan, P. A. Casey, L. Li, N. P. Ong, T. Klimczuk, C. Felser, R. J. Cava, *Mater. Res. Bull.* **2008**, *43*, 9.

[18] G. Bergman, L. T. Waugh, *Acta Crystallogr.* **1956**, *9*, 214.

[19] V. Hlukhyy, L. Siggelkow, T. F. Fässler, *in preparation* **2011**.

[20] M. Kolenda, A. Szytula, J. Leciejewicz, A. Pawlukojc, H. Ptasiewiczbak, *J. Magn. Magn. Mater.* **1990**, *89*, 26.

[21] F. C. Gennari, G. Urretavizcaya, J. J. A. Gamboa, G. Meyer, *J. Alloys Compd.* **2003**, *354*, 187.

[22] M. Y. Teslyuk, V. Y. Markiv, *Sov. Phys. Crystallogr.* **1962**, *7*, 103.

[23] G. Brauer, J. Tiesler, *Z. Anorg. Allg. Chem.* **1950**, *262*, 319.

[24] K. Schubert, K. Anderko, *Naturwissenschaften* **1951**, *38*, 259.

[25] K. H. Lieser, H. Witte, *Z. Metallk.* **1952**, *43*, 396.

[26] CrysAlis RED, *Scale3 / ABSPACK*, Version 1.171.33.34d, Oxford Diffraction Poland Sp. z o.o., **2009**.

[27] Bruker, APEX2, SAINT and SADABS, Bruker AXSinc., Madison, Wisconsin (USA), **2007**.

[28] G. M. Sheldrick, SHELXS-97 – *Program for the Determination of Crystal Structures*, University of Göttingen (Germany) **1997**.

[29] G. M. Sheldrick, SHELXL-97 – *Program for Crystal Structure Refinement*, University of Göttingen (Germany) **1997**.

[30] STOE, WinXPOW Version 2.08, STOE & Cie GmbH, Darmstadt **2003**.

[31] U. Müller, *Z. Anorg. Allg. Chem.* **2004**, *630*, 1519.

[32] H. Bärnighausen, *MATCH, Commun. Math. Chem.* **1980**, *9*, 139.

[33] A. E. Dwight, C. W. Kimball, *Acta Crystallogr., Sect. B: Struct. Sci.* **1974**, *30*, 2791.

[34] X. L. Yan, X. Q. Chen, A. Grytsiva, V. T. Witusiewicz, P. Rogl, R. Podloucky, V. Pomjakushin, G. Giester, *Int. J. Mater. Res.* **2006**, *97*, 450.

[35] A. Kerkau, D. Grüner, A. Ormeci, Y. Prots, H. Borrmann, W. Schnelle, E. Bischoff, Y. Grin, G. Kreiner, *Z. Anorg. Allg. Chem.* **2009**, *635*, 637.

[36] S. Ponou, N. Müller, T. F. Fässler, U. Häussermann, *Inorg. Chem.* **2005**, *44*, 7423.

Supporting Information

Table S1 Anisotropic displacement parameters (*Uij* / Å^2) for *cF*-$MgNi_{2-\delta}Ge_{\delta}$

Atom	U_{11}	U_{22}	U_{33}	U_{12}	U_{13}	U_{23}
Mg	0.017(2)	0.017 (2)	0.017(2)	0.00000	0.00000	0.00000
Ni	0.0128(9)	0.0128(9)	0.0128(9)	-0.0016(2)	-0.0016(2)	-0.0016(2)
Ge	0.0128(9)	0.0128(9)	0.0128(9)	-0.0016(2)	-0.0016(2)	-0.0016(2)

Table S2 Anisotropic displacement parameters (*Uij* / Å^2) for Mg_2Ni_3Ge

Atom	U_{11}	U_{22}	U_{33}	U_{12}	U_{13}	U_{23}
Mg	0.0122(7)	0.0122(7)	0.0112(11)	0.0061(4)	0.00000	0.00000
Ni	0.0083(5)	0.0110(4)	0.0100(5)	0.0041(3)	-0.0012(2)	-0.0006 (2)
Ge	0.0109(5)	0.0109(5)	0.0083(6)	0.0055(2)	0.00000	0.00000

Table S3 Anisotropic displacement parameters (*Uij* / Å^2) for *hP*-$MgNi_{2-x}Ge_x$ (x = 0.70(6))

Atom	U_{11}	U_{22}	U_{33}	U_{12}	U_{13}	U_{23}
Mg5	0.0110(8)	0.0118(5)	0.0100(3)	0.0055(4)	0.00000	0.0000(9)
Ni1	0.0100(3)	0.0117(2)	0.0080(3)	0.0058(2)	0.00000	0.00000
Ge1	0.0100(3)	0.0117(2)	0.0080(3)	0.0058(2)	0.00000	0.00000
Ni2	0.0108(4)	0.0103(3)	0.0076(5)	0.0054(2)	0.00000	0.00000
Ge2	0.0108(4)	0.0103(3)	0.0076(5)	0.0054(2)	0.00000	0.00000
Ni3	0.0102(2)	0.0102(2)	0.0071(4)	0.0051(1)	0.00000	0.00000
Ge3	0.0102(2)	0.0102(2)	0.0071(4)	0.0051(1)	0.00000	0.00000
Ni4	0.0133(4)	0.0133(4)	0.0064(8)	0.0067(2)	0.00000	0.00000
Ge4	0.0133(4)	0.0133(4)	0.0064(8)	0.0067(2)	0.00000	0.00000

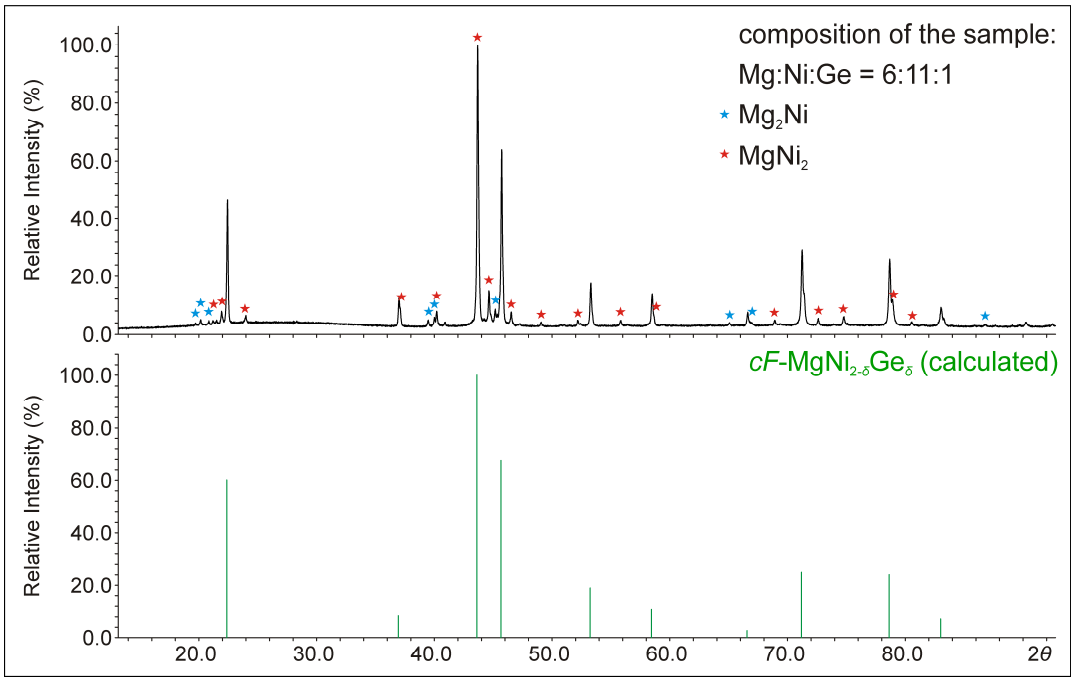

Figure S1 Experimental powder XRD pattern from sample loading Mg : Ni : Ge = 6 : 11 : 1 (top) and simulated powder XRD pattern of *cF*-$MgNi_{2-\delta}Ge_{\delta}$ (bottom). The synthesis was carried out using a tantalum ampoule as reaction wessel. The experimental powder XRD pattern was recorded in transmission geometry. Reflections of Mg_2Ni and $MgNi_2$ are labelled with blue and red stars, respectively.

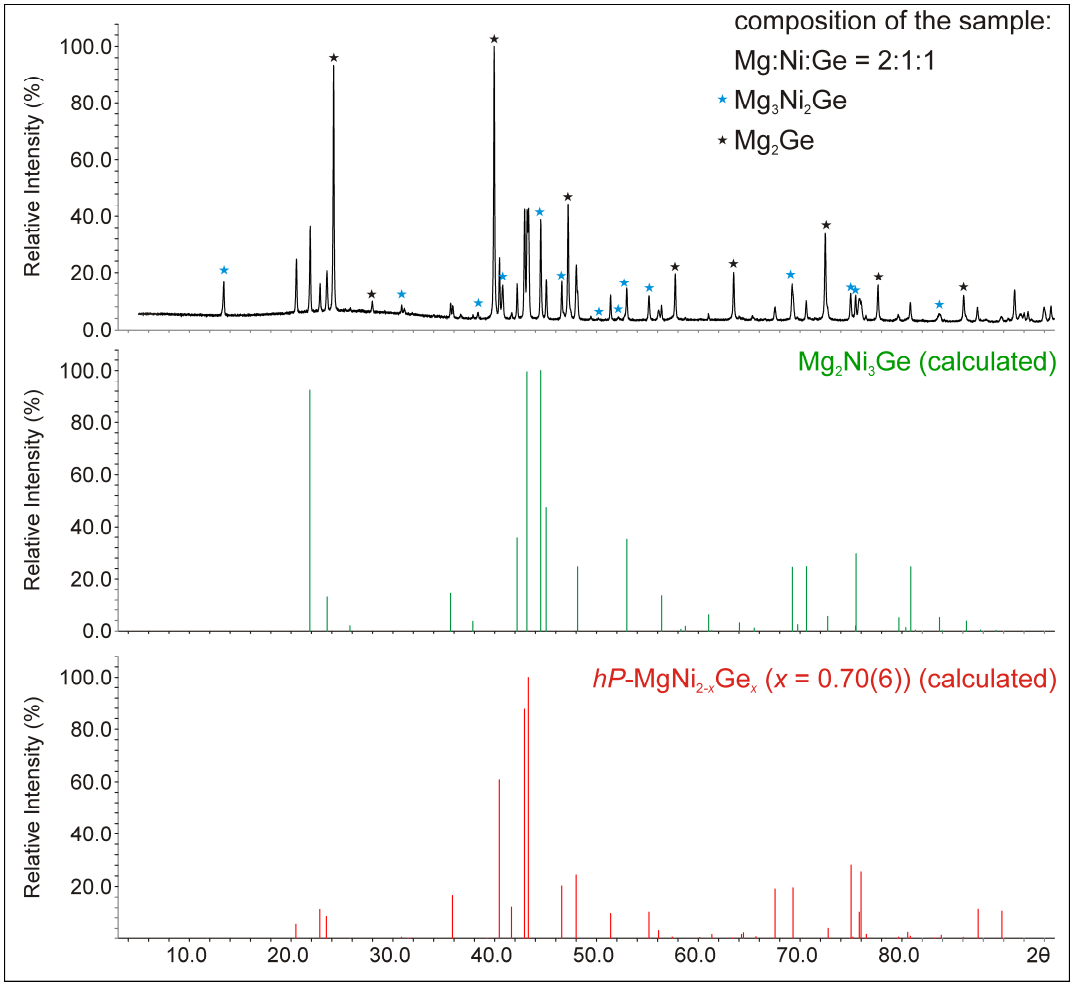

Figure S2 Experimental XRD powder pattern from sample loading Mg : Ni : Ge = 2 : 1 : 1 (top), simulated powder XRD pattern of Mg_2Ni_3Ge (middle) and *hP*-$MgNi_{2-x}Ge_x$ (x = 0.70(6)) (bottom). The synthesis was carried out using an alumina crucible as reaction wessel. The experimental powder XRD pattern was recorded in transmission geometry. Reflections of Mg_3Ni_2Ge and Mg_2Ge are labelled with blue and black stars, respectively.

Nickel Germanides of Alkaline Earth Metals – Structural Peculiarities and Relationships

Lisa Siggelkow, Viktor Hlukhyy, Thomas F. Fässler

to be submitted

Abstract

This article intends to give a comprehensive overall description of the various ternary polar intermetallic phases of the systems *Ae*/Ni/Ge (*Ae*: Ca, Sr, Ba). The discussion sheds light on numerous aspects concerning the crystal structures. For instance, the influence of an increasing *Ae* size on the dimensionality of the Ni-Ge polyanions is discussed on the example of compounds with composition 1:1:1 and 1:2:2, revealing that not only the number of valence electrons controls the occurrence of specific structure types. Further, $^{1}_{\infty}$[NiGe] ladder-type ribbons are shown to be a reoccurring structural motif. Most crystal structures of the systems *Ae*/Ni/Ge can be described using these ribbons as a basic module. Exceptions are the Ni rich compounds with low alkaline earth metal content and the clathrate $Ba_8Ni_{3.5}Ge_{42.1}$.

Furthermore, the discussion focuses on the composition triangle containing all ternary polar intermetallic phases of the systems *Ae*/Ni/Ge, which provides a useful guideline to reveal structural relationships. Special attention is paid to the lines connecting the elements with (sometimes hypothetical) binary compounds of the simple compositions 2:1, 1:1 and 1:2. It is shown that the gradual addition of the corresponding third element has a straightforward relation to the topology of the corresponding structures.

For a better understanding of the crystal structures, the comparison of the ternary polar intermetallic compounds of the systems *Ae*/Ni/Ge with binary compounds of the systems *Ae*/Ge, Ni/Ge and *Ae*/Ni proved to be beneficial. In this context, an approach describing the polar intermetallic phases in analogy to the Zintl-Klemm concept is discussed, using the binary compounds of the system Ni/Ge as a reference point.

I. Introduction

In 1935 Eduard Zintl described the crystal structure of NaTl, concluding that the Tl atoms adopt a diamond network as each Na atom donates its valence electrons to Tl [1]. Klemm generalized this powerful idea for compounds A_aE_x (*A*: alkali and alkaline earth metal; *E*: electronegative p-block metal) by proposing the pseudoatom concept for the electronegative components. Since then, the classical Zintl-Klemm concept [2, 3] was successfully applied to explain the crystal structures of many solid-state compounds and numerous reviews which summarize the manifold variety of Zintl phases were written (selected reviews [4-6]). The classical Zintl-Klemm concept was developed for salt-like valence compounds consisting of main group elements. In short, it is assumed that a formal electron transfer from the electropositive metal (such as alkali metal, alkaline earth metal or rare earth metal atoms) to the more electronegative p-block metal and semi metals takes place. The anions thus form covalently bonded polyanions according to the (8-*N*) rule. If only one sort of p-block elements is present, the anions adopt the structures of the corresponding element with the same valence electron number.

Most intermetallic compounds in the binary systems *Ae*/Ge (*Ae*: Ca, Sr, Ba) have crystal structures, which can be interpreted according to the Zintl-Klemm concept. For example, in the equiatomic phases CaGe [7], SrGe [8] and BaGe [9-11] (CrB structure type) the Ge atoms form zigzag chains of two-bonded (2b) atoms in analogy to the heavier group 16 elements. However, small alterations are observed, since the zigzag chains in the binaries are planar in contrast to the helical chains in specific modifications of the group 16 elements. Further, Zintl phases do not depend only on the nature of the constituting elements but also on the ratio of the elements involved. Structures at the borderline of the Zintl concept occur on the *A*/*Ae* (*A*: alkaline metal, *Ae*: alkaline earth metal) rich as well as on the *Tt* (*Tt*: tetrel) rich sides of binary phases diagrams. Examples, such as $NaSn_5$ [12], $BaSn_3$ [13] and $SrSn_4$ [14], are metallic and do not obey the (8-*N*) rule according to the Zintl concept. However, they contain other structure motifs with covalent Sn-Sn bonds.

In general, chemical bonding in intermetallic compounds that contain transition metals is least understood [15-17]. Atomic size effects as in Laves phases and some rules

considering the valence electron concentration (VEC) as described for Hume-Rothery phases are a basic approach to predict some structures of intermetallic compounds. Systematic investigations of ternary intermetallic compounds that contain active electropositive metals *A*, *Ae* or *Re* (*Re*: rare earth metal), more electronegative p-block metals as well as transition metals – named *polar* intermetallic compounds – might give further hints for the occurrence of specific structure motifs or stable building blocks in intermetallic compounds.

Recently, the first examples of intermetallic compounds that contain transition metals and allow a salt-like description were reported. The phase K_5CoSn_9 contains discrete $CoSn_9^{5-}$ clusters which were described using molecular concepts within the Wade-Mingos rules [18]. In $A_{12}Cu_{12}Sn_{21}$ (*A* = Na, K, Rb, Cs) discrete $Sn@Cu_{12}@Sn_{20}^{12-}$ clusters with a shell structure appear [19]. Even if no simple concept for their electron counts is available, the compounds are semiconducting and the molecular orbital approach reveals a salt-like description.

On the one hand no straightforward concept to predict the crystal structures of polar intermetallic compounds containing transition metals *T* is available. On the other hand, several of their crystal structures contain $[T_xTt_y]$ substructures, which are reminiscent of the polyanions in Zintl phases. Applying the Zintl-Klemm concept to the ternary polar intermetallic compounds $Ae_nT_mTt_p$, some open-ended questions remain. First of all, a charge has to be assigned to the transition metal *T*. The discussion in the literature concerning this point is in no way consistent. For example, a positive charge is assigned to the transition element in $CaNi_2P_2$ and $CaCu_{1.75}P_2$, assuming the transition metal to act as a electropositive constituent [20]. On the contrary, a negative charge is assigned for the platinum atoms in Ba_2Pt_8P [21]. Further points under discussion are the often neglected influence of the cations on the crystal structure and the failure of the concept to explain the manifold crystal structures of the ternary polar intermetallic phases which are transition metal rich.

In this article the wealth of ternary polar intermetallic compounds of the systems *Ae*/Ni/Ge (*Ae*: Ca, Sr, Ba), whose rich structural chemistry was introduced in recent years, shall be described. In contrast to the ternary systems *Re*/Ni/Ge (see [22]) until quite recently only a few compounds in the systems *Ae*/Ni/Ge were known. Our investigations showed that the Ni and Ge atoms form a manifold variety of $[Ni_xGe_y]$ substructures, that can be traced back to some unique building blocks: One-dimensional Ni-Ge structures are

found in SrNiGe (**1a**), BaNiGe (**1b**) [23] and Ba_2NiGe_3 (**23**) [24], two-dimensional Ni-Ge structures are found in CaNiGe (**2**) [25], LT-$BaNi_2Ge_2$ (**4a**) [26], HT-$BaNi_2Ge_2$ (**4b**) [26], $SrNi_2Ge$ (**8**) [27], $BaNi_2Ge$ (**9**) [28], $Ca_4Ni_4Ge_3$ (**10**) [28], $Ca_2Ni_3Ge_2$ (**14**) [29], , $SrNi_3Ge_2$ (**16**) [27] and $Ba_2Ni_5Ge_4$ (**15**) [30], whereas three-dimensional structures are found in MgNiGe (**3**) [23], $SrNi_2Ge_2$ (5) [31-33], $CaNi_2Ge_2$ (**6**) [25, 31-34], $SrNiGe_3$ (**7**) [23], $CaNiGe_2$ (**11a**) [35], $SrNiGe_2$ (**11b**) [35], $Ca_3Ni_3Ge_7$ (**12a**) [23], $Sr_3Ni_3Ge_7$ (**12b**) [23], $CaNiGe_3$ (**13**) [23, 36], $Ca_{10}Ni_{34}Ge_{16}$ (**17**) [23], $CaNi_5Ge_3$ (**18**) [37], $Ca_{15}Ni_{68}Ge_{37}$ (**19**) [37], $Ca_7Ni_{48.9(4)}Ge_{22.1(4)}$ (**20**) [37], $SrNi_9Ge_4$ (**21**) [24] and the clathrate $Ba_8Ni_{3.5}Ge_{42.1}$(**22**) [38-42]. The crystal structures as well as the electronic structures of these compounds were described elsewhere, but a comprehensive overall description pointing out relationships between the various structures types is still missing and shall be given here. In the course of the discussion numerous aspects will be pointed out, such as the influence of the size of the cations on the polyanionic networks, recurring structural motifs and the relationships to binary intermetallic phases in the systems *Ae*/Ni, Ni/Ge and *Ae*/Ge. In this context analogies between the [Ni_xGe_y] substructures and polyanions in Zintl phases are explored. In the final discussion an extended approach of the Zintl concept is discussed.

II. Synthesis

Generally, for the synthesis of polar intermetallic compounds of the systems *Ae*/Ni/Ge in a first step Ni and Ge were arc melted, allowing Ni (T_m(Ni) = 1453 °C) and Ge (T_m(Ge) = 937 °C) to react. In order to prevent a significant evaporation of the alkaline earth metal during arc melting, a lower temperature is applied after the addition of the *Ae* metals (T_m(Ca) = 839 °C, T_m(Sr) = 769 °C, T_m(Ba) = 725 °C). Stoichiometric amounts of the elements corresponding to a total mass of 0.5 g to 1 g were used. For both steps the resulting reguli were arc melted and turned-over three times in order to ensure homogeneity. After the arc melting procedures usually samples of low crystallinity were obtained. To grow single crystals the reguli obtained after arc melting were sealed in tantalum or niobium ampoules and heated in a water-cooled sample chamber of an induction furnace under flowing argon. After the melting procedure the samples were

cooled slowly to a moderate temperature and finally cooled down to room temperature in about one minute by switching off the furnace.

Alternatively, the samples obtained from arc melting were sealed in tantalum or niobium ampoules which in turn were sealed in a quartz amoule. These were placed in a resistant furnace at a temperature just below the melting point of the synthesized intermetallic phase. Samples of good homogeneity were obtained. The quality of the crystals is lower than the one obtained using a high frequency oven but certainly higher than the one obtained directly after arc melting.

Direct reaction of the elements in welded Ta/Nb ampoules using either an induction furnace or a resistance furnace is usually avoided. For this route the temperature has to be chosen very carefully in order to on the one hand prevent the reaction of Ge with the Ta/Nb ampoule and on the other hand to ensure that the high melting Ni participates in the reaction.

Large single crystals were grown for the clathrate $Ba_8Ni_{3.5}Ge_{42.1}$ (**22**), such that the measurement of the physical properties could be carried out on the single crystals. This was realized using the vertical Bridgman method with open graphite crucibles [40, 41]. Alternatively the physical measurements were carried out on powdered samples, which were compacted using the spark plasma sintering (SPS) technique [39, 42].

III. Composition triangles of the systems *Ae*/Ni/Ge

All intermetallic compounds presented in this article are listed in Table 1 and are shown in the composition triangles of the systems Ca/Ni/Ge (Figure 1), Sr/Ni/Ge (Figure 2) and Ba/Ni/Ge (Figure 3). The compounds are labelled according to the order in which they are discussed in this article. Further, they are classified in the composition triangles according to the occurrence of one- two- and three-dimensional Ni-Ge networks. The compositions of the binary phases are indicated for a maximum content of alkaline earth metal of 50%. The known binary phases are listed below (see also Table 2). Whenever comparing a ternary compound with a binary in this article, the crystal structure of the binary compound will be recalled as well.

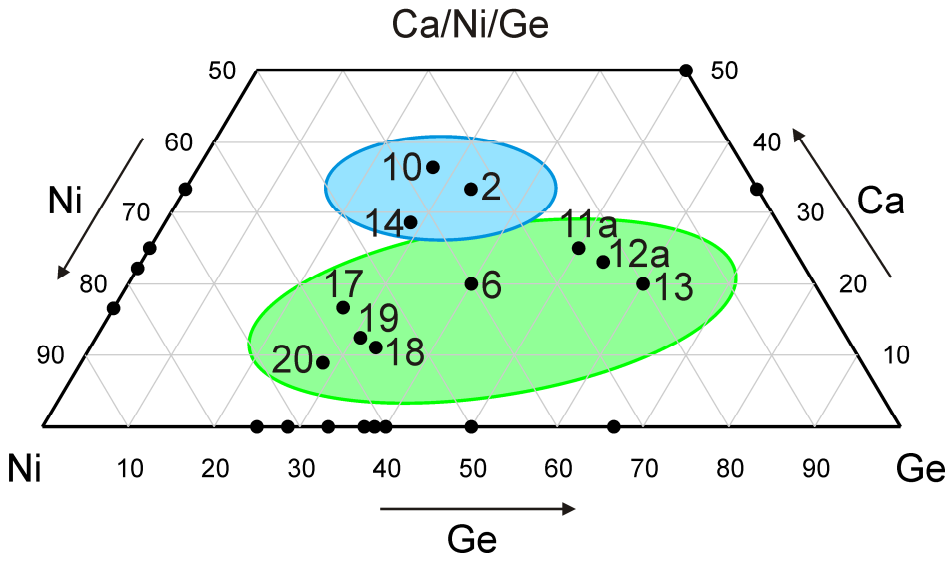

Figure 1 Composition triangle of the system Ca/Ni/Ge. The following ternary compounds are shown: CaNiGe (**2**), $CaNi_2Ge_2$ (**6**), $Ca_4Ni_4Ge_3$ (**10**), $Ca_2Ni_3Ge_2$ (**14**), $CaNiGe_2$ (**11a**), $Ca_3Ni_3Ge_7$ (**12a**), $CaNiGe_3$ (**13**), $Ca_{10}Ni_{34}Ge_{16}$ (**17**), $CaNi_5Ge_3$ (**18**), $Ca_{15}Ni_{68}Ge_{37}$ (**19**), $Ca_7Ni_{48.9(4)}Ge_{22.1(4)}$ (**20**). The compositions of the binary phases are indicated. The regions, in which three-dimensional and two-dimensional polyanionic networks are observed, are marked in green and blue, respectively.

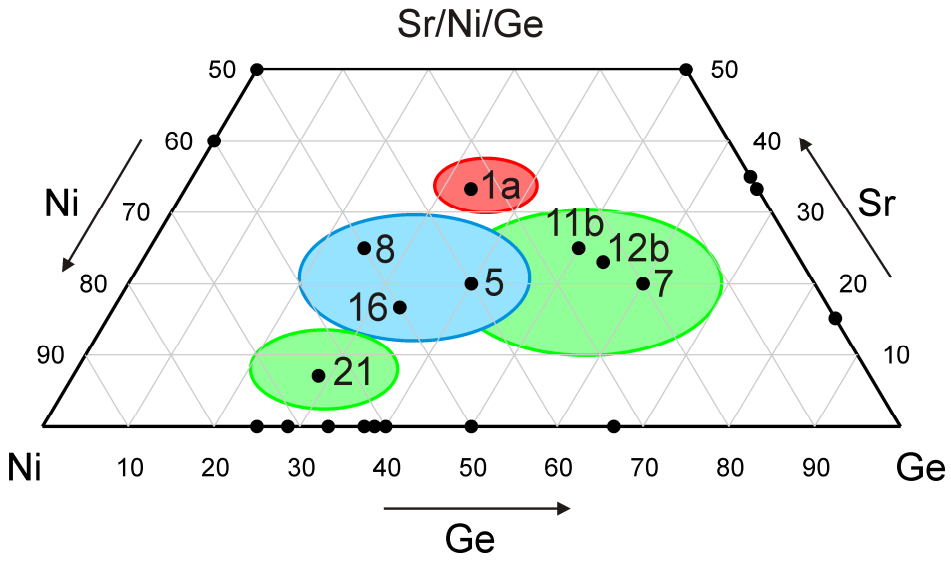

Figure 2 Composition triangle of the system Sr/Ni/Ge. The following ternary compounds are shown: SrNiGe (**1a**), $SrNi_2Ge_2$ (**5**), $SrNiGe_3$ (**7**), $SrNi_2Ge$ (**8**), $SrNiGe_2$ (**12a**), $Sr_3Ni_3Ge_7$ (**12b**), $SrNi_3Ge_2$ (**16**), $SrNi_9Ge_4$ (**21**). The compositions of the binary phases are indicated. The regions, in which three-, two- and one-dimensional polyanionic networks are observed, are marked in green, blue and red, respectively.

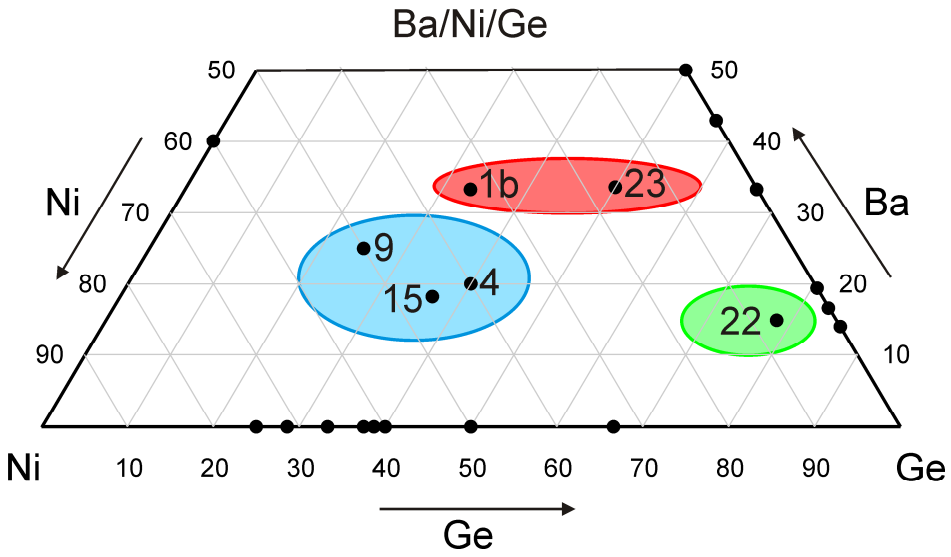

Figure 3 Composition triangle of the system Ba/Ni/Ge. The following ternary compounds are shown: BaNiGe (**1b**), LT-$BaNi_2Ge_2$ (**4a**), HT-$BaNi_2Ge_2$ (**4b**), $BaNi_2Ge$ (**9**), $Ba_2Ni_5Ge_4$ (**15**), $Ba_8Ni_{3.5}Ge_{42.1}$ (**22**), Ba_2NiGe_3 (**23**). The compositions of the binary phases are indicated. The regions, in which three-, two- and one-dimensional polyanionic networks are observed, are marked in green, blue and red, respectively.

Recently, the binary phase diagrams of Ca/Ge, Sr/Ge and Ba/Ge were reinvestigated [43-45]. Isolated Ge atoms are found in the binary phases with highest alkaline earth metal content, Ba_2Ge [46], Sr_2Ge [47] and Ca_2Ge [48], which is in agreement with the Zintl-Klemm concept. The compounds Ae_7Ge_6 [44, 49] are a borderline case, as they form Ge_2 dumbbells and Ge_4 four-membered chains. The resulting crystal structure can only be rationalized according to the (8-*N*) rule, if partial π bonding is taken into account. The compounds with lower alkaline earth metal content are valence compounds (Ba_5Ge_3 [50], BaGe [9-11], *β*-Ba_3Ge_4 [51], α-Ba_3Ge_4 [51], $BaGe_2$ [52-55] , Sr_5Ge_3 [56], SrGe [8, 9], $SrGe_{1.85}$ [45], $SrGe_2$ [57, 58], Ca_5Ge_3 [59], CaGe [7], $CaGe_2$ [44, 60, 61]). Only recently, the superconducting high pressure compound $BaGe_3$ [62], being isostructural to $BaSn_3$ [13, 63], was synthesized. The crystal structure of $BaSn_3$ was interpreted as a borderline case between Zintl phases and intermetallics. It contains three-membered Sn_3^{2-} rings, which are isoelectronic to the aromatic ($C_3R_3^+$). Strong interactions of the electronic π systems lead to metallic and even superconducting properties of $BaSn_3$. The Ge rich compounds Ba_6Ge_{25} [64-66], Ba_8Ge_{43} [67], $BaGe_5$ [68] and $SrGe_{5,56}$ [69] form various clathrate structures containing three- and four-bonded atoms. $BaGe_5$ is semiconducting and a Zintl phase [68]. It contains twenty Ge atoms per unit cell that are

three-bonded and thirty atoms that are four-bonded. Thus, $BaGe_5$ is electronically balanced: $[Ba^{2+}]_{10}[(3b)Ge^{-}]_{20}[(4b)Ge^{0}]_{30}$. On the contrary, Ba_6Ge_{25} and Ba_8Ge_{43} cannot be rationalized according to the Zintl-Klemm concept, as they contain an excess of electrons: $[Ba^{2+}]_6[(3b)Ge^{-}]_8[(4b)Ge^{0}]_{17}$ and $[Ba_{2+}]_8[(3b)Ge^{-}]_{12}[(4b)Ge^{0}]_{31}$.

In contrast to the systems Sr/Ge and Ba/Ge, no Ge rich compound (i.e. more than 67% Ge) is known in the system Ca/Ge. Note, that even though many crystal structures observed in the systems *Ae*/Ge correspond formally to salt-like Zintl phases, the calculations of the band structures often reveal metallic conductivity. Therefore, the term „metallic Zintl phase" is applied throughout the literature [20].

The intermetallic phases observed in the binary system Ni/Ge are summarized in [70]. The following phases were described, starting at the Ge rich site: $NiGe_2$ [71], NiGe [72], Ni_3Ge_2 [73] (broad homogeneity range), $Ni_{19}Ge_{12}$ [73, 74], ε'-Ni_5Ge_3 [73], ε-Ni_5Ge_3 [70] (reported as Ni_2Ge (ht) in [75]), Ni_2Ge (rt) [73], Ni_5Ge_2 [73] and β-Ni_3Ge [72]. For the Ni rich phases of this system, the relationship to the NiAs structure type was described [76].

Fewest compounds are reported in the systems *Ae*/Ni. In the system Ba/Ni only the intermetallic phase Ba_2Ni_3 [77] exists. In the system Sr/Ni the intermetallic phases Sr_2Ni_3 [78] as well as the SrNi ([79], hexagonal unit cell, no structure solution) are reported. In the system Ca/Ni the binary phases $CaNi_2$, $CaNi_3$, Ca_2Ni_7 and $CaNi_5$ were structurally characterized [80]. $CaNi_2$ is a cubic Laves phase and crystallizes in the $MgCu_2$ structure type. $CaNi_5$ crystallizes in the $CaCu_5$ structure type. Both structures contain different stacking sequences of Kagomé nets of Ni atoms. A combination of structural motifs of the crystal structures of $CaNi_2$ and $CaNi_5$ leads to the crystal structures of $CaNi_3$ and Ca_2Ni_7.

Table 1 Ternary polar intermetallic compounds of the systems *Ae*/Ni/Ge (*Ae*: Mg, Ca, Sr, Ba). The compounds are numbered according to the order in which they will be discussed in the article.

No.	Compound	Structure type	Space group	Unit cell dimensions	Distances / Å			Ref.
					Ni-Ge	Ni-Ni	Ge-Ge	
1a	SrNiGe	*anti*-SnFCl [81]	*Pnma*	a = 5.727(1) Å b = 4.174(1) Å c = 11.400(3) Å V = 270.4(2) Å^3 Z = 4 V/atom = 22.5 Å^3	2.30 - 2.38	2.58		[23]
1b	BaNiGe	*anti*-SnFCl [81]	*Pnma*	a = 5.969(4) Å b = 4.195(1) Å c = 11.993(5) Å V = 300.3(1) Å^3 Z = 4 V/atom = 25.0 Å^3	2.32 - 2.37	2.59		[23]
2	CaNiGe	MnAlGe [82]	*P*4/*nmm*	a = 4.19341(3) Å c = 6.6264(1) Å V = 116.18(7) Å^3 Z = 2 V/atom = 19.4 Å^3	2.43	2.96		[25]
3	MgNiGe	TiNiSi [83]	*Pnma*	a = 6.4742(2) Å b = 4.0716(1) Å c = 6.9426(2) Å V = 182.98(2) Å^3 Z = 4 V/atom=15.25 Å^3	2.39 - 2.44	2.95		[23]
4a	LT-$BaNi_2Ge_2$	own	*Pnma*	a = 8.4693(4) Å b = 11.3503(5) Å c = 4.3212(2) Å V = 415.4(2) Å^3 Z = 4 V/atom = 20.8 Å^3	2.28 - 2.39	2.81 - 2.83	2.93	[26]
4b	HT-$BaNi_2Ge_2$	$ThCr_2Si_2$ [33]	*I*4/*mmm*	a = 4.2665(1) Å c = 11.2545(3) Å V = 204.87(5) Å^3 Z = 2 V/atom = 20.5 Å^3	2.35	3.02		[26]
5	$SrNi_2Ge_2$	$ThCr_2Si_2$ [33]	*I*4/*mmm*	a = 4.17(1) Å c = 10.25(2) Å V = 178.2(9) Å^3 Z = 2 V/atom = 17.8 Å^3	2.38	2.95	2.83	[31-33]
6	$CaNi_2Ge_2$	$ThCr_2Si_2$ [33]	*I*4/*mmm*	a = 4.0749(7) Å c = 9.987(2) Å V = 166.1(9) Å^3 Z = 2 V/atom = 16.6 Å^3	2.36	2.89	2.61	[25, 31, 33]
7	$SrNiGe_3$	$BaNiSn_3$ [84]	*I*4*mm*	a = 4.3742(3) Å c = 9.9999(8) Å V = 191.33(2) Å^3 Z = 2 V/atom = 19.1 Å^3	2.37 - 2.41		2.72 - 3.09	[23]

No.	Compound	Structure type	Space group	Unit cell dimensions	Distances / Å Ni-Ge	Ni-Ni	Ge-Ge	Ref.
8	$SrNi_2Ge$	$GdPt_2Sn$ [85]	$P6_3/mmc$	a = 4.128(1) Å c = 10.479(6) Å V = 155.61(5) Å^3 Z = 2 V/atom = 19.5 Å^3	2.41	2.50		[27]
9	$BaNi_2Ge$	own	$Pmmn$	a = 6.6935(5) Å b = 4.1571(5) Å c = 5.9498(7) Å V = 165.56(5) Å^3 Z = 2 V/atom = 20.7 Å^3	2.42 - 2.43	2.48 - 2.52		[28]
10	$Ca_4Ni_4Ge_3$	own	$Cmcm$	a = 4.1824(8) Å b = 10.415(2) Å c = 19.864(4) Å V = 865.3(3) Å^3 Z = 4 V/atom = 19.7 Å^3	2.41 - 2.48	2.49 - 2.53		[28]
11a	$CaNiGe_2$	$CeNiSi_2$ [86]	$Cmcm$	a = 4.2213(7) Å b = 17.375(4) Å c = 4.0514(7) Å V = 297.2(2) Å^3 Z = 4 V/atom = 18.6 Å^3	2.34 - 2.46		2.50 - 2.93	[35]
11b	$SrNiGe_2$	$CeNiSi_2$ [86]	$Cmcm$	a = 4.429(1) Å b =17.420(4) Å c = 4.200(1) Å V = 324.0(2) Å^3 Z = 4 V/atom= 20.25Å^3	2.40 - 2.52		2.56 - 3.05	[35]
12a	$Ca_3Ni_3Ge_7$	$Ce_3Ni_2Si_8$ [87, 88]	$Cmmm$	a = 4.0951(8) Å b = 27.334(6) Å c = 4.2814(9) Å V = 479.2(2) Å^3 Z = 2 V/atom = 18.4 Å^3	2.30 – 2.45		2.52 – 2.96	[23]
12b	$Sr_3Ni_3Ge_7$	$Ce_3Ni_2Si_8$ [87, 88]	$Cmmm$	a = 4.2270(5) Å b = 27.338(4) Å c = 4.4107(8) Å V = 509.7(2) Å^3 Z = 2 V/atom = 19.6 Å^3	2.36 - 2.48		2.57 - 3.05	[23]
13	$CaNiGe_3$	$SmNiGe_3$ [89]	$Cmmm$	a = 4.0497(6) Å b = 21.992(4) Å c = 4.1593(9) Å V = 370.4(1) Å^3 Z = 4 V/atom = 18.4 Å^3	2.34 - 2.39		2.46 - 2.90	[23, 36]

No.	Compound	Structure type	Space group	Unit cell dimensions	Distances / Å Ni-Ge	Ni-Ni	Ge-Ge	Ref.
14	$Ca_2Ni_3Ge_2$	own	*Pmma*	a = 9.097(2) Å b = 4.014(1) Å c = 7.019(1) Å V = 256.30(8) Å^3 Z = 2 V/atom = 18.3 Å^3	2.35 - 2.62	2.55 - 2.58		[29]
15	$Ba_2Ni_5Ge_4$	own	*C*2/*m*	a = 12.523(5) Å b = 4.056(1) Å c = 9.503(6) Å β = 118.65(4)° V = 423.6(4) Å^3 Z = 2 V/atom = 19.3 Å^3	2.29 - 2.76	2.48 - 2.98		[30]
16	$SrNi_3Ge_2$	own	$P6_3/mmc$	a = 4.0511(1) Å c = 14.2187(6) Å V = 202.09(1) Å^3 Z = 2 V/atom = 16.8 Å^3	2.36 - 2.71	2.56 - 3.12		[27]
17	$Ca_{10}Ni_{34}Ge_{16}$	own	*Amm*2	a = 4.0255(2) Å b = 25.226(2) Å c = 8.9861(6) Å V = 915.5(1) Å^3 Z = 1 V/atom = 15.2 Å^3	2.34 - 3.01	2.44 - 3.09		[23]
18	$CaNi_5Ge_3$	own	*P*4/*mbm*	a = 8.0855(1) Å c = 7.8466(1) Å V = 512.97(1) Å^3 Z = 4 V/atom = 14.5 Å^3	2.37 - 3.01	2.46 - 3.04		[37]
19	$Ca_{15}Ni_{68}Ge_{37}$	own	$P\bar{6}2m$	a = 22.436(2) Å c = 3.9684(4) Å V = 1732.7(2) Å^3 Z = 1 V/atom = 14.4 Å^3	2.33 - 2.99	2.46 - 3.04		[37]
20	$Ca_7Ni_{49}Ge_{22}$	own	*P*6/*mmm*	a = 17.381(4) Å c = 4.046(1) Å V = 1058.5(6) Å^3 Z = 1 V/atom = 13.6 Å^3	2.34 – 3.05	2.44 – 3.00		[37]
21	$SrNi_9Ge_4$	$CeNi_{8.5}Si_{4.5}$ [90]	*I*4/*mcm*	a = 7.9903(1)Å c = 11.8371(2) Å V = 755.74(2)Å^3 Z = 4 V/atom = 13.5 Å^3	2.40 - 2.59	2.43 - 3.75		[24]
22	$Ba_8Ni_{3.5}Ge_{42.1}$	K_8Si_{46} [91]	$Pm\bar{3}n$	a = 10.5179(4) Å V =1218.12(7) Å^3 Z = 1 V/atom = 22.6 Å^3	2.39		2.46 - 2.61	[38-42]
23	Ba_2NiGe_3	Ba_2NiSi_3 [92]	$P\bar{6}2m$	a = 11.455(2)Å c = 4.0095(8)Å V = 455.6(2)Å^3 Z = 3 V/atom = 25.2 Å^3	2.49 - 2.50		2.56 - 2.60	[24]

Table 2 Binary intermetallic compounds of the systems *Ae*/Ge, Ge/Ni and *Ae*/Ni (*Ae*: Ca, Sr, Ba). The Ni-Ge, Ni-Ni and Ge-Ge distances shorter than 3 Å are given.

Compound	Structure type	Space group	Unit cell dimensions	Distances / Å			Literature
				Ni-Ge	Ni-Ni	Ge-Ge	
***Ae*-Ge**							
Ba_2Ge	β-Co_2Si [93]	*Pnma*	*a* = 8.38(2) Å *b* = 5.48(2) Å *c* = 10.04(2) Å *V* = 461.06(6) Å^3 *Z* = 4 *V*/atom = 38.4 Å^3			-	[46]
Sr_2Ge	β-Co_2Si [93]	*Pnma*	*a* = 8.13(2) Å *b* = 5.20(2) Å *c* = 9.58(2) Å *V* = 405.00(6) Å^3 *Z* = 4 *V*/atom = 33.8 Å^3			-	[47]
Ca_2Ge	β-Co_2Si [93]	*Pnma*	*a* = 7.734(7) Å *b* = 4.834(4) Å *c* = 9.069(9) Å *V* = 339.06(6) Å^3 *Z* = 4 *V*/atom = 28.3 Å^3			-	[48]
Ba_7Ge_6	Ca_7Sn_6 [94]	*Pnma*	*a* = 8.124(2) Å *b* = 24.627(5) Å *c* = 9.010(2) Å *V* = 1802.62(1) Å^3 *Z* = 4 *V*/atom = 34.7 Å^3			2.50 - 2.59	[95]
Sr_7Ge_6	Ca_7Sn_6 [94]	*Pnma*	*a* = 7.777(2) Å *b* = 23.595(4) Å *c* = 8.563(1) Å *V* = 1571.30(1) Å^3 *Z* = 4 *V*/atom = 30.2 Å^3			2.53 - 2.59	[95]
Ca_7Ge_6	Ca_7Sn_6 [94]	*Pnma*	*a* = 7.375(1) Å *b* = 22.362(4) Å *c* = 8.120(1) Å *V* = 1339.15(1) Å^3 *Z* = 4 *V*/atom = 30.2 Å^3			2.53 - 2.57	[44]
Ba_5Ge_3	Ba_5Si_3 [96]	*P*4/*nnc*	*a* = 8.519(4) Å *c* = 16.554(8) Å *V* = 1201.38(2) Å^3 *Z* = 4, [50] *V*/atom = 37.5 Å^3			2.56	[50, 97]
Sr_5Ge_3	Cr_5B_3 [98]	*I*4/*mcm*	*a* = 8.134(4) Å *c* = 15.771(8) Å *V* = 1043.44(1) Å^3 *Z* = 4, [56] *V*/atom = 32.6 Å^3			2.59	[56, 97]

Compound	Structure type	Space group	Unit cell dimensions	Distances / Å			Literature
				Ni-Ge	Ni-Ni	Ge-Ge	
Ca_5Ge_3	Cr_5B_3 [98]	*I*4/*mcm*	*a* = 7.74(2) Å *c* = 14.66(2) Å *V* = 878.25(4) Å^3 *Z* = 4, [100] *V*/atom = 27.45 Å^3			2.56	[59, 97, 99]
BaGe	CrB [101]	*Cmcm*	***a*** = 5.058(5) Å ***b*** = 11.98(1) Å ***c*** = 4.300(2) Å *V* = 260.56(2) Å^3 *Z* = 4, [10] *V*/atom = 32.6 Å^3			2.63	[9-11]
SrGe	CrB [101]	*Cmcm*	***a*** = 4.86(1) Å ***b*** = 11.40(1) Å ***c*** = 4.19(1) Å *V* = 232.14(3) Å^3 *Z* = 4, [8] *V*/atom = 29.0 Å^3			2.63	[8, 9]
CaGe	CrB [101]	*Cmcm*	*a* = 4.575(2) Å *b* = 10.845(1) Å *c* = 4.001(1) Å *V* = 198.51(4) Å^3 *Z* = 4, [7] *V*/atom = 24.8 Å^3			2.59	[7, 102]
β-Ba_3Ge_4 (ht)	Ba_3Si_4 [103]	*P*4$_2$/*mnm*	***a*** = 8.621(6) Å ***c*** = 12.031(8) Å *V* = 894.16(1) Å^3 *Z* = 4 *V*/atom = 31.9 Å^3			2.56 -2.71	[51]
α-Ba_3Ge_4 (rt)	own	*Cmmm*	***a*** = 11.799(6) Å ***b*** = 12.210(6) Å ***c*** = 12.097(6) Å *V* = 1742.76 (2) Å^3 *Z* = 8 *V*/atom = 31.1 Å^3			2.57 - 2.87	[51]
$SrGe_{1.85}$	AlB_2 [104]	*P*6/*mmm*	*a* = 4.259(1) Å *c* = 4.578(1) Å *V* = 71.9(1) Å^3 *Z* = 1 *V*/atom = 25.2 Å^3			2.46	[45]
$BaGe_2$	$BaSi_2$ [105]	*Pnma*	*a* = 9.078(3) Å *b* = 6.829(2) Å *c* = 11.653(3) Å *V* = 722.41(1) Å^3 *Z* = 8, [55] *V*/atom = 30.1 Å^3			2.54 - 2.59	[52-55]
hp $BaGe_2$	$ThSi_2$ [106]	*I*4$_1$/*amd*	*a* = 4.769(3) Å *c* = 14.737(9) Å *V* = 335.17(1) Å^3 *Z* = 4 *V*/atom = 27.93 Å^3			2.45 - 2.68	[107]

Compound	Structure type	Space group	Unit cell dimensions	Distances / Å			Literature
				Ni-Ge	Ni-Ni	Ge-Ge	
$SrGe_2$	$BaSi_2$ [105]	*Pnma*	*a* = 8.739(2) Å *b* = 6.567(1) Å *c* = 11.215(2) Å *V* = 643.62(1) Å^3 *Z* = 8, [45] *V*/atom = 26.8 Å^3			2.50 - 2.58	[45, 57]
hp $SrGe_2$	$EuGe_2$ [108]	$P\bar{3}m$	*a* = 4.104(3) Å *c* = 5.165(5) Å *V* = 120.0(1) Å^3 *Z* = 3 *V*/atom = 26.8 Å^3			2.56	[58]
α-$CaGe_2$	KSnAs [109]	$P6_3mc$	*a* = 3.9966(9) Å *c* = 10.211(4) Å *V* = 141.24(7) Å^3 *Z* = 2 *V*/atom = 23.54 Å^3			2.54	[61]
β-$CaGe_2$	$CaSi_2$ [110]	$R\bar{3}m$	*a* = 3.9492 Å *c* = 30.7176 Å *V* = 421.1(2) Å^3 *Z* = 6 *V*/atom = 23.4 Å^3			2.52 - 2.55	[60]
$BaGe_3$	$BaSn_3$ [13, 63]	$P6_3/mmc$	*a* = 6.814(1) Å *c* = 5.027(8) Å *V* = 233.41(1) Å^3 *Z* = 2 *V*/atom = 29.17 Å^3			2.61 - 2.93	[62]
Ba_6Ge_{25}	K_6Sn_{25} [111]	$P4_132$	*a* = 14.5564(2) Å *V* = 3084.34 (1) Å^3 *Z* = 4, [64] *V*/atom = 24.9 Å^3			2.48 - 2.57	[64-66]
Ba_8Ge_{43}	own, clathrate	$Ia\bar{3}d$	*a* = 21.3123(5) Å *V* = 9680.34(1) Å^3 *Z* = 8, [67] *V*/atom = 23.7 Å^3			2.44 - 2.61	[67, 112]
$BaGe_5$	own, clathrate	*Pmna*	*a* = 10.727(1) Å *b* = 9.2844(7) Å *c* = 14.794(1) Å *V* = 1473.39(1) Å^3 *Z* = 10 *V*/atom = 24.6 Å^3			2.39 - 2.95	[68]
$SrGe_{6-\delta}$	$EuGa_2Ge_4$ [113]	*Cmcm*	*a* = 4.0981(6) Å *b* = 11.159(1) Å *c* = 12.6825(8) Å *V* = 579.98(1) Å^3 *Z* = 4 *V*/atom = 20.7 Å^3			2.44 - 2.92	[69]

Compound	Structure type	Space group	Unit cell dimensions	Distances / Å			Literature
				Ni-Ge	Ni-Ni	Ge-Ge	
Ni-Ge							
$NiGe_2$	$CoGe_2$ [114]	*Cmce*	a = 10.830(5) Å b = 5.763(3) Å c = 5.762(3) Å V = 359.63(2) Å^3 Z = 8 V/atom = 15.0 Å^3	2.49 - 2.53	2.48	2.53 - 3.09	[71]
NiGe	FeAs [115]	*Pnma*	a = 5.381 Å b = 3.428 Å c = 5.811 Å V = 107.19 Å^3 Z = 4 V/atom = 13.4 Å^3	2.33 - 2.49	2.78	2.82	[72]
Ni_3Ge_2	$Co_{1.75}Ge$ [116]	*P*6$_3$/*mmc*	a = 3.864 Å c = 5.042 Å V = 65.19 Å^3 Z = 1 V/atom = 13.0 Å^3	2.23 - 2.56	2.52 - 2.56		[73]
$Ni_{19}Ge_{12}$	own	*C*121	a = 11.631 Å b = 6.715 Å c = 10.048 Å β = 90.0° V = 784.77 Å^3 Z = 2, [73] V/atom = 12.6 Å^3	2.12 - 2.88	2.38 - 2.81		[73, 74]
Ni_5Ge_3	own	*C*121	a = 11.682(6) Å b = 6.737(3) Å c = 6.264(3) Å β = 52.11(1)° V = 389.06(2) Å^3 Z = 4 V/atom = 12.2 Å^3	2.14 - 2.92	2.41 - 2.72		[73]
Ni_2Ge (ht) (also reported as ε- as Ni_5Ge_3)	$Co_{1.75}Ge$ [116]	*P*6$_3$/*mmc*	a = 3.910(1) Å c = 5.036(1) Å V = 66.68(1) Å^3 Z = 2, [75] V/atom = 11.1 Å^3	2.26 - 2.58	2.52 - 2.58		[70, 75]
Ni_2Ge (rt)	β-Co_2Si [93]	*Pnma*	a = 5.113(3) Å b = 3.830(2) Å c = 7.264(4) Å V = 142.25(1) Å^3 Z = 4 V/atom = 11.9 Å^3	2.33 - 2.84	2.63 - 2.78		[73]
Ni_5Ge_2	Pd_5Sb_2 [117]	*P*6$_3$*cm*	a = 6.827(3) Å c = 12.395(5) Å V = 500.31(1) Å^3 Z = 6 V/atom = 11.9 Å^3	2.26 - 3.00	2.49 - 3.06		[73]
β-Ni_3Ge	Cu_3Au [118]	*Pm*$\bar{3}$*m*	a = 3.567(3) Å V = 45.39(1) Å^3 Z = 1 V/atom = 10.8 Å^3	--	2.52		[72]

Compound	Structure type	Space group	Unit cell dimensions	Distances / Å			Literature
				Ni-Ge	Ni-Ni	Ge-Ge	
***Ae*-Ni**							
SrNi	No structure solution	-	-				[79]
Ba_2Ni_3	Sr_2Ni_3 [78]	$P\bar{3}m1$	a = 4.2010(2)Å c = 9.1371(6)Å V = 139.65(2)Å^3 Z = 1 V/atom = 27.8 Å^3		2.43		[77]
Sr_2Ni_3	own	$P\bar{3}m1$	a = 4.1262(1) Å c = 8.6857(1) Å V = 128.1(1) Å^3 Z = 1 V/atom = 25.6 Å^3		2.41 - 2.49		[78]
$CaNi_2$	$MgCu_2$ [119]	$Fd\bar{3}m$	***a*** = 7.239 Å V = 379.35 Å^3 Z = 8 V/atom = 15.8 Å^3		2.56		[80]
$CaNi_3$	$PuNi_3$ [120]	$R\bar{3}m$	***a*** = 5.030 Å ***c*** = 24.27 Å V = 531.79 Å^3 Z = 9 V/atom = 14.8 Å^3		2.47 - 2.90		[80]
Ca_2Ni_7	Gd_2Co_7 [121]	$R\bar{3}m$	***a*** = 5.009 Å ***c*** = 36.06 Å V = 783.53 Å^3 Z = 6 V/atom = 14.5 Å^3		2.44 - 2.89		[80]
$CaNi_5$	$CaCu_5$ [122]	$P6/mmm$	***a*** = 4.955 Å ***b*** = 4.955 Å ***c*** = 3.941 Å V = 83.80 Å^3 Z = 1 V/atom = 14.0 Å^3		2.43 - 2.86		[80]

IV. Crystal structures

IV.1 Scope and outline

The ternary polar intermetallic compounds of the systems *Ae*/Ni/Ge display a wide range of different crystal structures ranging from one-dimensional to complex three-dimensional Ni-Ge structures. The crystal structures will be regarded on the basis of these Ni-Ge substructures, in analogy to the polyanionic structures of the *Tt* atoms in Zintl phases. Certainly, the description of the chemical bonding in the phases of the systems *Ae*/Ni/Ge is more complex compared to the binary Zintl phases, since the charge assignment to the Ni atoms is not well defined. However, structural similarities between Zintl phases and polar intermetallic phases are noticeable: for example, the Ni-Ge bonds in the ternary compounds $Ae_xNi_yGe_z$ are slightly elongated in comparison to the shortest Ni-Ge bonds observed in the binary compounds Ni_xGe_y as well as in comparison to the covalent Ni-Ge bonds in uncharged molecules such as [Ni(*bn*NHGe)$_4$] (*d*(Ni-Ge) = 2.23 Å), which was obtained from the benzo-anellated germylene (*bn*NHGe) and Ni(1,5-cod)$_2$ [123]. This relates to the *Tt*-*Tt* bonds in binary Zintl phases Ae_xTt_y in comparison to the bondlength of the elemental modifications. The increase of the bond distance originates from the electrostatic repulsion of charges located on the atoms of the polyanion.

In this article common and different structural features of the Ni-Ge substructures observed in the crystal structures of the ternary compounds $Ae_xNi_yGe_z$ shall be discussed, focusing on various aspects:

- In chapter IV.2 the structural motif of the $^1_\infty$[NiGe] ribbons is introduced as a fundamental building unit. It appears in the isotypic compounds SrNiGe (**1a**) and BaNiGe (**1b**) without further Ni-Ge bonds to neighboring Ni or Ge atoms. A schematic description of various structures constructed of the $^1_\infty$[NiGe] ribbons is given in Figure 4.
- In chapter IV.3 the influence of the size of the *Ae* atoms on the dimensionality of the Ni-Ge polyanions is demonstrated on the basis of the compounds with the composition 1:1:1 (**1a** – **3**) and 1:2:2 (**4a** – **6**).

- In chapter IV.4 a systematic view of the crystal structures in the systems *Ae*/Ni/Ge in terms of above mentioned $^{1}_{\infty}$[NiGe] ribbons is established. We are able to trace back the broad variety of crystal structures of the compounds **1a** to **16** to the same structural motif of the $^{1}_{\infty}$[NiGe] ribbons. An overview of the structures of the compounds **1a** to **16** is given in Figure 5.
- In chapter IV.5 the Ni rich intermetallic phases (**17** – **21**) are discussed. As it will become obvious in the course of the following discussion, the crystal structures of the compounds **17** to **21** vary significantly from those of the compounds **1** to **16**. For example, the crystal structures of compounds **1** to **16** can be derived in a straightforward way from the common motif of the $^{1}_{\infty}$[NiGe] ribbons, while more complex structures are observed for **17** to **22**.
- In chapter IV.6 and IV.7 two rather outstanding compounds are discussed: the Ge rich clathrate $Ba_8Ni_{3.5}Ge_{42.1}$ (**22**) as well as Ba_2NiGe_3 (**23**). Their crystal structures deviate clearly from all the other ternary compounds observed in the systems *Ae*/Ni/Ge.

Throughout the article, two more aspects will superimpose the descriptions of the crystal structures indicated above. The first aspect is a principle governing the relationships between the crystal structures, which becomes evident when examining a composition triangle *Ae*/Ni/Ge containing all compounds (Figure 6): Most intermetallic compounds are situated on the connecting lines between the elements and the simple binary compositions (2:1, 1:1, 1:2). The lines ① to ④ given in Figure 6 will be discussed in detail. In the systems *Ae*/Ni/Ge compounds with compositions deviating from those lines are the Ni rich compounds $Ca_{10}Ni_{34}Ge_{16}$ (**17**), $CaNi_5Ge_3$ (**18**), $Ca_{15}Ni_{68}Ge_{37}$ (**19**), $Ca_7Ni_{49}Ge_{22}$ (**20**) as well as $SrNi_9Ge_4$ (**21**). A similar situation was observed for the systems *Re*/*M*/Ge (*Re*: Rare Earth, *M*: s- or d-element) by P.S. Salamankha [124].

The second aspect is the structural relationship of the ternary intermetallic phases and binary phases of the systems *Ae*/Ni/Ge. Whenever such a relationship exists, this is pointed out. As it will be shown, most compounds of the systems *Ae*/Ni/Ge can be deduced from binary compounds of the systems *Ae*/Ni, Ni/Ge or *Ae*/Ge by formal addition of a third element (Ge, *Ae* or Ni, respectively).

IV.2 $^{1}_{\infty}$[NiGe] ribbons – a basic module in various structure motifs

A basic module for many compounds in the systems *Ae*/Ni/Ge is the $^{1}_{\infty}$[NiGe] ribbon which consist of a square ladder of alternating Ni and Ge atoms (Figure 4a). Depending on the characteristics of the crystal structures, these ribbons are subject to a more or less pronounced folding (Figure 4b) and rhombic distortion leading to the formation of short bonds along one of the diagonals of the Ni_2Ge_2 squares (dashed lines in Figure 4c). In Figure 4d to Figure 4l various combinations of the $^{1}_{\infty}$[NiGe] ribbons are schematically discussed in order to facilitate the following discussion of the crystal structures.

A schematic view of the ribbons is shown in Figure 4b. A parallel alignment of these ribbons and a *transoid* connection by the formation of Ni-Ge bonds (as shown in Figure 4d) leads to a square atom layer of one type of atoms (Ni or Ge) which is alternately capped below and above by atoms of the second type (Ge or Ni, respectively, Figure 4e and Figure 4f). This PbO-type motif is discussed with different possibilities of the atom occupation in Figure 4g to Figure 4i, since it is an important structural motif in the systems *Ae*/Ni/Ge. The PbO-type layer with Ni atoms on the square layers and Ge atoms on the capping positions is shown in Figure 4g. The Ni atoms are tetrahedrally coordinated by Ge atoms, the Ge atoms are situated on the top of a square pyramid Ni_4Ge.The anti-PbO-type layer with Ge atoms on the square layers and Ni on the capping positions is shown in Figure 4h. The Ge atoms are tetrahedrally coordinated by Ni atoms, the Ni atoms are situated on top of the square pyramid Ge_4Ni. In the systems *Ae*/Ni/Ge this anti-PbO-type is only observed if a further Ni-Ge bond, connecting the capping Ni atoms with an additional structure motif, exists. Thus, the Ni atoms have five nearest Ge neighbors. In Figure 4i a superstructure of the anti-PbO-type is presented: the square atom layer as well as the capping positions above this layer are occupied by Ge atoms, the capping positions below this layer are occupied by Ni atoms. Thus, slabs with the composition $^{2}_{\infty}$[$NiGe_3$] result.

In Figure 4j the $^{1}_{\infty}$[NiGe] ribbons are arranged vertically. The parallel arrangement allows the formation of Ni-Ge bonds to the neighboring ribbon such that hexagonal prisms result. Each prism is centered by an additional Ni atom. A linear arrangement of hexagonal prisms that share rectangular faces results, having the overall composition $^{1}_{\infty}$[$Ni@Ni_2Ge_2Ni_{4/2}Ge_{4/2}$].

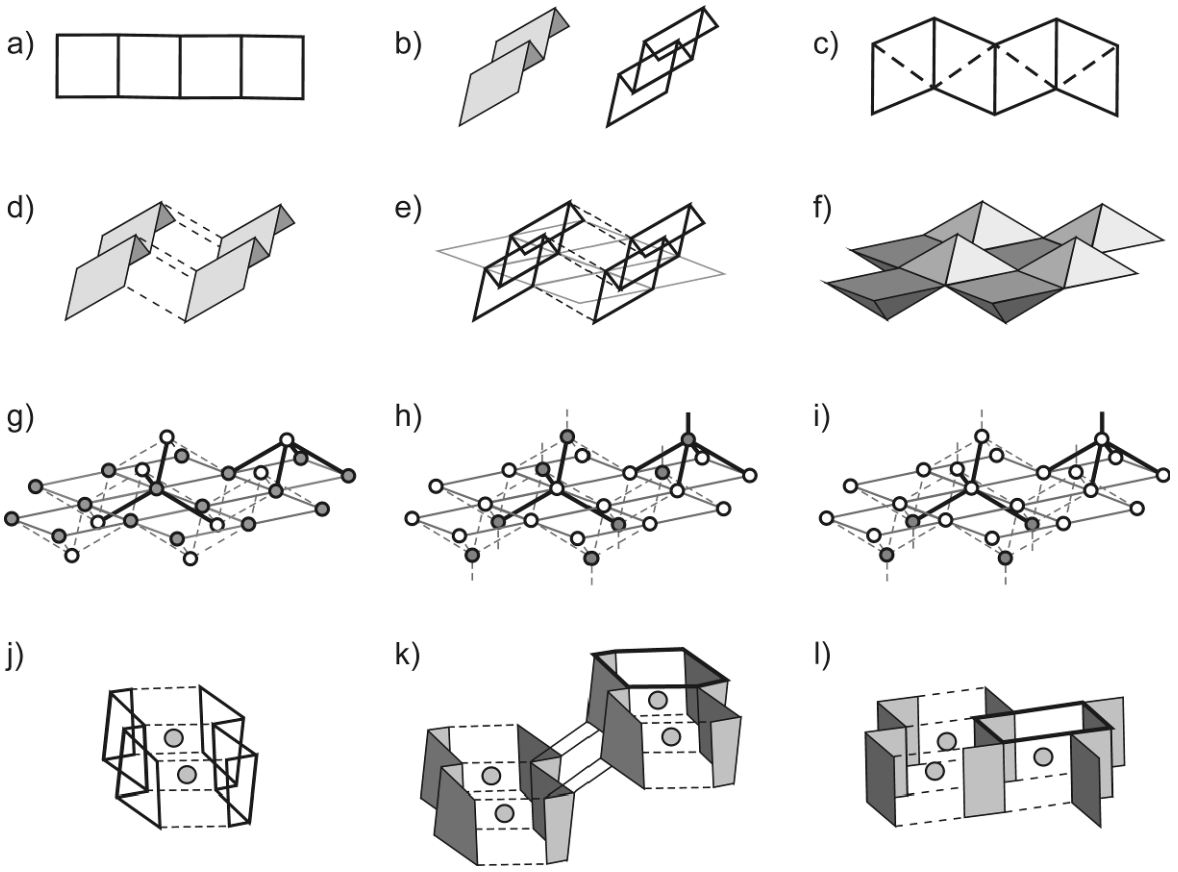

Figure 4 Schematic construction of structure motifs observed in the systems *Ae*/Ni/Ge. (a) The basic module are distorted square $^{1}_{\infty}$[NiGe] ladders. (b) Folding of the ladder to a Ni-Ge ribbon (as observed in **2**). (c) Rhombic distortion of the ladder (as observed in **1a** and **1b**) leading to the formation of Ni-Ni bonds (dashed lines). (d) *Transoid* connection of two parallel ribbons. (e) and (f) Formation of a square net alternately capped with atoms below and above the square plane from ribbons. (g) PbO-type layer with Ni atoms forming a square atom layer and Ge at the capping positions. (h) Anti-PbO-type layer with Ge on the square net and Ni on the capping positions. Upright bonds from the capping Ni atoms to further parts of the structure are indicated. (i) Superstructure of the anti-PbO-type with Ge atoms forming the square atom layer. Ge atoms act as square caps on one side and Ni atoms on the other side (j) *Cisoid* arrangement of parallel $^{1}_{\infty}$[NiGe] ribbons which are linked via Ni-Ge bonds. The resulting hexagonal prisms are Ni-centered. (k) *Transoid* arrangement of one-dimensional rods of Ni-centered hexagonal prisms of Figure 4j. (l) Two-dimensional layer of Ni-centered hexagonal prisms as a result of the full connection of $^{1}_{\infty}$[NiGe] ribbons. The Ni and Ge atoms are given in grey and white, respectively.

In Figure 4k a combination of two one-dimensional rods of face-sharing hexagonal prisms is shown. These are connected via Ni-Ge bonds and are arranged *transoid* to each other. The resulting two-dimensional layer has the composition $^{2}_{\infty}$[Ni_5Ge_4]. Directly connecting $^{1}_{\infty}$[NiGe] ribbons as indicated in Figure 4j leads to two-dimensional layers of

Ni-centered face-sharing hexagonal prisms (Figure 4l). The layers have the composition $^{2}_{\infty}[Ni_3Ge_2]$.

The similarities of the compounds **1** – **16** based on the basic building unit $^{1}_{\infty}[NiGe]$ ribbons, are presented in Figure 5. Note, that the description of the various networks containing $^{1}_{\infty}[NiGe]$ ribbons is not deduced from a variation of the bond length, it is merely an aid in order to allow the comparison of the various crystal structures. Furthermore notice, that the compounds $SrNiGe_3$ (**7**), $Ca_3Ni_3Ge_7$ (**12a**), $Sr_3Ni_3Ge_7$ (**12b**) and $CaNiGe_3$ (**13**) do not contain $^{1}_{\infty}[NiGe]$ ribbons. They are nevertheless included in Figure 5 as they can be deduced in a straightforward way from SrNiGe (**1a**) and BaNiGe (**1b**).

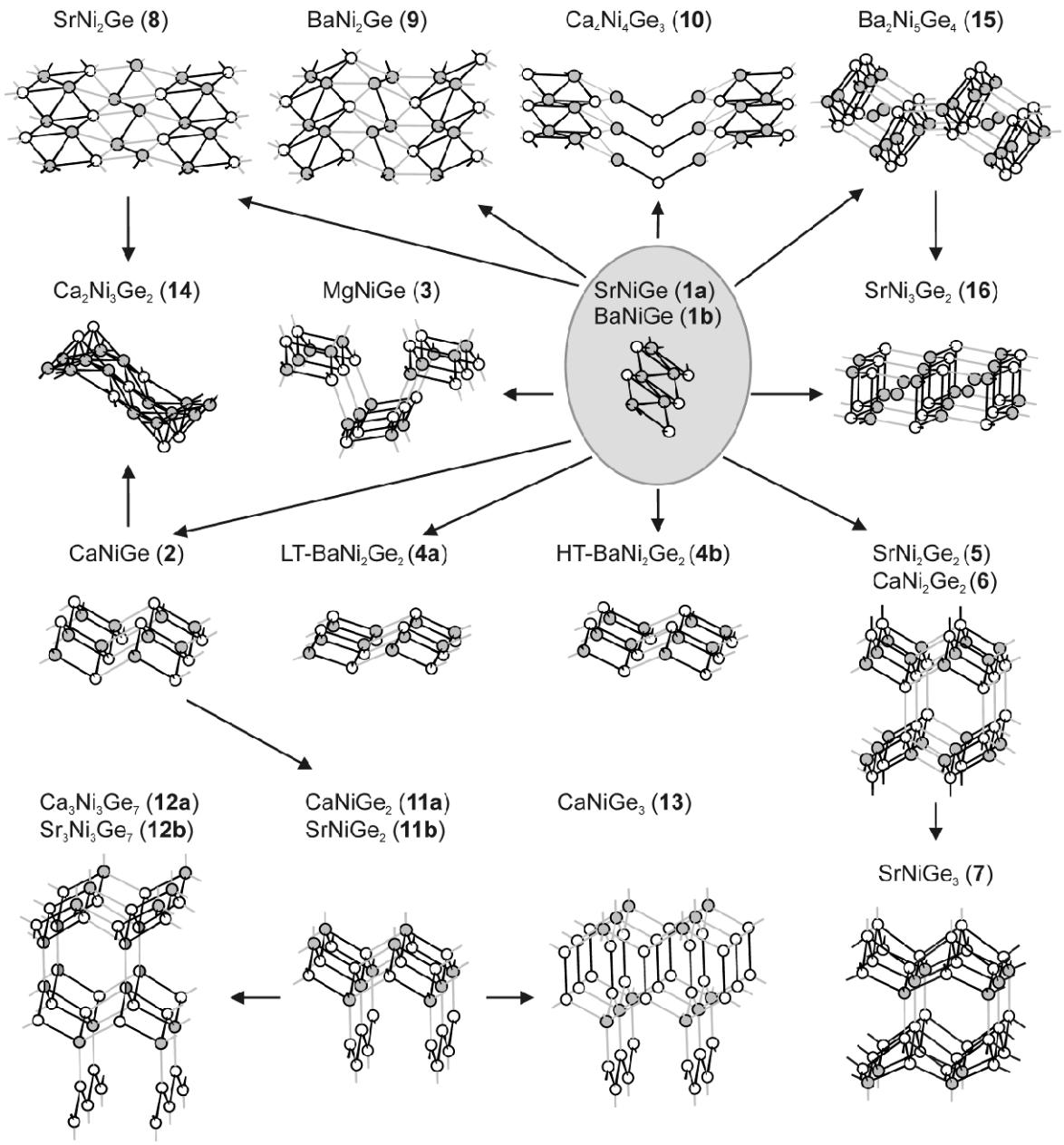

Figure 5 Cutouts of the polyanionic Ni-Ge networks observed in the crystal structures of the compounds **1** – **16**. Chosen bonds are emphasized in order to demonstrate the relationship of the networks with the $^{1}_{\infty}$[NiGe] ribbons observed in SrNiGe (**1a**) and BaNiGe (**1b**). The Ni and Ge atoms are drawn in grey and white, respectively.

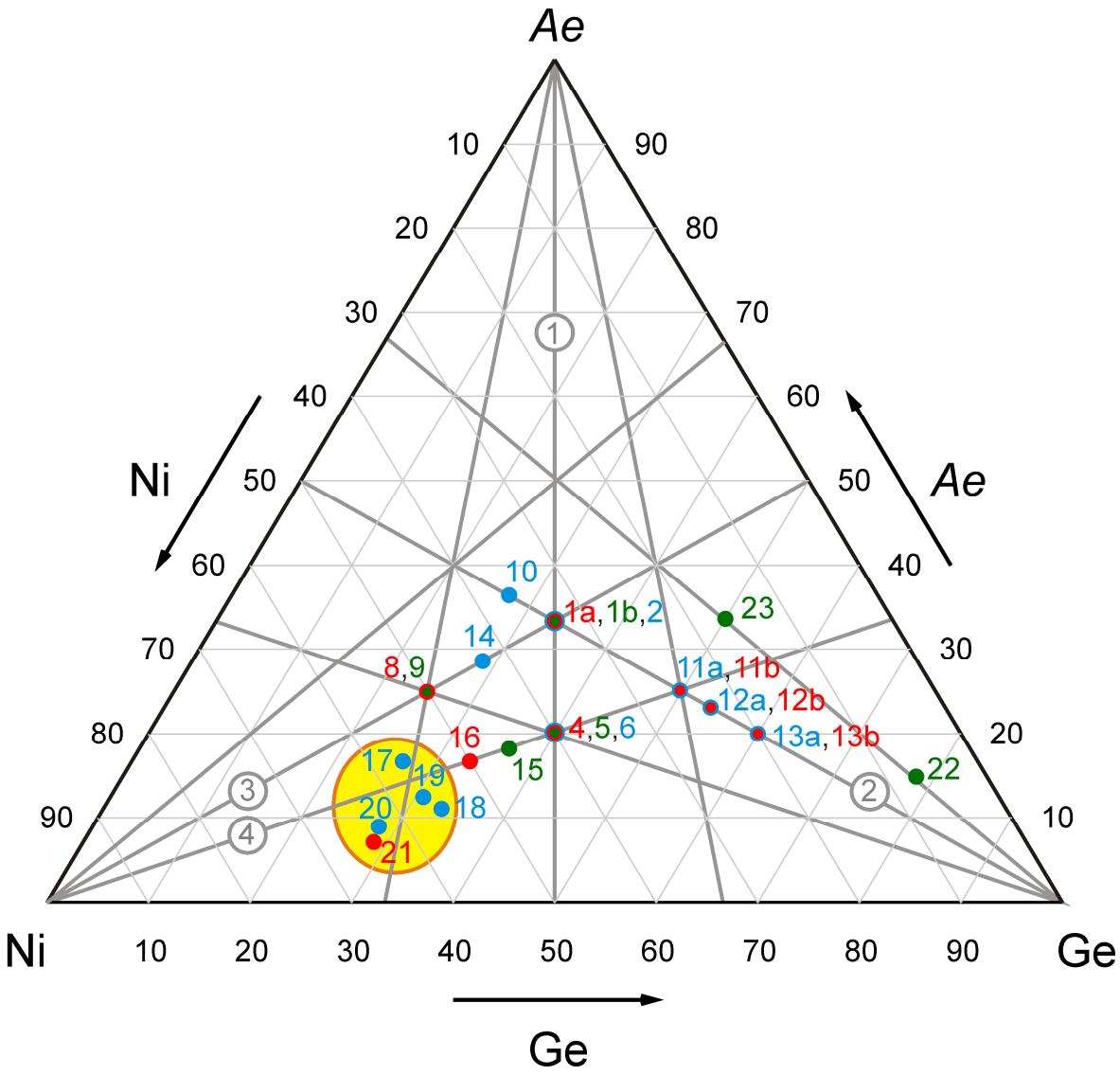

Figure 6 Composition triangle of the systems *Ae*/Ni/Ge (*Ae*: Ca, Sr, Ba). The compounds $Ca_xNi_yGe_z$ are given in blue, the compounds $Sr_xNi_yGe_z$ in red and the compounds $Ba_xNi_yGe_z$ in green. Additionally, the lines connecting the elements with the – partly hypothetical – compounds of simple composition (2:1, 1:1, 1:2) are given. The lines which are discussed in more detail in the text are numbered as lines ① to ④. The field in which the intermetallic compounds found are not situated on these lines is highlighted in yellow. For the sake of clarity the binary compounds were neglected.

IV.3 Influence of an increasing size of *Ae* on the dimensionality of the Ni-Ge polyanions

The influence of the size of the alkaline earth metals on the dimensionality of the Ni-Ge polyanions becomes obvious regarding the series of compounds *Ae*NiGe ([23, 25]) and *Ae*Ni_2Ge_2 ([26, 32]).

IV.3.1 The series AeNiGe (Ae = Mg, Ca, Sr, Ba)

Equiatomic intermetallic compounds *Ae*NiGe were observed for *Ae* = Mg, Ca, Sr and Ba. The isotypic compounds SrNiGe (**1a**) and BaNiGe (**1b**) crystallize in the space group *Pnma*, with one-dimensional $^1_\infty$[NiGe] ribbons running parallel to the *b* axis (Figure 7a and Figure 7b). The ribbon was introduced above as a basic structural unit that occurs in many other compounds of the systems *Ae*/Ni/Ge. A rhombic distortion of this Ni-Ge ladder leads to shorter Ni-Ni contacts (SrNiGe: *d*(Ni-Ni) = 2.58 Å, BaNiGe: *d*(Ni-Ni) = 2.59 Å) along the diagonal of the Ni_2Ge_2 rhomb (compare with Figure 4c). The resulting coordination numbers are three for the Ge (3 × Ni) and five for the Ni (3 × Ge + 2 × Ni) atoms.

Reducing the size of the alkaline earth cation leads to a two-dimensional polyanionic $^2_\infty$[NiGe] layer of the PbO-type [125] in CaNiGe (**2**). This layer consists of a regular square net of Ni atoms (*d*(Ni-Ni) = 2.96 Å) being alternately capped by Ge atoms and thus all Ni-Ge distances are equal (*d*(Ni-Ge) = 2.43 Å). However, as shown in Figure 4d to Figure 4g these layers may also be described by fusion of one-dimensional $^1_\infty$[NiGe] ribbons of SrNiGe (**1a**) and BaNiGe (**1b**) that are connected via Ni-Ge bonds. Due to this connection the rhombic distortion of the ladders is less pronounced: While the Ni-Ni distances of SrNiGe (**1a**) (2.58 Å) and BaNiGe (**1b**) (2.59 Å) compare to those found in *fcc*-Ni (Ni-Ni = 2.49 Å [126]), the corresponding Ni-Ni distance in CaNiGe (**2**) is significantly longer (2.96 Å). Within the PbO-type layer the Ni atoms adopt a distorted tetrahedral coordination of Ge atoms ($\sphericalangle$Ge-Ni-Ge = 119.0°).

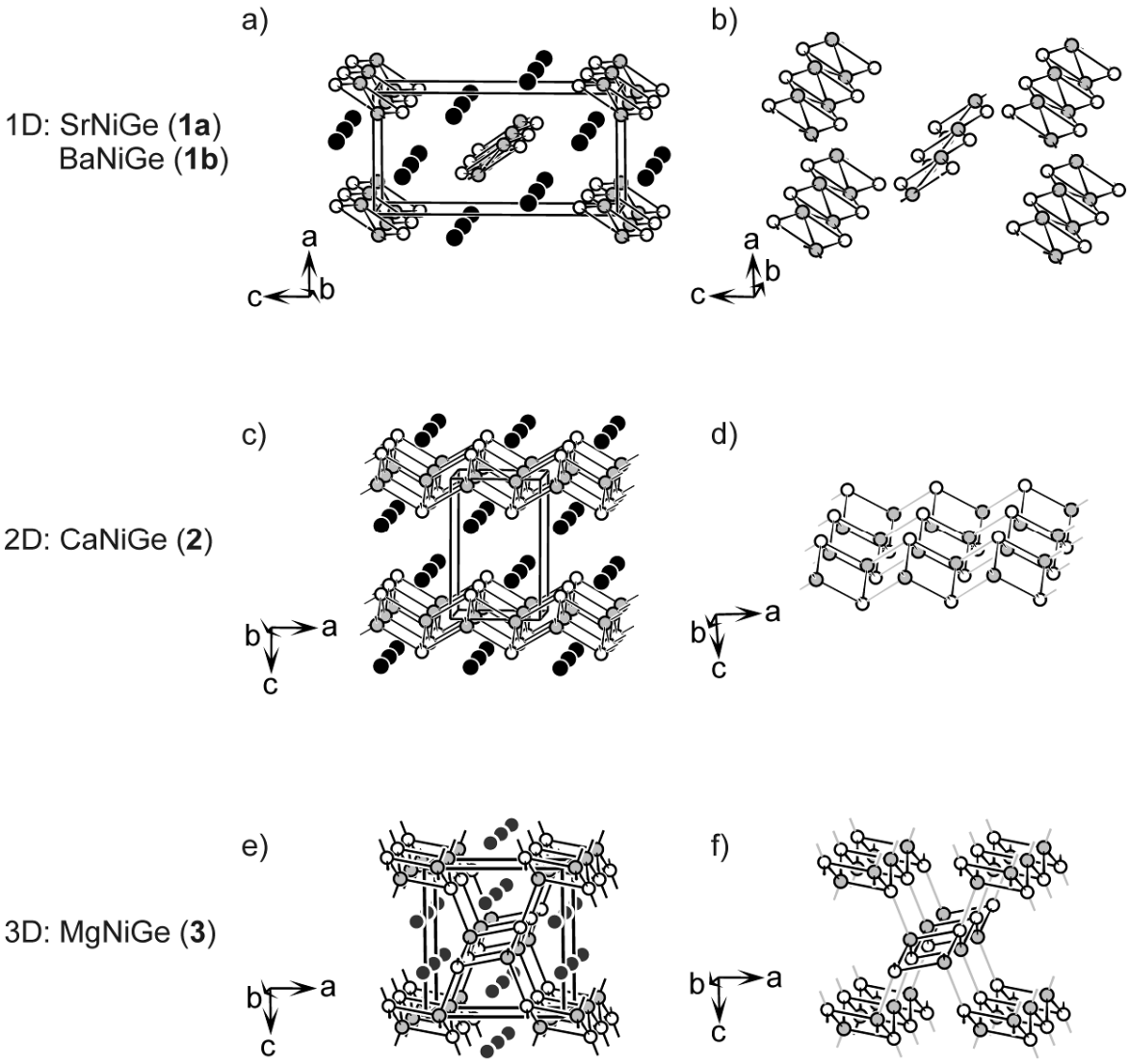

Figure 7 Crystal structures of a-b) SrNiGe (**1a**), BaNiGe (**1b**), c-d) CaNiGe (**2**) and e-f) MgNiGe (**3**). In b), d) and f) the polyanionic Ni-Ge networks are given. For CaNiGe (**2**) and MgNiGe (**3**) the Ni-Ge bonds are given in different colors, emphasizing the construction from the one-dimensional $^{1}_{\infty}$[NiGe] ribbons. The alkaline earth metal atoms are drawn in black, the Ni and Ge atoms in grey and white, respectively.

In contrast, the Ge atoms adopt a fourfold coordination of Ni atoms by forming the top of a square pyramid with a Ni_4 base.

The further reduction of the size of the cation in MgNiGe (**3**) leads to a three-dimensional $^{3}_{\infty}$[NiGe] network with exclusively fourfold connected Ni and Ge atoms (within the ribbons: ∢Ge-Ni-Ge = ∢Ni-Ge-Ni = 116.7°, connecting the ribbons: ∢Ge-Ni-Ge = 121.9°, ∢Ni-Ge-Ni = 100.4°). As emphasized in Figure 7f the structure can

further be described using the $^{1}_{\infty}$[NiGe] ribbons as basic building units. The ribbons are connected under formation of exclusively Ni-Ge bonds.

As a result, six-membered rings with chair conformation are formed between the $^{1}_{\infty}$[NiGe] ribbons. The Ni-Ni distance (2.95 Å) within the $^{1}_{\infty}$[NiGe] ribbons is comparable to the one found in CaNiGe. The Ni-Ge distances within the $^{1}_{\infty}$[NiGe] ribbons of 2.39 Å and 2.40 Å are slightly shorter than those connecting the ribbons (2.44 Å).

Most of the intermetallic compounds with the composition 1:1:1 of the systems *Re*/Ni/Ge, containing the even smaller rare earth cations, crystallize just as MgNiGe (**3**) in the TiNiSi structure type (*Re*NiGe with *Re* = Y, Ce, Pr, Nd, Gd, Tb, Dy, Ho, Er, Tm, Lu) [127-129]. The high temperature modification of LuNiGe (HT-LuNiGe) crystallizes in an own structure type, which also contains a three-dimensional polyanionic network. The coordination numbers in HT-LuNiGe vary between three to six for Ge and four to five for Ni. The relationship of HT-LuNiGe with the TiNiSi structure type was shown in [130]. A two-dimensional crystal structure is found for the largest rare earth metal cation EuNiGe [131], underlining the linkage of the dimensionality and the size of the cation.

IV.3.2 The series $AeNi_2Ge_2$ (Ae = Ca, Sr, Ba)

A similar trend concerning the changes of dimensionality is observed for the compounds AeNi$_2$Ge$_2$ (*Ae* = Ca, Sr, Ba). As emphasized in Figure 8, due to the lower portion of *Ae* no one-dimensional structural motifs occur, but two-dimensional $^{2}_{\infty}$[NiGe] layers are formed for $BaNi_2Ge_2$. The $^{2}_{\infty}$[Ni_2Ge_2] layers of HT-$BaNi_2Ge_2$ (**4b**) and LT-$BaNi_2Ge_2$ (**4a**) can be described analogously to the $^{2}_{\infty}$[NiGe] layer of CaNiGe (**2**) as being built up by the basic unit $^{1}_{\infty}$[NiGe]. For HT-$BaNi_2Ge_2$ (**4b**) regular PbO-type nets, which consist of square layers of Ni atoms (*d*(Ni-Ni) = 3.02 Å) that are capped by Ge atoms (*d*(Ni-Ge) = 2.35 Å), result ($\sphericalangle$Ge-Ni-Ge = $\sphericalangle$Ni-Ge-Ni = 130.0°). The distances and thus the rhombic distortion of the $^{1}_{\infty}$[NiGe] ribbons is comparable to CaNiGe (**2**). In LT-$BaNi_2Ge_2$ (**4a**) a distortion of the square layer of Ni atoms takes place. Consequently, the rhombic distortion varies significantly from those described before: next to a reduction of the Ni-Ni distances (*d*(Ni-Ni) = 2.81 Å to *d*(Ni-Ni) = 2.83 Å) short Ge-Ge distances result (*d*(Ge-Ge) = 2.93 Å). In contrast, the Ni-Ge distances (2.28 Å to 2.39 Å) remain in the same range (HT-$BaNi_2Ge_2$ (**4b**): d(Ni-Ge) = 2.35 Å).

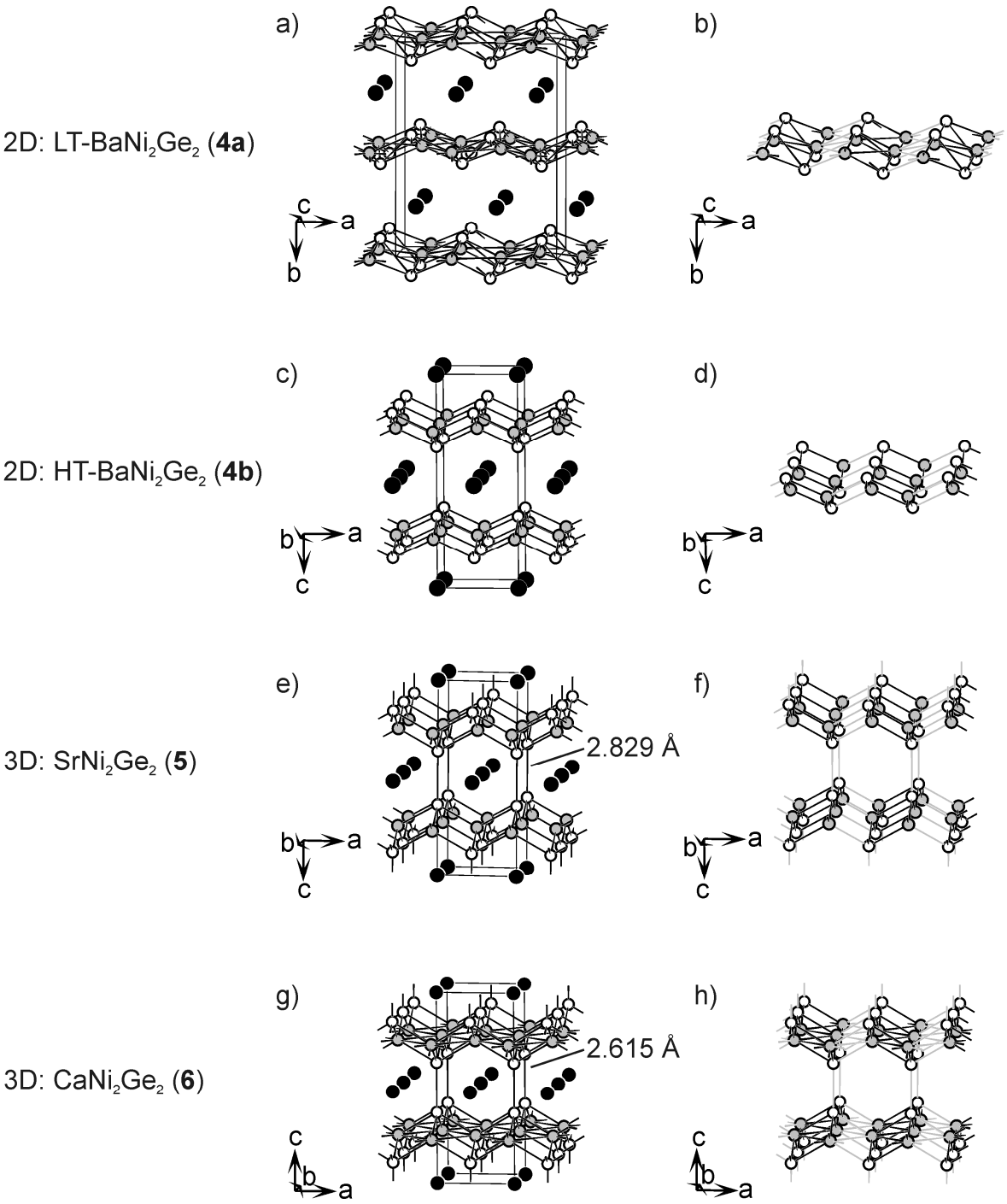

Figure 8 Crystal structures of a-b) LT-$BaNi_2Ge_2$ (**4a**), c-d) HT-$BaNi_2Ge_2$ (**4b**), e-f) $SrNi_2Ge_2$ (**5**), g-h) $CaNi_2Ge_2$ (**6**). In b), d), f) and h) the polyanionic Ni-Ge networks are given. The alkaline earth metal atoms are drawn in black, the Ni and Ge atoms in grey and white, respectively.

The shortest interlayer distance is found between Ge atoms (LT-$BaNi_2Ge_2$ (**4a**): $d_{interlayer}$(Ge-Ge) = 3.95 Å and HT-$BaNi_2Ge_2$ (**4b**): $d_{interlayer}$(Ge-Ge) = 3.64 Å). These distances underline the two-dimensional character of these compounds. This interlayer

distance is drastically reduced to 2.83 Å for $SrNi_2Ge_2$ (**5**). However, the Ge-Ge distance is still longer than in elemental Ge (2.45 Å [132]).

For $CaNi_2Ge_2$ (**6**), the interlayer Ge-Ge distance is further reduced to 2.62 Å. This clearly indicates covalent bonding, which was confirmed by a topological analysis of the ELF [25]. Similar to $CaNi_2Ge_2$ (**6**), the compounds *Re*Ni_2Ge_2 (*Re*: La, Ce, Pr, Nd, Sm, Eu, Gd, Tb, Ho, Er, Yb, Lu) [33, 133], which contain small rare earth metal atoms, crystallize in the $ThCr_2Si_2$ structure type with short interlayer distances, indicating covalent bonding between the Ge atoms.

IV.3.3 Removal of Ca - from AeNiGe to $AeNi_2Ge_2$ and NiGe (Line① in the composition triangle)

The intermetallic compounds *Ae*NiGe, *Ae*Ni_2Ge_2 and NiGe are situated on line ①, as shown in the composition triangle of the systems *Ae*/Ni/Ge (Figure 6). The topological relationship of their crystal structures is shown in Figure 9. The two compounds CaNiGe and *Ae*Ni_2Ge_2 contain the same PbO-type layers. These are square nets of Ni atoms, each square being alternately capped above and below the plane by Ge atoms. Due to the relatively high amount of Ca atoms, in CaNiGe (**2**) the layers are well separated by Ca atoms. Therefore, no bonding interactions occur between the layers that are stacked according to the primitive stacking sequence AA. In *Ae*Ni_2Ge_2 (*Ae*: Ca, Sr, Ba) 50% of the alkaline earth metal atoms are removed and due to the layer sequence ABAB shorter distances between the Ge atoms are possible. For the smaller *Ae* atoms Ca and Sr covalent bonds between the Ge atoms form, for HT-$BaNi_2Ge_2$ (**4b**) longer Ge-Ge contacts (3.64 Å) result. Removing all Ca atoms and allowing a stacking of the PbO-type layers according to the sequence AA leads to the formation of Ni-Ge bonds between the layers. The resulting structure is the binary NiGe structure [72] (FeAs structure type), which clearly consists of a three-dimensional network of Ni and Ge atoms (Figure 8c) with Ni-Ge distances varying in the range from 2.33 Å to 2.48 Å. Furthermore, the NiGe structure can be traced back to $^1_\infty$[NiGe] ribbons that are connected via Ni-Ge bonds.

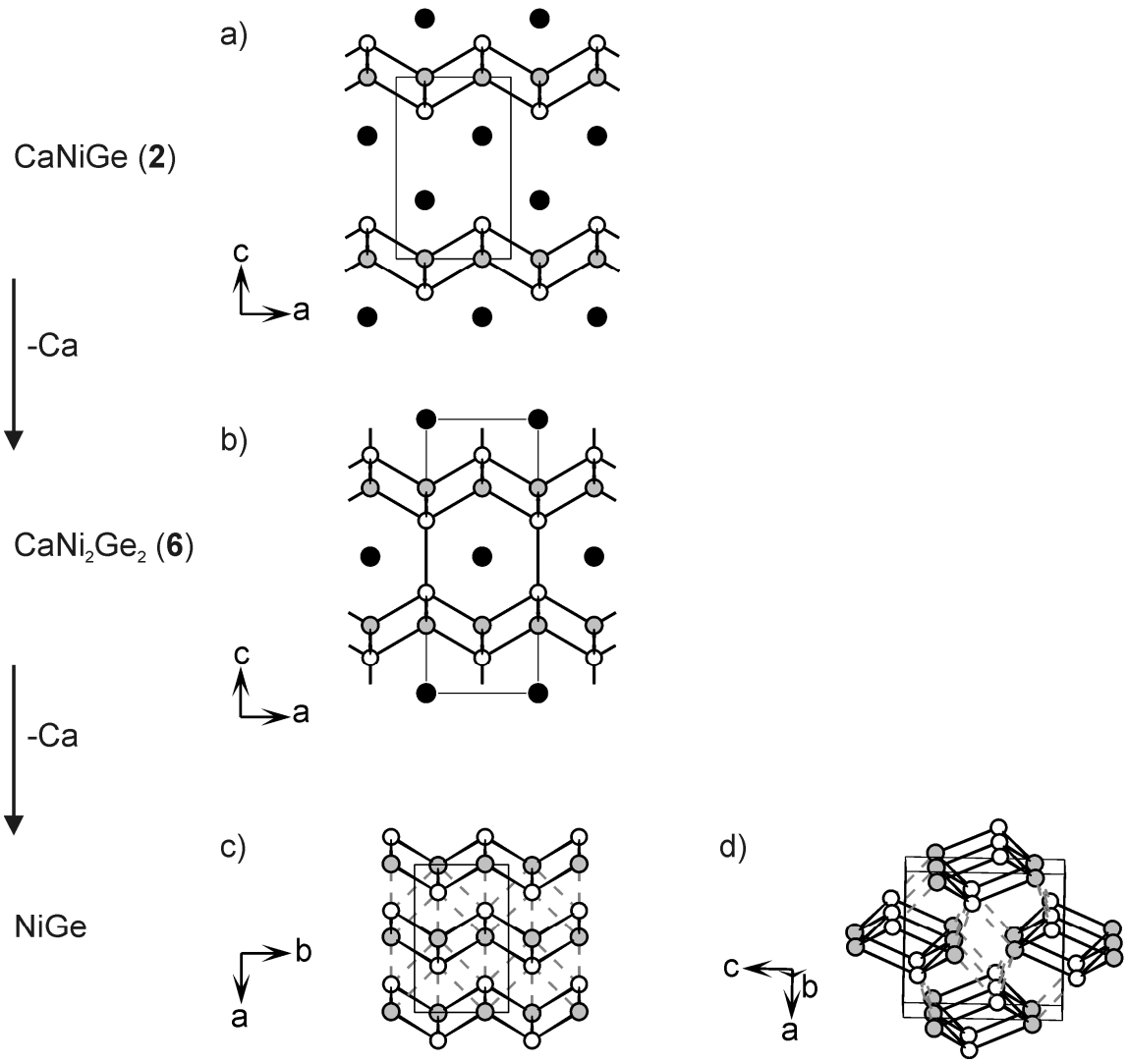

Figure 9 Crystal structures of a) CaNiGe (**2**), b) $CaNi_2Ge_2$ (**6**) and c) to d) NiGe. The Ca atoms are drawn in black, the Ni and Ge atoms in grey and white, respectively.

Changing the point of view one might say, that the insertion of alkaline earth metal atoms into the structure of NiGe leads to the formation of the crystal structures of *Ae*Ni_2Ge_2 and *Ae*NiGe.

In recent years the alkaline earth metal and alkaline metal iron arsenides have attracted attention, being either superconducting themselves or becoming superconducting upon doping. The intermetallic compounds of NaFeAs [134] (CeFeSi structure type [135]) and *Ae*/*A*Fe_2As_2 (*Ae*: Sr, Ba [136], *A*: K [137]; $ThCr_2Si_2$ structure type [138]) crystallize in the same structure types as CaNiGe and *Ae*Ni_2Ge_2 (*Ae*: Ca, Sr, Ba). Thus, a topological similar series leading to FeAs can be described concerning the reduction of the amount of *Ae*/*A*. A further superconductor is FeSe [139], which crystallizes in the PbO structure type

[125]. Its layered structure can be considered as an empty prototype, which is filled with alkaline metal and alkaline earth metal atoms in NaFeAs, *Ae*/*A*Fe_2As_2, *Ae*NiGe and *Ae*Ni_2Ge_2.

IV.4 The compounds 7 – 16 of the systems *Ae*/Ni/Ge

The polyanionic networks observed in the crystal structures of the compounds **2** to **16** can all be derived from the $^1_\infty$[NiGe] ribbons found in SrNiGe (**1a**) and BaNiGe (**1b**) as it was presented already above for compounds **2** to **6** (Figure 4).

IV.4.1 $SrNiGe_3$ (7)

$SrNiGe_3$ (**7**) ([23], Figure 10) contains a three-dimensional $^3_\infty$[$NiGe_3$] network. The network consists of two-dimensional layers which are connected via Ni-Ge bonds. The atomic arrangement within the layers is an ordered variant of the anti-PbO-type layers and was presented in Figure 4i. Square nets of Ge atoms are capped on one side of the plane by Ge and on the other side with Ni atoms. The caps of two neighboring layers are connected by Ni-Ge bonds of 2.373 Å. The Ge atoms within the square nets are coordinated tetrahedrally by two Ni and two Ge atoms. The capping Ni atoms are situated on the top of a square pyramid Ge_4Ni and are bonded to an additional Ge atom of the neighboring layer. A new coordination environment is observed for the capping Ge atoms, which are situated on the top of a square pyramid Ge_4Ge and are further bonded to a capping Ni atom of the neighboring layer. Thus, the Ge atoms have five nearest neighbors, 4 × Ge (d(Ge-Ge) = 2.718 Å) and 1 × Ni (d(Ni-Ge) = 2.373 Å).

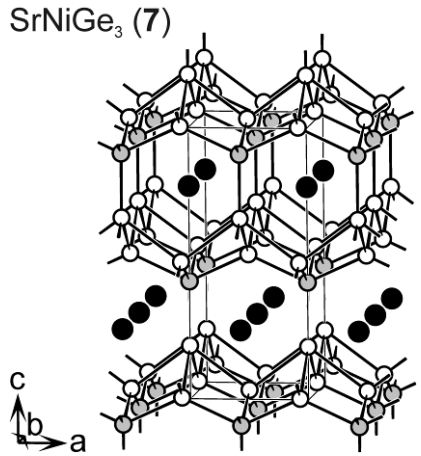

Figure 10 Crystal structure of $SrNiGe_3$ (**7**). The Ca atoms are drawn in black, the Ni and Ge atoms in grey and white, respectively.

*IV.4.2 $SrNi_2Ge$ (**8**) and $BaNi_2Ge$ (**9**)*

The $^2_\infty[Ni_2Ge]$ layers observed in $SrNi_2Ge$ (**8**) and $BaNi_2Ge$ (**9**) are separated by Sr and Ba atoms, respectively (Figure 11a to Figure 11d). The layers can be deduced from $^1_\infty[NiGe]$ ribbons which are connected via a zigzag chain of Ni atoms. The rhombic distortions of the $^1_\infty[NiGe]$ ribbons are comparable to the ones observed in **1a** and **1b**, the Ni-Ni distance in $SrNi_2Ge$ (**8**) is 2.50 Å, the Ni-Ni distance in $BaNi_2Ge$ (**9**) is 2.53 Å (dashed lines in Figure 4c). Based on the formula of SrNiGe (**1a**) or BaNiGe (**1b**), containing isolated $^1_\infty[NiGe]$ ribbons, the formal addition of one Ni atom per formula unit leads to the empirical formula of **8** and **9**: *Ae*NiGe + "Ni" $\rightarrow$ *Ae*Ni_2Ge. The Ni atoms of the chain form three Ni-Ni and three Ni-Ge bonds to the atoms of the neighboring ribbons. As a result, corrugated 6^3 nets of Ni atoms are formed. The Ni hexagons are centered by Ge atoms. Different orientations of Ni zigzag chains connecting the parallel $^1_\infty[NiGe]$ ribbons lead to a different puckering of the $^2_\infty[Ni_2Ge]$ layers in $SrNi_2Ge$ (**8**) and $BaNi_2Ge$ (**9**): in $SrNi_2Ge$ (**8**) the Ni hexagons have exclusively chair conformation, whereas in $BaNi_2Ge$ (**9**) rings with entirely boat conformation are present.

Comparing $SrNi_2Ge$ (**8**) and $BaNi_2Ge$ (**9**) with the binary compounds of similar composition, the intermetallic phases Sr_2Ni_3 and Ba_2Ni_3 ([77, 78], Figure 11e and Figure 11f) have to be mentioned. In these compounds the Ni atoms form the same puckered hexagonal layers as observed for the Ni-Ge layers in $SrNi_2Ge$ (**8**). The Ni-Ni distances in $SrNi_2Ge$ (**8**) (d(Ni-Ni) = 2.50 Å) and $BaNi_2Ge$ (**9**) (d(Ni-Ni) = 2.48 Å to d(Ni-Ni) = 2.52 Å) are in good agreement with the corresponding Ni-Ni distances in Sr_2Ni_3

(*d*(Ni-Ni) = 2.41 Å to *d*(Ni-Ni) = 2.49 Å) and Ba_2Ni_3 (*d*(Ni-Ni) = 2.43 Å). Furthermore, the relationship of $SrNi_2Ge$ (**8**) with AlB_2 [104], NiAs [140] and Ni_2Si [141] was shown in [27].

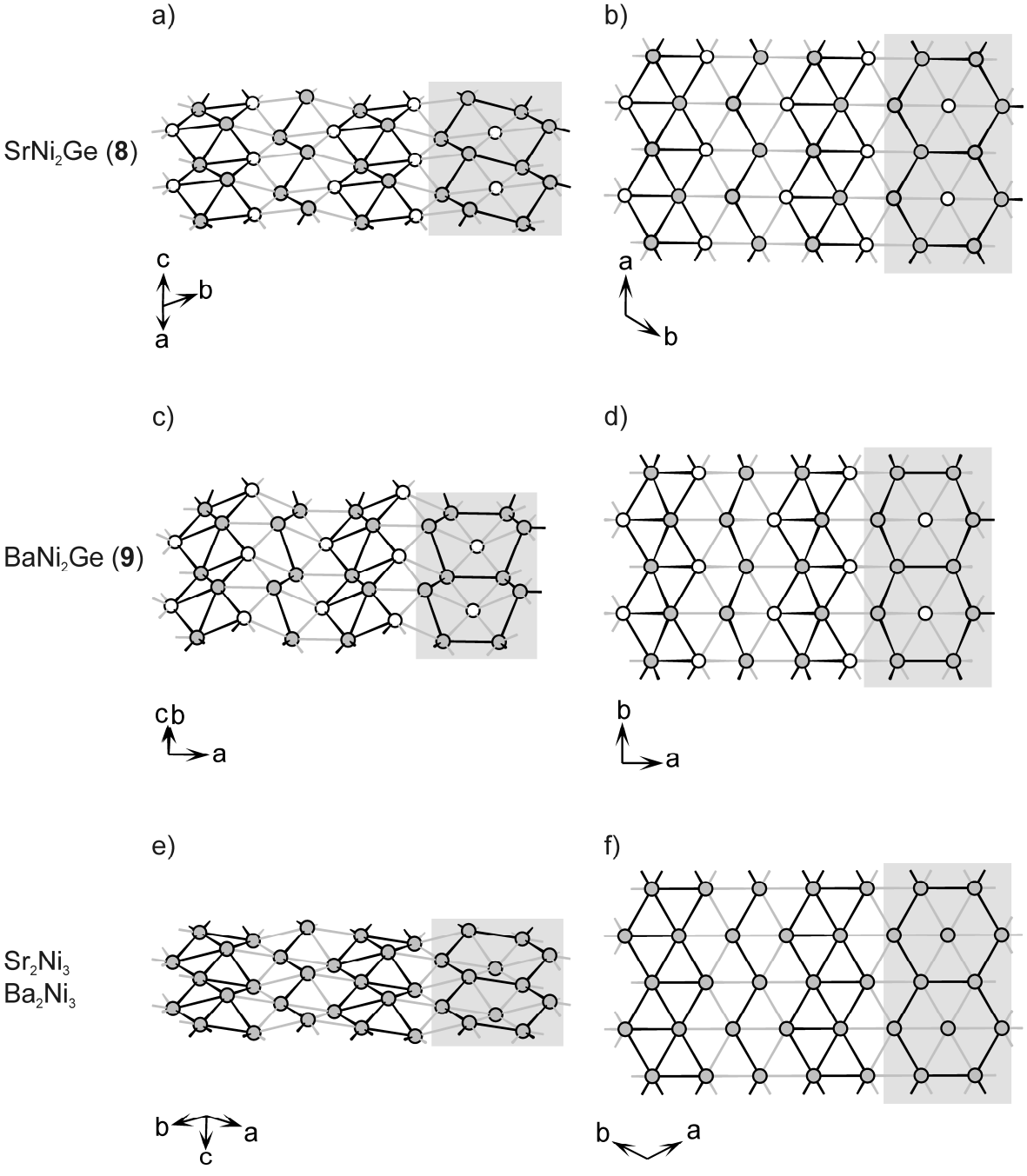

Figure 11 Polyanionic networks observed in a-b) $SrNi_2Ge$ (**8**), c-d) $BaNi_2Ge$ (**9**), e-f) Sr_2Ni_3 and Ba_2Ni_3 [77, 78]. The Ni-Ge and Ni-Ni bonds are drawn in black and grey, such that the following structural motifs are emphasized: $^1_\infty$[NiGe] ribbons, chains of Ni atoms, six-membered Ge-centered Ni rings in chair conformation (a,b and e,f) and boat conformation (c,d). The Ni and Ge atoms are drawn in grey and white, respectively.

*IV.4.3 $Ca_4Ni_4Ge_3$ (**10**)*

$Ca_4Ni_4Ge_3$ (**10**) contains two-dimensional $^2_\infty[Ni_4Ge_3]$ layers. They can be described as being built up of $^1_\infty[NiGe]$ ribbons which are linked via a Ni-Ge-Ni bridge (see Figure 12). Between these layers the Ca atoms are situated. The Ni atoms of the Ni-Ge-Ni bridge form three bonds to the atoms of the neighboring $^1_\infty[NiGe]$ ribbons (2 × Ni-Ge and 1 × Ni-Ni). This bonding situation is the same as found between the Ni atoms of the zigzag chain and one neighboring $^1_\infty[NiGe]$ ribbon in **8** and **9**. However, while in **8** and **9** the ribbons are arranged parallel to each other, in $Ca_4Ni_4Ge_3$ (**10**) every second $^1_\infty[NiGe]$ ribbon is shifted along the *a* axis. The "bridging" (two-fold coordinated) Ge atom (Ge1), is a unique structure motif in the compounds of the systems *Ae*/Ni/Ge.

The two-dimensional $^2_\infty[Ni_4Ge_3]$ layers were further described as a defect variant $^2_\infty[Ni_4\square_2Ge_3]$ of the layers of $SrNi_2Ge$ (**8**) by formally removing two Ni atom of $^2_\infty[Ni_6Ge_3]$ in **8** (Figure 11b) and adding one additional *Ae* atom.

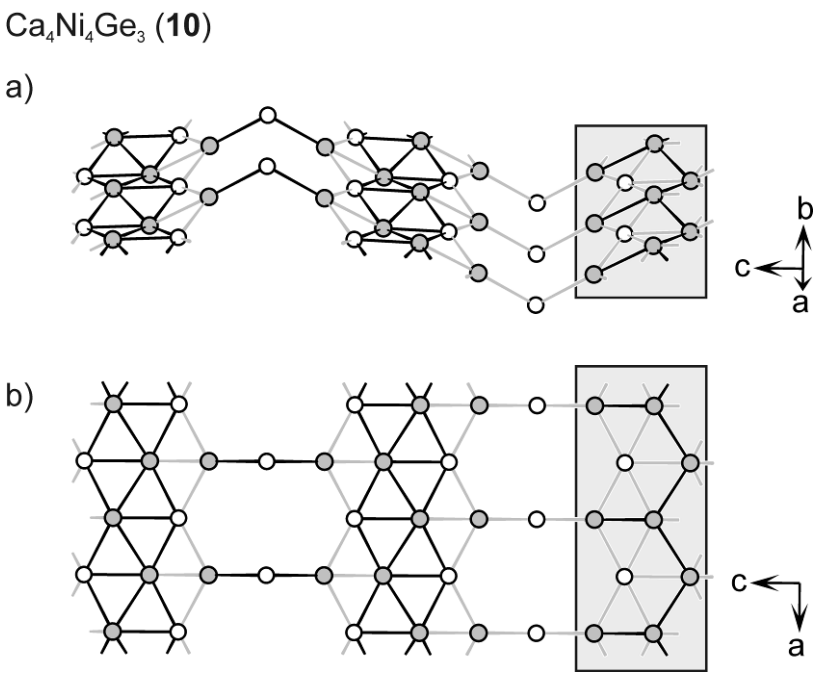

Figure 12 Polyanionic network observed in $Ca_4Ni_4Ge_3$ (**10**). The Ni-Ge and Ni-Ni bonds are drawn in black and grey such that the following structural motifs are emphasized: $^1_\infty[NiGe]$ ribbons, Ni-Ge-Ni bridge as well as six-membered Ge-centered Ni rings with one vacant position (highlighted with a grey background). The Ni and Ge atoms are drawn in grey and white, respectively.

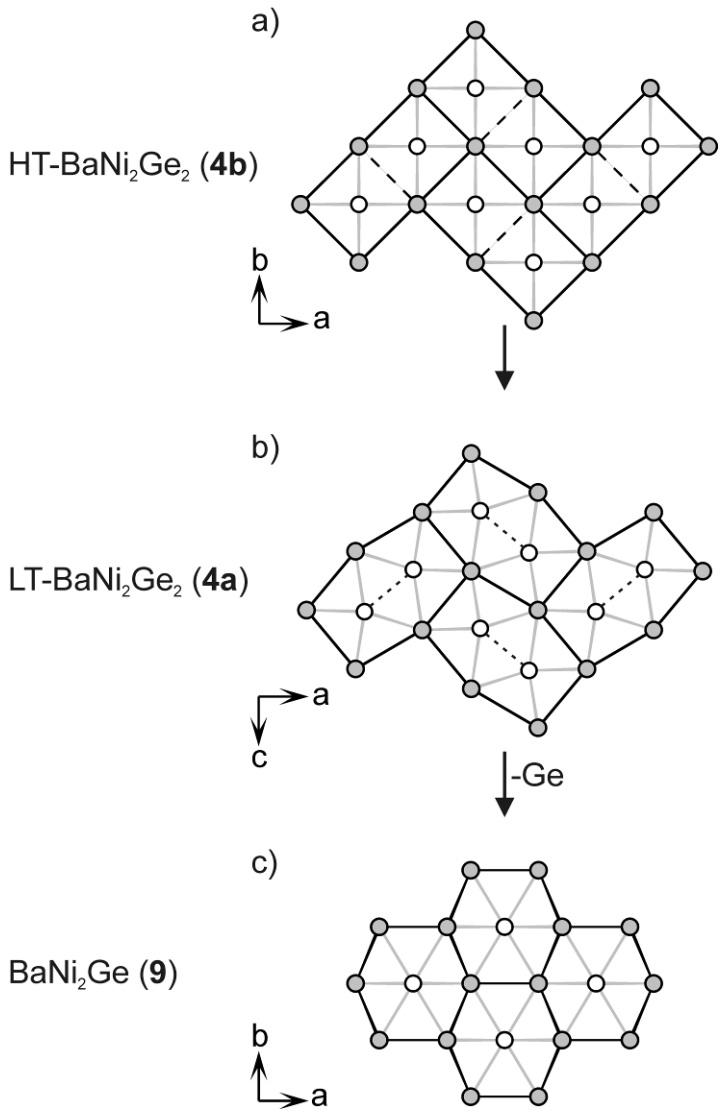

Figure 13 Polyanionic networks observed in a) HT-$BaNi_2Ge_2$ (**4b**), b) LT-$BaNi_2Ge_2$ (**4a**) and c) $BaNi_2Ge$ (**9**). The Ni-Ge and Ni-Ni contacts are drawn in black and grey in order to emphasize the change from square to hexagonal polyanionic layers. The Ba atoms are drawn in black, the Ni and Ge atoms in grey and white, respectively.

IV.4.4 From square nets to hexagonal layers

The predominant features of the Ni-Ge substructures described so far in the systems *Ae*/Ni/Ge are Ni-Ge nets with square (CaNiGe (**2**), HT-$BaNi_2Ge_2$ (**4b**), $SrNi_2Ge_2$ (**5**), $CaNi_2Ge_2$ (**6**)) or hexagonal ($SrNi_2Ge$ (**8**) and $BaNi_2Ge$ (**9**)) symmetry. LT-$BaNi_2Ge_2$ (**4a**) can be considered as a linking element between these two groups as shown in Figure 13. In HT-$BaNi_2Ge_2$ (**4b**) a regular square net of Ni atoms is observed with d(Ni-Ni) = 3.02 Å. In Figure 13a one Ni-Ni contact is drawn as dashed line in order to indicate, that this Ni-Ni

contact is elongated in LT-$BaNi_2Ge_2$ (**4a**) (*d*(Ni-Ni) = 3.78, Figure 13b). As a consequence, the Ge-Ge distance is shortened from 3.61 Å in **4b** to 2.93 Å in **4a** (dashed contacts in Figure 13b). The replacement of such a pair of Ge atoms in LT-$BaNi_2Ge_2$ (**4a**) by a single Ge atom and the deformation of the Ni layers to a hexagonal Ni atom layer leads to the structure of $BaNi_2Ge$ (**9**, Figure 13c) and $SrNi_2Ge$ (**8**, Figure 11a and Figure 11b). The same intermediate structure [28] is observed for $BaNi_2Si_2$ [142] (a distorted version of $ThCr_2Si_2$, space group *Cmcm*), containing strongly deformed $^2_\infty[Ni_2Si_2]$ layers.

*IV.4.5 Insertion of Ge - from CaNiGe (**2**) to $CaNiGe_2$ (**11a**), $SrNiGe_2$ (**11b**), $Ca_3Ni_3Ge_7$ (**12a**), $Sr_3Ni_3Ge_7$ (**12b**) and $CaNiGe_3$ (**13**)*

Examining the lines of the composition triangle (Figure 6) reveals that most compounds are situated along the line ②, i.e. numerous compounds are related by monotone insertion of Ge: $Ca_3Ni_3Ge_3$ (CaNiGe, **2**), $Ca_3Ni_3Ge_6$ ($CaNiGe_2$, **11a**), $Sr_3Ni_3Ge_6$ ($SrNiGe_2$, **11b**), $Ca_3Ni_3Ge_7$ (**12a**), $Sr_3Ni_3Ge_7$ (**12b**) and $Ca_3Ni_3Ge_9$ ($CaNiGe_3$, **13**). A straightforward relationship between the crystal structures is obvious (Figure 14).

As described above, CaNiGe (**2**) contains PbO-type $^2_\infty[NiGe]$ layers, which consist of square Ni nets capped alternately by Ge atoms. Between the $^2_\infty[NiGe]$ layers two square layers of Ca atoms are situated. Thus, labelling the square polyanionic $^2_\infty[NiGe]$ layers as A and the Ca layers as B and B', the stacking sequence observed here is ABB'. B' is identical to B, with an offset of $x = ½$ and $y = ½$ within the *ab* plane (Figure 14a).

The formal addition of one Ge atom per formula unit into CaNiGe (**2**) leads to $CaNiGe_2$ (**11a**) and $SrNiGe_2$ (**11b**). The inserted Ge atoms form zigzag chains of Ge (layer C) between the $^2_\infty[NiGe]$ layers (Figure 14b). Such chains also occur in the CaGe structure (CrB structure type). The Ge-Ge distances within the zigzag chains indicate covalent bonding (2.50 Å in **11a** and 2.56 Å in **11b**). These distances are shorter than those in the binary Zintl phases CaGe [7], SrGe [8] and BaGe [9-11] with 2.59 Å for CaGe, 2.63 Å for SrGe and BaGe. Notice that within the $^2_\infty[NiGe]$ layers the Ni and Ge atoms in **11a** and **11b** have exchanged their positions in comparison to CaNiGe (**2**). Therefore, a square net of Ge atoms capped alternately by Ni atoms results. These anti-PbO-type layers are presented in Figure 4h. For the description of the stacking sequence, they are labelled as α. The capping Ni atoms bind to the Ge atoms of the zigzag chain.

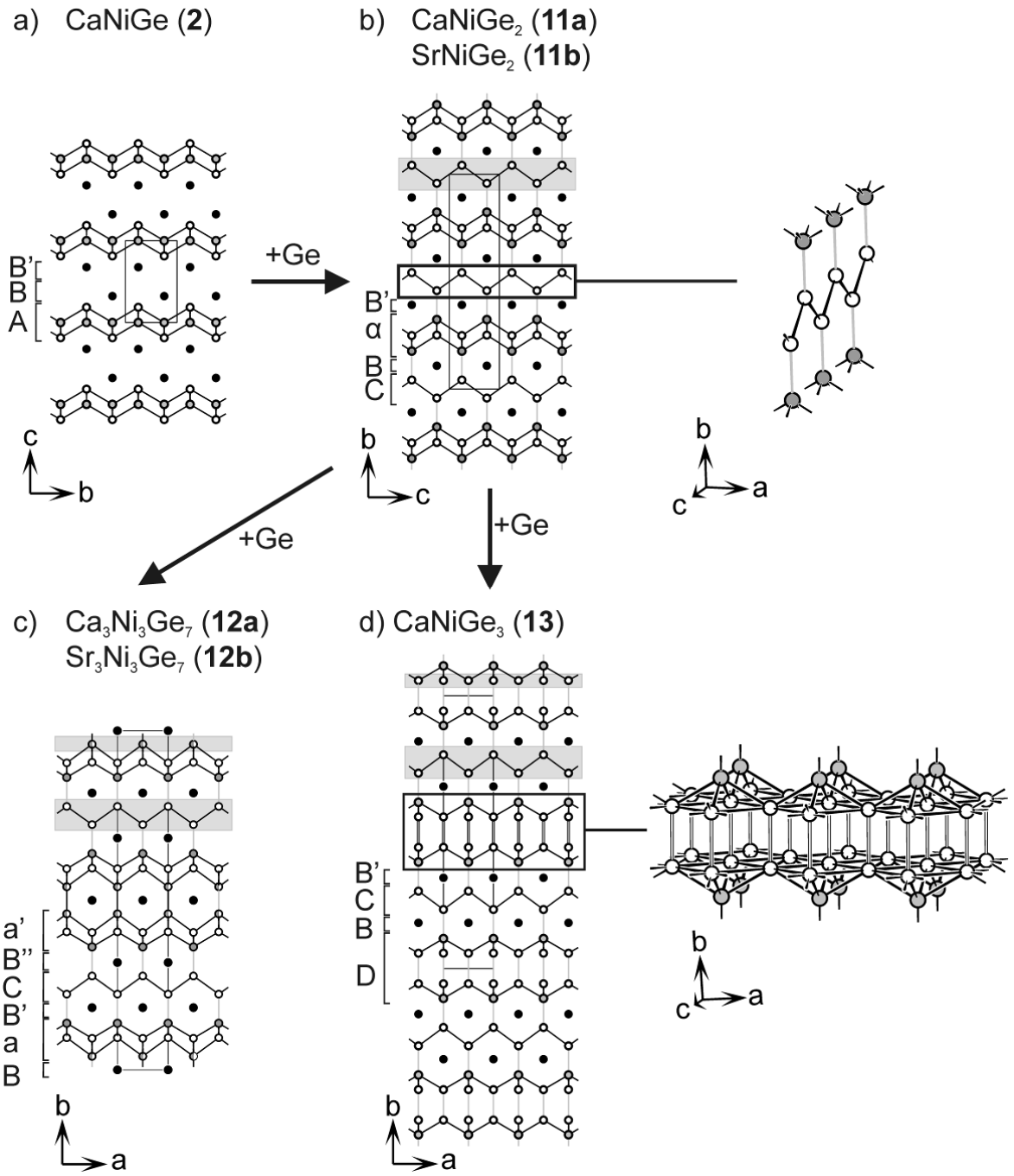

Figure 14 Crystal structures of a) CaNiGe (**2**), b) $CaNiGe_2$ (**11a**) and $SrNiGe_2$ (**11b**), c) $Ca_3Ni_3Ge_7$ (**12a**) and $Sr_3Ni_3Ge_7$ (**12b**) and d) $CaNiGe_3$ (**13**). For $CaNiGe_2$ (**11a**) and $CaNiGe_3$ (**13**) the structural motifs of the zigzag chain of Ge atoms as well as the $^{2}_{\infty}[NiGe_3]$ layers are highlighted. The Ca atoms are drawn in black, the Ni and Ge atoms in grey and white, respectively.

The resulting stacking sequence is (CBαB')(CBαB')', the second block being shifted along the *a* axis by $x = ½$. The PbO-type as well as the anti-PbO-type layers

observed in **2** as well as in **11** coexist in the crystal structures of representatives of the $CaBe_2Ge_2$ structure type [143] (e.g. $CeNi_2Ge_2$ [144]).

In the Ni-Ge networks of the isotypic compounds $Ca_3Ni_3Ge_7$ (**12a**) and $Sr_3Ni_3Ge_7$ (**12b**) CrB-type zigzag chains of Ge are again present (Figure 14c). The second structural motif is a square layer $^2_\infty[Ni_3Ge_5]$. Like the $^2_\infty[NiGe_3]$ layers observed in $SrNiGe_3$ (**7**), the square layers $^2_\infty[Ni_3Ge_5]$ are an ordered variant of the anti-PbO-type layers: In $Ca_3Ni_3Ge_7$ (**12a**) and $Sr_3Ni_3Ge_7$ (**12b**) a square atomic layer of Ge is capped alternately with Ni atoms on one side of the layer plane and a mixture of approximately 50% Ni and 50% Ge on the other side of the layer plane. This mixed occupancy on one capping position might be explained by an overlap of the $^2_\infty[Ni_2Ge_2]$ layer known from $CaNiGe_2$ (**11a**) as well as $SrNiGe_2$ (**11b**) and the $^2_\infty[NiGe_3]$ layers of $SrNiGe_3$ (**7**). Two of these resulting square layers $^2_\infty[Ni_3Ge_5]$ are linked via Ni/Ge-Ni/Ge bonds (d(Ni/Ge-Ni/Ge) = 2.29 Å in **12a** and d(Ni/Ge-Ni/Ge) = 2.36 Å in **12b**) and thus form a double layer. Between two neighboring double layers, zigzag chains of Ge are situated. Naming the square layers $^2_\infty[Ni_3Ge_5]$ a, the following stacking sequence results: (BaB'CB''a')(BaB'CB''a')', the second block being shifted along the a axis by x = ½. Similar to **11a** and **11b** the Ge-Ge distances within the zigzag Ge chains indicate covalent bonding ($d(Ge_{chain}\text{-}Ge_{chain})$ = 2.52 Å in **12a** and $d(Ge_{chain}\text{-}Ge_{chain})$ = 2.57 Å in **12b**).

The $^3_\infty[NiGe_3]$ network of $CaNiGe_3$ (**13**) can be best understood starting with the network of $CaNiGe_2$ (**11a**) or isotypic $SrNiGe_2$ (**11b**). The zigzag chains of Ge remain basically unchanged, preserving the covalent character of the Ge-Ge bond ($d(Ge_{chain}\text{-}Ge_{chain})$ = 2.51 Å in **13**). Adding formally Ge to the anti-PbO-type layers of **11a** and **11b** leads to the formation of square layers of parallel aligned Ge_2 dumb-bells. Within these layers short Ge-Ge contacts are observed parallel to the b axis (d(Ge-Ge) = 2.46 Å). The Ge-Ge contacts between neighboring Ge_2 dumbbells within the square nets parallel to the ac plane are significantly longer (d(Ge-Ge) = 2.90 Å). This square layer of Ge_2 is capped alternately below and above by Ni atoms. A new layer $^2_\infty[NiGe_2]$, named D, results for $CaNiGe_3$ (**13**). The resulting stacking sequence is (DBCB')(DBCB')', the second block being shifted along the a axis by x = ½.

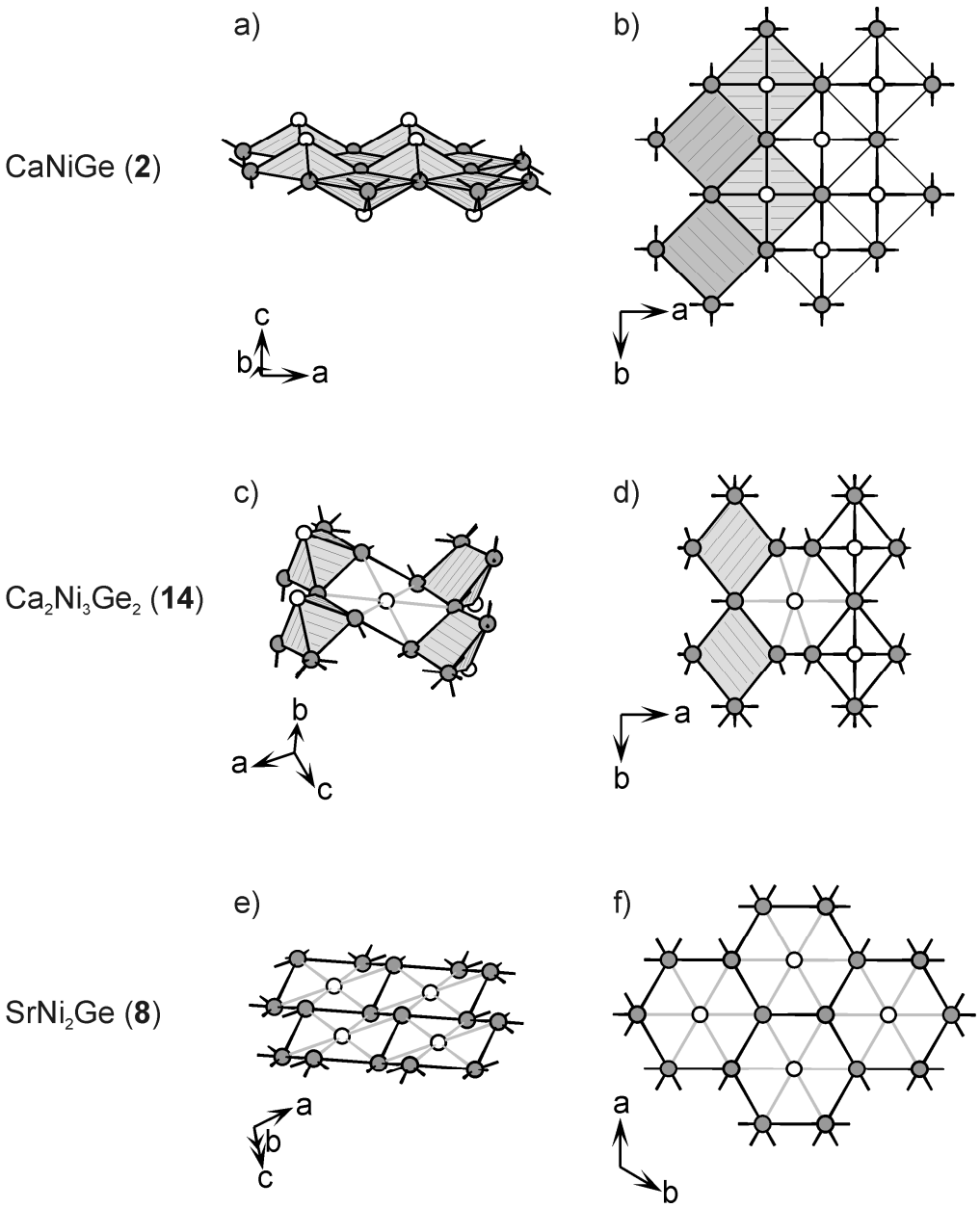

Figure 15 Polyanionic networks observed in the crystal structures of a-b) CaNiGe (**2**), c-d) $Ca_2Ni_3Ge_2$ (**14**) and e-f) $SrNi_2Ge$ (**8**). The square Ni_4Ge pyramids (a, b) as well as the Ge-centered six-membered Ni rings with chair conformation (b, c) are emphasized. The Ni and Ge atoms are drawn in grey and white, respectively.

Note, that while the compounds of the composition 1:1:2 and 3:3:7 are isotypic for Ca and Sr, the crystal structures of $SrNiGe_3$ (**7**) and $CaNiGe_3$ (**13**) vary significantly. Seemingly, crystal structures of the Ge richer compounds are more sensible to size effects, which result from the change of the alkaline earth metal atoms. None of these crystal structures was observed for compounds of the system Ba/Ni/Ge.

*IV.4.6 Line ③: $Ca_2Ni_3Ge_2$ (**14**) – Intergrowth of two structures*

The crystal structures of the intermetallic compounds situated on line ② follow a common building block principle, the addition of Ge leads to the insertion of new structural motifs. A similar construction using building blocks is observed for the compounds situated on line ③ (from Ni to CaGe): the crystal structure of $Ca_2Ni_3Ge_2$ (**14**) corresponds to a 1:1 combination of cutouts of the NiGe networks of CaNiGe (**2**) and hypothetical "$CaNi_2Ge$" (with $SrNi_2Ge$-type structure) according to $Ca_2Ni_3Ge_2$ = CaNiGe + "$CaNi_2Ge$" [29]. This is depicted in Figure 15: the square PbO-type layers in CaNiGe (**2**) can be described as built up of edge-sharing square Ni_4Ge pyramids. The hexagonal layers in $SrNi_2Ge$ (**8**) consist of Ge-centered six-membered Ni rings with chair conformation. The polyanionic $^2_\infty[Ni_3Ge_2]$ layers of $Ca_2Ni_3Ge_2$ (**14**) contain structural motifs of both neighboring compounds: the square Ni_4Ge pyramids share vertices to form ribbons which are linked via Ge-centered six-membered Ni rings with chair conformation.

*IV.4.7 Line ④: Insertion of Ni – from HT-$BaNi_2Ge_2$ (**4b**) to $Ba_2Ni_5Ge_4$ (**15**) and $SrNi_3Ge_2$ (**16**)*

Along the line ④ (from *Ae*Ge_2 to Ni) a formal stepwise extension due to the insertion of Ni atoms takes place. A similar extension was discussed above for line ③ for the insertion of Ge atoms. Indeed the topological relationship of the crystal structures of HT-$BaNi_2Ge_2$ (**4b**), $Ba_2Ni_5Ge_4$ (**15**) and $SrNi_3Ge_2$ (**16**) may be explained by formally adding Ni to the $^2_\infty[Ni_2Ge_2]$ layers of **4b**. This is shown in Figure 16.

The main structural motif observed in this series was indicated in Figure 4j to Figure 4l. Vertical $^1_\infty$[NiGe] ribbons are aligned parallel to each other, neighboring ribbons being respective mirror images. Between these ribbons additional Ni atoms are inserted. The ribbons are connected via horizontal Ni-Ge bonds such that Ni-centered hexagonal prisms result. These prisms are found in $Ba_2Ni_5Ge_4$ (**15**) (compare Figure 4k) as well as in $SrNi_3Ge_2$ (**16**) (compare Figure 4l).

In HT-$BaNi_2Ge_2$ (**4b**) parallel aligned $^1_\infty$[NiGe] ribbons are linked via *transoid* Ni-Ge bonds (grey bonds in Figure 13a and Figure 13b). An alternative connection of the $^1_\infty$[NiGe] ribbons is realized in $Ba_2Ni_5Ge_4$ (**15**) (Figure 13c and Figure 13d). Pairs of

parallel vertical ribbons are connected by Ni-Ge bonds to form a one-dimensional chain of face-sharing hexagonal prisms. The vertices of the prisms are alternately occupied by Ni and Ge atoms. The hexagonal faces have chair conformation with an folding angle of 14.2°. The chains are further connected through *transoid* Ni-Ge bonds to form two-dimensional $^{2}_{\infty}[Ni_5Ge_4]$ layers shown in Figure 13c and Figure 13d. The additional Ni atom fills the cavities of the distorted hexagonal prisms.

Direct connection of the chains of hexagonal prisms leads to the formation of slabs of hexagonal prisms that share all rectangular faces. These slabs correspond to two only slightly corrugated α-As-type layers with primitive staple order. In contrast to **15** twice the number of prisms is generated, thus the filling of all prisms with Ni leads to $^{2}_{\infty}[Ni_3Ge_2]$ layers in $SrNi_3Ge_2$ (**16**). The group-subgroup relationship of $SrNi_3Ge_2$ (**16**) and AlB_2 is given in [27].

The replacement of the Sr atoms in **16** by Ni atoms and allowing the formation of Ni-Ge bonds between the atom slabs leads to the AlB_2 analogue hypothetical structure "Ni_4Ge_2". In this structure all newly formed hexagonal prisms are centered with Ni atoms. While Ni_2Ge does not exist, Co_2Ge was reported [116]. However, the topology of this structure is observed for Ni_3Ge_2 [73], with one Ni position of the Ni_4Ge_2 structure being not fully occupied (Figure 16g and Figure 16h). In fact, a phase $Ni_{4-x}Ge_2$ with a broad homogeneity range from $x = 0.44$ to $x = 1.26$ is observed [132].

In the composition triangle elemental Sr, $SrNi_3Ge_2$ (**16**) and Ni_3Ge_2 are situated on one straight line. Thus, the derivation of the crystal structure of $SrNi_3Ge_2$ (**16**) from the one of Ni_3Ge_2 by the insertion of Sr suggests itself, just as the crystal structures of $CaNi_2Ge_2$ (**6**) and CaNiGe (**2**) can be derived from NiGe by the insertion of Ca.

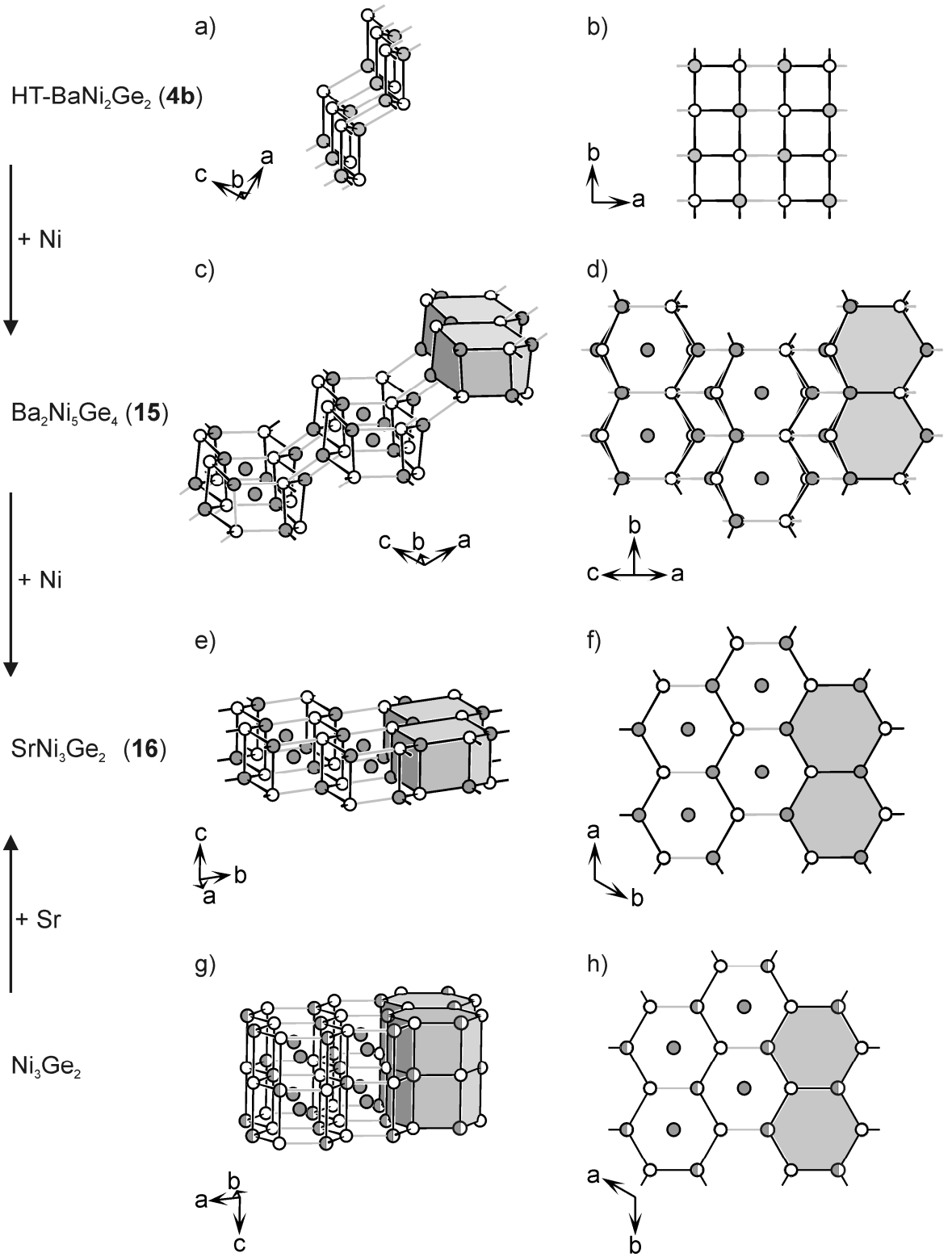

Figure 16 Polyanionic networks observed in the crystal structures of a-b) HT-$BaNi_2Ge_2$ (**4b**), c-d) $Ba_2Ni_5Ge_4$ (**15**), e-f) $SrNi_3Ge_2$ (**16**) and g-h) Ni_3Ge_2 [73]. The $^{1}_{\infty}$[NiGe] ribbons as well as the Ni-centered hexagonal prisms are emphasized. The Ni and Ge atoms are drawn in grey and white, respectively. In Ni_3Ge_2 the positions of Ni2 are occupied with 50 % Ni. These Ni positions, that are not fully occupied, are drawn two-colored in grey and white.

IV.5 Ni rich compounds

IV.5.1 $Ca_{10}Ni_{34}Ge_{16}$ (17)

$Ca_{10}Ni_{34}Ge_{16}$ (**17**) has a higher Ca content than the intermetallic compounds **18** − **20**. Its crystal structure is depicted in Figure 17. In agreement with its composition, its crystal structure can be considered as a bridge between the structures of the Ni rich compounds **18** – **20** and those of the Ni poorer compounds **1** – **16**. Analysing the crystal structure, a combination of different structural motifs is found, which are either observed in the Ni rich compounds **18** – **20** or in the Ni poorer compounds **1** – **16.** Thus, **17** represents an important borderline compound between compounds with dominating localized bonds and intermetallics with fully delocalized bond description.

The coordination polyhedron of Ca3 is a hexagonal prism Ni_6Ge_6. The rectangular faces of these prisms are capped by further Ni atoms. Along the *a* axis the prisms form rods of prisms which are linked via their hexagonal faces (structural motif ① in Figure 17). The coordination polyhedra of Ca1 and Ca2 also consist of hexagonal prisms with one atom per six-membered face being vacant (structural motif ② in Figure 17a and Figure 17c). These defective hexagonal prisms form rods along the *a* axis, which are nested within each other. Again, the outer rectangular faces of the prisms are further capped by Ni and Ge atoms. Comparable structural motifs to ① and ② are observed in the Ni rich compounds $CaNi_5Ge_3$ (**18**) $Ca_{15}Ni_{68}Ge_{37}$ (**19**) and $Ca_7Ni_{48.9(4)}Ge_{22.1(4)}$ (**20**) and will be discussed in the following.

The Ni-Ge network between the rods of face-sharing hexagonal prisms consists of square pyramids with Ge atoms capping the Ni_4 square, as observed for example in CaNiGe (**2**) and $Ca_2Ni_3Ge_2$ (**14**). These are connected via Ge-centered Ni_6 hexagons, as found in $SrNi_2Ge$ (**8**) and $BaNi_2Ge$ (**9**) (structural motif ③ in Figure 17a and Figure 17d).

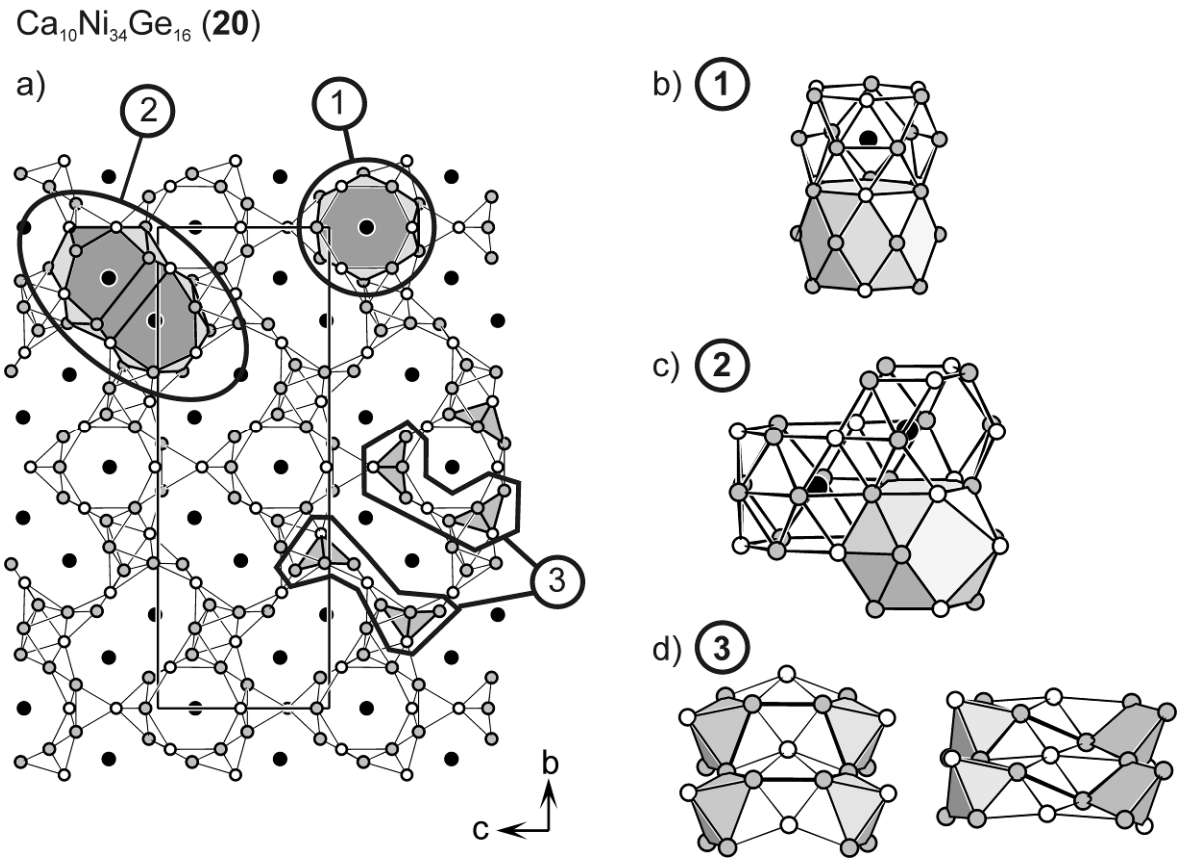

Figure 17 a) Crystal structure of $Ca_{10}Ni_{34}Ge_{16}$ (**17**). The following structural motifs are emphasized: b) coordination polyhedra of Ca3 (structure motif ①), c) coordination polyhedra of Ca1 and Ca2 (structure motif ②) and d) Ni_4Ge square pyramids which are connected via Ge-centered six-membered Ni_6 rings with chair and boat conformation. The Ca atoms are drawn in black, the Ni and Ge atoms in grey and white, respectively.

While in $Ca_2Ni_3Ge_2$ (**14**) the square pyramids Ni_4Ge were connected exclusively via Ge-centered Ni_6 hexagons with a chair conformation (known from **8**), in $Ca_{10}Ni_{34}Ge_{16}$ (**17**) the square pyramids Ni_4Ge are connected via Ge-centered Ni_6 hexagons with both chair and boat conformation. Consequently, in $Ca_2Ni_3Ge_2$ (**14**) two-dimensional layers $^2_\infty[Ni_3Ge_2]$ are observed (Figure 15c), while in $Ca_{10}Ni_{34}Ge_{16}$ (**17**) a three-dimensional network $^3_\infty[Ni_{34}Ge_{16}]$ is present.

IV.5.2 $CaNi_5Ge_3$ (18), $Ca_{15}Ni_{68}Ge_{37}$ (19) and $Ca_7Ni_{48.9(4)}Ge_{22.1(4)}$(20)

The complex three-dimensional networks of the crystal structures of $CaNi_5Ge_3$ (**18**), $Ca_{15}Ni_{68}Ge_{37}$ (**19**) and $Ca_7Ni_{48.9(4)}Ge_{22.1(4)}$ (**20**) are shown in Figure 18. The crystal structures vary significantly from the crystal structures **1** − **16**. Only $CaNi_5Ge_3$ (**18**) can be

described, in analogy to the descriptions above, as being built up of PbO-type layers (Figure 18d). These consist of a square net of Ni atoms being capped alternately above and below the plane by Ge atoms. Two such layers are interconnected by sharing a capping Ge atom. A Ni atom is placed into the resulting cavity, which is a quadrangular prism of four Ni and four Ge atoms. The Ni-Ge layers obtained were described as two-dimensional cutouts of the Ni_3Ge structure [72]. These PbO-type double layers are further connected via short contacts between capping Ge atoms of two neighboring double layers (*d*(Ge-Ge) = 2.55 Å), comparable to the connection of layers in $CaNi_2Ge_2$ (**6**). Thus, as shown in Figure 18c, the crystal structure of $CaNi_5Ge_3$ (**18**) can be described as built up of two-dimensional cutouts of Ni_3Ge [72] (Figure 18a) and $CaNi_2Ge_2$ (**6,** Figure 18b).

In Figure 18a, a slab of the Ni_3Ge structure, represented as elongated Ge- and Ni-centered cuboids with Ni atoms on the vertices, is shown. Furthermore, the coordination polyhedra of Ge and Ni (regular cuboctahedron) are shown once for each centering Ge and Ni atom. As shown in Figure 18c to Figure 18f, low-dimensional cutouts of the Ni_3Ge structure are observed in **18** − **20**. Even though all three compounds **18** − **20** have a three-dimensional network of Ni and Ge, a correlation of the content of Ca and the dimensionality of the Ni-Ge substructures resulting from the cutouts of the Ni_3Ge structure is noted: within the series of the three compounds $Ca_7Ni_{48.9(4)}Ge_{22.1(4)}$ (**20**), $CaNi_5Ge_3$ (**18**), and $Ca_{15}Ni_{68}Ge_{37}$ (**19**) the increasing content of Ca leads to three-, two- and one-dimensional Ni-Ge substructures, respectively [37]. This can be compared to the series of Zintl phases $CaGe_2$, CaGe and Ca_2Ge, in which Ca scissors the diamond-like structure of Ge under formation of two- one- and zero-dimensional Ge substructures. Of course, the Ni-Ge substructures are not fully separated in **18** − **20**, since further Ni and Ge atoms are situated between the low-dimensional cutouts of the Ni_3Ge structure.

The cutouts of the Ni_3Ge structure are separated by Ca atoms. The resulting coordination polyhedra of the Ca atoms (condensed hexagonal prisms of Ni and Ge atoms) are a further characteristic feature of these structures, being similar to those observed in $CaNi_2Ge_2$ (**6,** Figure 18b) as well as to the coordination polyhedra of the Ca atoms observed in $Ca_{10}Ni_{34}Ge_{16}$ (**17**).

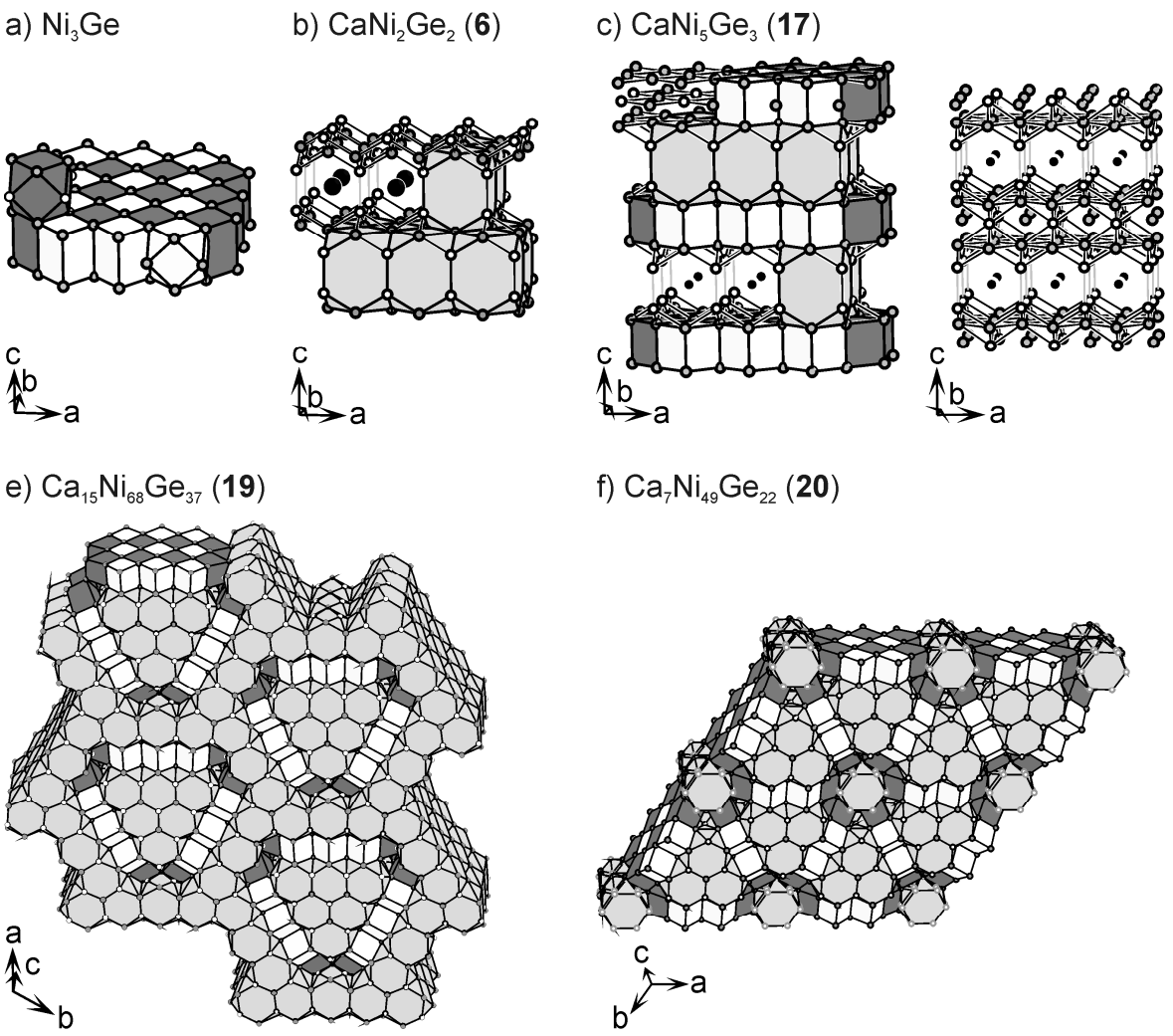

Figure 18 Crystal structures of a) Ni_3Ge, b) $CaNi_2Ge_2$ (**6**), c-d) $CaNi_5Ge_3$ (**17**), e) $Ca_{15}Ni_{68}Ge_{37}$ (**18**) and f) $Ca_7Ni_{49}Ge_{22}$ (**19**). The Ca atoms are drawn in black, the Ni and Ge atoms in grey and white, respectively. The polyhedra centered by Ca, Ni and Ge are drawn in black, grey and white, respectively.

Similar coordination polyhedra of Ca are also found in the binary system Ca/Ni (Figure 19). The intermetallic phase $CaNi_2$ crystallizes in the structure type of the cubic Laves phase $MgCu_2$ [119] (Figure 19a). The crystal structure consists of a three-dimensional network of edge-sharing Ni tetrahedra in whose cavities the Ca atoms are situated. Describing the network of Ni atoms being built up of atom layers, it consists of stacking alternately Kagomé nets (6.3.6.3) and hexagonal nets (3^6). Considering exclusively the Kagomé nets, these are stacked according to a cubic stacking ABC.

Further insertion of atom layers to the crystal structure of $CaNi_2$, namely a Kagomé net (6.3.6.3) of Ni atoms and a hexagonal net (3^6) of alternating Ni and Ca atoms, leads to

the crystal structure of $CaNi_3$ (Figure 19b). The resulting stacking sequence of the Kagomé nets is AABBCC. Consequently, two building blocks result. The first block can be derived from the Laves phase $CaNi_2$ and consists of two Kagomé nets (6.3.6.3) in between which a hexagonal net (3^6) of Ni atoms is situated. The Ni atoms of the hexagonal net cap every second triangular face of the Kagomé nets. In the resulting cavities the Ca atoms are situated. The second block consists of two Kagomé nets (6.3.6.3), in between which a hexagonal net (3^6) of alternating Ni and Ca atoms is situated. The Ni atoms of the hexagonal net cap all triangular faces of the Kagomé nets. In this second block, the resulting coordination polyhedra of Ca are hexagonal prisms of Ni, comparable to the polyhedra of Ca observed for the crystal structures **17** – **20**.

The formal addition of two further atom layers to the crystal structure of $CaNi_3$ (a Kagomé net (6.3.6.3) of Ni atoms and a hexagonal net (3^6) of alternating Ni and Ca atoms) leads to the crystal structure of Ca_2Ni_7 (Figure 19c). The resulting stacking sequence of the Kagomé nets is AAABBBCCC. This results in the same building blocks as described for $CaNi_2$.

$CaNi_5$ crystallizes in the $CaCu_5$ structure type (Figure 19d). Sets of one Kagomé net (6.3.6.3) of Ni atoms and one hexagonal net (3^6) of alternating Ni and Ca atoms are stacked according to the primitive series AAA. Thus, a three-dimensional network of face-sharing hexagonal Ni prisms centered by Ca, results.

In accordance with the crystal structures the empirical formulas of $CaNi_3$ and Ca_2Ni_7 result from the formal addition of $CaNi_5$ and $CaNi_2$: "$CaNi_3 = CaNi_2 + ½\ CaNi_5$" and "$Ca_2Ni_7 = CaNi_2 + CaNi_5$".

Note, that in the intermetallic systems Sr/Ni/Ge and Ba/Ni/Ge no compound with a crystal structure comparable to **17** − **20** is observed. Most likely this is due to the absence of Ni rich compounds in the binary systems Sr/Ni and Ba/Ni.

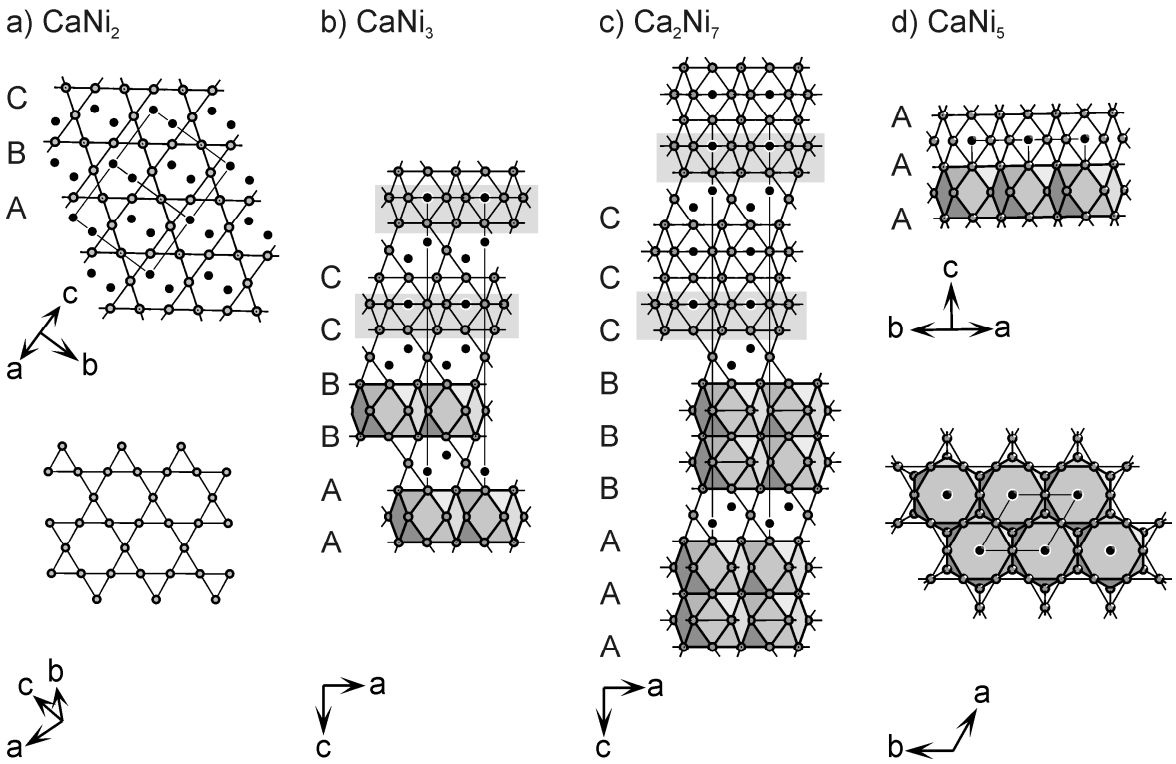

Figure 19 Crystal structures of a) $CaNi_2$, b) $CaNi_3$, c) Ca_2Ni_7 and d) $CaNi_5$ [80]. The Ca and Ni atoms are drawn in black and grey, respectively.

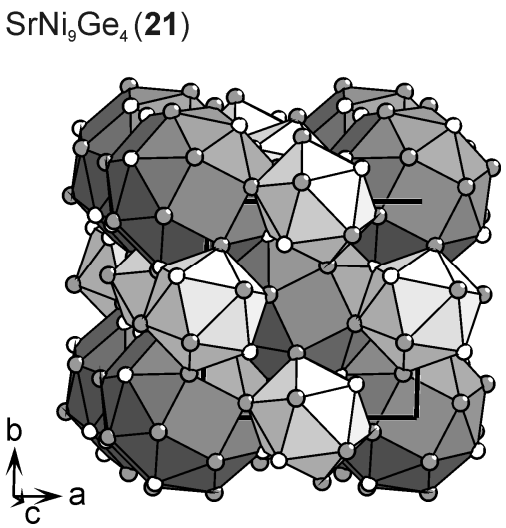

Figure 20 Crystal structure of $SrNi_9Ge_4$ (**21**). The Sr atoms are drawn in black, the Ni and Ge atoms in grey and white, respectively. The coordination polyhedra of Sr and Ni are drawn in dark and light grey, respectively.

*IV.5.3 $SrNi_9Ge_4$ (**21**)*

The crystal structure of $SrNi_9Ge_4$ (**21**) corresponds to a typical intermetallic compound (Figure 20). I.e. structure motifs containing localized Ni-Ge bonds, which govern the Ni poorer structures **1** – **16**, are replaced by structure motifs that allow a maximization of the coordination number of all atoms under consideration. It represents an ordered ternary variant of the cubic $NaZn_{13}$ structure type ([145], space group $Fm\bar{3}c$). In $SrNi_9Ge_4$ (**21**), the Sr atoms are coordinated by 16 Ni and 8 Ge atoms with ordered occupation. The 24 atom polyhedron (snub cube) consists of 32 triangular and six quadrangular faces. The polyhedra are face linked via the quadrangular faces, such that icosahedra of Ni and Ge atoms result. These are centered by Ni atoms.

Note, that even though the crystal structure of $SrNi_9Ge_4$ (**21**) varies significantly from the previously described Ni rich compounds in the systems *Ae*/Ni/Ge (**17** – **20**), its crystal structure is well known and other intermetallic phases of the systems *Ae*/*T*/*Tt* (*Ae*: alkaline earth / rare earth, *T*: transition metal, *Tt*: tetrel) also crystallize in this structure type. For example, using copper as a transition metal, the intermetallic phases $AeCu_9X_4$ (*Ae*: Sr, Ba; *X*: Si,Ge [146]) were described.

IV.6 $Ba_8Ni_{3.5}Ge_{42.1}$ (22)

In the Ge rich part of the phase diagram Ba/Ge the three clathrates were reported, namely the clathrate *cP*124 Ba_6Ge_{25} [64-66], the clathrate-I Ba_8Ge_{43} [67] and the clathrate *oP*60 $BaGe_5$ [68]. Therefore, it doesn't come as a surprise that in the Ge rich part of the system Ba/Ni/Ge the clathrate $Ba_8Ni_{6-x}Ge_{40+x}$ was reported. It crystallizes in the clathrate I structure type [42] with an homogeneity range of $0 \leq x \leq 0.6$ that lately was corrected to the composition to $Ba_8Ni_{3.5}Ge_{42.1}\square_{0.4}$ [41] (**22**) (Figure 21). The Ni atoms and the vacancies accumulate on the 6*c* position. The thermoelectric properties of **22** were presented in [39-42]. Typically, in clathrat I structures covalent bonds between the four-fold connected network atoms occur. For $Ba_8Ni_{3.5}Ge_{42.1}\square_{0.4}$ an almost charge balanced Zintl phase results according to $[Ba^{2+}]_8[Ni^0]_{3.5}[(4b)Ge^0]_{26.5}[(3b]Ge^{1-}]_{15.6}$, as each Ni and each vacancy atom produce four $(3b\text{-}Ge)^-$ and thus (3.5 + 0.4) x 4 = 15.6 negative charges result.

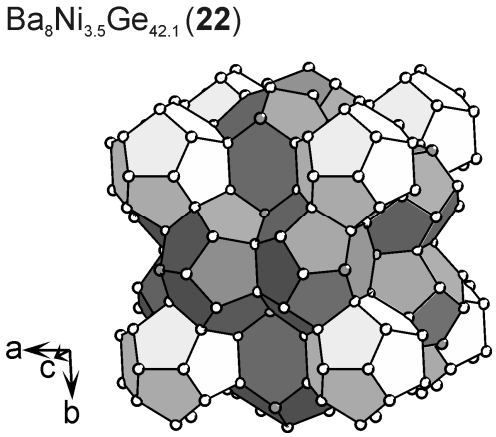

Figure 21 Crystal structure of $Ba_8Ni_{3.5}Ge_{42.1}$ (**22**). The Ba atoms are drawn in black, the Ni and Ge atoms in grey and white, respectively. The coordination polyhedra of Ba2 and Ba1 are drawn in dark and light grey, respectively.

IV.7 Ba_2NiGe_3 (23)

The structure of Ba_2NiGe_3 (**23**) crystallizes in the Ba_2NiSi_3 structure type [24] and contains one-dimensional $^1_\infty[NiGe_3]$ rods, which are separated by Ba atoms. The rods consist of three-membered rings of Ge atoms that are capped by Ni atoms. $NiGe_3$ trigonal pyramids result, which are vertex-sharing via the Ni caps and face-sharing via the Ge_3 base to form one-dimensional columns.

The distance between Ge atoms in the three-membered rings is *d*(Ge1-Ge1) = 2.60 Å and *d*(Ge2-Ge2) = 2.56 Å. Thus, considering the Ge-Ge distance in elemental Ge (*d*(Ge-Ge) = 2.45 Å [132]), covalent Ge-Ge bonding is present here.

A similar structure is observed in the Ni_3Sn structure type [147]. Here, one-dimensional rods of face- and vertex-sharing trigonal pyramids Ni_3Sn are found. These rods are comparable to the $^1_\infty[NiGe_3]$ rods described for **23**. In Ni_3Sn the rods are further connected via Ni-Sn bonds to form a three-dimensional network.

Another binary phase crystallizing in the Ni_3Sn structure type is the recently described binary phase $BaGe_3$ [62], in which three-membered rings of Ge are connected to one-dimensional columns. Adding formally Ni to $BaGe_3$ leads to an insertion of the Ni atoms in the columns and thus to the one-dimensional $^1_\infty[NiGe_3]$ rods which are observed in Ba_2NiGe_3 (**23**). In order to describe the overall bonding situation, the $^1_\infty[NiSi_3]^{4-}$ chains of Ba_2NiSi_3 were described as the solid-state analogue of an eclipsed (η^3-Si_3)Ni polymer [92].

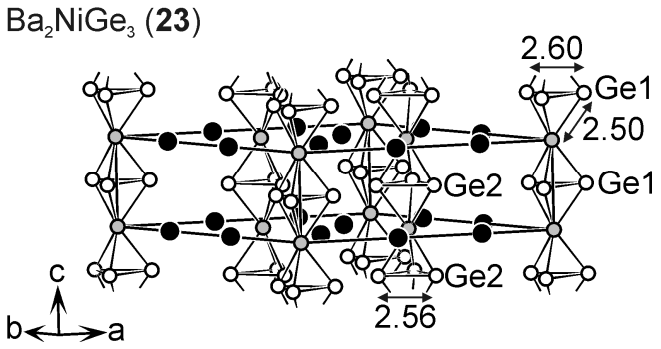

Figure 22 Crystal structure of Ba_2NiGe_3 (**23**). The Ba atoms are drawn in black, the Ni and Ge atoms in grey and white, respectively.

Assigning a positive charge of 2+ to the Ni atoms, the polar intermetallic phase Ba_2NiGe_3 (**23**) can be interpreted as a Zintl phase. The three-membered rings of two-bonded Ge atoms have an overall charge of 6− which is counterbalanced by the Ni^{2+} and the two Ba^{2+}. Alternatively, the three-membered rings of Ge can be interpreted as Ge_3^{2-} in analogy to the description of $BaSn_3$ [13] and $BaGe_3$ [62]. Thus, a charge of 0 is assigned to the Ni atoms.

V. Summary and conclusion

V.1.1 Description of polar intermetallic compounds in analogy to the Zintl-Klemm concept

Some of the relationships described above between binary and ternary polar intermetallic compounds of the systems *Ae*/Ni/Ge should be briefly recalled:

It has been shown that structural motifs observed in ternary compounds with a composition at the extreme right (Ge rich) or left (Ni rich) of the composition triangle were found the systems *Ae*/Ge and *Ae*/Ni. For example, the topology of the $^{2}_{\infty}[Ni_2Ge]$ network of $SrNi_2Ge$ relates to that of the Ni network in Sr_2Ni_3.

Further, starting at NiGe the insertion of alkaline earth metal atoms leads to the compounds $AeNi_2Ge_2$ and *Ae*NiGe and the insertion of Sr into Ni_3Ge_2 leads to the compound $SrNi_3Ge_2$. Most impressivly, the influence of inserted Ca was shown for the Ni rich compounds of the system Ca/Ni/Ge. Within the series of the three compounds $Ca_7Ni_{48.9(4)}Ge_{22.1(4)}$, $CaNi_5Ge_3$ and $Ca_{15}Ni_{68}Ge_{37}$, the increasing content of Ca leads to three-, two- and one-dimensional Ni-Ge substructures, respectively, which can be traced back to cutouts of the Ni_3Ge structure.

Focusing on these relationships between binary and ternary intermetallic compounds, binary intermetallic compounds of the systems *T*/*Tt* suggest themselves as a reference point for the description of ternary polar intermetallic compounds *Ae*/*T*/*Tt*. The formal addition of *Ae* to binary intermetallic phases T_xTt_y, leads to the formation of ternary polar intermetallic compounds. The electropositive element *Ae* partially transfers electrons to the more electronegative *T*-*Tt* network. Due to this electron transfer the resulting network *T*-*Tt* is reduced and adopts a structure which is reminiscent to those of binary intermetallic phases. Therefore, the understanding of binary intermetallic phases seems to be necessary for the understanding and the prediction of ternary polar intermetallic compounds.

This approach for the description of ternary polar intermetallic compounds allows answering some questions raised in the introduction. For example, it allows to understand ternary intermetallic phases containing various amounts of transition metals. Furthermore,

the assignment of explicit charges to the transition metal can be neglected: in the polyanionic network $[T_xTt_y]^{m-}$ metallic bonding and thus an overall distribution of the negative charge is present. The exact distribution of the charge within the polyanionic network $[T_xTt_y]^{m-}$ follows the same rules as in a binary intermetallic phase T_xTt_y. The topological analyses of the Electron Localization Function (ELF) [148-150] of various intermetallic compounds of the systems *Ae*/Ni/Ge underline this idea: disynaptic valence basins were usually observed for short Ge-Ge contacts but not for short Ni-Ge or Ni-Ni contacts, even though high –iCOHP (integrated Crystal Orbital Hamilton Populations [151]) values were found. This might indicate metallic bonding within the polyanionic network.

V.1.2 Prediction of new intermetallic compounds

Furthermore, the findings concerning the structural relationships discussed in this article allow "educated guesses" for the prediction of possible compositions of new intermetallic phases. For example, in the systems *Ae*/Ni/Ge the compounds *Ae*NiGe and *Ae*Ni_2Ge_2 exist for *Ae* = Ca, Sr and Ba, the compounds *Ae*Ni_2Ge and *Ae*$NiGe_2$ exist for *Ae* = Sr and Ba and for *Ae* = Ca and Sr, respectively. In the composition triangle each of these compounds is situated on the intersections of three lines, connecting the elements with (sometimes hypothetical) binary compounds of the simple compositions 2:1, 1:1 and 1:2. Therefore, the existence of polar intermetallic phases, such as "Ae_2NiGe_2" and "Ae_2Ni_2Ge", with compositions according to further intersections of these lines, can be assumed.

Similarily, the prediction of binaries can be discussed. As described above, the structural motifs of $Ca_{10}Ni_{34}Ge_{16}$ (**17**), $CaNi_5Ge_3$ (**18**), $Ca_{15}Ni_{68}Ge_{37}$ (**19**) and $Ca_7Ni_{48.9(4)}Ge_{22.1(4)}$ (**20**) are also observed in the binary compounds Ni_3Ge, $CaNi_3$, Ca_2Ni_7 and $CaNi_5$. In contrary, the crystal structure of the Ni rich polar intermetallic compound $SrNi_9Ge_4$ (**21**) has no counterpart neither among the binary nor among the ternary compounds in the systems *Ae*/Ni/Ge. Hence, one might predict the existence of for example a binary phase "$SrNi_{13}$".

V.1.3 Summary

In this article various ternary polar intermetallic phases of the systems *Ae*/Ni/Ge (*Ae*: Ca, Sr, Ba) were described. The discussion revealed that, even though the systems *Ae*/Ni/Ge present a manifold variety of crystal structures, most of these can be traced back to a rather limited number of structure motifs. In detail, description focused on the following aspects:

- The influence of an increasing *Ae* size on the dimensionality of the Ni-Ge polyanions was discussed on the example of the compounds of the composition 1:1:1 (**1a** – **3**) and 1:2:2 (**4a** – **6**), showing that not only the number of valence electrons controls the occurrence of specific structure types.
- The $^{1}_{\infty}$[NiGe] ladder-type ribbons turned out to be the dominant structure motif in many phases described in this review. All the crystal structures of compounds **1** – **16** can be derived from these ribbons as a main building unit.
- The crystal structures of the Ni rich phases (**17** – **21**) as well as the Ge rich phases (**22** – **23**) were presented.
- Further, structural relationships are presented on the basis of the composition triangle containing all ternary polar intermetallic phases of the systems *Ae*/Ni/Ge. The ternary composition triangle was shown to provide a useful guideline to reveal structural relationships, as pointed out with special attention to the lines connecting the elements with (sometimes hypothetical) binary compounds of the simple compositions 2:1, 1:1 and 1:2. It is shown that the gradual addition of the respective third element (*Ae*, Ni or Ge) has a straightforward relation to the topology of the corresponding structures.
- The comparison of the ternary polar intermetallic compounds of the systems *Ae*/Ni/Ge with binary compounds of the systems *Ae*/Ge, Ni/Ge and *Ae*/Ni proved beneficial for a better understanding of the crystal structures.
- The description of polar intermetallic phases, using the binary compounds of the system Ni/Ge as a reference point, was discussed in analogy to the Zintl-Klemm concept.
- Possible ways to predict the compositions of new polar intermetallic compounds were suggested.

VI. Literature

[1] E. Zintl, G. Woltersdorf, *Z. Elektrochem.* **1935**, *41*, 876.

[2] E. Zintl, *Angew. Chem.* **1939**, *52*, 1.

[3] W. Klemm, *Proc. Chem. Soc., London* **1958**, 329.

[4] *Zintl Phases: Principles and Recent Developements, 139*, Springer-Verlag, Editor T.F. Fässler **2011**.

[5] J. D. Corbett, *Angew. Chem. Int. Ed.* **2000**, *39*, 670.

[6] H. Schäfer, B. Eisenman, W. Müller, *Angew. Chem. Int. Ed. Engl.* **1973**, *12*, 694.

[7] P. Eckerlin, H. J. Meyer, E. Wolfel, *Z. Anorg. Allg. Chem.* **1955**, *281*, 322.

[8] A. Betz, H. Schäfer, A. Weiss, *Z. Naturforsch., B: J. Chem. Sci.* **1967**, *B 22*, 103.

[9] W. Rieger, E. Parthe, *Acta Crystallogr.* **1967**, *22*, 919.

[10] F. Merlo, M. L. Fornasini, *J. Less Common Met.* **1967**, *13*, 603.

[11] V. V. Burnasheva, E. I. Gladyshevskii, *Inorg. Mater.* **1966**, *2*, 804.

[12] T. F. Fässler, C. Kronseder, *Angew. Chem. Int. Ed.* **1998**, *37*, 1571.

[13] T. F. Fässler, C. Kronseder, *Angew. Chem. Int. Ed. Engl.* **1997**, *36*, 2683.

[14] S. Hoffmann, T. F. Fässler, *Inorg. Chem.* **2003**, *42*, 8748.

[15] L. C. Allen, J. K. Burdett, *Angew. Chem. Int. Ed. Engl.* **1995**, *34*, 2003.

[16] W. P. Anderson, J. K. Burdett, P. T. Czech, *J. Am. Chem. Soc.* **1994**, *116*, 8808.

[17] J. C. Schön, *Angew. Chem. Int. Ed. Engl.* **1995**, *34*, 1081.

[18] V. Hlukhyy, T. F. Fässler, *private communications* **2011**.

[19] S. Stegmaier, T. F. Fässler, *J. Am. Chem. Soc.* **2011**, 19758.

[20] S. M. Kauzlarich, *Chemistry, Structure, and Bonding of Zintl Phases and Ions*, VCH Publishers, Inc. , New York, **1996**.

[21] P. S. Chizhov, Y. Prots, E. V. Antipov, Y. Grin, *Z. Anorg. Allg. Chem.* **2009**, *635*, 1863.

[22] P. S. Salamakha, *Handbook on the Physics and Chemistry of Rare Earths* **1999**, *27*, 225.

[23] V. Hlukhyy, L. Siggelkow, T. F. Fässler, *in preparation* **2011**.

[24] V. Hlukhyy, T. F. Fässler, *in preparation* **2011**.

[25] V. Hlukhyy, N. Chumalo, V. Zaremba, T. F. Fässler, *Z. Anorg. Allg. Chem.* **2008**, *634*, 1249.

[26] V. Hlukhyy, A. Senyshyn, D. Trots, T. F. Fässler, *HASYLAB Ann. Rep.* **2007**, *1*, 1021.

[27] V. Hlukhyy, T. F. Fässler, *Z. Anorg. Allg. Chem.* **2008**, *634*, 2316.

[28] L. Siggelkow, V. Hlukhyy, T. F. Fässler, *Z. Anorg. Allg. Chem.* **2010**, *636*, 1870.

[29] V. Hlukhyy, T. F. Fässler, *Z. Anorg. Allg. Chem.* **2010**, *636*, 100.

[30] L. Siggelkow, V. Hlukhyy, T. F. Fässler, *Z. Anorg. Allg. Chem.* **2011**, *637*, 2000.

[31] O. I. Bodak, E. I. Gladyshevskii, *Dopov. Akad. Nauk. Ukr. RSR* **1968**, *30*, 944.

[32] W. Dörrscheidt, N. Niess, H. Schäfer, *Z. Naturforsch., B: J. Chem. Sci.* **1976**, *31*, 890.

[33] W. Rieger, E. Parthe, *Monatsh. Chem.* **1969**, *100*, 439.

[34] G. Venturini, B. Malaman, *J. Alloys Compd.* **1996**, *235*, 201.

[35] V. Hlukhyy, S. Eck, T. F. Fässler, *Inorg. Chem.* **2006**, *45*, 7408.

[36] V. Hlukhyy, T. F. Fässler, *Proc. of GDCh-Jahrestagung,* Düsseldorf (Germany), **2005**, Mat020.

[37] L. Siggelkow, V. Hlukhyy, B. Wahl, T. F. Fässler, *Eur. J. Inorg. Chem.* **2011**, 4012.

[38] G. Cordier, P. Woll, *J. Less Common Met.* **1991**, *169*, 291.

[39] H. Zhang, J. T. Zhao, M. B. Tang, Z. Y. Man, H. H. Chen, X. X. Yang, *J. Phys. Chem. Solids* **2009**, *70*, 312.

[40] L. T. K. Nguyen, U. Aydemir, M. Baitinger, J. Custers, A. Haghighirad, R. Hofler, K. D. Luther, F. Ritter, Y. Grin, W. Assmus, S. Paschen, *J. Electron. Mater.* **2010**, *39*, 1386.

[41] L. T. K. Nguyen, U. Aydemir, M. Baitinger, E. Bauer, H. Borrmann, U. Burkhardt, J. Custers, A. Haghighirad, R. Hofler, K. D. Luther, F. Ritter, W. Assmus, Y. Grin, S. Paschen, *Dalton Trans.* **2010**, *39*, 1071.

[42] S. Johnsen, A. Bentien, G. K. H. Madsen, M. Nygren, B. B. Iversen, *Phys. Rev. B* **2007**, *76*, 9.

[43] M. Pani, A. Palenzona, *J. Alloys Compd.* **2008**, *462*, L9.

[44] A. Palenzona, P. Manfrinetti, M. L. Fornasini, *J. Alloys Compd.* **2002**, *345*, 144.

[45] A. Palenzona, M. Pani, *J. Alloys Compd.* **2005**, *402*, 136.

[46] K. Turban, H. Schafer, *Z. Naturforsch., B: J. Chem. Sci.* **1973**, *B 28*, 220.

[47] B. Eisenmann, H. Schäfer, K. Turban, *Z. Naturforsch., B: J. Chem. Sci.* **1975**, *30*, 677.

[48] P. Eckerlin, E. Wolfel, *Z. Anorg. Allg. Chem.* **1955**, *280*, 321.

[49] Siggelkow L., Hlukhyy V., T. F. Fässler, *in preparation* **2011**.

[50] R. Nesper, F. Zürcher, *Z. Kristallogr. - New Cryst. Struct.* **1999**, *214*, 22.

[51] F. Zürcher, R. Nesper, *Angew. Chem. Int. Ed.* **1998**, *37*, 3314.

[52] V. G. Andrianov, K. A. Bol'shakov, E. B. Sokolov, A. V. Chirkin, A. V. Chirkin, P. I. Fedorov, *Inorg. Mater.* **1966**, *2*, 1784.

[53] A. Betz, H. Schäfer, A. Weiss, R. Wulf, *Z. Naturforsch., B: J. Chem. Sci.* **1968**, *B 23*, 878.

[54] R. Kröner, *Dissertation, Universität Stuttgart* **1989**.

[55] J. T. Vaughey, G. J. Miller, S. Gravelle, E. A. Leon-Escamilla, J. D. Corbett, *J. Solid State Chem.* **1997**, *133*, 501.

[56] R. Nesper, F. Zürcher, *Z. Kristallogr. - New Cryst. Struct.* **1999**, *214*, 21.

[57] A. Betz, H. Schäfer, A. Weiss, R. Wulf, *Z. Naturforsch., B: J. Chem. Sci.* **1968**, *B 23*, 878.

[58] J. Evers, G. Oehlinger, A. Weiss, *Z. Naturforsch., B: J. Chem. Sci.* **1979**, *34*, 524.

[59] Eisenman.B, H. Schafer, *Z. Naturforsch., B: J. Chem. Sci.* **1974**, *B 29*, 460.

[60] H. J. Wallbaum, *Naturwissenschaften* **1944**, *32*, 76a.

[61] P. H. Tobash, S. Bobev, *J. Solid State Chem.* **2007**, *180*, 1575.

[62] H. Fukuoka, Y. Tomomitsu, K. Inumaru, *Inorg. Chem.* **2011**, *50*, 6372.

[63] R. Kröner, K. Peters, H. G. von Schnering, *Z. Kristallogr. - New Cryst. Struct.* **1998**, *213*, 663.

[64] W. Carrillo-Cabrera, J. Curda, H. G. von Schnering, S. Paschen, Y. Grin, *Z. Kristallogr. - New Cryst. Struct.* **2000**, *215*, 207.

[65] H. Fukuoka, K. Iwai, S. Yamanaka, H. Abe, K. Yoza, L. Haming, *J. Solid State Chem.* **2000**, *151*, 117.

[66] S. J. Kim, S. Q. Hu, C. Uher, T. Hogan, B. Q. Huang, J. D. Corbett, M. G. Kanatzidis, *J. Solid State Chem.* **2000**, *153*, 321.

[67] W. Carrillo-Cabrera, S. Budnyk, Y. Prots, Y. Grin, *Z. Anorg. Allg. Chem.* **2004**, *630*, 2267.

[68] U. Aydemir, L. Akselrud, W. Carrillo-Cabrera, C. Candolfi, N. Oeschler, M. Baitinger, F. Steglich, Y. Grin, *J. Am. Chem. Soc.* **2010**, *132*, 10984.

[69] H. Fukuoka, S. Yamanaka, E. Matsuoka, T. Takabatake, *Inorg. Chem.* **2005**, *44*, 1460.

[70] Y. Q. Liu, D. J. Ma, Y. Du, *J. Alloys Compd.* **2010**, *491*, 63.

[71] H. Takizawa, K. Uheda, T. Endo, *J. Alloys Compd.* **2000**, *305*, 306.

[72] H. Pfisterer, K. Schubert, *Z. Metallk.* **1950**, *41*, 358.

[73] M. Ellner, T. Gödecke, K. Schubert, *J. Less-Common Met.* **1971**, *24*, 23.

[74] A. K. Larsson, R. Withers, *J. Alloy. Compd.* **1998**, *264*, 125.

[75] M. Ellner, *Z. Metallk.* **1976**, *67*, 246.

[76] M. Ellner, *J. Less Common Met.* **1976**, *48*, 21.

[77] P. Höhn, U. Burkhardt, S. Hoffmann, F. Jach, R. Kniep, *Z. Anorg. Allg. Chem.* **2011**, *637*, 1957.

[78] P. Höhn, S. Agrestini, A. Baranov, S. Hoffmann, M. Kohout, F. Nitsche, F. R. Wagner, R. Kniep, *Chem.-Eur. J.* **2011**, *17*, 3347.

[79] Y. Takeuchi, K. Mochizuki, M. Watanabe, I. Obinata, *Metall (Heidelberg)* **1966**, *20*, 2.

[80] K. H. J. Buschow, *J. Less Common Met.* **1974**, *38*, 95.

[81] C. Geneys, S. Vilminot, L. Cot, *Acta Crystallogr., Sect. B: Struct. Sci.* **1976**, *32*, 3199.

[82] J. H. Wernick, W. J. Romanow, S. E. Haszko, *J. Appl. Phys.* **1961**, *32*, 2495.

[83] C. B. Shoemaker, D. P. Shoemaker, *Acta Crystallogr.* **1965**, *18*, 900.

[84] W. Dorrscheidt, H. Schafer, *J. Less Common Met.* **1978**, *58*, 209.

[85] D. B. DeMooij, K. H. J. Buschow, *J. Less Common Met.* **1984**, *102*, 113.

[86] O. P. Bodak, E. I. Gladyshevskii, *Sov. Phys. Crystallogr.* **1970**, *14*, 859.

[87] J. A. Stepien, Lukaszew.K, Hladysze.Ei, O. Bodak, *Bulletin De L Academie Polonaise Des Sciences-Serie Des Sciences Chimiques* **1972**, *20*, 1029.

[88] V. Fritsch, S. Bobev, J. D. Thompson, J. L. Sarrao, *J. Alloys Compd.* **2005**, *388*, 28.

[89] O. I. Bodak, V. K. Pecharskii, O. Y. Mruz, V. Y. Zavodnik, G. M. Vitvitska, P. S. Salamakha, *Dopov. Akad. Nauk. Ukr. RSR* **1985**, *2*, 36.

[90] O. I. Bodak, *Kristallografiya* **1979**, *24*, 1280.

[91] J. Gallmeier, H. Schafer, A. Weiss, *Z. Naturforsch., B: J. Chem. Sci.* **1967**, *B 22*, 1080.

[92] J. Goodey, J. G. Mao, A. M. Guloy, *J. Am. Chem. Soc.* **2000**, *122*, 10478.

[93] S. Geller, *Acta Crystallogr.* **1955**, *8*, 83.

[94] A. Palenzona, P. Manfrinetti, M. L. Fornasini, *J. Alloys Compd.* **2000**, *312*, 165.

[95] L. Siggelkow, V. Hlukhyy, T. F. Fässler, *J. Solid State Chem.* **2012**, *accepted*

[96] K. Janzon, H. Schafer, A. Weiss, *Z. Naturforsch., B: J. Chem. Sci.* **1966**, *B 21*, 287.

[97] E. A. Leon-Escamilla, J. D. Corbett, *J. Solid State Chem.* **2001**, *159*, 149.

[98] Y. B. Kuz'ma, V. S. Telegus, D. A. Kovalyk, *Sov. Powder Metall. Met. Ceram.* **1969**, *8*, 403.

[99] A. V. Mudring, J. D. Corbett, *J. Am. Chem. Soc.* **2004**, *126*, 5277.

[100] B. Eisenman, H. Schäfer, *Z. Naturforsch., B: J. Chem. Sci.* **1974**, *B 29*, 460.

[101] A. J. Frueh, *Acta Crystallogr.* **1951**, *4*, 66.

[102] J. Evers, A. Weiss, *Solid State Commun.* **1975**, *17*, 41.

[103] B. Eisenman, K. H. Janzon, H. Schafer, A. Weiss, *Z. Naturforsch., B: J. Chem. Sci.* **1969**, *B 24*, 457.

[104] W. Hofmann, W. Jaeniche, *Naturwissenschaften* **1935**, *23*, 851.

[105] K. H. Janzon, H. Schafer, A. Weiss, *Z. Anorg. Allg. Chem.* **1970**, *372*, 87.

[106] G. Brauer, A. Mitius, *Z. Anorg. Allg. Chem.* **1942**, *249*, 325.

[107] J. Evers, G. Oehlinger, A. Weiss, *Z. Naturforsch., B: J. Chem. Sci.* **1977**, *32*, 1352.

[108] E. I. Gladyshevskii, *Dopov. Akad. Nauk. Ukr. RSR* **1964**, *2*, 209.

[109] K. H. Lii, R. C. Haushalter, *J. Solid State Chem.* **1987**, *67*, 374.

[110] K. H. Janzon, H. Schafer, A. Weiss, *Z. Naturforsch., B: J. Chem. Sci.* **1968**, *B 23*, 1544.

[111] T. F. Fässler, C. Kronseder, *Z. Anorg. Allg. Chem.* **1998**, *624*, 561.

[112] W. Carrillo-Cabrera, J. Curda, K. Peters, S. Paschen, M. Baenitz, Y. Grin, H. G. von Schnering, *Z. Kristallogr. - New Cryst. Struct.* **2000**, *215*, 321.

[113] J. D. Bryan, G. D. Stucky, *Chem. Mater.* **2001**, *13*, 253.

[114] K. Schubert, H. Pfisterer, *Z. Metallk.* **1950**, *41*, 433.

[115] R. D. Heyding, L. D. Calvert, *Can. J. Chem.* **1957**, *35*, 449.

[116] F. Laves, H. J. Wallbaum, *Z. Angew. Mineral.* **1942**, *4*, 17.

[117] M. El Boragy, S. Bhan, K. Schubert, *J. Less-Common Met.* **1970**, *22*, 445.

[118] C. H. Johansson, J. O. Linde, *Ann. Phys.* **1925**, *78*, 439.

[119] J. B. Friauf, *J. Am. Chem. Soc.* **1927**, *49*, 3107.

[120] D. T. Cromer, C. E. Olsen, *Acta Crystallogr.* **1959**, *12*, 689.

[121] V. F. Novy, R. C. Vickery, E. V. Kleber, *Transactions of the Metallurgical Society of Aime* **1961**, *221*, 588.

[122] W. Haucke, *Z. Anorg. Allg. Chem.* **1940**, *244*, 17.

[123] A. Kul, Y. Topkaya, *Hydrometallurgy* **2008**, *92*, 87.

[124] P. S. Salamankha, *Handbook on the Physics and Chemistry of Rare Earths* **1999**, *27*, 225.

[125] W. J. Moore, L. Pauling, *J. Am. Chem. Soc.* **1941**, *63*, 1392.

[126] P. Villars, L. D. Calvert*, Vol. 2nd Edition*, ASM International, Materials Park, OH, **1991**.

[127] P. Salamakha, M. Konyk, O. Sologub, O. Bodak, *J. Alloys Compd.* **1996**, *236*, 206.

[128] Y. K. Gorelenko, P. K. Starodub, V. A. Bruskov, R. V. Skolozdra, V. I. Yarovetz, O. I. Bodak, V. K. Pecharsky, *Ukrainskii Fizicheskii Zhurnal* **1984**, *29*, 867.

[129] M. F. Fedyna, V. K. Pecharsky, O. I. Bodak, *Dopov. Akad. Nauk. Ukr. RSR Seria B* **1987**, 50.

[130] G. M. Koterlyn, O. I. Bodak, V. V. Pavlyuk, J. Stepien-Damm, A. Pietraszko, *J. Alloys Compd.* **1999**, *291*, 110.

[131] B. D. Oniskovets, V. K. Belsky, V. K. Pecharsky, O. I. Bodak, *Kristallografiya* **1987**, *32*, 888.

[132] P. Villars, K. Cenzual*, Vol. Version 1.0*, ASM International @, Materials Park, Ohio, USA, **2007/8**.

[133] O. I. Bodak, E. I. Gladyshevskii, P. I. Krypyakevych, *Inorg. Mater.* **1966**, *2*, 1861.

[134] D. R. Parker, M. J. Pitcher, P. J. Baker, I. Franke, T. Lancaster, S. J. Blundell, S. J. Clarke, *Chem. Commun.* **2009**, 2189.

[135] O. I. Bodak, E. I. Gladyshevskii, A. V. Kardash, E. E. Cherkashin, *Izv.Akad.Nauk, Neorg.Mater.* **1970**, *6*, 935.

[136] M. Pfisterer, G. Nagorsen, *Z. Naturforsch., B: J. Chem. Sci.* **1980**, *35*, 703.

[137] S. Rozsa, H. U. Schuster, *Z. Naturforsch., B: J. Chem. Sci.* **1981**, *36*, 1668.

[138] Z. Ban, M. Sikirica, *Acta Crystallogr.* **1965**, *18*, 594.

[139] G. Hägg, A. L. Kindström, *Z. Phys. Chem. (Abt. B)* **1933**, *22*, 453.

[140] G. Aminoff, *Z. Kristallogr.* **1923**, *58*, 203.

[141] K. Toman, *Acta Crystallogr.* **1952**, *5*, 329.

[142] W. Dörrscheidt, H. Schäfer, *Z. Naturforsch., B: J. Chem. Sci.* **1980**, *35*, 297.

[143] B. Eisenman, H. Schafer, N. May, W. Muller, *Z. Naturforsch., B: J. Chem. Sci.* **1972**, *B 27*, 1155.

[144] F. Steglich, U. Ahleheim, C. Schank, C. Geibel, S. Horn, M. Lang, G. Sparn, A. Loidl, A. Krimmel, *J. Magn. Magn. Mater.* **1990**, *84*, 271.

[145] E. Zintl, W. Haucke, *Z. Elektrochem.* **1938**, *44*, 104.

[146] C. Kranenberg, A. Mewis, *Z. Anorg. Allg. Chem.* **2003**, *629*, 1023.

[147] A. L. Lyubimtsev, A. I. Baranov, A. Fischer, L. Kloo, B. A. Popovkin, *J. Alloys Compd.* **2002**, *340*, 167.

[148] A. D. Becke, K. E. Edgecombe, *J. Chem. Phys.* **1990**, *92*, 5397.

[149] T. F. Fässler, *Chem. Soc. Rev.* **2003**, *32*, 80.

[150] A. Savin, R. Nesper, S. Wengert, T. F. Fassler, *Angew. Chem. Int. Ed. Engl.* **1997**, *36*, 1809.

[151] R. Dronskowski, P. E. Blochl, *J. Phys. Chem.* **1993**, *97*, 8617.

4.4 Polar Intermetallic Phases in the Systems Ca/Co/Si and Ba/Co/Ge

4.4.1 Synthesis, Structure and Chemical Bonding of $CaCo_2Si_2$ and $BaCo_2Ge_2$ – Two New Compounds with $ThCr_2Si_2$ Structure Type

Published:

L. Siggelkow, V. Hlukhyy, T. F. Fässler, *Z. Anorg. Allg. Chem*. **2010**, *636,* 378–384.

Appendix

Table A1 Anisotropic displacement parameters (U_{ij} / Å^2) for $CaCo_2Si_2$

Atom	U_{11}	U_{22}	U_{33}	U_{12}	U_{13}	U_{23}
Ca	0.0060(1)	0.0060(1)	0.0070(2)	0.00000	0.00000	0.00000
Si	0.0053(2)	0.0053(2)	0.0068(2)	0.00000	0.00000	0.00000
Co	0.0046(1)	0.00464(7)	0.00543(8)	0.00000	0.00000	0.00000

Table A2 Anisotropic displacement parameters (U_{ij} / Å^2) for $BaCo_2Ge_2$

Atom	U_{11}	U_{22}	U_{33}	U_{12}	U_{13}	U_{23}
Ba	0.0089(3)	0.0089(3)	0.0080(3)	0.00000	0.00000	0.00000
Co	0.0070(3)	0.0070(3)	0.0102(4)	0.00000	0.00000	0.00000
Ge	0.0070(3)	0.0070(3)	0.0155(4)	0.00000	0.00000	0.00000

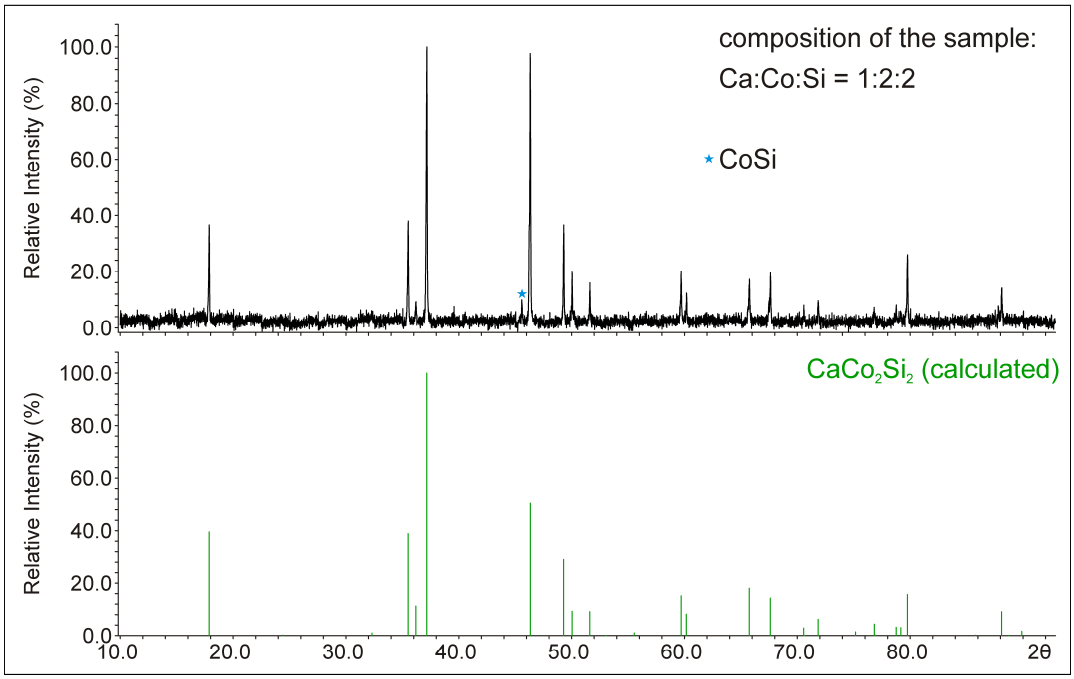

Figure A1 Experimental powder XRD pattern (top) from sample loading Ca : Co : Si = 1 : 2 : 2 and simulated powder XRD pattern (bottom) of $CaCo_2Si_2$. The experimental powder XRD pattern was recorded in transmission geometry and its background has been subtracted. Reflections of CoSi are labelled with a blue star.

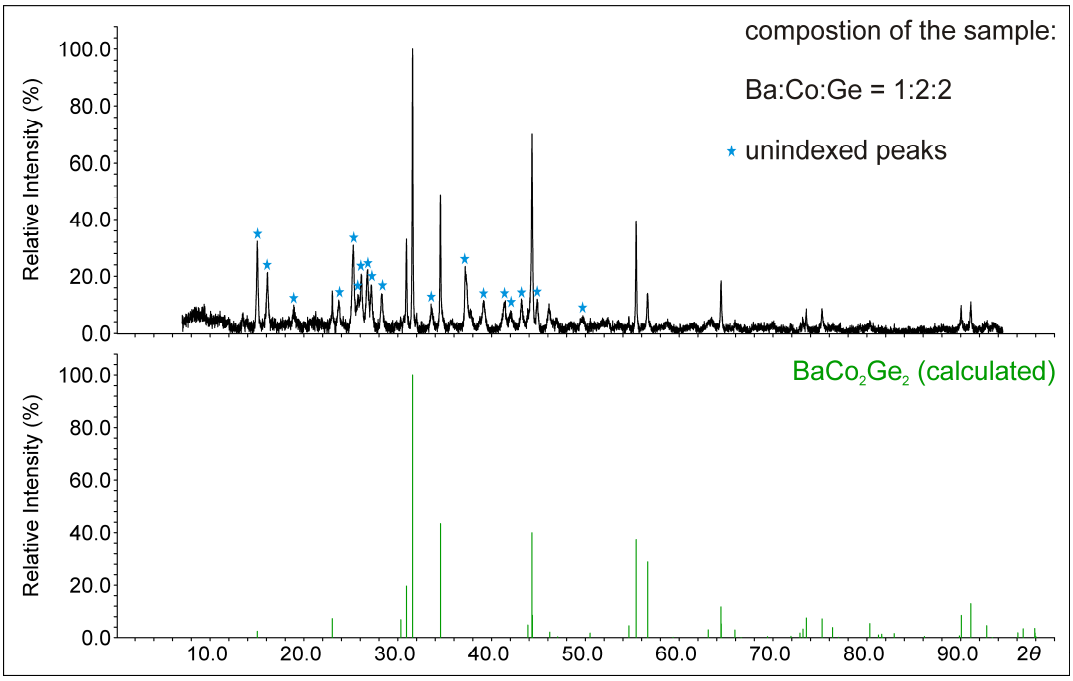

Figure A2 Experimental powder XRD pattern (top) from sample loading Ba : Co : Ge = 1 : 2 : 2 and simulated powder XRD pattern (bottom) of $BaCo_2Ge_2$. The sample has been exposed to air. Thus, the air sensitive α-Ba_3Ge_4 is oxidized and the peaks of $BaCo_2Ge_2$ are seen more clearly (compare Figure A3). The resulting new peaks most likely belong to the oxidation product, but cannot be assigned to a certain phase. The experimental powder XRD pattern was recorded in transmission geometry and its background has been subtracted. Unindexed reflections are labelled with a blue star.

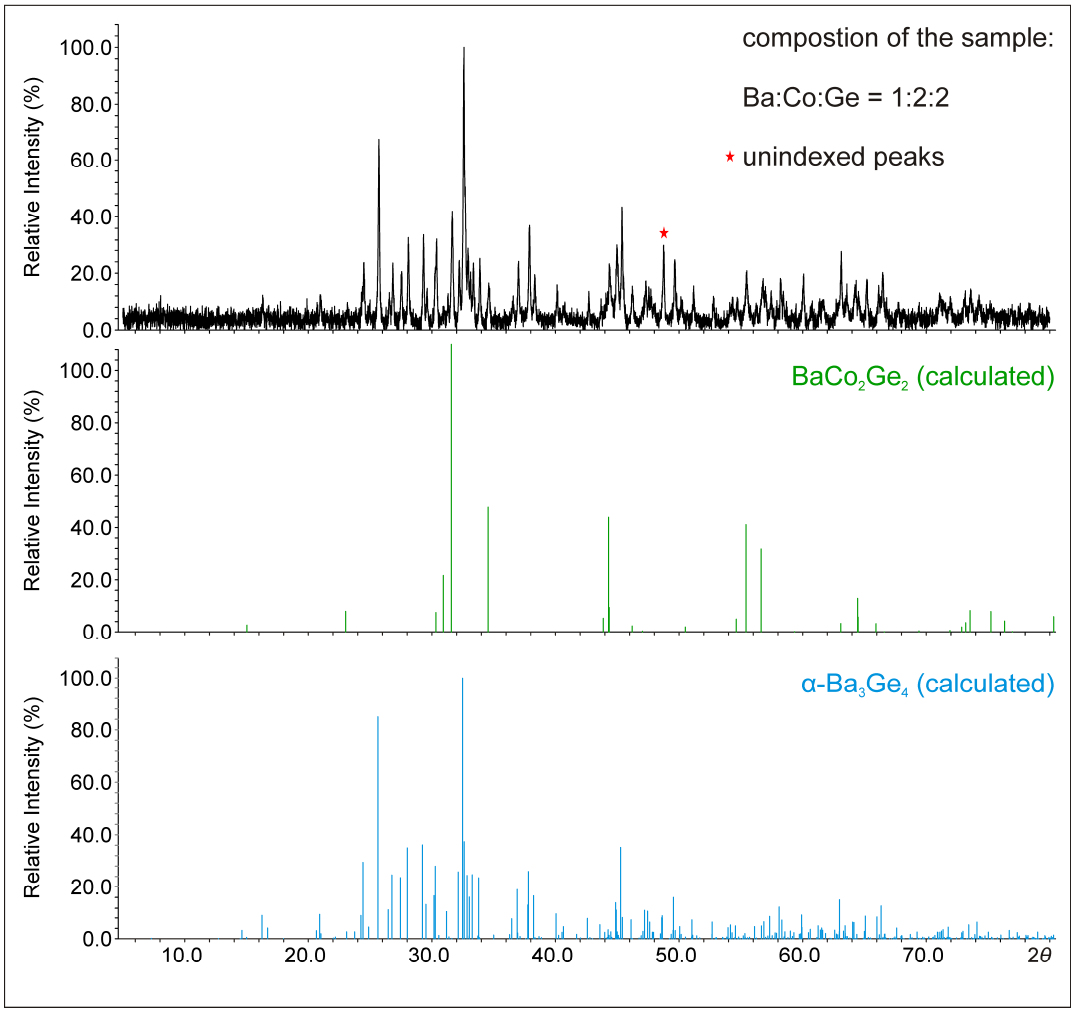

Figure A3 Experimental powder XRD pattern (top) from sample loading Ba : Co : Ge = 1 : 2 : 2 and simulated powder XRD pattern of $BaCo_2Ge_2$ (middle) as well as of α-Ba_3Ge_4 (bottom). The experimental powder XRD pattern was recorded in Debye Scherrer geometry and its background has been subtracted. Unindexed reflections are labelled with a red star.

4.5 Polar Intermetallic Phases in the Systems *Ae*/Ni/Sn (*Ae*: Mg, Ca)

4.5.1 Ca_2NiSn_2 – A Polymorphic Intermetallic Phase: Atomic and Electronic Structure as well as Topological Description of the Phase Transition by a Sigmatropic-Type Rearrangement of Ni and Sn Atoms

Published:
L. Siggelkow, V. Hlukhyy, T. F. Fässler, *Eur. J. Inorg. Chem.* **2012**, 987–997.

4.5.2 $Mg_{0.39(2)}NiSn_{1.61(2)}$ and $Mg_{2.61(2)}Ni_4Sn_{3.39(2)}$ – Two New Intermetallic Phases in the System Mg/Ni/Sn

$Mg_{0.39(2)}NiSn_{1.61(2)}$ and $Mg_{2.61(2)}Ni_4Sn_{3.39(2)}$ – Two New Intermetallic Phases in the System Mg/Ni/Sn

Lisa Siggelkow, Thomas F. Fässler

to be submitted

Abstract.

The intermetallic compounds $Mg_{0.39(2)}NiSn_{1.61(2)}$ and $Mg_{2.61(2)}Ni_4Sn_{3.39(2)}$ were prepared by reaction of the elements in welded tantalum ampoules in a resistant furnace. The crystal structures and composition of the compounds were investigated by single crystal X-ray diffraction. $Mg_{0.39(2)}NiSn_{1.61(2)}$ crystallizes in the α-$PdSn_2$ structure type, with the space group $I4_1/acd$, a = 6.1941(4) Å, c = 23.498(2) Å, wR_2 = 0.078 (all data), 303 F^2 values, 19 variable parameters. The main building block of $Mg_{0.39(2)}NiSn_{1.61(2)}$ is a $Ni_2@(Mg/Sn)_{12}$ polyhedron, which consist of two face-sharing Ni-centered square antiprisms. The polyhedra share vertices to form a three-dimensional network of Mg/Sn.

$Mg_{2.61(2)}Ni_4Sn_{3.39(2)}$ crystallizes in an own structure type, with space group $P\bar{3}m1$, a = 4.3230(9) Å, c = 10.490(3) Å, wR_2 = 0.037 (all data), 216 F^2 values, 21 variable parameters. The crystal structure of $Mg_{2.61(2)}Ni_4Sn_{3.39(2)}$ is described as an intermediate of a Heusler and a Half-Heusler type structure. Further, the group-subgroup relationship of β-CuZn, $MgNi_2Sn$ and $Mg_{2.61(2)}Ni_4Sn_{3.39(2)}$ is described.

Keywords: Stannides, Intermetallic Phases, Heusler Phase

Introduction

In recent years, a number of ternary polar intermetallic compounds in the systems *Ae*/Ni/*Tt* (*Ae*: Ca, Sr, Ba, *Tt*: Ge, Sn) [1-9] were described. The crystal structure of these intermetallic compounds mostly consists of a polyanionic [Ni_xTt_y] network, in whose cavities the alkaline earth metal atoms are situated. Extending the studies to the system Mg/Ni/Ge, similar three-dimensional polyanionic networks containing Ni and Ge atoms appear in the compounds MgNiGe, $Mg_6Ni_{16}Ge_7$, $MgNi_6Ge_6$ and $MgNi_{2-x}Ge_x$ [10-13]. In contrast, Mg/Sn mixed site occupancies are observed in the system Mg/Ni/Sn. Due to the similar radii of Mg and Sn, this does not come as a surprise and was described before for the system Mg/Ni/Sn as well as for similar systems, such as Mg/Ru/Sn (mixing of Mg and Sn) and Mg/Ir/In (mixing of Mg and In) (e.g. [14-16] and references therein). Further examples of the rich chemistry of stannides and intermetallic Sn compounds were reviewed in [17].

Until now the following ternary intermetallic compounds were described in the system Mg/Ni/Sn: $MgNi_2Sn$ [18] (Heusler phase, Cu_2MnAl structure type [19]), Mg_xNiSn_{2-x} [15] (Mg_2Ni structure type [20] for $x = 1.85$ and Mg_2Cu structure type [21] for $x = 1.78$, 1.60) as well as $Mg_{74.5}Ni_{14.5}Sn_{11}$ [22] (own structure type). Herein we report the synthesis and crystal structures of two new intermetallic phases: $Mg_{0.39(2)}NiSn_{1.61(2)}$ (Mg_xNiSn_{2-x} with $x = 0.39(2)$) and $Mg_{2.61(2)}Ni_4Sn_{3.39(2)}$ ($Mg_{3-x}Ni_4Sn_{3+x}$ with $x = 0.39(2)$).

Experimental Section

Syntheses

Starting materials for the synthesis of $Mg_{0.39(2)}NiSn_{1.61(2)}$ and $Mg_{2.61(2)}Ni_4Sn_{3.39(2)}$ were commercially available elements: ingots of the magnesium (ChemPur), nickel powder (Acros Organics) and tin drops (ChemPur), all with stated purities higher than 99.5%.

Pieces of the elements were enclosed in tantalum tubes under argon atmosphere (Mini Arc Melting System, MAM-1, Johanna Otto GmbH). The tantalum tubes were then

sealed in a quartz tube and heated in a resistant furnace (LOBA, HTM Reetz GmbH) to 700 °C. At this temperature the samples were tempered for two weeks. Finally the samples were quenched in water.

Furthermore, syntheses using a high frequency furnace were carried out: the elements were sealed in tantalum ampoules under argon atmosphere (Mini Arc Melting System, MAM-1, Johanna Otto GmbH) and placed in a water-cooled sample chamber of an induction furnace (Hüttinger Elektronik, Freiburg, Typ TIG 2.5/300). The ampoules were then heated under flowing argon up to approximately 920 °C and held at this temperature for 30 minutes. After the melting procedure, the samples were cooled within half an hour to approximately 700 °C and finally cooled down to room temperature in about one minute by switching off the furnace.

In detail, the reaction of 0.7 g of the elements in the ratio Mg : Ni : Sn = 2 : 1 : 2 in the resistant furnace led to a mixture of Mg_2Sn (main phase), $Mg_{0.39(2)}NiSn_{1.61(2)}$ and at least one other, yet unreported phase. The reaction of 0.7 g of the elements in the ratio 2 : 1 : 2 using the induction furnace led to a mixture of $Mg_{2.61(2)}Ni_4Sn_{3.39(2)}$, $Mg_{0.39(2)}NiSn_{1.61(2)}$, Mg_2Sn, Mg_9Sn_5 and Sn.

Attempts to obtain $Mg_{0.39(2)}NiSn_{1.61(2)}$ as pure products in the resistance furnace by mixing stoichiometric amounts of the elements were not successful. Mixing 0.7 g of the elements in the ratio 13 : 33.3 : 53.7 led to the formation of the binary phases Ni_3Sn_2 [23] and Ni_3Sn_4 [24]. The highest yield of $Mg_{2.61(2)}Ni_4Sn_{3.39(2)}$ was obtained by mixing 0.7 g of the elements in the ratio 18 : 47 : 32, leading to $Mg_{2.61(2)}Ni_4Sn_{3.39(2)}$ and Ni_3Sn_2 [23].

After cooling to room temperature, the samples exhibiting metallic lustre could easily be separated from the tantalum crucible. Both compounds are stable against air and moisture. Single crystals with platelet shape were isolated from the crushed sample.

Powder X-ray Diffraction Studies

The composition of the sample was checked using a STOE STADI P powder diffractometer equipped with a curved imaging plate and a linear position sensitive detector (IP-PSD and L-PSD) using Cu $K_{\alpha 1}$ radiation ($\lambda = 1.54060$ Å, Ge(111) monochromator). Data were recorded at room temperature within a 2θ range of 7 - 90° from finely ground sample held between two scotch films or filled in glass capillaries. The

obtained data were analyzed using the program package WinXPOW [25]. The powder X-ray diffraction patterns are given in the supporting information (Figure S1 and S2).

Single crystal X-ray diffraction studies and structure refinement

Air stable single crystals of $Mg_{0.39(2)}NiSn_{1.61(2)}$ and $Mg_{2.61(2)}Ni_4Sn_{3.39(2)}$ were found in samples of the composition Mg : Ni : Sn = 2 : 1 : 2 and Mg : Ni : Sn = 1 : 1 : 2, respectively. They were fixed on the top of a glass fibre on air using nail polish. Single crystal X-ray diffraction intensity data were collected at room temperature using an IPDS 2T with graphite monochromatized MoK_α ($\lambda = 0.71073$ Å) radiation. The raw data were corrected for background, polarization and Lorentz factor. Further, the data were numerically corrected for absorption [26, 27]. The atomic position parameters were deduced from an automatic interpretation of direct methods with SHELXS-97 [28]. The structures were refined using SHELXL-97 (full-matrix least-squares on F_o^2) [29] with anisotropic atomic displacement parameters for all atoms. Mixed occupancies of Mg and Sn were refined for both compounds. Positions and atomic displacement parameters (ADPs) for Mg and Sn were set to be equal at the respective atom sites. Particular free variables with an overall occupancy of 1 were applied to determine the occupation ratio at these positions. For $Mg_{0.39(2)}NiSn_{1.61(2)}$ mixing of Mg and Sn was observed on the Wyckoff positions 16*e* and 16*f*. The refinement of the occupancy parameters led to 0.74(1) for Sn1, 0.26(1) for Mg1, 0.87(1) for Sn2 and 0.13(1) for Mg2. For $Mg_{2.61(2)}Ni_4Sn_{3.39(2)}$ mixed occupancies of Sn and Mg were observed on the Wyckoff positions 2*d* and 1*a*. Refinement of the occupancy parameters led to 0.92(1) for Sn1, 0.08(1) for Mg1, 0.77(1) for Sn2 and 0.23(1) for Mg2. The positions of the Ni atoms as well as those occupied exclusively by Sn in $Mg_{2.61(2)}Ni_4Sn_{3.39(2)}$ were fully occupied (free refinement of the occupancy parameters led to 1.01(1) for Sn3, 1.01(1) for Sn4, 0.99(1) for Ni1 and 0.95(1) for Ni2).

All relevant crystallographic data for the data collection and evaluation are listed in Table 1. The positional parameters and selected interatomic distances are listed in Tables 2 and 3. The anisotropic displacement parameters are given in the supporting information, Table S1 and S2.

EDX Measurement

After X-ray diffraction measurement the single crystals were analyzed with a JEOL SEM 5900LV scanning electron microscope. A qualitative EDX analysis of well-shaped single crystals revealed the presence of all three elements Mg, Ni, and Sn and the absence of elements heavier than Na. A semi-quantitative EDX analysis of the ratio Ni/Sn confirmed the ratios obtained by single crystal X-ray diffraction: For $Mg_{0.39(2)}NiSn_{1.61(2)}$ a Ni/Sn ratio of 0.6(2) (calculated: 0.63) and for $Mg_{2.61(2)}Ni_4Sn_{3.39(2)}$ a Ni/Sn ratio of 1.1(2) (calculated: 1.18) was obtained.

Table 1 Crystal data and structure refinement for $Mg_{0.39(2)}NiSn_{1.61(2)}$ and $Mg_{2.61(2)}Ni_4Sn_{3.39(2)}$

Empirical formula	**$Mg_{0.39(2)}NiSn_{1.61(2)}$**	**$Mg_{2.61(2)}Ni_4Sn_{3.39(2)}$**
Formula weight	258.34 g/mol	700.65 g/mol
Space group, Z	$I4_1/acd$, $Z = 16$	$P\bar{3}m$, $Z = 1$
Unit cell dimensions	a = 6.1941(4) Å c = 23.498(2) Å V = 901.5(1) Å^3	a = 4.3230(9) Å c = 10.490(3) Å V = 169.77(7) Å^3
Calculated density	7.613 g/cm^3	6.660 g/cm^3
Absorption coefficient	25.58 mm^{-1}	23.22 mm^{-1}
F(000)	1805	313
Crystal size	0.03 × 0.08 × 0.09 mm	0.02 × 0.05 × 0.08 mm
θ range	5° to 29.1°	5.5° to 29.2°
Range in hkl	±8, ±8, ±32	± 5, ± 5, ± 14
Reflections collected	10592	1704
Independent reflections	303 (R_{int} = 0.049)	216 (R_{int} = 0.026)
Reflections with $I \geq 2\sigma(I)$	282 (R_{sigma} = 0.013)	206 (R_{sigma} = 0.011)
Data/parameters	255 / 19	216 / 20
GOF on F^2	1.267	1.328
Final R indices [$I > 2\sigma(I)$]	R_1 = 0.033 wR_2 = 0.077	R_1 = 0.020 wR_2 = 0.048
R indices (all data)	R_1 = 0.034 wR_2 = 0.078	R_1 = 0.022 wR_2 = 0.048
Extinction coefficient	0.003(1)	0.025(2)
Largest diff. peak and hole	1.79 / – 1.36 e/Å^3	0.77 / – 1.36 e/Å^3

Table 2 Atomic coordinates and equivalent isotropic displacement parameters ($Å^2 \times 10^3$) for $Mg_{0.39(2)}NiSn_{1.61(2)}$ (space group $I4_1/acd$) and $Mg_{2.61(2)}Ni_4Sn_{3.39(2)}$ (space group $P\bar{3}m$).

Atom	Wyckoff position	Occ. ≠ 1	*x*	*y*	*z*	U_{eq} (A^2) × 10^3
$Mg_{0.39(2)}NiSn_{1.61(2)}$						
Mg1	16*e*	0.26(1)	0.2558(2)	0	¼	12(1)
Sn1	16*e*	0.74(1)	0.2558(2)	0	¼	12(1)
Mg2	16*f*	0.13(1)	0.6657(1)	0.0844(1)	3/8	15(1)
Sn2	16*f*	0.87(1)	0.6657(1)	0.0844(1)	3/8	15(1)
Ni	16*d*	1	½	¼	0.18230(4)	11(1)
$Mg_{2.61(2)}Ni_4Sn_{3.39(2)}$						
Mg1	2*d*	0.921(6)	2/3	1/3	0.3214(2)	13(1)
Sn1	2*d*	0.080(6)	2/3	1/3	0.3214(2)	13(1)
Mg2	1*a*	0.768(8)	0	0	0	13(1)
Sn2	1*a*	0.231(8)	0	0	0	13(1)
Sn3	2*d*	1	1/3	2/3	0.17532(4)	11(1)
Sn4	1*b*	1	0	0	0.5	8(1)
Ni1	2*d*	1	1/3	2/3	0.42872(9)	9(1)
Ni2	2*d*	1	1/3	2/3	0.92901(9)	10(1)

Table 3 Interatomic distances (Å) calculated with the lattice parameters taken from X-ray diffraction single crystal data.

		distance(Å)			distance(Å)
$Mg_{0.39(2)}NiSn_{1.61(2)}$					
Mg1/Sn1	Ni	2.6863(8) (2×)	Mg2/Sn2	Ni	2.6748(6) (4×)
	Ni	2.7273(8) (2×)		Mg2/Sn2	2.902(2) (1×)
	Mg2/Sn2	3.0350(4) (2×)		Mg2/Sn2	3.2685(4) (4×)
	Mg1/Sn1	3.0970(2) (4×)			
			Ni	Ni	2.693(2) (1×)
$Mg_{2.61(2)}Ni_4Sn_{3.39(2)}$					
Mg1/Sn1	Ni1	2.621(3) (1×)	Sn3	Ni2	2.584(2) (1×)
	Ni2	2.626(3) (1×)		Ni1	2.658(2) (1×)
	Ni1	2.738(2) (3×)		Ni2	2.7253(7) (3×)
	Sn3	2.929(2) (3×)			
	Sn4	3.121(2) (3×)	Sn4	Ni1	2.6055(6) (6×)
Mg2/Sn2	Ni2	2.6046(6) (6×)	Ni1	Ni1	2.910(1) (3×)
	Sn3	3.1003(6) (6×)			
			Ni2	Ni2	2.906(2) (3×)

Results and Discussion

Crystal Structure of $Mg_{0.39(2)}NiSn_{1.61(2)}$

$Mg_{0.39(2)}NiSn_{1.61(2)}$ crystallizes in the α-$PdSn_2$ structure type [30-33][1], with the space group $I4_1/acd$, a = 6.1941(4) Å, c = 23.498(2) Å, wR_2 = 0.077. The Ni atoms are situated on the Pd positions, Mg/Sn mixtures occupy the two Sn positions of the α-$PdSn_2$ structure type. The crystal structure of $Mg_{0.39(2)}NiSn_{1.61(2)}$ is shown in detail in Figure 1. The network

[1] α refers to the room temperature modification of $PdSn_2$, a high temperature modification of $PdSn_2$ was indicated, but was not confirmed.

of Mg/Sn atoms is described by alternating 4^4 (Wyckoff position 16*e,* Figure 1a*)* and 3^2.4.3.4 atom layers (Wyckoff position 16*f,* Figure 1b), which are labelled as atom layer A and atom layer B, respectively. The layers are stacked along the *c* direction according to the sequence ABAB'AB''AB''', with A being stacked primitively and B, B′, B′′ and B′′′ being identical layers which are mapped onto each other by rotation around the four-fold rotational axis. In both layers mixed site occupancies of Mg and Sn occur. However, a preferential occupation of the Mg atoms on layer A (27.6(8)% Mg) compared to layer B (13.6(9)% Mg) is noticeable.

Mg/Sn-Mg/Sn distances are *d*(Mg1/Sn1-Mg1/Sn1) = 3.0970(2) Å in the 4^4 layer A. The 3^2.4.3.4 layer B can be deduced from A by distorting every second square towards a rhomb by forming one short contact along one diagonal of the square (*d*(Mg2/Sn2-Mg2/Sn2) = 2.902(2) Å). The remaining distances are considerably elongated to *d*(Mg2/Sn2-Mg2/Sn2) = 3.2685(4) Å. The shortest distances between atoms of different layers are in the same range *(d*(Mg1/Sn1-Mg1/Sn1) = 3.0350(4) Å). Thus, a three-dimensional Mg/Sn network results. The Mg/Sn-Mg/Sn distances are in the range as the distances in the elemental modifications of Sn (*α*-Sn: *d*(Sn-Sn) = 2.81; *β*-Sn: *d*(Sn-Sn) = 3.02 and *d*(Sn-Sn) = 3.18 Å) as well as the shortest distances in the elemental modification of Mg (*d*(Mg-Mg) = 3.20 Å).

Stacking of the neighbouring layers A and B and filling the voids above and below the squares of the B layer with Ni atoms leads to Ni-centered square antiprisms. As stated above, the Mg/Sn-Mg/Sn bonds which belong to layer A (3.0970(2) Å) are shorter than those belonging to 3^2.4.3.4 layer B (3.2685(4) Å). The Ni-Mg/Sn distances vary between *d*(Ni-Mg2/Sn2) = 2.6748(6) Å and *d*(Ni-Mg1/Sn1) = 2.7273(8) Å.

The main building blocks of $Mg_{0.39(2)}NiSn_{1.61(2)}$ consist of pairs of face-sharing coordination polyhedra of Ni (Figure 1d). A short Ni-Ni distance (*d*(Ni-Ni) = 2.693(2) Å) results. These building blocks $Ni_2@(Mg/Sn)_{12}$ are further interconnected via their vertices in layer A, to build up a three-dimensional network. Thus, above and below the polyhedron shown in Figure 1d no Ni atoms are located and the coordination number of each Ni atom adds up to 9 (8 Mg/Sn + 1 Ni). The Ni-Ni distance (*d*(Ni-Ni) = 2.693(2) Å) is longer than the shortest nearest neighbour distances in the elemental modification of Ni (*d*(Ni-Ni) = 2.49 Å) as well as in binary intermetallic compounds such as NiAs (*d*(Ni-Ni) = 2.52 Å), but nevertheless short enough to be considered as weakly bonding.

The occurrence of such pairs of coordination polyhedra is well known from crystal structures of $PdSn_n$ (n = 2,3,4), which are built up of different stacking possibilities of $Pd_2@Sn_{12}$ polyhedra [30]. Very recently, the synthesis of a ternary intermetalloid cluster anion $[Ni_2@Sn_7Bi_5]^{3-}$ obtained from solution based Zintl anion chemistry was reported [34]. Its structure corresponds to the described building block $Ni_2@(Mg/Sn)_{12}$ of the title phase $Mg_{0.39(2)}NiSn_{1.61(2)}$.

Furthermore, similar building blocks $T_2@Tt_{12}$ (*T*: transition metal, *Tt*: tetrel element) of face-sharing distorted square antiprisms are observed in various binary germanides and stannides, for example in $CoGe_2$ [33], $CoSn_2$ [35], in the two modifications of $CoSn_3$ [36], in Ir_3Sn_7 [37] and Ir_3Ge_7 [33]. In $CoGe_2$ a different stacking sequence of the building blocks causes the variation of the crystal structure. In $CoSn_2$ the building blocks are face linked via the square faces. Hence, one-dimensional chains result. This corresponds to a primitive stacking sequence of the building blocks and of the atom layers (ABAB). In both modifications of $CoSn_3$ the building blocks are connected via their edges to form layers parallel to the *ab* plane.

In the cubic crystal structures of Ir_3Sn_7 and Ir_3Ge_7 Ir_2 dumbbells are observed parallel to all three axes and the building blocks are linked via their vertices. The ternary compounds $Mg_xIr_3Sn_{7-x}$ [38] as well as $Mg_xRh_3Sn_{7-x}$ [16] crystallize in the Ir_3Ge_7 structure type, with pronounced mixing of Mg and Sn. As observed for the title compound $Mg_{0.39(2)}NiSn_{1.61(2)}$, in the above mentioned compounds short distances between the pairs of transition metal within the building block result ($CoGe_2$: *d*(Co-Co) = 2.45 Å, $CoSn_2$: *d*(Co-Co) = 2.73 Å, RT-$CoSn_3$: *d*(Co-Co) = 2.69 Å, HT-$CoSn_3$: *d*(Co-Co) = 2.69 Å, Ir_3Sn_7: *d*(Ir-Ir) = 2.96 Å, Ir_3Ge_7: *d*(Ir-Ir) = 2.76 Å, α-$PdSn_2$: *d*(Pd-Pd) = 2.84 Å). Note that no Ni-Sn compound with a Sn content higher than 58% was described until now.

While, for example, the ternary phase $Mg_xIr_3Sn_{7-x}$ can be described as a solid solution of Mg in Ir_3Sn_7, no binary phase "$NiSn_2$" corresponding to the title compound $Mg_{0.39(2)}NiSn_{1.61(2)}$ exists.

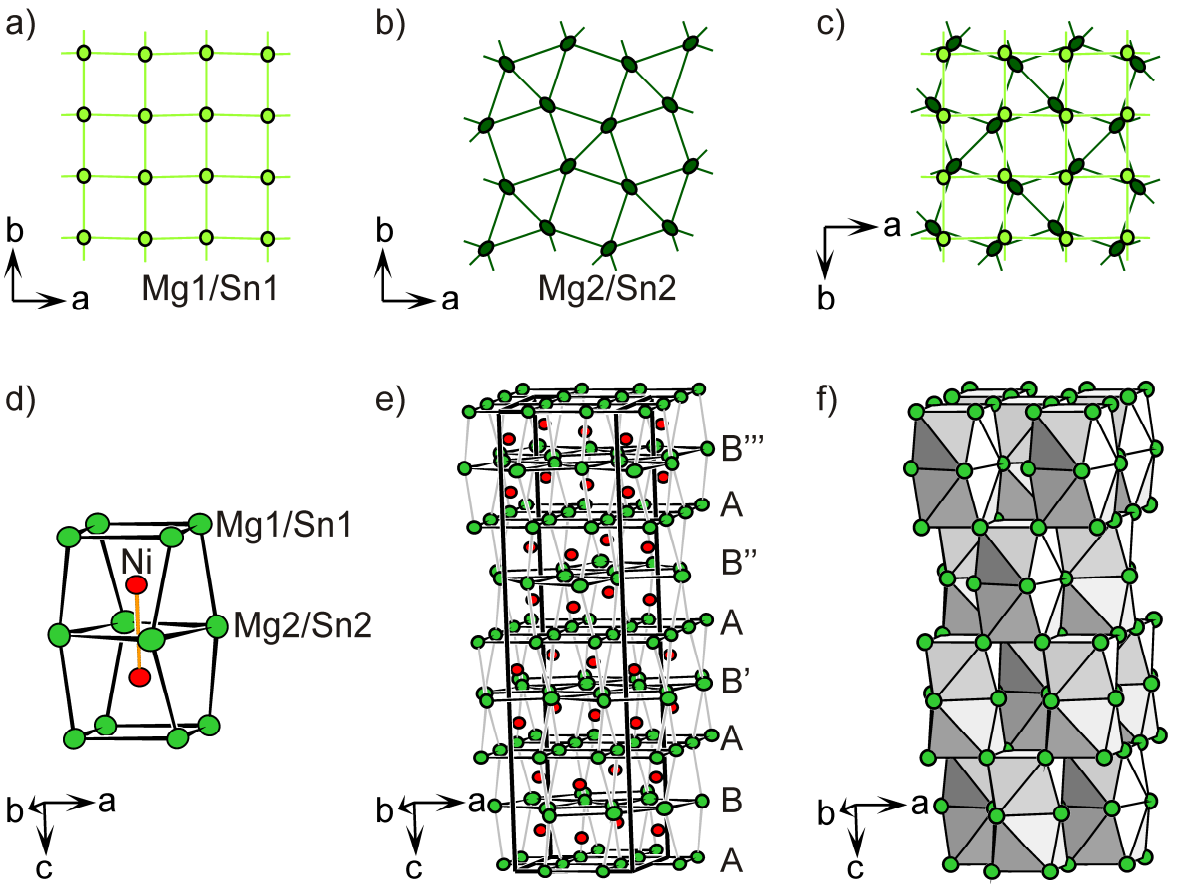

Figure 1 Crystal structure of $Mg_{0.39(2)}NiSn_{1.61(2)}$: a) layer A ($4^4$) in the *ab* plane, b) layer B ($3^2.4.3.4$) in the *ab* plane, c) layer A and B in the *ab* plane, d) two coordination polyhedra of Ni atoms are face linked, e) unit cell, viewing direction along the *b* axis, the layers A and B are emphasized, f) stacking of the resulting building blocks. The Ni and Mg/Sn atoms are drawn in red and green, respectively. In (a) to (c) the Wyckoff positions 16*e* and 16*f* are drawn in light and dark green, respectively. The displacement ellipsoids are drawn with 95 % probability level.

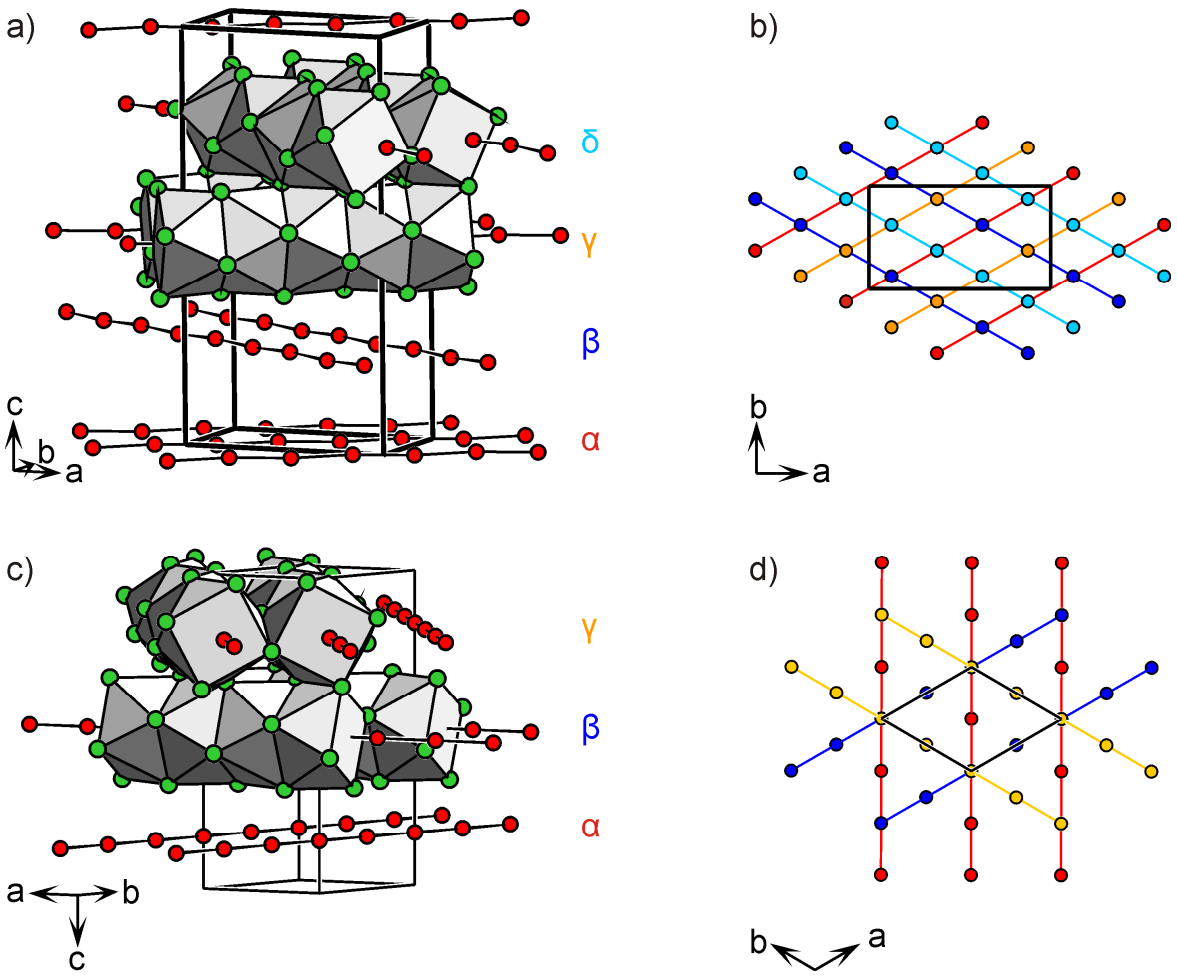

Figure 2 a) Crystal structure of $Mg_{1.78(1)}NiSn_{0.22(1)}$ and $Mg_{1.60(1)}NiSn_{0.40(1)}$ (Mg_2Cu structure type), b) chains of Ni atoms in $Mg_{1.78(1)}NiSn_{0.22(1)}$ and $Mg_{1.60(1)}NiSn_{0.40(1)}$, c) Crystal structure of $Mg_{1.85(1)}NiSn_{0.15(1)}$ (Mg_2Ni structure type), d) chains of Ni atoms in $Mg_{1.85(1)}NiSn_{0.15(1)}$. The Ni-Ni bonds as well as the coordination polyhedra of Ni are emphasized. In (a) and (c) Ni and the Mg/Sn atoms are drawn in red and green, respectively. In (b) and (d) the Ni atoms are colored with rising *z* value in red, blue, yellow and light-blue, in order to illustrate the orientations of the Ni chains.

In the ternary phase diagram Mg/Ni/Sn two intermetallic phases on the more Mg rich side, which have the same content of Ni and the same overall content of Mg/ Sn, are known. They crystallize in two different parent structure types: the intermetallic phase Mg_xNiSn_{2-x} adopts the Mg_2Ni structure type [20] for $x = 1.85$ and the Mg_2Cu structure type [21] for $x = 1.78$ and 1.60 [15]. While the overall ratio Ni : Mg/Sn remains constant (1 : 2) for the phases Mg_xNiSn_{2-x} ($x = 1.85$, $x = 1.78$, $x = 1.60$) and the title phase $Mg_{0.39(2)}NiSn_{1.61(2)}$ (Mg_xNiSn_{2-x} with $x = 0.39(2)$), the ratio Mg : Sn varies significantly.

In $Mg_{1.85(1)}NiSn_{0.15(1)}$, $Mg_{1.78(1)}NiSn_{0.22(1)}$ and $Mg_{1.60(1)}NiSn_{0.40(1)}$ (Mg_xNiSn_{2-x} with $x = 1.85$, $x = 1.78$ and 1.60) the Mg/Sn atoms build up a three-dimensional network in

which the Ni atoms are situated (Figure 2). The coordination polyhedron of Ni is a distorted square antiprism. In contrast to the title compound $Mg_{0.39(2)}NiSn_{1.61(2)}$ these square antiprisms are face-linked via both square faces with a further antiprism. Consequently, the coordination number of the Ni atoms is 10 (8+2) and one-dimensional chains of Ni atoms are formed. The Ni-Ni distances (d(Ni-Ni) = 2.60 Å to d(Ni-Ni) = 2.62 Å) are comparable to the one found in $Mg_{0.39(2)}NiSn_{1.61(2)}$.

The one-dimensional chains are linked among each other via edges to form a layer within the *ab* plane. Further linkage of the planes via the edges of the square antiprims leads to a three-dimensional Mg/Sn network. The layers are stacked according to the stacking sequence αβγδ for $Mg_{1.78(1)}NiSn_{0.22(1)}$ and $Mg_{1.60(1)}NiSn_{0.40(1)}$. The one-dimensional chains in layer α and layer γ as well as the chains in layer β and layer δ are oriented in the same direction. In $Mg_{1.85(1)}NiSn_{0.15(1)}$ the layers are stacked according to the stacking sequence αβγ, the chains of each layer being oriented differently.

Crystal Structure of $Mg_{2.61(2)}Ni_4Sn_{3.39(2)}$

$Mg_{2.61(2)}Ni_4Sn_{3.39(2)}$ crystallizes in an own structure type, with the space group $P\bar{3}m$, a = 4.3230(9) Å, c = 10.490(3) Å, wR_2 = 0.037. The same Wyckoff sequence *d*4*ba* is reported for FeO(OH) [39] as well as for Li_2NiO_2 [40], but the atom arrangements are quite different from the one found in the title compound.

The crystal structure of $Mg_{2.61(2)}Ni_4Sn_{3.39(2)}$ can be described as a distorted cubic network of alternating Sn and Mg/Sn, in which 2/3 of the distorted cubes are filled with Ni and 1/3 of the distorted cubes are empty. Therefore, $Mg_{2.61(2)}Ni_4Sn_{3.39(2)}$ can be regarded as an intermediate of a Heusler-type structure (all cubes are filled) and a half-Heusler-type structure (1/2 of the cubes are filled).

In Figure 3 the crystal structure of $Mg_{2.61(2)}Ni_4Sn_{3.39(2)}$ is shown in detail. Note that the anisotropic displacement parameters of Sn as well as Mg/Sn are not constant, leading to “egg-shaped” atoms. However, no hints for split positions or twinning were found during structure refinement.

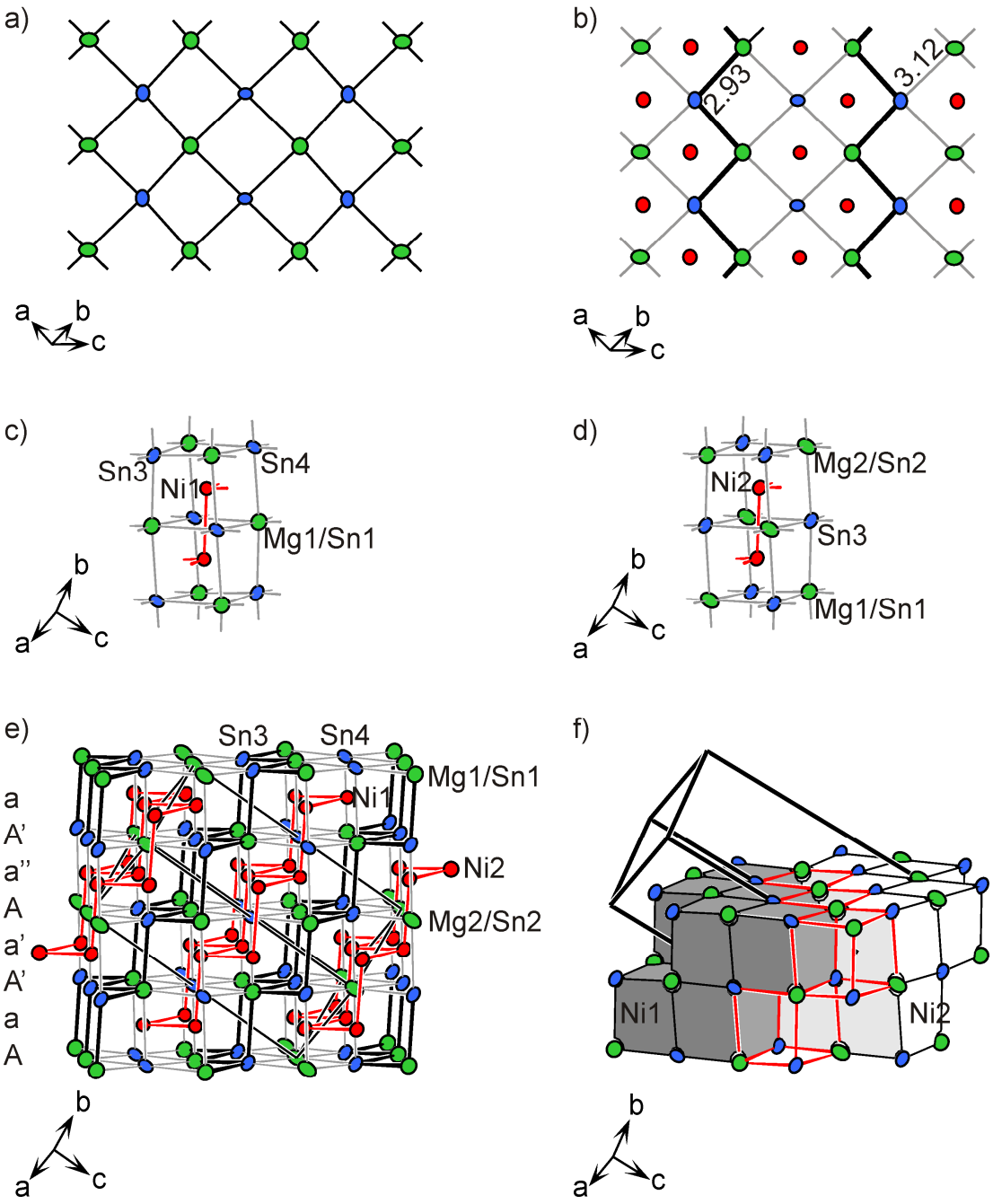

Figure 3 Crystal structure of $Mg_{2.61(2)}Ni_4Sn_{3.39(2)}$: a) layer A ($4^4$) parallel to the *hkl* plane (-1 1 2), b) two third of the squares of layer A are capped by Ni atoms, c) coordination polyhedron of Ni1, d) coordination polyhedron of Ni2, e) unit cell, the layers a and A are emphasized, f) double layers of coordination polyhedra of Ni1 (dark grey) and Ni1 (light grey), empty distorted cubes of Mg/Sn and Sn are indicated with red lines. The Ni, Mg/Sn and Sn atoms are drawn in red, green and blue respectively. In (b) and (e) short Mg/Sn-Mg/Sn contacts (d = 2.929(2) Å) are drawn in black and longer Mg/Sn-Mg/Sn contacts (d = 3.121(2) Å) are drawn in grey. The displacement ellipsoids are drawn with 95 % probability level.

The three-dimensional distorted cubic network of Mg/Sn and Sn is described by 4^4 atom layers (Figure 3a) parallel to the *hkl* plane (-1 1 2) with alternating Sn and Mg/Sn. These atom layers are stacked according to the sequence AA'AA'. A and A' are identical atom layers within the *hkl* plane (-1 1 2) with an offset of $x = 1$.

In Figure 3b the positions of the Ni atoms in relation to the atom layers of Mg/Sn and Sn are given. The Ni atoms cap 2/3 of the square in the 4^4 atom layers. The resulting atom layers of Ni atoms are stacked following the sequence aa'a''. a, a' and a'' are identical atom layers of Ni atoms within the *hkl* plane (-1 1 2) with an offset of $x = 1$. Consequently, an overall stacking sequence AaA'a'Aa''A'a results (Figure 3e).

The coordination polyhedra of Ni are given in Figure 3c and Figure 3d. Due to the topology of two neighboring layers A, these polyhedra are distorted cubes. The vertices of the cubes are alternately occupied by Mg/Sn and Sn atoms. For the sake of comparison of the two title compounds, two face-sharing coordination polyhedra of Ni1 and Ni2 are given. The distances of the Sn and Mg/Sn atoms towards the centering Ni atoms in $Mg_{2.61(2)}Ni_4Sn_{3.39(2)}$ (from *d*(Sn3-Ni2) = 2.584(2) Å to *d*(Mg1/Sn1-Ni1) = 2.738(2) Å) are comparable to those observed in $Mg_{0.39(2)}NiSn_{1.61(2)}$. However, the coordination number of the Ni atoms in $Mg_{2.61(2)}Ni_4Sn_{3.39(2)}$ adds up to 11 (4 Sn + 4 Mg/Sn + 3 Ni). Thus, each coordination polyhedron is connected via its faces with three further polyhedra. The resulting network of Ni atoms is given in Figure 3e. The Ni atoms form puckered hexagonal 6^3 layers analog to grey arsenic. The six membered Ni rings have a chair conformation with a fold angle of 90°. Note that the distances of the Ni atoms (d(Ni1-Ni1) = 2.910(1) Å and d(Ni2-Ni2) = 2.906(2) Å) are significantly longer than those observed for $Mg_{0.39(2)}NiSn_{1.61(2)}$.

Due to the puckered 6^3 atom layers of Ni, double layers of square prisms of Sn and Mg/Sn, which are centered by Ni, result. These are shown in Figure 3f. The double layers of the coordination polyhedra of Ni1 and Ni2 are named α and β, respectively.

These double layers of face sharing distorted square prisms are connected with each other via their edges. The crystal structure of $Mg_{2.61(2)}Ni_4Sn_{3.39(2)}$ can be described by a primitive stacking of these double layers according to the sequence αβαβ. Due to the connection of the double layers via their edges empty square prism, which are indicated with red borders in Figure 3f, result between the layers.

The distances within the Mg/Sn-Sn atom layers (*d*(Mg1/Sn1-Sn3) = 2.929(2) Å to *d*(Mg1/Sn1-Sn4) = *d*(Mg2/Sn2-Sn3) = 3.121(2) Å) are the same as those in between the

atom layers and are comparable to those observed for $Mg_{0.39(2)}NiSn_{1.61(2)}$. The shorter Mg1/Sn1-Sn3 distances within the cubic network of Mg/Sn and Sn correspond to the edges which link the double layers α and β. In Figure 3b as well as in Figure 3e the shorter Mg1/Sn1-Sn3 distances are drawn with black lines, the longer Mg1/Sn1-Sn4 and Mg2/Sn2-Sn3 distances are drawn with grey lines. Focusing on the shorter distances exclusively, hexagonal Mg1/Sn1-Sn3 layers which are analog to grey arsenic and parallel to the 6^3 layers of Ni result.

Comparing the coordination polyhedra of Ni1 and Ni2 in $Mg_{2.61(2)}Ni_4Sn_{3.39(2)}$ with those of the Ni atoms in $Mg_{0.39(2)}NiSn_{1.61(2)}$ as well as those in $Mg_{2-x}NiSn_x$ ($x = 1.85$, $x = 1.78$ and $x = 1.60$) two aspects should be mentioned. At first, the coordination polyhedra of Ni are square antiprisms in the intermetallic phases with a Ni content of 33.3% ($Mg_{1.85(1)}NiSn_{0.15(1)}$, $Mg_{1.78(1)}NiSn_{0.22(1)}$, $Mg_{1.60(1)}NiSn_{0.40(1)}$ and $Mg_{0.39(2)}NiSn_{1.61(2)}$), whereas the coordination polyhedron of Ni1 in the nickel richer phase $Mg_{2.61(2)}Ni_4Sn_{3.39(2)}$ is a slightly distorted square prism. In order to quantify this, the rotation angle of the squares is considered: the distorted square antiprisms of $Mg_{0.39(2)}NiSn_{1.61(2)}$ and $Mg_{2-x}NiSn_x$ ($x = 0.15$ and $x = 0.40$) possess a maximum rotation angle of the two squares of 20° in $Mg_{0.39(2)}NiSn_{1.61(2)}$, 35° in $Mg_{1.85(1)}NiSn_{0.15(1)}$ and 34° in $Mg_{1.60(1)}NiSn_{0.40(1)}$. In contrast, the slightly distorted square prisms of $Mg_{2.61(2)}Ni_4Sn_{3.39(2)}$ possesses a rotation angle of the two squares of at most 5°.

Secondly, the coordination number of the Ni atoms varies with the Mg and Ni content: The highest coordination number of 11 (8+3) is found for the Mg poor and Ni rich phase $Mg_{2.61(2)}Ni_4Sn_{3.39(2)}$, the medial coordination number of 10 (8+2) is observed in the Mg richer and Ni poorer phases $Mg_{1.85(1)}NiSn_{0.15(1)}$, $Mg_{1.78(1)}NiSn_{0.22(1)}$ as well as $Mg_{1.60(1)}NiSn_{0.40(1)}$ and the lowest coordination number of 9 (8+1) is found in the Mg poorest phase $Mg_{0.39(2)}NiSn_{1.61(2)}$.

For $Mg_{2.61(2)}Ni_4Sn_{3.39(2)}$ the coordination polyhedra of Mg/Sn and Sn are shown in Figure 4. Due to the distorted cubic network, each Sn atom has six neighbors of Mg/Sn and vice versa with distorted octahdedral arrangement. As the Ni atoms occupy 2/3 of the distorted cubes of the Mg/Sn and Sn network, Mg1/Sn1 as well as Sn3 have five nearest neighbors of Ni (Figure 4a and Figure 4b) and Mg2/Sn2 as well as Sn4 have six nearest neighbors of Ni (Figure 4c and Figure 4d).

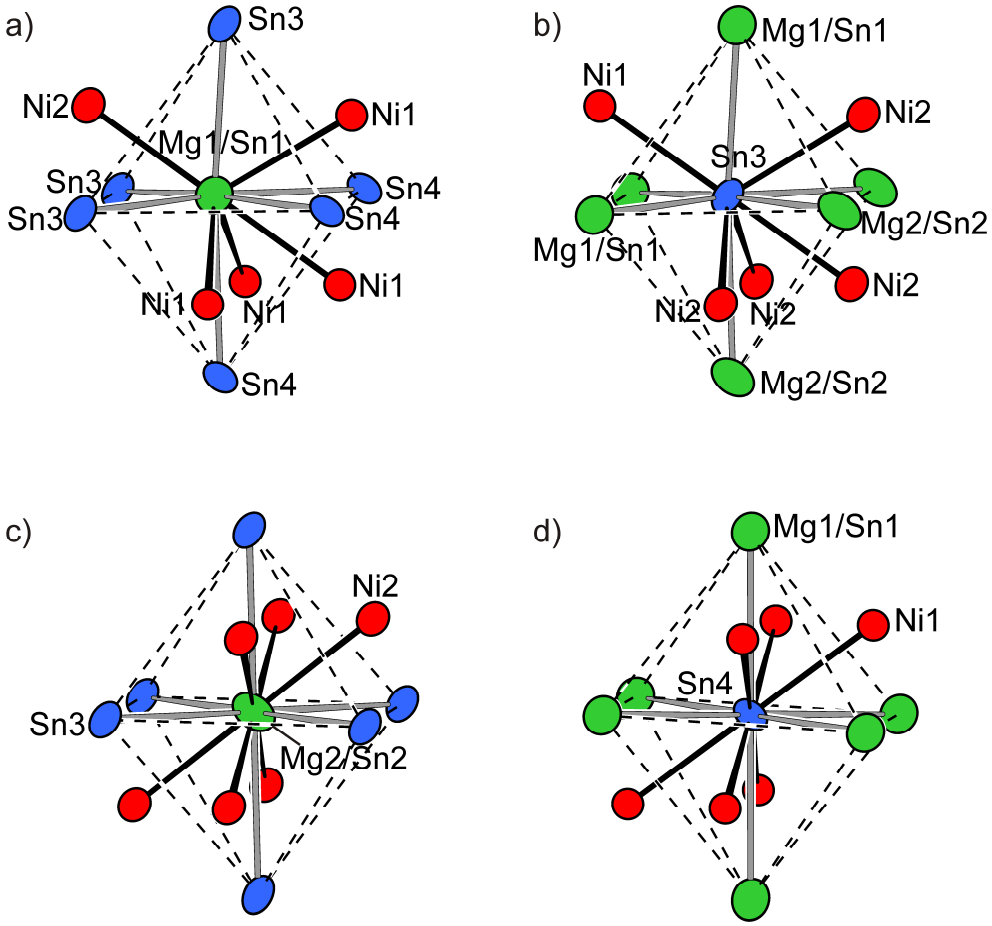

Figure 4 Crystal structure of $Mg_{2.61(2)}Ni_4Sn_{3.39(2)}$: coordination polyhedra of a) Mg1/Sn1, b) Sn3, c) Mg2/Sn2 and d) Sn4. The Ni, Mg/Sn and Sn atoms are drawn in red, green and blue respectively. The displacement ellipsoids are drawn with 95 % probability level.

This underlines again the intermediate character of the title phase $Mg_{2.61(2)}Ni_4Sn_{3.39(2)}$ between a Heusler and a half-Heusler type structure: while for the Heusler phase $MgNi_2Sn$ the Sn and Mg have eight nearest neighbors of Ni in an octahedral coordination, the Sn and Mg atoms of the corresponding hypothetical half-Heusler phase would have only four nearest neighbors of Ni atoms in a tetrahedral coordination.

Group-Subgroup Relationship

Examining the relationship between $Mg_{2.61(2)}Ni_4Sn_{3.39(2)}$ ($Mg_{3-x}Ni_4Sn_{3+x}$ with $x = 0.39(2)$) and $MgNi_2Sn$, a first approach is visible comparing their compositions. The composition of the Heusler phase $MgNi_2Sn$ can be expressed as $Mg_3Ni_6Sn_3$. Partial occupancy of the Ni atoms situated on Wyckoff position 8*c* leads to the composition $Mg_3Ni_4\square_2Sn_3$. Allowing Mg/Sn mixed site occupancies, this corresponds to the composition of the title compounds $Mg_{3-x}Ni_4Sn_{3+x}$ with $x = 0.39(2)$.

This approach is underlined by the crystal structures of $MgNi_2Sn$ and $Mg_{2.61(2)}Ni_4Sn_{3.39(2)}$. The crystal structure of $Mg_{2.61(2)}Ni_4Sn_{3.39(2)}$ is an intermediate of an Heusler phase and a half-Heusler phase. Therefore, it can be described via its group-subgroup relationship with $MgNi_2Sn$ [18] (Heusler phase, Cu_2MnAl structure type [41]), which itself was described in 1937 as a superstructure *β*-CuZn [42, 43] (CsCl structure type, space group $Pm\bar{3}m$).

In Figure 5 this group-subgroup relationship is discussed, using a compact graphical representation as introduced by *Bärnighausen* [44, 45]. In order to illustrate this group-subgroup relationship the cubes of Sn and Mg/Sn as well as of Cu, which are centered by Ni as well as Zn respectively, are indicated. Starting from the well known β-CuZn structure, an isomorphic transition of index 28 (*i*27) leads to $MgNi_2Sn$ (space group $Fm\bar{3}m$), which is derived from β-CuZn via doubling of all cell parameters: the Wyckoff positions 1*a* (Cu) in *β*-CuZn are split in the crystal structure of $MgNi_2Sn$ to the positions 4*b* and 4*a*, which are occupied by Mg and Sn respectively. Further, a *translationengleiche* transition of index 4 (*t*4) followed by a *klassengleiche* transition of index 3 (*k*3) leads to $Mg_{2.61(2)}Ni_4Sn_{3.39(2)}$ (space group $P\bar{3}m$). Due to the reduction of symmetry from $MgNi_2Sn$ to $Mg_{2.61(2)}Ni_4Sn_{3.39(2)}$, the cubes of Sn and Mg/Sn are distorted compared to those in *β*-CuZn and $MgNi_2Sn$. Additionally a vacancy □ is generated on the Wyckoff position 2*c*, resulting in an empty distorted cube of alternating Mg/Sn and Sn.

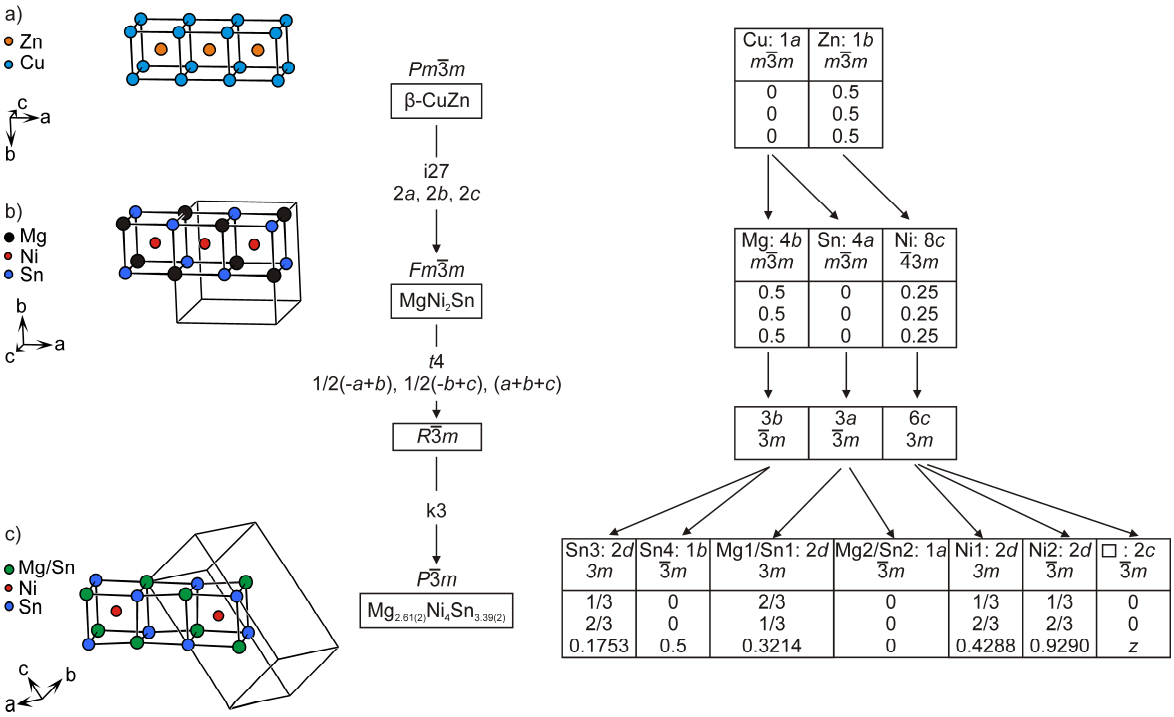

Figure 5 Group-subgroup relationship for the structures of a) β-CuZn, b) $MgNi_2Sn$ and c) $Mg_{2.61(2)}Ni_4Sn_{3.39(2)}$. The indices for the *translationengleiche* (t), *klassengleiche* (k) and isomorphic (i) transitions as well as the unit cell transformations are given together with the evolution of the atomic parameters. Vacancies are denoted by □.

Summary and Conclusion

The novel intermetallic phases $Mg_{0.39(2)}NiSn_{1.61(2)}$ and $Mg_{2.61(2)}Ni_4Sn_{3.39(2)}$ were synthesized by reaction of the elements in welded tantalum ampoules in a resistant furnace. The crystal structures were characterized using single crystal X-ray diffraction data.

$Mg_{0.39(2)}NiSn_{1.61(2)}$ crystallizes in the α-$PdSn_2$ structure type. The Ni atoms are situated on the Pd positions, Mg/Sn mixtures occupy the two Sn postions of the α-$PdSn_2$ structure type. The main building block $Ni_2@(Mg/Sn)_{12}$ observed in the crystal structure consists of two square, Ni-centred, face-linked antiprisms. The crystal structure was compared to those of various binary and ternary compounds (in $CoGe_2$, $CoSn_2$, two modifications of $CoSn_3$, Ir_3Sn_7, Ir_3Ge_7, $Mg_xIr_3Sn_{7-x}$ and $Mg_xRh_3Sn_{7-x}$).

Furthermore, the coordination polyhedron of Ni observed for $Mg_{0.39(2)}NiSn_{1.61(2)}$ is compared to those of $Mg_{1.85(1)}NiSn_{0.15(1)}$, $Mg_{1.78(1)}NiSn_{0.22(1)}$ and $Mg_{1.60(1)}NiSn_{0.40(1)}$. All four intermetallic compounds can be described by the formula Mg_xNiSn_{2-x} with varying values of x. Thus, while the overall Mg/Sn : Ni ratio remains constant (2 : 1), the Mg : Sn ratio varies significantly. This is reflected by the different crystal structures: The coordination number of the Ni atoms in the title compounds $Mg_{0.39(2)}NiSn_{1.61(2)}$ is 9 (8 Mg/Sn + 1 Ni) and thus two face linked Ni-centred antiprisms result. In contrast, the coordination number of the Ni atoms in $Mg_{1.85(1)}NiSn_{0.15(1)}$, $Mg_{1.78(1)}NiSn_{0.22(1)}$ and $Mg_{1.60(1)}NiSn_{0.40(1)}$ is 10 (8 Mg/Sn + 2 Ni) and rods of Ni-centered faces linked antiprisms result.

In contrast to $Mg_{0.39(2)}NiSn_{1.61(2)}$, a partial ordering of the Sn atoms on the square nets of Sn and Mg atoms is observed in the title phase $Mg_{2.61(2)}Ni_4Sn_{3.39(2)}$. The crystal structure of $Mg_{2.61(2)}Ni_4Sn_{3.39(2)}$ is an intermediate of a Heusler and a half-Heusler type structure. It crystallizes in an own structure type and can be described as a superstructure of $MgNi_2Sn$, which contains ordered vacancies □. $MgNi_2Sn$ itself is a superstructure of β-CuZn. The resulting crystal structure of $Mg_{2.61(2)}Ni_4Sn_{3.39(2)}$ contains a distorted cubic network of Sn and Mg/Sn. 2/3 of the distorted cubic voids of this network are occupied by Ni. The resulting coordination number of Ni is 10 (8 Mg/Sn + 2 Ni).

Polar intermetallic phases of the systems *Ae*/Ni/*Tt* (*Ae*: Ca, Sr, Ba; *Tt*: Si, Ge, Sn) often contain one-, two- or three-dimensional polyanionic networks of Ni-*Tt*, being reminiscent of the polyanions observed in Zintl phases. Due to Mg/Sn mixing, the title

compounds $Mg_{0.39(2)}NiSn_{1.61(2)}$ and $Mg_{2.61(2)}Ni_4Sn_{3.39(2)}$ exclude themselves from this description. However, the recent description of the ternary intermetalloid cluster anion $[Ni_2Sn_7Bi_5]^{3-}$, which relates to the main building block $Ni_2@(Mg/Sn)_{12}$ of $Mg_{0.39(2)}NiSn_{1.61(2)}$, reinforces the relationship between intermetalloid cluster anions obtained from solution based Zintl anion chemistry and intermetallic "solid state" compounds.

References

[1] V. Hlukhyy, N. Chumalo, V. Zaremba, T. F. Fässler, *Z. Anorg. Allg. Chem.* **2008**, *634*, 1249.

[2] V. Hlukhyy, S. Eck, T. F. Fässler, *Inorg. Chem.* **2006**, *45*, 7408.

[3] V. Hlukhyy, T. F. Fässler, *Z. Anorg. Allg. Chem.* **2008**, *634*, 2316.

[4] V. Hlukhyy, T. F. Fässler, *Z. Anorg. Allg. Chem.* **2010**, *636*, 100.

[5] V. Hlukhyy, F. Raif, P. Claus, T. F. Fässler, *Chem.-Eur. J.* **2008**, *14*, 3737.

[6] V. Hlukhyy, A. Senyshyn, D. Trots, T. F. Fässler, *HASYLAB Ann. Rep.* **2007**, *1*, 1021.

[7] L. Siggelkow, V. Hlukhyy, T. F. Fässler, *Z. Anorg. Allg. Chem.* **2010**, *636*, 1870.

[8] L. Siggelkow, V. Hlukhyy, B. Wahl, T. F. Fässler, *Eur. J. Inorg. Chem.* **2011**, 4012.

[9] L. Siggelkow, V. Hlukhyy, T. F. Fässler, *in preparation* **2011**.

[10] V. Hlukhyy, T. F. Fässler, *in preparation* **2011**.

[11] W. Buchholz, H. U. Schuster, *Z. Anorg. Allg. Chem.* **1981**, *482*, 40.

[12] M. Y. Teslyuk, V. Y. Markiv, *Sov. Phys. Crystallogr.* **1962**, *7*, 103.

[13] V. Y. Markiv, M. Y. Teslyuk, E. I. Gladyhevskii, *Dopov. Akad. Nauk Ukr. RSR* **1964**, *7*, 914.

[14] V. Hlukhyy, R. D. Hoffmann, R. Pöttgen, *Intermetallics* **2004**, *12*, 383.

[15] V. Hlukhyy, U. C. Rodewald, R. Pottgen, *Z. Anorg. Allg. Chem.* **2005**, *631*, 2997.

[16] M. Schlüter, A. Kunst, R. Pöttgen, *Z. Anorg. Allg. Chem.* **2002**, *628*, 2641.

[17] R. Pöttgen, *Z. Naturforsch., B: J. Chem. Sci.* **2006**, *61*, 677.

[18] P. Rahlfs, *Metallwirtschaft, Metallwissenschaft, Metalltechnik* **1937**, *16*, 640.

[19] O. Heusler, *Ann. Phys.* **1934**, *19*, 155.

[20] K. Schubert, K. Anderko, *Naturwissenschaften* **1951**, *38*, 259.

[21] K. Schubert, K. Anderko, *Z. Metallk.* **1951**, *42*, 321.

[22] M. Boudard, P. Bordet, H. Vincent, F. Audebert, *J. Alloys Compd.* **2004**, *372*, 121.

[23] M. Ellner, *J. Less Common Met.* **1976**, *48*, 21.

[24] W. Jeitschko, B. Jaberg, *Acta Crystallogr., Sect. B: Struct. Sci.* **1982**, *38*, 598.

[25] STOE, WinXPOW Version 2.08, STOE & Cie GmbH, Darmstadt **2003**.

[26] X-RED32 - *Data Reduction Program*, Version 1.48, Stoe & Cie GmbH, Darmstadt (Germany), **2008**.

[27] X-SHAPE - *Crystal Optimization for Numerical Absorption Correction*, Version 2.11, STOE & Cie GmbH, Darmstadt (Germany), **2008**.

[28] G. M. Sheldrick, SHELXS-97 – *Program for the Determination of Crystal Structures*, University of Göttingen (Germany) **1997**.

[29] G. M. Sheldrick, SHELXL-97 – *Program for Crystal Structure Refinement*, University of Göttingen (Germany) **1997**.

[30] J. Nylen, G. F. J. Garcia, B. D. Mosel, R. Pottgen, U. Häussermann, *Solid State Sci.* **2004**, *6*, 147.

[31] E. Hellner, *Z. Kristallogr.* **1956**, *107*, 99.

[32] B. Künnen, D. Niepmann, W. Jeitschko, *J. Alloy. Compd.* **2000**, *309*, 1.

[33] K. Schubert, H. Pfisterer, *Z. Metallk.* **1950**, *41*, 433.

[34] F. Lips, S. Dehnen, *Angew. Chem. Int. Ed.* **2011**, *50*, 955.

[35] O. Nial, *Z. Anorg. Allg. Chem.* **1938**, *238*, 287.

[36] A. Lang, W. Jeitschko, *Z. Metallk.* **1996**, *87*, 759.

[37] H. N. Nowotny, K. Schubert, U. Dettinger, *Metallforschung* **1946**, *1*, 137.

[38] M. Schlüter, U. Häussermann, B. Heying, R. Pöttgen, *J. Solid State Chem.* **2003**, *173*, 418.

[39] M. H. Francombe, H. P. Rooksby, *Clay Minerals Bulletin* **1959**, *4*, 1.

[40] I. J. Davidson, J. E. Greedan, U. Vonsacken, C. A. Michal, W. R. McKinnon, *J. Solid State Chem.* **1993**, *105*, 410.

[41] D. P. Oxley, K. C. Williams, R. S. Tebble, *J. Appl. Phys.* **1963**, *34*, 1362.

[42] S. S. Rao, Ananthar.Tr, *Z. Metallk.* **1969**, *60*, 312.

[43] L. H. Beck, C. S. Smith, *J. Metals* **1952**, *4*, 1079.

[44] U. Müller, *Z. Anorg. Allg. Chem.* **2004**, *630*, 1519.

[45] H. Bärnighausen, *MATCH, Commun. Math. Chem.* **1980**, *9*, 139.

Supporting Information

Table S1 Anisotropic displacement parameters (U_{ij} / Å^2) for $Mg_{0.39(2)}NiSn_{1.61(2)}$

Atom	U_{11}	U_{22}	U_{33}	U_{12}	U_{13}	U_{23}
Sn1	0.0105(5)	0.0160(5)	0.0106(5)	0.00000	0.00000	0.0009(3)
Mg1	0.0105(5)	0.0160(5)	0.0106(5)	0.00000	0.00000	0.0009(3)
Sn2	0.0159(4)	0.0159(4)	0.0132(5)	-0.0065(3)	-0.0002(2)	-0.0002(2)
Mg2	0.0159(4)	0.0159(4)	0.0132(5)	-0.0065(3)	-0.0002(2)	-0.0002(2)
Ni1	0.0115(8)	0.0118(8)	0.0088(7)	-0.0003(5)	0.00000	0.00000

Table S2 Anisotropic displacement parameters (U_{ij} / Å^2) for $Mg_{2.61(2)}Ni_4Sn_{3.39(2)}$

Atom	U_{11}	U_{22}	U_{33}	U_{12}	U_{13}	U_{23}
Sn1	0.014(2)	0.014(2)	0.012(2)	0.0070(6)	0.00000	0.00000
Mg1	0.014(2)	0.014(2)	0.012(2)	0.0070(6)	0.00000	0.00000
Sn2	0.010(1)	0.010(1)	0.020(2)	0.0047(5)	0.00000	0.00000
Mg2	0.010(1)	0.010(1)	0.020(2)	0.0047(5)	0.00000	0.00000
Sn3	0.0136(3)	0.0136(3)	0.0067(3)	0.0068(2)	0.00000	0.00000
Sn4	0.0062(3)	0.0062(3)	0.0124(3)	0.00312)	0.00000	0.00000
Ni1	0.0085(4)	0.0085(4)	0.0088(4)	0.0042(2)	0.00000	0.00000
Ni2	0.0113(4)	0.0113(4)	0.0086(4)	0.0057(2)	0.00000	0.00000

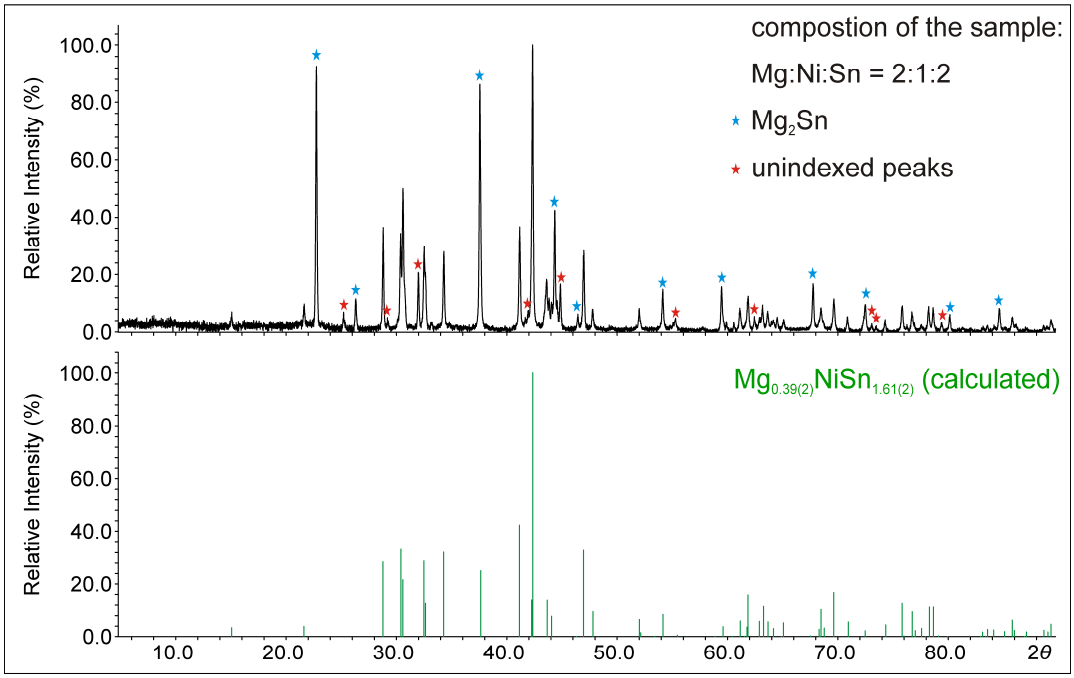

Figure S1 Experimental XRD powder pattern (top) from sample loading Mg : Ni : Sn = 2 : 1 : 2 and simulated powder XRD pattern (bottom) of $Mg_{0.39(2)}NiSn_{1.61(2)}$. The experimental XRD powder pattern was recorded in transmission geometry and its background has been subtracted. Reflections Mg_2Sn are labelled with a blue star, those of unindexed peaks are labeled with a red star.

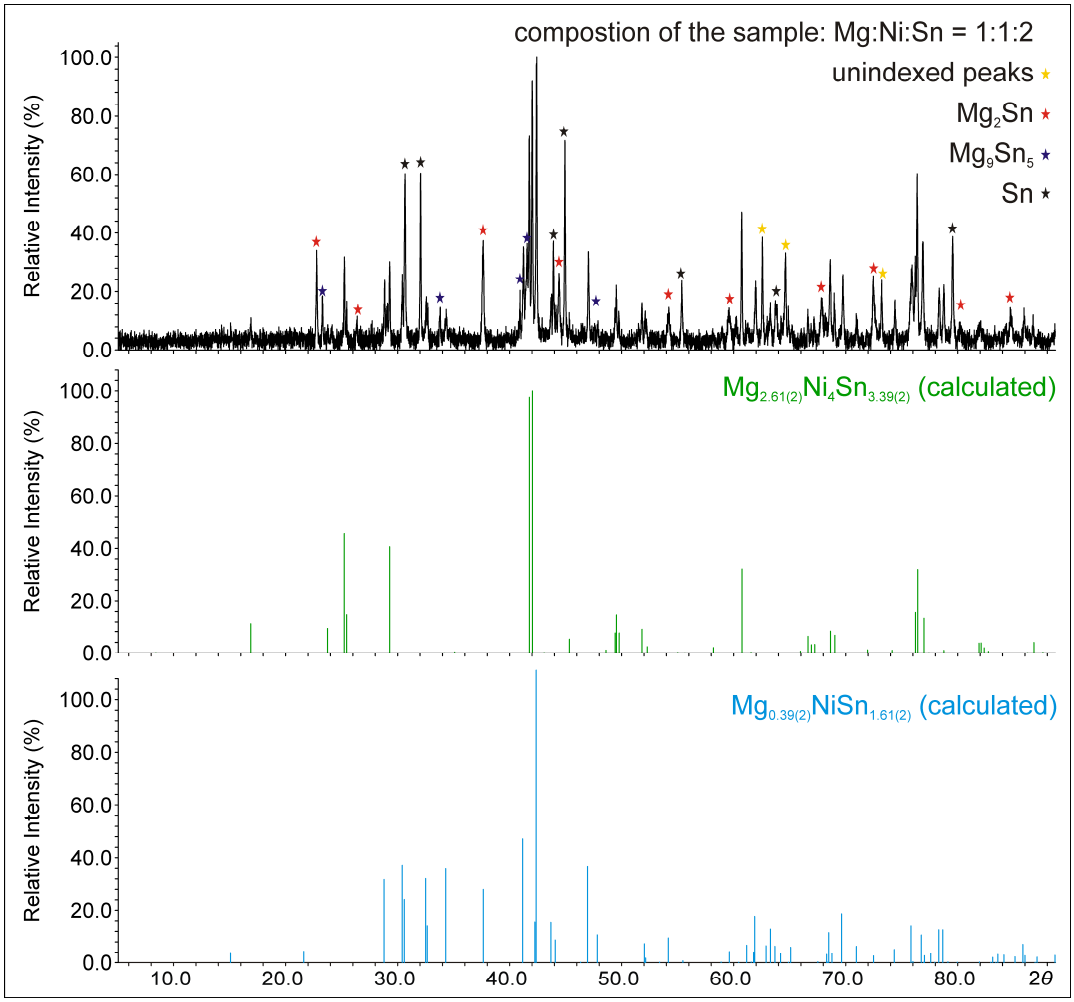

Figure S2 Experimental XRD powder pattern (top) from sample loading Mg : Ni : Sn = 1 : 1 : 2 and simulated powder XRD pattern of $Mg_{2.61(2)}Ni_4Sn_{3.39(2)}$ (middle) and $Mg_{0.39(2)}NiSn_{1.61(2)}$ (bottom). The experimental XRD powder pattern was recorded in Debye Scherrer geometry and its background has been subtracted. The unindexed peaks as well as the reflexes of Mg_2Sn, Mg_9Sn_5 and Sn are labelled with a yellow, red, purple and black star respectively.

5 Appendix

Composition Triangles of the Systems *Ae*/*T*/*Tt*
(*Ae*: Mg, Ca, Sr, Ba, *T*: Ni, Co, *Tt*: Si, Ge, Sn)

In the following the composition triangles of the systems *Ae*/*T*/*Tt* (*Ae*: Mg, Ca, Sr, Ba, *T*: Ni, Co, *Tt*: Si, Ge, Sn), which contain intermetallic phases presented in this work, are listed.

Mg/Ni/Ge

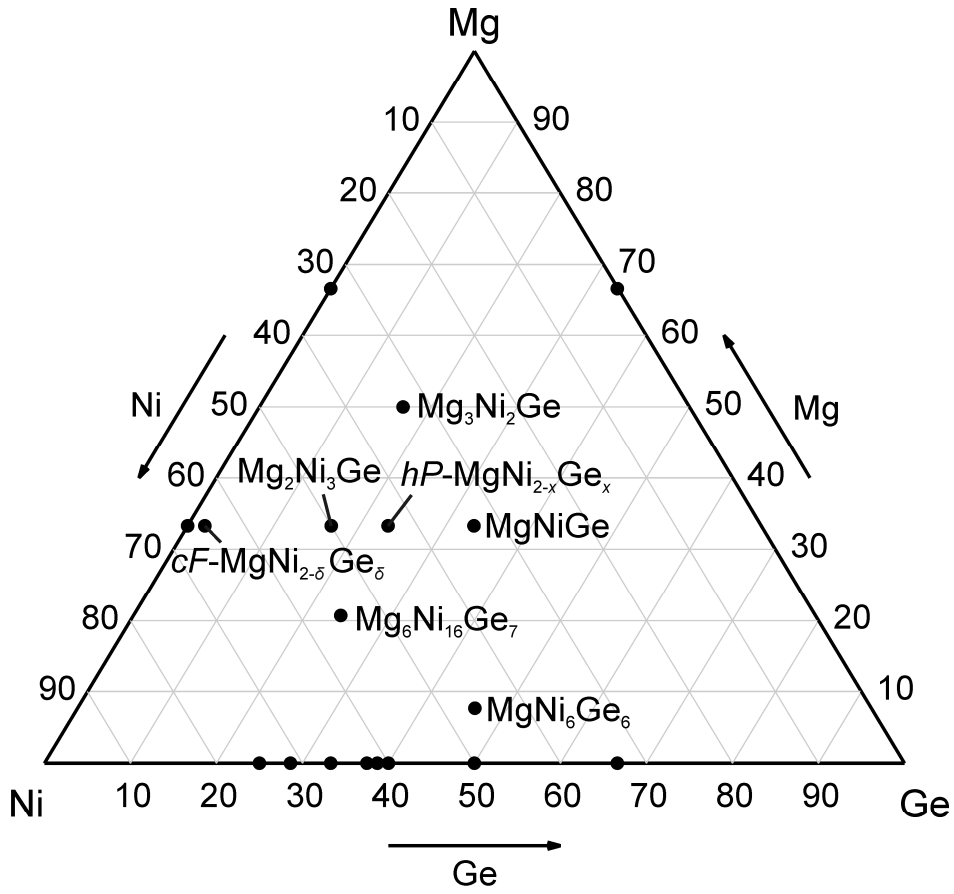

Figure A1 Composition triangle of the system Mg/Ni/Ge. The following ternary compounds are shown: Mg_3Ni_2Ge, *cF*-$MgNi_{2-\delta}Ge_\delta$ (chapter 4.3.4), Mg_2Ni_3Ge (chapter 4.3.4), *hP*-$MgNi_{2-x}Ge_x$ (x = 0.70(6), chapter 4.3.4), MgNiGe, $Mg_6Ni_{16}Ge_7$, $MgNi_6Ge_6$. The compositions of the binary phases are indicated.

Ca/Ni/Ge

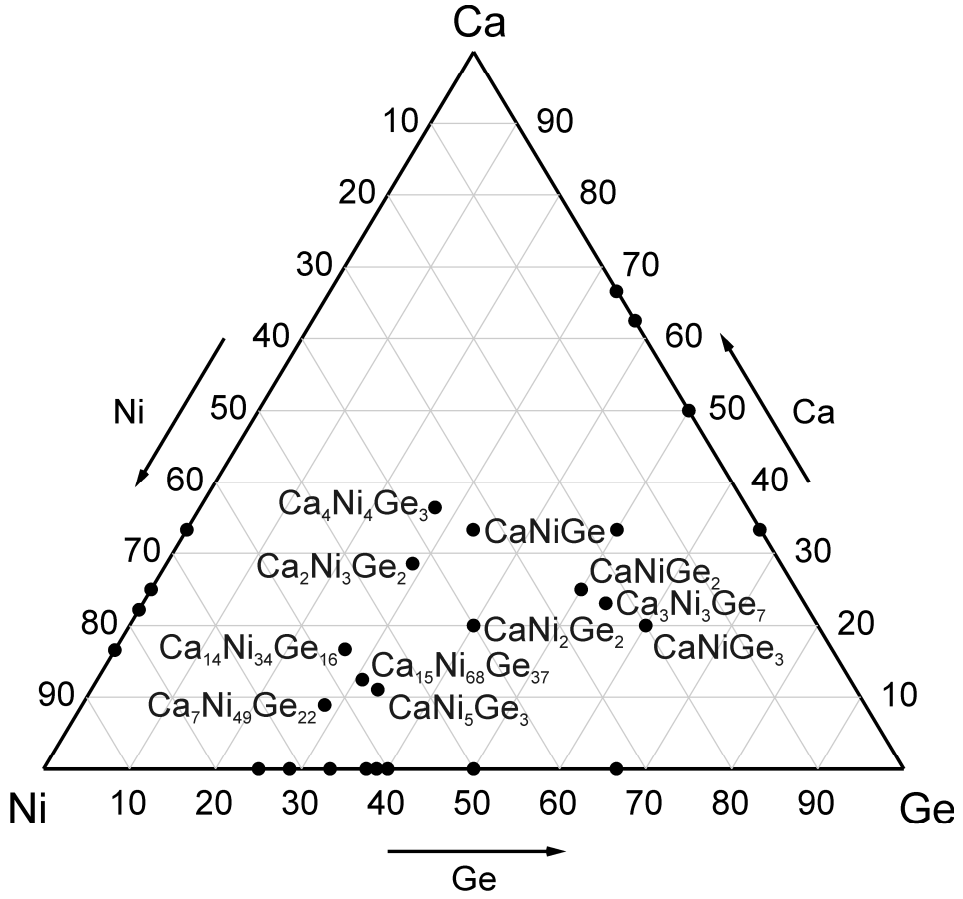

Figure A2 Composition triangle of the system Ca/Ni/Ge (chapter 4.3.5). The following ternary compounds are shown: CaNiGe, $CaNi_2Ge_2$, $Ca_4Ni_4Ge_3$ (chapter 4.3.1), $Ca_2Ni_3Ge_2$, $CaNiGe_2$, $Ca_3Ni_3Ge_7$, $CaNiGe_3$, $CaNi_5Ge_3$ (chapter 4.3.3), $Ca_{15}Ni_{68}Ge_{37}$ (chapter 4.3.3), $Ca_7Ni_{49}Ge_{22}$ (chapter 4.3.3) and $Ca_{10}Ni_{34}Ge_{16}$. The compositions of the binary phases are indicated.

Sr/Ni/Ge

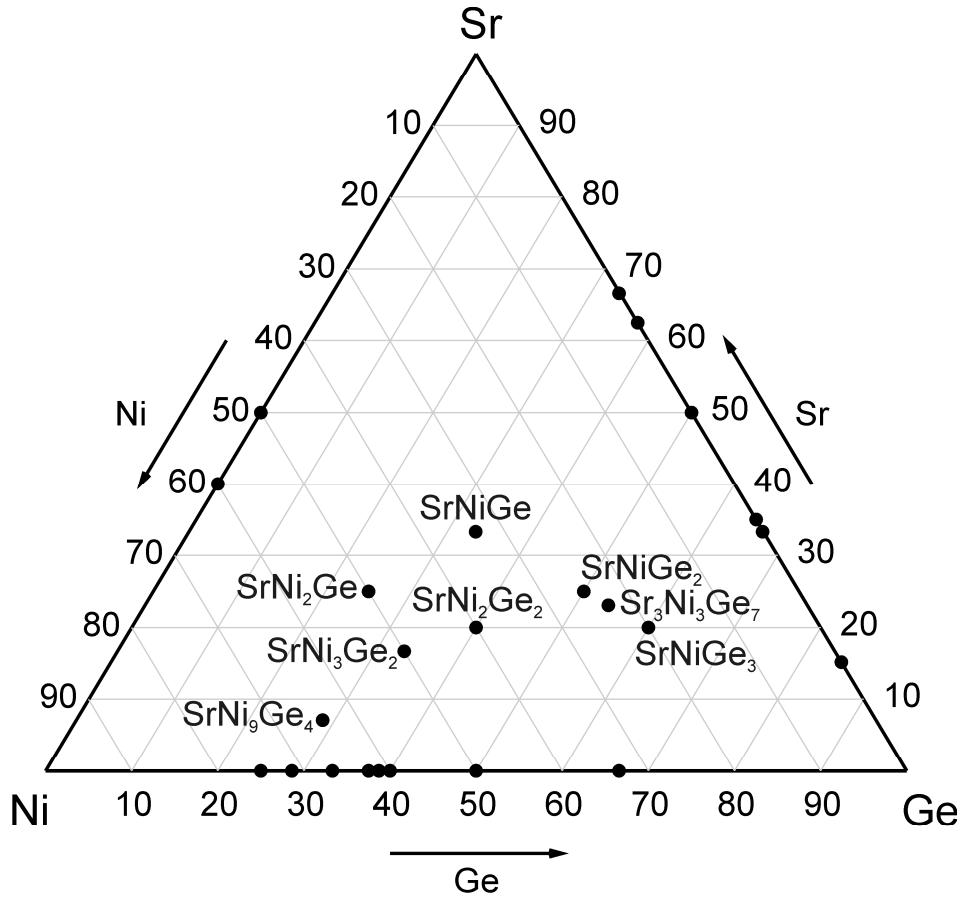

Figure A3 Composition triangle of the system Sr/Ni/Ge (chapter 4.3.5). The following ternary compounds are shown: SrNiGe, $SrNi_2Ge_2$, $SrNiGe_3$, $SrNi_2Ge$, $SrNiGe_2$, $Sr_3Ni_3Ge_7$, $SrNi_3Ge_2$, $SrNi_9Ge_4$. The compositions of the binary phases are indicated.

Ba/Ni/Ge

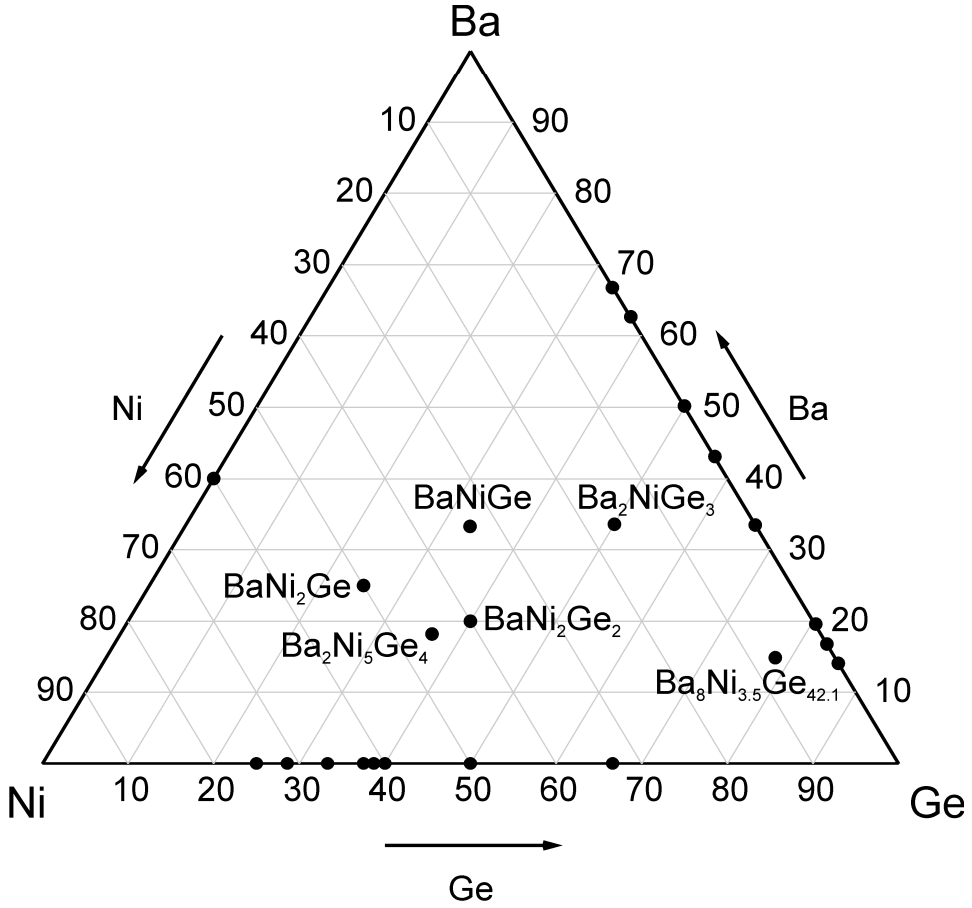

Figure A4 Composition triangle of the system Ba/Ni/Ge. The following ternary compounds are shown: BaNiGe, LT-$BaNi_2Ge_2$, HT-$BaNi_2Ge_2$, $BaNi_2Ge$ (chapter 4.3.1), $Ba_2Ni_5Ge_4$ (chapter 4.3.2), $Ba_8Ni_{3.5}Ge_{42.1}$, Ba_2NiGe_3. The compositions of the binary phases are indicated.

Ba/Co/Ge

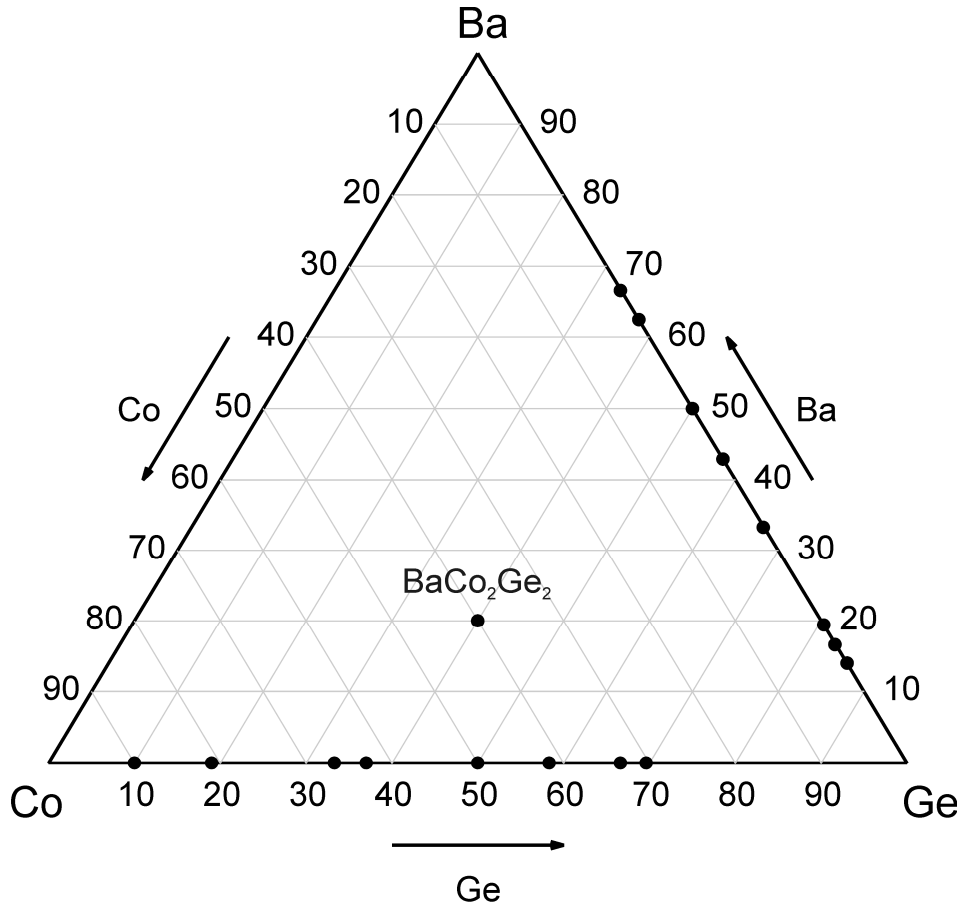

Figure A5 Composition triangle of the system Ba/Co/Ge. The ternary compound $BaCo_2Ge_2$ (chapter 4.4.1) is shown. The compositions of the binary phases are indicated.

Ca/Co/Si

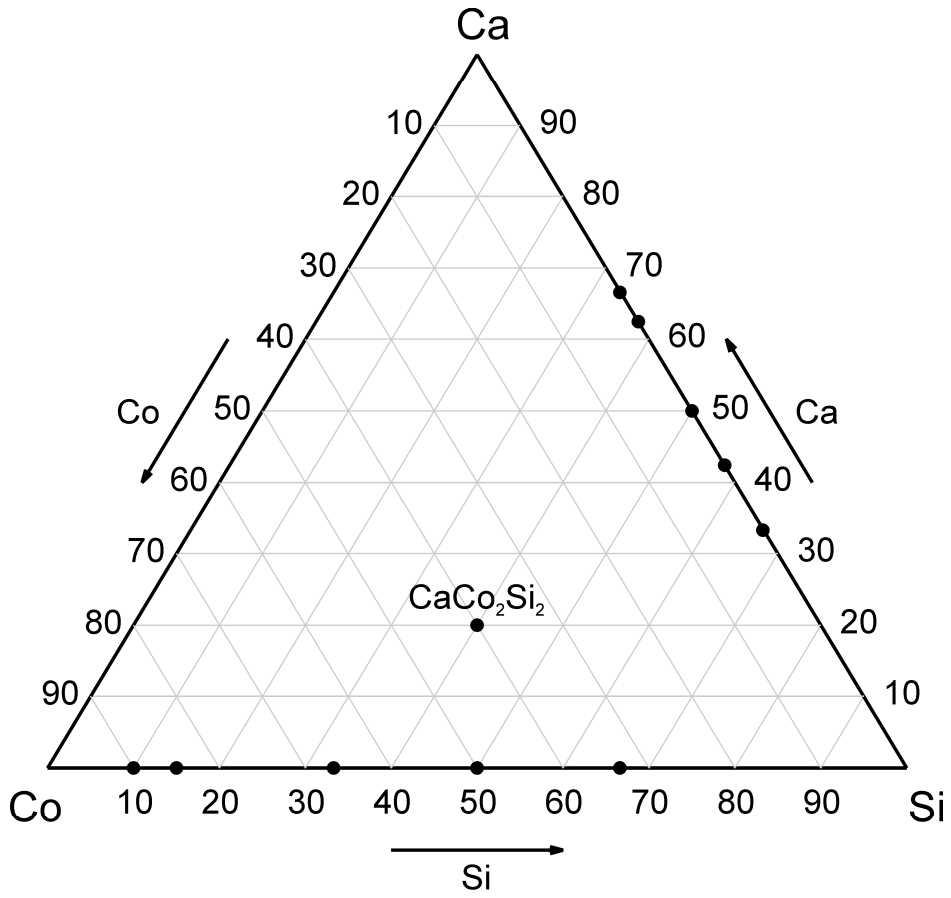

Figure A6 Composition triangle of the system Ca/Co/Si. The ternary compound $CaCo_2Si_2$ (chapter 4.4.1) is shown. The compositions of the binary phases are indicated.

Mg/Ni/Sn

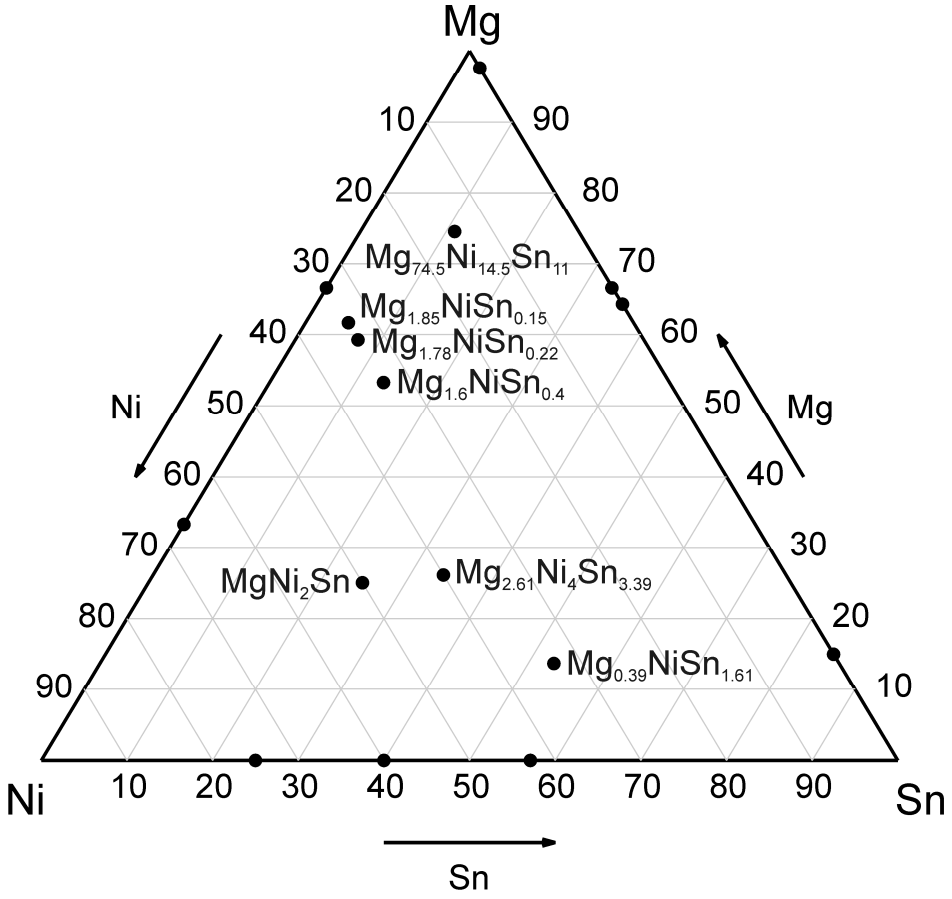

Figure A7 Composition triangle of the system Mg/Ni/Sn. The following ternary compounds are shown: $Mg_{74.5}Ni_{14.5}Sn_{11}$, $Mg_{2-x}NiSn_x$ (x = 0.15, x = 0.22 and x = 0.4), $MgNi_2Sn$, $Mg_{2.61(1)}Ni_4Sn_{3.39(2)}$ (chapter 4.5.2), $Mg_{0.39(2)}NiSn_{1.61(2)}$ (chapter 4.5.2). The compositions of the binary phases are indicated.

Ca/Ni/Sn

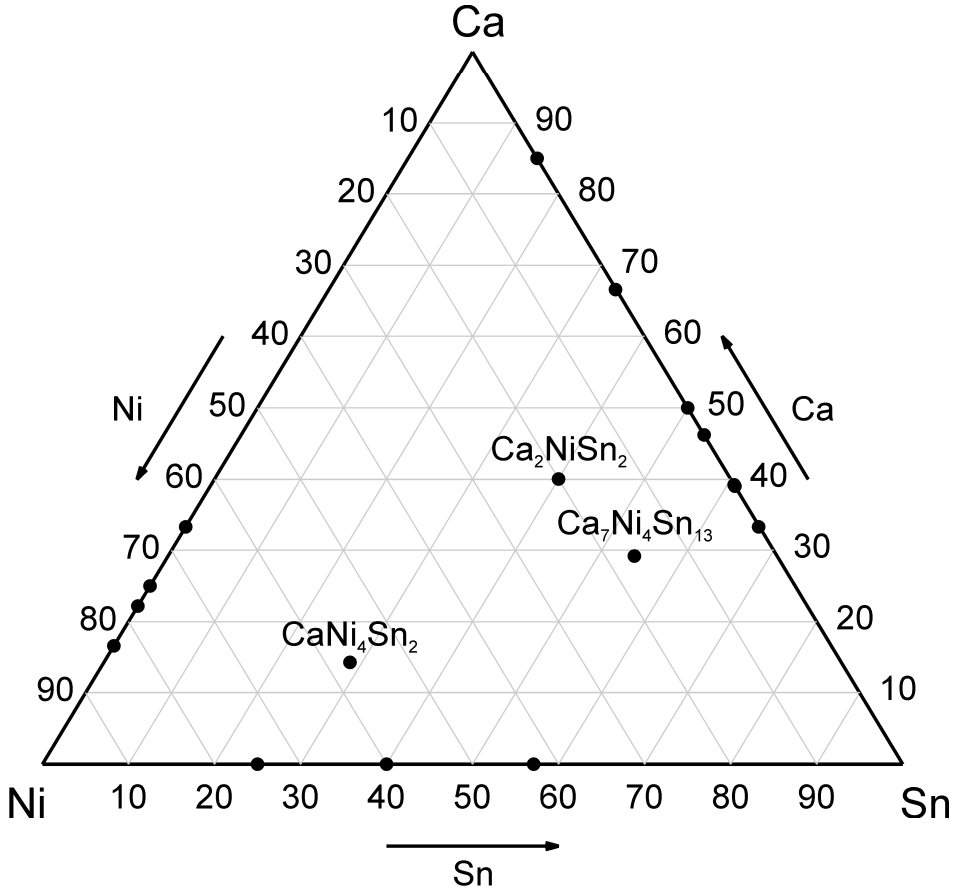

Figure A8 Composition triangle of the system Ca/Ni/Sn. The following ternary compounds are shown: $CaNi_4Sn_2$, $Ca_7Ni_4Sn_{13}$ and Ca_2NiSn_2 (two modifications, chapter 4.5.1). The compositions of the binary phases are indicated.